



## Copyright Statement

The digital copy of this thesis is protected by the Copyright Act 1994 (New Zealand). This thesis may be consulted by you, provided you comply with the provisions of the Act and the following conditions of use:

- Any use you make of these documents or images must be for research or private study purposes only, and you may not make them available to any other person.
- Authors control the copyright of their thesis. You will recognise the author's right to be identified as the author of this thesis, and due acknowledgement will be made to the author where appropriate.
- You will obtain the author's permission before publishing any material from their thesis.

To request permissions please use the Feedback form on our webpage.  
<http://researchspace.auckland.ac.nz/feedback>

## General copyright and disclaimer

In addition to the above conditions, authors give their consent for the digital copy of their work to be used subject to the conditions specified on the Library [Thesis Consent Form](#)

# **Modelling Breast Tissue Mechanics Under Gravity Loading**

by Vijayaraghavan Rajagopal.

Supervised by Assoc. Prof. Poul.M.F. Nielsen and Dr.  
Martyn.P. Nash.

A thesis submitted in partial fulfilment of the requirements  
for the degree of Doctor of Philosophy in Bioengineering,  
The University of Auckland, 2007.



Bioengineering Institute  
The University of Auckland  
New Zealand  
January 2007



# Abstract

This thesis presents research that was conducted to develop anatomically realistic finite element models of breast deformation under a variety of gravity loading conditions to assist clinicians in tracking suspicious tissues across multiple imaging modalities.

Firstly, the accuracy of the modelling framework in predicting deformations of a homogeneous body was measured using custom designed silicon gel phantoms. The model predicted surface deformations with an average RMS error of  $1.5 \text{ mm} \pm 0.2 \text{ mm}$  and tracked internal marker locations with an average RMS error of  $1.4 \text{ mm} \pm 0.7 \text{ mm}$ .

A novel method was then developed to determine the reference configuration of a body, when given its mechanical properties, boundary conditions and a deformed configuration. The theoretical validity of the technique was confirmed with an analytic solution. The accuracy of the method was also measured using silicon gel experiments, predicting the reference configuration surface with an average RMS error of  $1.3 \text{ mm} \pm 0.1 \text{ mm}$ , and tracking internal marker locations with an average error of  $1.5 \text{ mm} \pm 0.8 \text{ mm}$ .

Silicon gel composites were then created to measure the accuracy of standard techniques to model heterogeneity. The models did not match the experimentally recorded deformations. This highlighted the need for further validation exercises on modelling heterogeneity before modelling them in the breast.

A semi-automated algorithm was developed to fit finite element models to the skin and muscle surfaces of each individual, which were segmented from breast MR images. The code represented the skin with an average RMS error of  $1.46 \text{ mm} \pm 0.32 \text{ mm}$  and the muscle with an average RMS error of  $1.52 \text{ mm} \pm 0.3 \text{ mm}$ .

The framework was then tested using images of the breast obtained under different gravity loading conditions and neutral buoyancy. A homogeneous model was first developed using the neutral buoyancy images as a representation of the reference configuration. The model did not accurately capture the regional deformations of the breast under gravity loading. However, the gross shape of the breast was

reproduced, indicating that a biomechanical model of the breast could be useful to reliably track tissues across multiple images for cancer diagnosis.

# Acknowledgments

This thesis would not have been possible without the generous funding from the Foundation of Research Science and Technology NZ (FRST) through the Top Achiever Doctoral Scheme and the University of Auckland through the Doctoral Scholarship. I would also like to thank the University Research Office for providing travel expenses for conferences via the Graduate Research Fund.

The MR images used in this thesis would not have been available without the hard work of Dr. Ruth Warren to obtain Local Regional Ethical Committee (LREC) approval for the use of her images from Cambridge, UK. Thanks to Sandra Wilson, Shelley Park and our volunteer for providing their time to obtain additional MR images at the Center for Advanced MRI (CAMRI), here in Auckland, NZ.

The advisory committee, consisting of Drs. Ralph Highnam, Elijah Van Houten, Associate Prof. Alistair Young and Prof. Peter Hunter has been excellent at giving me very valuable feedback throughout the duration of this thesis.

I would also like to thank the people at the Bioengineering Institute for their help and support throughout this thesis. The reverse method would not have been developed without Dr. David Bullivant's insights. I would like to thank Kevin Augenstein for his invaluable discussions on finite elasticity theory, nonlinear optimisation and everything else that is interesting in life, Rob Kirton for the time he gave to discuss any new experimental designs and ideas, Sharif Malak's experience with tools such as the CNC milling machine were very important for the progression of the silicon gel phantom studies and Peter Blythe's appointment at the Institute proved to be very valuable. I am also indebted to Yme Kvistedal, David Nickerson and Alice Boit for their open ears to discussions ranging from breast biomechanics to jazz, comedy and the spelling of badabing badabum. I should acknowledge my office mates for putting up with my noise. Thanks also go to the other large group of people who open their doors for me to disturb them with the minutiae of my life - Rita, Zoar, Leo, Travis, David, Annalisa to just name a few.

A separate paragraph is required to highlight the importance of the Admin and IT staff for their help. It has been a pleasure to see the smiling faces at the reception

during my daily strolls around the institute. Thanks to Andrew Cantell, Tiong Lim and Stephen Poon for maintaining I.T. order in such a rapidly growing research department.

My summer students, Kenneth Tran, Xiao Bo Liu and Angela Lee have played a very important in the completion of this work. I thank them for their assistance.

Special thanks goes to Jae Chung who has been a colleague and friend whom I have worked with closely during this PhD. It has been a pleasure working as a team with what could arguably be considered as the toughest challenge to mankind - silicon gel.

This thesis could not have reached this far without the guidance of my supervisors Associate Professor Poul Nielsen and Dr. Martyn Nash. Their objective critique of my work and trust in my abilities shall never be forgotten. I am greatful for their open door policy and the support they have provided me in these years gone by.

Finally, I would like to dedicate this thesis to four people who mean more to me than my own life - My parents and two brothers. Their patience, love, support and guidance throughout my life has made me the person I am today and therefore I am forever indebted to them.

**Srimannarayana**

# Contents

<b>I Motivation and Background</b>	<b>1</b>
<b>1 Introduction</b>	<b>3</b>
1.1 Motivation . . . . .	3
1.2 Non-rigid Registration of Breast Images . . . . .	7
1.3 Thesis Overview and Contributions . . . . .	10
<b>2 Background</b>	<b>15</b>
2.1 Anatomy of the Breast . . . . .	15
2.1.1 External parts of the breast . . . . .	18
2.1.2 Internal components of the breast . . . . .	20
2.1.3 Microanatomy of breast tissues . . . . .	26
2.1.4 Changes in breast anatomy . . . . .	26
2.2 Finite Elasticity Theory . . . . .	32
2.2.1 Kinematics . . . . .	32
2.2.2 Stress tensors for finite elasticity . . . . .	35
2.2.3 Stress equilibrium and principle of virtual work . . . . .	36
2.2.4 Boundary conditions . . . . .	38
2.2.5 Generalization for different coordinate systems . . . . .	39
2.2.6 Constitutive relations . . . . .	39
2.3 Finite Elements for Finite Elasticity . . . . .	44
2.3.1 The finite element technique . . . . .	44
2.3.2 Implementation of finite elasticity . . . . .	47
2.4 Biomechanical Properties of Breast Tissues . . . . .	54
2.5 Previous Finite Element Models of Breast Biomechanics . . . . .	57
2.6 Thesis Research Proposal . . . . .	61
<b>II Validation of the Biomechanics Modelling Framework</b>	<b>65</b>
<b>3 Forward Mechanics of a Homogeneous Body</b>	<b>67</b>

3.1	Validation with an Analytic Solution . . . . .	68
3.2	Experimental Framework . . . . .	69
3.2.1	Modelling mechanical properties of silicon gel . . . . .	70
3.2.2	Phantom geometry and boundary conditions . . . . .	74
3.2.3	Applying loading conditions . . . . .	75
3.2.4	Displacement convergence analysis of phantom model . . . . .	78
3.3	Validation Experiments . . . . .	82
3.3.1	Validation method . . . . .	82
3.3.2	Validation results . . . . .	84
3.3.3	Discussion . . . . .	89
3.4	Conclusion . . . . .	90
<b>4</b>	<b>Reverse Mechanics of a Homogeneous Body</b>	<b>91</b>
4.1	Directly Calculating a Reference State - The Reverse Method . . . . .	92
4.2	Validation with an Analytic Solution . . . . .	94
4.3	Validation with an Experiment . . . . .	95
4.3.1	Validation results . . . . .	96
4.3.2	Discussion . . . . .	101
4.4	Conclusion . . . . .	104
<b>5</b>	<b>Forward Mechanics of a Heterogeneous Body</b>	<b>105</b>
5.1	The Interface between Skin and Breast Tissue . . . . .	107
5.1.1	Validation experiment . . . . .	107
5.1.2	3D-3D tight coupling . . . . .	109
5.1.3	2D-3D tight coupling . . . . .	112
5.1.4	ABAQUS . . . . .	114
5.2	The Interface between Fat and Fibroglandular Tissues . . . . .	115
5.2.1	Validation experiment . . . . .	116
5.2.2	3D-3D tight coupling . . . . .	116
5.3	Discussion . . . . .	119
5.4	Conclusion . . . . .	120
<b>III</b>	<b>Modelling the Breast</b>	<b>121</b>
<b>6</b>	<b>Modelling Breast Geometry</b>	<b>123</b>
6.1	Background and Previous Work . . . . .	124
6.2	Creating Individual-Specific Models . . . . .	125
6.2.1	Tissue segmentation and digitisation . . . . .	126

6.2.2	Initial geometry . . . . .	129
6.2.3	Automatic model generation . . . . .	133
6.2.4	Fitting Results . . . . .	137
6.3	Discussion . . . . .	143
6.4	Conclusions . . . . .	143
<b>7</b>	<b>Modelling Breast Mechanics - The Clinical Setting</b>	<b>145</b>
7.1	Clinical Experimental Plan . . . . .	146
7.1.1	Imaging the breast under gravity loading conditions . . . . .	146
7.1.2	Imaging the breast in neutral buoyancy . . . . .	151
7.2	Modelling the Clinical Experiments . . . . .	156
7.2.1	Neutral buoyancy to gravity loading - a homogeneous model .	156
7.2.2	Using the reverse method . . . . .	169
7.2.3	Using the prone gravity-loaded configuration . . . . .	177
7.3	Discussion . . . . .	184
7.4	Conclusions . . . . .	186
<b>IV</b>	<b>Thesis Review</b>	<b>187</b>
<b>8</b>	<b>Conclusions and Future Work</b>	<b>189</b>
8.1	Silicon Gel Studies . . . . .	189
8.2	Clinical Studies . . . . .	190
8.3	Future Work . . . . .	191
8.4	List of Publications . . . . .	193
<b>V</b>	<b>Appendices</b>	<b>195</b>
<b>A</b>	<b>Phantom Mould Design</b>	<b>197</b>
<b>B</b>	<b>Model Validation Using X-Ray Images</b>	<b>203</b>
B.1	Methods . . . . .	203
B.1.1	X-Ray Distortion and Biplane Registration . . . . .	204
B.2	Results . . . . .	207
B.3	Discussion . . . . .	211
<b>C</b>	<b>The Reverse Optimisation Method</b>	<b>213</b>
C.1	Preliminary Study . . . . .	214
C.2	Results . . . . .	218

C.3 Discussion . . . . .	218
<b>D Comparing ABAQUS and CMISS Simulations</b>	<b>221</b>
<b>E Defining Constitutive Models in CMISS Using CellML</b>	<b>227</b>
<b>F A Review on Characterising Mechanical Properties of Breast Tissues</b>	<b>229</b>
F.1 Yu-Neifert (1995) . . . . .	229
F.2 Krouskop et al. (1998) . . . . .	230
F.3 Wellman (1999) . . . . .	231
F.4 Williams (2000) . . . . .	232
F.5 Discussion . . . . .	234
<b>G Automatic Generation of Breast Geometries</b>	<b>237</b>
G.1 Scaling and Repositioning the Initial Mesh . . . . .	237
G.2 Further Customisation of the Initial Mesh . . . . .	242
G.3 Modelling the Skin Contour . . . . .	246
G.4 Scaling and Repositioning the Skin Fitted Mesh . . . . .	249
G.5 Modelling the Muscle Contour . . . . .	253
G.6 Adjusting Derivatives Through the Thickness . . . . .	255

# List of Figures

1.1	Typical breast compression protocols.	3
1.2	A typical mammogram of the breast.	4
1.3	Benign lesion obscured by overlapping tissue structures.	5
1.4	An ultrasound image of a simple breast cyst within the glandular layer of breast tissue.	6
1.5	A MR image of the breasts of a volunteer.	7
2.1	Gross anatomy of the breast.	17
2.2	External parts of the breast.	19
2.3	A section of the mammary gland through the nipple.	21
2.4	Lactiferous ducts and glandules.	22
2.5	Arteries, veins and nerves in the breast.	25
2.6	Microanatomy of the breast.	27
2.7	Changes in breast parenchyma during the menstrual cycle.	29
2.8	Microanatomy of the lactating breast.	30
2.9	Involution of breast parenchyma.	30
2.10	Body in reference and current configuration.	33
2.11	Deformation of line segment $d\mathbf{X}$ to $d\mathbf{x}$ .	34
2.12	A line segment with a function $u$ represented with field values $U_1$ and $U_2$ at the boundary points and linear basis functions.	48
2.13	Linear Lagrange basis functions.	48
2.14	Variation in breast biomechanical properties.	56
3.1	The tensile testing rig used to model the behaviour of the material.	70
3.2	Force-displacement data experimentally recorded and reproduced by model for the uniaxial extension of the silicon gel.	72
3.3	Comparison of finite element prediction of deformation of silicon gel under gravity.	73
3.4	Mould, gel and model.	76
3.5	Orientation of gel under different gravity loading conditions.	77

3.6	(top) Three-dimensional view of initial phantom model and data points at which strains were calculated. (bottom) Predicted mode of deformation using 30 SI gravity loading condition . . . . .	79
3.7	Graph showing the convergence of RMS error in displacements of points inside mesh (Fig 3.6) with increasing resolution. . . . .	80
3.8	Mesh resolution (with 4200 degrees of freedom) chosen for this study. . . . .	81
3.9	MRI of gel in the reference, supine and 20 SI configurations. . . . .	86
3.10	Visual representation of surface deformation matching accuracy. . . . .	87
3.11	Visual representation of the internal marker tracking accuracy for 20 SI deformation. . . . .	88
4.1	Algorithm to solve for the reference state, given a deformed state and loading conditions . . . . .	93
4.2	Convergence rate of reverse method. . . . .	95
4.3	Finite element model fitted to data from 20 SI deformation. . . . .	98
4.4	Reference configuration surface matching accuracy from the 20 SI deformation. . . . .	99
4.5	Internal marker tracking accuracy for 20 SI deformation. . . . .	100
4.6	Two predicted reference state surface data sets using the reverse method. . . . .	103
5.1	Mould and composite phantom used to validate interface models . . .	108
5.2	Data points at which displacements are recorded for convergence analysis. . . . .	110
5.3	Model convergence of RMS error in displacements of selected points inside the mesh (Fig 5.2) with increasing mesh resolution. . . . .	111
5.4	Comparison of model prediction (shaded) to experimental data (gold spheres). . . . .	111
5.5	Model convergence of the RMS error in displacements of selected points inside the mesh (Fig 5.2) with increasing mesh resolution. . . .	112
5.6	Comparison of model prediction (shaded) to experimental data (gold spheres). . . . .	113
5.7	Node used to compare between ABAQUS and CMISS shown as a gold sphere. . . . .	115
5.8	Data points at which displacements are compared for convergence analysis. . . . .	117
5.9	Model convergence of RMS error in Euclidean displacements of selected points inside the mesh (Fig 5.8) with increasing mesh resolution.	118

5.10 Comparison of model prediction (lines) to experimental data (gold spheres). . . . .	118
6.1 Segmenting different tissue types. . . . .	127
6.2 3D digital representation of the various breast tissue components obtained from manual segmentation. . . . .	128
6.3 First attempt at creation of initial mesh specific to each individual. . . . .	130
6.4 Surface fitted initial mesh showing distorted volume elements. . . . .	131
6.5 The initial mesh used to model breast geometry. . . . .	132
6.6 Scaling and translation of the initial mesh to the skin data cloud . . . . .	134
6.7 The new mesh for a particular image set, showing that the scaling and repositioning was not sufficient to produce a good initial mesh. . . . .	135
6.8 Further customisation of the initial mesh. . . . .	136
6.9 Fitting results. . . . .	138
6.10 Repositioning of the mesh. . . . .	139
6.11 Fitting results. . . . .	140
6.12 Recalculating $\xi_3$ derivatives changes the shape of the volume (in blue for example) to be less distorted, making the model usable for large deformation mechanics problems . . . . .	141
6.13 Final breast surface geometry for each individual following the fitting procedure . . . . .	142
7.1 A typical breast coil used for MR imaging of the breast. . . . .	147
7.2 (a): Polystyrene board with hole to position breasts in prone position with no contact. (b) Polystyrene board with a 11.5 degree incline. . . . .	149
7.3 Polystyrene boards used to support the lower half of the volunteer's body . . . . .	150
7.4 Overlay of cylinder on surface of mannequin breast. . . . .	152
7.5 Profile of points on mannequin and MR dataset that intersect with the cylinder opening. . . . .	153
7.6 Cylinder used for neutral buoyancy imaging. . . . .	154
7.7 Image of the breast in neutral buoyancy. . . . .	155
7.8 Generic breast mesh fitted to the skin and bone surface data points from neutral buoyancy images. . . . .	159
7.9 Data points at which displacements are recorded for convergence analysis. . . . .	160
7.10 Convergence of RMS error in Euclidean displacements of selected points inside the model (Fig 7.9) with increasing mesh resolution. . . . .	161

7.11	Mesh resolution (with 5184 degrees of freedom) chosen for this study.	162
7.12	Comparison of model prediction (lines, surfaces) to experimental data (blue spheres) for the prone orientation. . . . .	163
7.13	Comparison of model prediction to experimental data in the prone orientation. . . . .	164
7.14	Comparison of model prediction (lines, surfaces) to experimental data (blue spheres) with volunteer arched upward in MR machine. . . . .	165
7.15	Comparison of model prediction (lines, surfaces) to experimental data (blue spheres) with volunteer arched downward in MR machine. . . . .	166
7.16	Comparison of model prediction (lines, surfaces) to experimental data (blue spheres) with volunteer oriented with the right shoulder down. .	167
7.17	Comparison of model prediction (lines, surfaces) to experimental data (blue spheres) in supine position. . . . .	168
7.18	Flow chart of the material parameter optimisation algorithm to characterise the mechanical behaviour of the breast. . . . .	170
7.19	Generic mesh fitted to the skin and bone surface data points from prone gravity-loaded images. . . . .	171
7.20	Comparison of model prediction from computed reference configuration to experimental data with volunteer in “head up” position in MR machine (blue spheres). . . . .	172
7.21	Comparison of model prediction (lines, surfaces) to experimental data (blue spheres) in the “head up” orientation. . . . .	173
7.22	Comparison of model prediction (lines, surfaces) from computed reference configuration to experimental data (blue spheres) with volunteer arched downward in MR machine. . . . .	174
7.23	Comparison of model prediction (lines, surfaces) from computed reference configuration to experimental data (blue spheres) with volunteer oriented with the right shoulder down. . . . .	175
7.24	Comparison of model prediction (lines, surfaces) from computed reference configuration to experimental data (blue spheres) in supine position. . . . .	176
7.25	Comparison of model prediction (lines, surfaces) from the prone gravity-loaded configuration to experimental data (blue spheres) with volunteer in “head up” position in MR machine. . . . .	179
7.26	Comparison of model prediction (lines, surfaces) to experimental data (blue spheres) in the “head up” orientation. . . . .	180

7.27 Comparison of model prediction (lines, surfaces) from the prone gravity-loaded configuration to experimental data (blue spheres) with volunteer arched downward in MR machine. . . . .	181
7.28 Comparison of model prediction (lines, surfaces) from the prone gravity-loaded configuration to experimental data (blue spheres) with volunteer oriented with the right shoulder down. . . . .	182
7.29 Comparison of model prediction (lines, surfaces) from the prone gravity-loaded configuration to experimental data (blue spheres) in supine position. . . . .	183
A.1 Draft view of mould created for phantom studies . . . . .	198
A.2 Base plate of mould . . . . .	199
A.3 Bottom lid of mould . . . . .	200
A.4 Assembly of the parts into the mould . . . . .	201
B.1 X-ray image of a acrylic grid. No distortion visible . . . . .	204
B.2 Acrylic phantom and its x-ray images taken from orthogonal views. . . . .	206
B.3 X-ray images of the gel phantom used to measure internal marker tracking errors. . . . .	208
B.4 Visual representation of surface deformation matching accuracy in the supine deformation. . . . .	209
B.5 Visual representation of the internal marker tracking accuracy for the supine deformation. . . . .	210
C.1 The reverse optimisation method: Proposed method of estimating the reference state. . . . .	216
C.2 (a): Undeformed state and data cloud. (b): Predicted deformed state and tracked data cloud (c): undeformed state (gold lines), and initial guess at undeformed state (blue lines overlayed on undeformed) . . . . .	217
D.1 First one-element unit cube problem set up for comparison between CMISS and ABAQUS. . . . .	222
D.2 Comparison of deformed state (blue lines), predicted from the reference state (green lines) using ABAQUS and CMISS. . . . .	223
D.3 Second one-element unit cube problem set up for comparison between CMISS and ABAQUS. . . . .	223
D.4 Comparison of deformed state (blue lines), predicted from the reference state (green lines) using ABAQUS and CMISS. . . . .	224



# List of Tables

2.1	Mean and standard deviation values of the calculated Young's modulus summarizing the tested 169 breast tissue samples (From Samani et al. (2007)) . . . . .	55
3.1	Parameters used for validation purposes using analytic solution for pressure inflation, and extension of a thick-walled cylinder . . . . .	69
3.2	Deformed internal and external radii predicted for different mesh refinements of the reference state . . . . .	69
3.3	Root-mean-squared errors (RMSE) in tracking surface deformations and Euclidean distance (ED) between predicted and measured internal marker positions for the silicon gel phantom imaged using MRI. . . . .	85
4.1	Root-mean-squared errors (RMSE) in fitting finite element model surfaces to laser scanned surface deformation data. . . . .	96
4.2	Root-mean-squared errors (RMSE) in matching the reference configuration surface and Euclidean distance (ED) between predicted and measured internal marker positions for the silicon gel phantom imaged using MRI. . . . .	97
6.1	RMS errors and time for geometric fitting of skin and muscle surfaces of the finite element model to skin and muscle from MR images of breasts from six individuals. . . . .	137
B.1	Root-mean-squared errors (RMSE) in tracking surface deformations and Euclidean distance between predicted and measured internal marker (Int. Mk.) positions for a silicon gel phantom imaged using x-ray. . . . .	207
C.1	Performance of the reverse optimisation method in estimating the reference configuration with increasing degrees of freedom. . . . .	219



## **Part I**

### **Motivation and Background**



# Chapter 1

## Introduction

### 1.1 Motivation

Approximately 10% of all women will develop breast cancer during their lives and the World Health Organization estimated that 1.2 million women would be diagnosed with breast cancer world wide in 2003 alone. Currently, the best imaging modality for the early detection of breast cancer is mammography (x-ray imaging of the breast). However, the American Cancer Society<sup>1</sup> has reported that the correct interpretation of mammograms is affected by the experience of the clinician performing the diagnosis. (*Mammograms: Room for Improvement Cited*, 2004).

Figure 1.1: Typical compression protocols used for breast cancer diagnosis using mammograms (reprinted from Kita et al. (1998))

---

<sup>1</sup>URL:<http://www.cancer.org/docroot/home/index.asp>

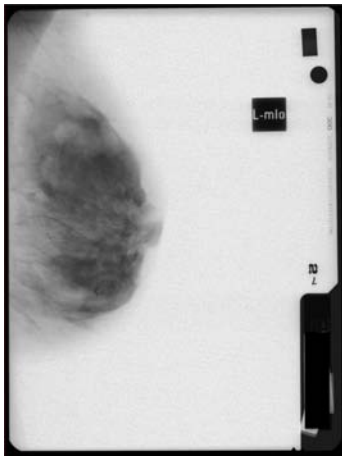


Figure 1.2: A typical mammogram of the breast. (Printed with approval from Local Regional Ethical Committee (LREC), Cambridge, UK.)

During mammography, the breast is compressed between two plates<sup>2</sup> and x-rays are transmitted through the breast to produce an image (Fig. 1.2). Compression is necessary to reduce the dosage of x-rays transmitted through the breast and increase the image contrast. Contrast of a mammogram depends on the amount of tissue that the x-rays must penetrate. Analysis of these images can become difficult if the contrast is poor or if the image is blurred. Boundary definition, for instance, is a very important way of characterising a region of tissue as benign or malignant. Benign masses generally have well defined boundaries, while malignant tumour boundaries appear blurred because the tumour tends to grow and spread through the breast tissue (Fig. 1.3). However, tissues fold over each other during compression and therefore they can introduce difficulties by obscuring boundaries of suspicious regions of tissue.

Tumour diagnosis is further impeded, because no two images show the same portion of the breast. Large deformations of soft tissues during the compression procedure make it difficult to determine the location of abnormal tissue in the breast. In the case of palpable masses, tissue deformation is not an issue since a clinician can localise the position of the mass by palpating the breast. However, in the case of smaller, non-palpable regions of tissue, it is harder to localise their positions and

---

<sup>2</sup>Typically two views are taken. A craniocaudal image and a mediolateral oblique image (Fig. 1.1)

Figure 1.3: Benign lesion obscured by overlapping tissue structures - lesion was characterized as malignant. (From *Interactive Mammography Analysis Web Tutorial* (1999))

therefore large tissue deformations can cause difficulties for diagnosis.

Apart from mammograms, clinicians also utilise additional imaging modalities such as magnetic resonance (MR) and ultrasound to further examine and characterise breast lesions. Ultrasound (or sonography) imaging involves the use of high frequency sound waves, which reflect from various tissues to form an image of the internal structure (Fig. 1.4). It is typically used for further evaluation of palpable lumps or suspicious tissue found using x-ray mammography. Ultrasound is especially useful in identifying benign tissues because of its high contrast resolution. It is also used in initial examinations of patients with dense breast tissue, since, in such cases, it is hard to identify suspicious tissues using x-ray mammograms. However, it does not have as high a spatial resolution as mammography and therefore it cannot identify microcalcifications, which are early indicators of breast cancer development. Ultrasound is also very operator-dependent, the results of an exam depending on the experience of the operator in managing the equipment (*Ultrasound Imaging of the Breasts*, 2006).

MR imaging (MRI) involves the manipulation of magnetic fields and radio waves to create images of the breast (Fig. 1.5). MRI is often used with contrast-enhancing agents to detect breast cancer. It is also useful for determining the size and location of a tumour (known as staging). MRI has a high sensitivity, and can therefore detect small abnormalities, sometimes missed with other imaging modalities. MRI

Figure 1.4: An ultrasound image of a simple breast cyst (dark object) within the glandular layer of breast tissue (From *Ultrasound Imaging of the Breasts* (2006)).

is also helpful in determining the spread of breast cancer into the chest wall. If overlooked, the spread of cancer in the chest wall can result in a patient requiring chemotherapy. However, MRI has a low specificity, making it difficult to distinguish between cancerous and non-cancerous tumours. Like ultrasound, it is also hard to identify microcalcifications, making mammography a necessity to detect early stages of breast cancer. The cost of running an MR machine and the time it takes to obtain a detailed set of images makes MRI less accessible than mammography.

Each modality has its own strengths and weaknesses, and studies such as Malur et al. (2001) and *Researchers Study The Benefits of Using Ultrasound On Women With Dense Breast Tissue* (2002) have indicated that a combination of the three imaging modalities provides a more effective way of detecting breast cancer. Accurate collocation of the suspicious regions across multiple modalities is important for a reliable diagnosis. Alignment of these images requires a non-rigid image registration technique that maps one image onto another.

**The overarching aim of this project is to equip clinicians with a software tool that assists them in their diagnostic procedures by providing**

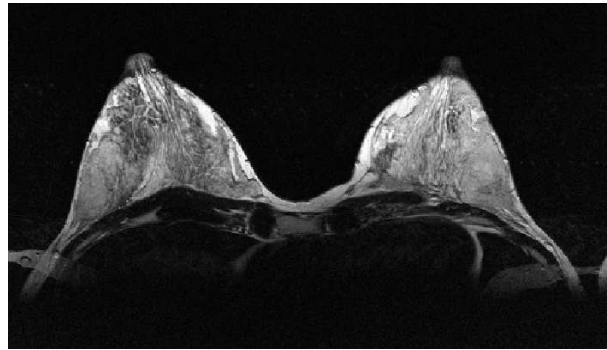


Figure 1.5: A MR image of the breasts of a volunteer. (Printed with approval from University of Auckland Ethics Committee.)

**information on the location and shape of a region of interest across multiple imaging modalities.**

## 1.2 Non-rigid Registration of Breast Images

There are two main clinical applications that the software tool could assist in:

1. Intra-modality, intra-subject registration: As mentioned earlier, it is necessary to align two mammographic images of the same breast that were obtained with two different compression protocols. Images of the breast can be taken over time to observe the spread of cancer or the response of tumour growth to radiation. Non-rigid registration of these temporal images can highlight the tumour metastasis.
2. Inter-modality, intra-subject registration: This involves the registration of breast images of the same patient obtained using different modalities. Different modalities can highlight different aspects of disease progression and therefore a registration algorithm would help to assimilate the information from different sources into one image for analysis.

Non-rigid registration is essentially an optimisation problem to find the transformation that results in an alignment with the least error between the images. Conceptually, the registration process involves the deformation of one image (slave)

so that it aligns with another image (target). There are a wide variety of approaches to solving the optimisation problem based on the type of error measure used and transformations that are performed during the registration process.

On one extreme, algorithms have been developed to use models of the object being imaged, which are realistic in depicting its mechanical behaviour. The model restricts the deformations imposed on the slave to be physically realistic. At the other extreme, algorithms have been developed to model the deformations imposed on the images using basis functions. In this type of algorithm, landmarks are identified between the two images to be registered and a transformation is computed to register these landmarks. A basis function is then used as an interpolant between the landmarks and the rest of the points in the images. In the field of breast image registration, a number of non-rigid registration algorithms have been proposed for mammographic, dynamic MR, and 3D ultrasound images. A brief overview of some of the techniques in the literature is provided in this section. The reader is directed to Wirth (2000) and Dawant (2002), who provide more detailed reviews on the broad range of methods implemented to solve the optimisation problem. Sivaramakrishna (2005) also provides a useful discussion on methods for breast image registration.

**Mammography:** Registration of mammogram sequences is an area of research that has not been given much attention until recently. Earlier methods used rigid body transformations, but more recent methods utilise non-rigid registration techniques.

Engeland et al. (2003) performed a validation and comparison study on four typical methods of mammogram registration :

1. Nipple alignment - alignment of nipple location in two images allowing translation alone.
2. Center of mass alignment - alignment of centers of mass of the two breast images allowing translation alone.
3. Mutual information - alignment based on mutual information, allowing rotation, translation, scaling and shearing. Mutual information measures the amount of information one image has about another image. A mutual information maximisation problem can be developed to provide the best non-rigid alignment of images across multiple modalities and views.

4. Warping - involves alignment of automatically detected control points and warping of the image by interpolating between the control points using a thin plate spline interpolation function (similar to (Marias et al., 1999)).

Experiments showed that the mutual information alignment method performed best (mean of 7.9 mm between lesions in the two views) and warping (24.5 mm between lesions across the two views) performed the worst due to limitations in its boundary surface matching procedure. The success of the mutual information method was attributed to the use of internal breast tissue information in the registration process. It was also clear from the study that correct segmentation of the nipple and pectoral muscle were critical to the accuracy of the first two methods of alignment.

**Ultrasound:** A majority of methods for ultrasound image registration consisted of control-point based semi-automatic approaches (Sivaramakrishna, 2005). Ultrasound images are more difficult to register due to problems such as shadowing, geometric distortions (due to refraction) and low contrast. Xiao et al. (2002) performed non-rigid registration on free-hand ultrasound images of the breast. Free-hand acquisition involves the recording of the position and orientation of each 2D scan obtained by a clinician who holds the ultrasound probe and manipulates it over regions of interest. The localizer recording is then used to reconstruct the 3D anatomy. Since the breast deforms during the ultrasound scans, the 3D reconstruction typically appears blurred. Xiao et al. (2002) used local statistics and a “block matching” registration technique to align the reconstruction images. A reference image was sampled at a set of grid points and each sample was a block of voxels centered on a grid point. The block was then moved to several positions within a search window and a similarity measure (based on voxel intensities) was evaluated between the target and slave images. The position that maximised the local voxel similarity measure was chosen as the best alignment.

**MR:** In the case of MR registration, a large part of the research has focused on the registration of pre- and post-contrast MR images, which contain motion artifacts due to patient movement and breathing. Rueckert et al. (1999) performed affine transformations to align contrast-enhanced MRI globally and used free-form deformations with B-splines to align local breast motion. Mutual information was used as a similarity measure and MR images of volunteers and patients were regis-

tered using the algorithm. It was shown that non-rigid registration produced better results than affine and rigid body transformations. Registration accuracy was measured as the squared sum of intensity differences and was 12.5 intensity units for the alignments registered using the aforementioned technique and 23.63 intensity units with rigid registration (registration accuracy was 38.52 intensity units before registration).

Both Tanner et al. (2002) and Rohlfing & Maurer (2003) showed that the method proposed in (Rueckert et al., 1999) could be improved by introducing a volume-preserving penalty term into the algorithm. This restricted non-rigid deformations from changing the volume of the breast represented in the image. Rohlfing & Maurer (2003) showed that, without a volume-preserving constraint, volumes of contrast enhanced lesions decreased by 1%-78% when registering pre- and post-contrast MR images of the breasts of 17 patients.

The need for volume-preserving constraints indicated that non-rigid registration algorithms require further validation to measure the accuracy of the transformations in capturing the tissue deformations during imaging. A number of registration techniques have produced promising results, but it is still unclear whether the registration algorithms use physically plausible deformations to align the images. The validation method of Schnabel et al. (2001) in using breast biomechanics models, and the improvement in using volume-preserving constraints, show that an anatomically realistic computer model of the breast can not only help validate non-rigid registration algorithms, but could also be used in a non-rigid registration algorithm to provide accurate registration of breast images. To this end, there has been a growing interest in developing computer models of the breast to predict tissue deformation under a variety of image loading conditions.

**We believe that anatomically realistic models of the breast will provide the necessary constraints to non-rigid registration algorithms and improve the accuracy of the alignment process.**

### 1.3 Thesis Overview and Contributions

**The work in this thesis focusses on the development of anatomically realistic finite element models of the breast for accurate simulation of breast**

**deformation under gravity loading conditions.** These predictions can be useful in the clinical setting, for example, when a patient moves from a prone to a supine position. A patient typically lies prone on a dedicated MR breast coil during MR imaging, and supine for ultrasound or breast biopsy procedures. The significant change in shape of the breast between these orientations can make the localisation of non-palpable masses difficult. Simulations of deformed configurations under different gravity loading conditions can be useful in mapping the locations of the masses between these images.

This thesis is divided into four major parts, each consisting of a set of chapters focused on a specific area of work. An overview of the parts and chapters in this thesis are provided here, highlighting the contributions made by this body of work to the field of breast biomechanics.

## Part I: Motivation and Background

Part I provides an introduction and background information to the work in this thesis.

- **Chapter 2** provides background information on the anatomy of the breast and the mechanics theory and basic modelling framework used to predict breast deformation. The chapter concludes with a review of the literature in breast biomechanics modelling and describes the approach taken in this thesis to address important questions unanswered in the literature.

## Part II: Validation of the Biomechanics Modelling Framework

Part II describes the work done towards validating the basic modelling framework for modelling large deformations.

- An important contribution of this thesis is the experimental framework that has been developed to systematically examine the different sources of error in the modelling framework. Silicon gel phantoms have been custom-made and subjected to loading conditions similar in nature to those applied to the breast, providing a measure of the accuracy of predictions using controllable boundary conditions, material properties, and accurate models of the geometry. **Chapter 3** describes the experimental framework and results of a study

to track surface and internal marker deformations of a homogeneous phantom. This study validates the basic finite elasticity framework that is used to predict large deformations of soft tissues.

- As the breast is under gravity loading at all times, a model of the reference state cannot be obtained from current imaging techniques - an aspect that has been overlooked by previous researchers. **Chapter 4** focusses on the problem of identifying a reference state when given a number of deformed states under different gravity loading conditions, and the material behaviour is known. Once again, validation experiments were conducted on silicon gel phantoms to assess the performance of the method proposed.
- The breast is a heterogeneous body with an outer layer of skin enclosing fatty and fibroglandular tissue. **Chapter 5** describes what is, to the author's knowledge, the first set of experiments (on silicon gel phantoms) conducted to validate the framework for modelling heterogeneous bodies. The focus of the chapter starts with the interface between a stiff thin membrane enclosing a soft gel and moves to modelling the interface between two gels of similar proportions, but of different stiffnesses.
- Apart from validating heterogeneous material deformations, it was also necessary to develop the modelling software, CMISS<sup>3</sup>, to be able to model the heterogeneities in the breast. It was decided to use the CellML<sup>4</sup> language to define the constitutive relations of the different breast tissues. The CellML language project is under active development at the Bioengineering Institute for the dynamic specification of mathematical models of electrical activation in the heart at run-time. While Nickerson (2005) incorporated CellML into CMISS for easy use of plug-and-play cardiac activation models, CMISS was further developed in this thesis for describing mechanical constitutive relations using CellML. This development, described in Appendix E, is an important contribution to the IUPS Physiome project<sup>5</sup>. For example, it has enabled a

---

<sup>3</sup>[www.cmiss.org](http://www.cmiss.org)

<sup>4</sup>[www.cellml.org](http://www.cellml.org)

<sup>5</sup>[www.physiome.org.nz](http://www.physiome.org.nz)

number of researchers to create CellML files describing a tissue mechanical behaviour without the need to learn the CMISS computational implementations. The implementation also allows for fine resolution regional variation of material parameters, rather than simply varying between mesh elements. Thus it allows more freedom for the modeller to decide the best way of modelling heterogeneity, and can potentially avoid highly refined models which result in expensive computations.

### Part III: Modelling the Breast

Although silicon gel phantom studies are important to validate the modelling framework, clinical validation is essential for developing a reliable tool for clinicians and convincing them of its utility. Part III shows the work done to develop a clinical validation framework.

- **Chapter 6** describes a semi-automatic algorithm that was developed to create finite element geometries of volunteers' breasts from MRI data. Although previous studies in the literature have developed methods to automatically generate models, none have used cubic-Hermite basis functions to model the geometry. This not only makes the models look more realistic, but also has the potential of giving more accurate and efficient deformation predictions with fewer degrees of freedom and detail than those developed in the literature (Nielsen et al., 1991).
- **Chapter 7** describes the clinical experimental framework that has been developed for validating models of the breast to predict gravity loaded deformations. The experimental framework provides a rich set of data, previously unavailable, and is an important contribution towards the breast biomechanics field. The chapter then demonstrates the performance of the modelling framework described and developed in part II using the breast images of a volunteer obtained from the experiments.

### Part IV: Thesis Review

- **Chapter 8** summarises the work presented in this thesis and outlines future directions towards developing a clinically applicable tool. A list of publications

arising from this work is also provided at the end of the chapter.

# Chapter 2

## Background

This chapter provides the necessary background information to develop an anatomically realistic computational model of the breast. Section 2.1 provides a description of the gross and micro anatomy of the breast. This is followed by a description of finite elasticity theory (Section 2.2) and its implementation using the finite element method (Section 2.3). Biomechanical properties of breast tissues are discussed in Section 2.4 and a general review of the previous work in modelling breast biomechanics is then provided in Section 2.5. The chapter concludes with a description of the approach taken in this thesis to develop a reliable finite element model of the breast (Section 2.6).

### 2.1 Anatomy of the Breast

An understanding of the tissue organisation is important for any biomechanical model development, since the mechanics of a body is influenced by the structure and mechanical properties of its constituents. This section first provides an overview of the gross and micro anatomy of the breast. The section then highlights some of the changes in structure and composition of the constituents of the breast with age, disease and physiological condition. The gross anatomical overview is predominantly based on the work conducted by Cooper (1840), while the microscopic anatomical description is based on Vorherr (1974). The reader is directed to these books for more in-depth information.

Fig. 2.1 depicts the gross anatomical structure and organisation of the female

breast. The mammary glands are situated on the anterior and lateral parts of the chest. They extend from the second or third rib, resting on the platysma myoides muscle and terminating at the sixth or seventh rib placed upon the external oblique muscle. The inner (sternal) side of the breast rests on the pectoralis major and cartilages of the ribs, while the outer (axillary) side rests on the fascia of the thorax, serratus major and external oblique muscles. The breast thickness varies at different regions. It is very dense and compact in the axillary margin and the abdominal margin at the seventh rib while it is much thinner at the sternal and superior margins at the third rib.

The breast components can be classified as either external or internal. External components consist of the nipple, areola, tubercles and some glands. The internal part consists of the secretory gland to produce the milk necessary to feed an infant.

Figure 2.1: Gross anatomy of the breast (Reproduced from (Netter, 1997)).

### 2.1.1 External parts of the breast

#### The nipple

The nipple (shown in Fig 2.1 and Fig. 2.2(a)) is a conical shaped, cutaneous projection on the breast, which is attached to the areola at its base. The nipple contains the terminations of nerves, blood vessels and the ducts from the internal breast gland (carrying milk for the infant), which are all encased by fibrous tissue. It is situated nearer the abdominal margin of the breast than the superior, clavicular margin. Its centre surface area is cibriformed with the numerous terminations of nerves and lactiferous ducts that perforate it.

The nipple is covered by a texture called the cuticle. On the inner surface, the cuticle forms irregular meshes and adheres to the cutis<sup>1</sup> of the nipple by passing between projections and entering its pores (shown in Fig. 2.2(b)).

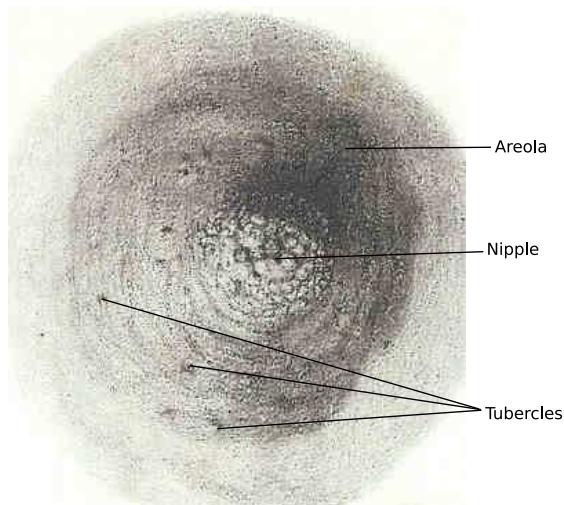
The cutis of the nipple is made up of two surfaces: The first is a disk consisting of a large number of papillae (needed for adhesion to lips of the infant while suckling) forming an erectile and highly sensitive tissue. The second is a broad, flat, truncated apex in which the terminations of milk tubes may be seen. The inner side of the cutis is lined by fibrous tissue passing from the surface of the breast to the skin. This fibrous structure connects the nipple to the gland of the breast and restricts the deformation of the nipple. A cellular elastic tissue is also constituted in the nipple to allow some flexibility and encloses the lactiferous ducts, nerves, absorbent vessels, and blood vessels. This fibrous tissue is more organised in the nipple than the fibrous tissue elsewhere in order to have controlled secretion of milk for the infant.

#### The areola

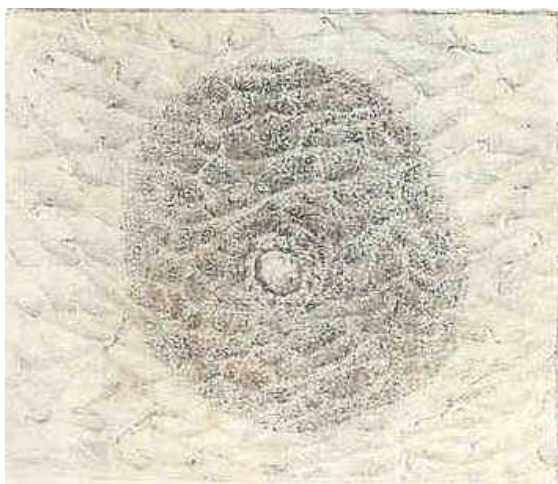
The areola (shown in Fig. 2.1 and Fig. 2.2(a)) is the part of the skin that forms the circular base of the nipple. The cuticle covering the areola is thin and passes between the papillae and into the folds of the cutis of the areola. The areola also consists of papillae, smaller than those of the nipple, which can be found on the surface, providing greater adhesion of the lips of an infant during suckling. In addition to

---

<sup>1</sup>Cutis: Combined term for the epidermis and the dermis, the two outer layers of the skin.



(a)



(b)



(c)

Figure 2.2: (a) Nipple and areola. Tubercles appear upon various parts of the areola, forming a circle around the nipple. (b) The inner side of the cuticle of the nipple, areola and surrounding breast showing the folds which are formed to sink into the cutis of the nipple. (c) A tubercle filled with red injection. (Reproduced from (Cooper, 1840))

the papillae, the areola consists of tubercles (Fig. 2.2(a) and 2.2(c)), which discharge a lubricating secretion and add firmness to the adhesion of the lips of an infant.

### 2.1.2 Internal components of the breast

#### Fascia mammae and Cooper's ligaments

The fascia mammae are divided into a superficial and a deeper layer of the breast, between which the gland of the breast is situated. Both layers are attached to the ligamentous substance that covers the sternum. Fig. 2.3 shows the separation of the fascia at the left edge of the image and the reconnection on the right edge of the image (a→a).

The superficial layer passing over the breast gland forms a fibrous cover, passing between the gland and the skin and also entering the interior of the gland. Fibrous extensions proceed from the superficial layer to the posterior surface of the skin. These fibrous extensions are called Cooper's ligaments (or suspensory ligaments) and provide firmness to the breast (the Cooper's ligaments can be seen connecting the breast to the skin in Fig. 2.3). At the superficial layer, these ligaments are spread over the top of the secretory gland. They support folds of the glandular structure and connect the portions of the glands to each other by penetrating the gland. The ligaments also connect the nipple to the gland. The deeper layer of the breast also sends fibres into the gland to unite its parts, and sends fibres backwards to attach to the pectoralis major (bottom of Fig. 2.3). The breast is cushioned between these two fibrous layers and the fat lobes between the Cooper's ligaments to protect it from pressure and harm. All the glandular components are interconnected by the fibrous innervations of these layers into the gland.

#### Lactiferous tubes

The openings of the lactiferous ducts (shown in Fig. 2.4(a) and Fig. 2.4(c)) that transport milk from the glandules in the breast are situated at the surface of the apex of the nipple. The orifices are arranged radially around the surface and range between fifteen and twenty in number. At the apex of the nipple, the surface is cribriform and constitutes a mixture of fibrous tissue that help relax the orifices from the high pressure of milk. In this region of the breast, the lactiferous tubes are

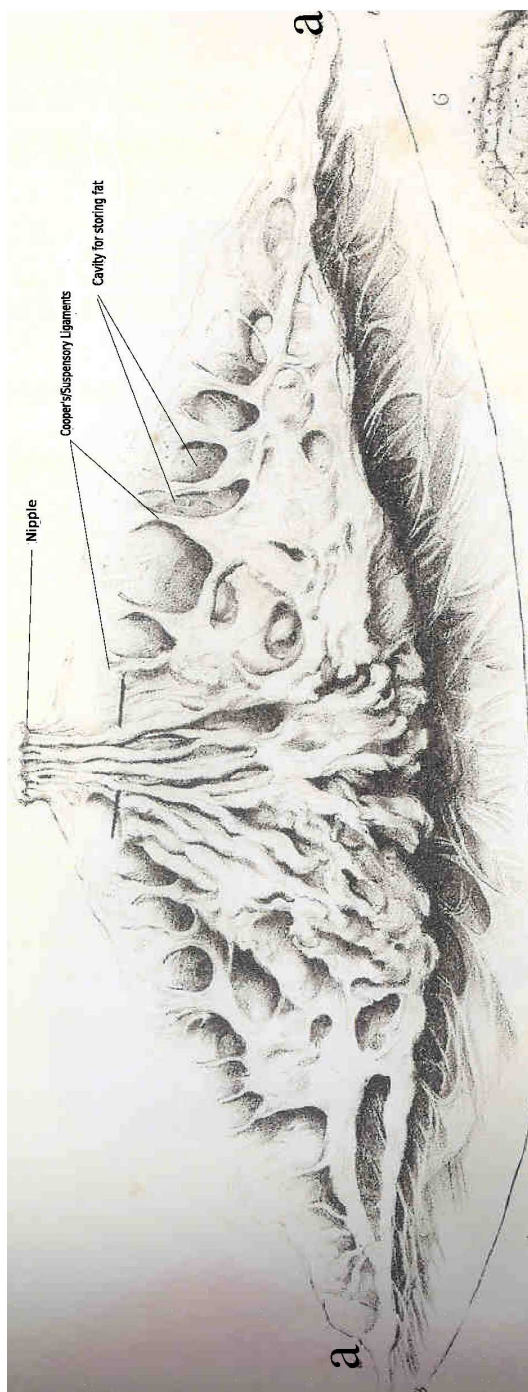


Figure 2.3: A section of the mammary gland through the nipple. (Reproduced from (Cooper, 1840))

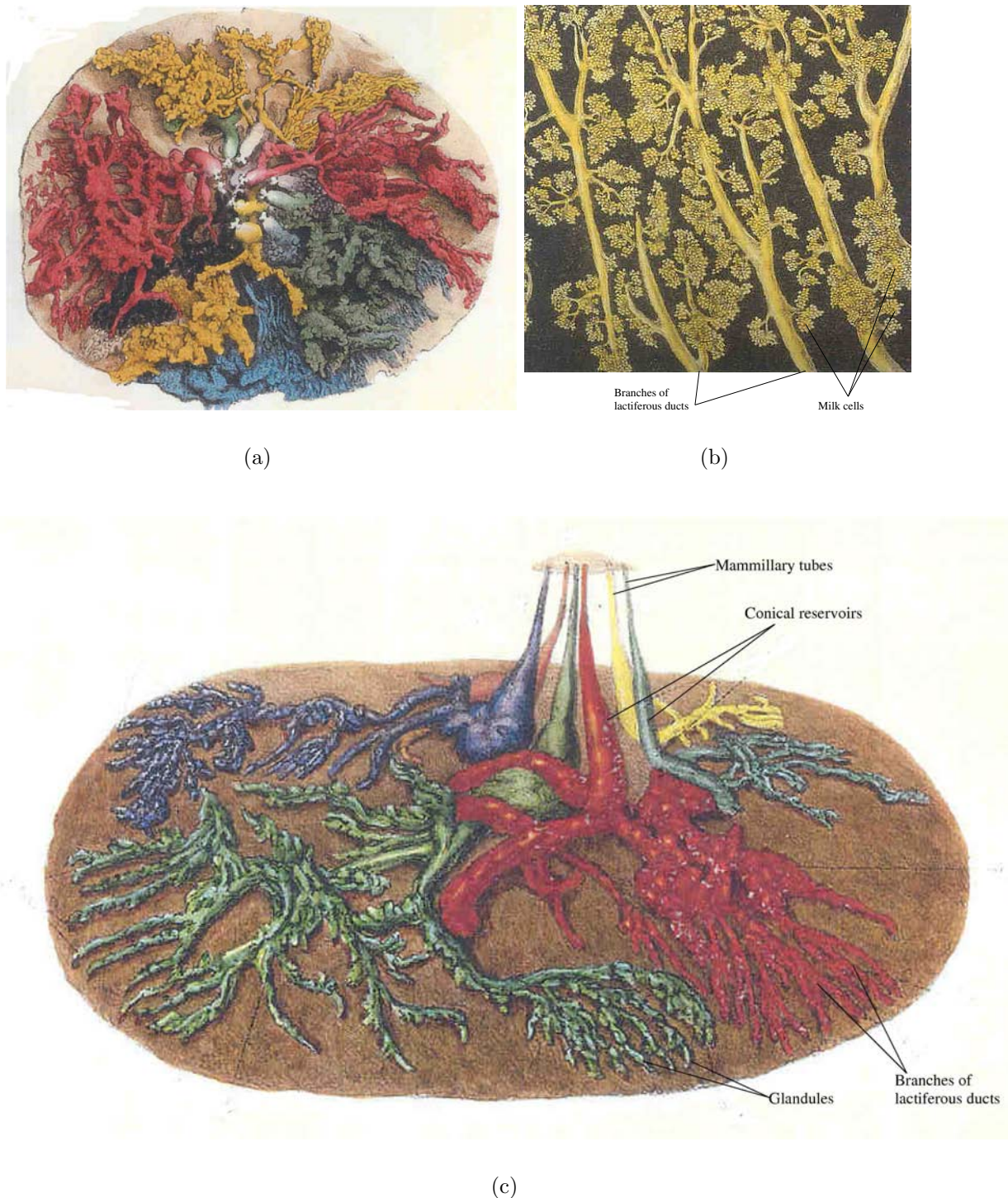


Figure 2.4: (a) Lactiferous ducts and the glandules from which they originate, injected with green, blue, red, yellow and black wax. The ducts in the lower part run over each other to provide a cushion. The ducts in the upper region are singular. (b) The branches of the lactiferous ducts extending to the glandules consisting of a group of milk cells. (c) A view of a preparation of six milk tubes injected from the nipple, showing the path from mammillary tubes to glandules. (Reproduced from (Cooper, 1840))

straight and distinguished from other regions of the breast by the name mammillary tubes. From the orifice, the mammillary tubes dilate and take a conical form as they increase in diameter to the base of the nipple. The fibrous tissue is interspersed between the tubes to keep them in place and provide strength. The tubes are lined with an elastic, highly vascular mucous membrane. The tubes lose pressure from the nipple and are much larger at the base of the nipple. These enlarged tubes are conical reservoirs and are lined on the inside with a vascular mucus membrane with a fibrous coat to provide resistance against high pressure loads from the milk stored.

The milk in these reservoirs comes from five or six branches of milk tubes. These milk ducts (or mammary ducts), which terminate at the reservoirs, begin as small branches from the glandules and increase in size at termination (see Fig. 2.4(c)). The greater thickness of the breast in the axillary and abdominal margins is due to multiple branches of three or four milk ducts that radiate from the centre to the circumference of the breast. Only a single duct radiates to the thinner sternal and superior margins. The branches do not radiate equally and therefore some branches are longer than others. Some of these longer branches turn over the gland and provide a further thickening of the breast (shown in Fig. 2.4(a)). The overall ductal organisation of the breast can be visualised like the roots of trees growing next to one another, without a distinct pattern being formed or any connections between them.

## Glandules

The breast constitutes a number of glandules (shown in Fig. 2.4(c)) connected by the fibrous or fascial tissue of the gland. Mammary ducts arise from these milk sources as little branches that grow larger until they terminate at the reservoirs at the base of the nipple.

## Milk cells

Each glandule is filled with a large number of elastic milk cells (also known as alveoli, shown in Fig. 2.4(b)) which are lined with the same mucus membrane that lines the lactiferous ducts. The milk cells store the milk that is secreted from the blood, which is carried to them by arteries. This allows the blood that has not been converted to

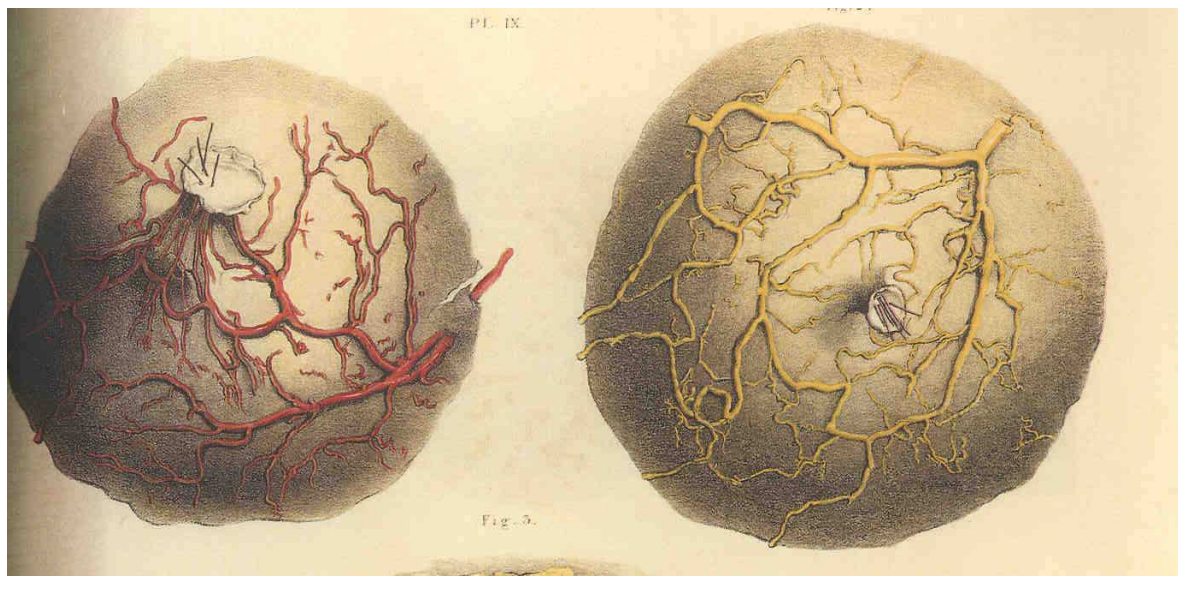
milk to carry on through the veins back into the circulation.

### **Fat**

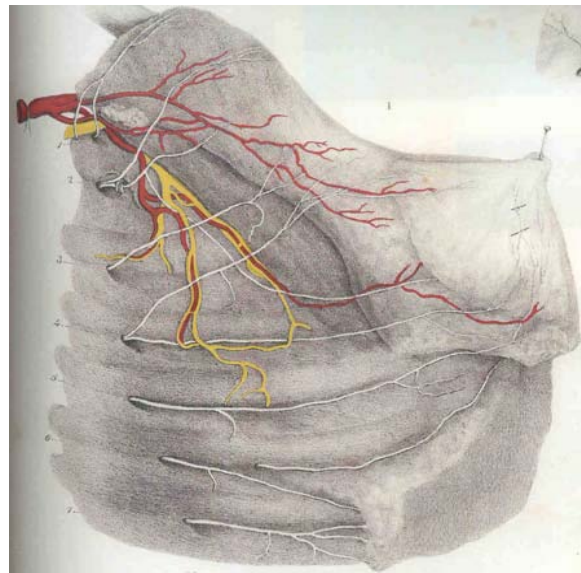
Fat is a predominant tissue type in the breast that fills up depressions between glandules, large lobes between Cooper's ligaments (fat cells also line the suspensory ligaments to form a vascular membrane), between anterior folds of the glandular tissue and between the two layers of fascia mammae (cavities in Fig. 2.3 and Fig. 2.1).

### **Arteries, veins, absorbent vessels and nerves**

The breast consists of a number of arteries, veins and nerves to make it a functional organ that secretes milk according to demands of an infant. Absorbent vessels are situated in the breast, acting to reduce the amount of water in the milk in order to make it more nutritious. These vessels also act to avoid accumulation of milk in the ducts in the absence of an infant. These networks of vessels and nerves are currently not considered to be influential in the mechanical behaviour of the breast during compression. Hence the organisation of these structures shall not be outlined in this thesis. However, for an overview of the organisation, examples are shown in Fig. 2.5. The reader is pointed to (Cooper, 1840) further information.



(a)



(b)

Figure 2.5: (a) Left: The arteries going to the breast and nipple. Right: The veins returning the blood from the nipple and breast. (b) A nerve going to the breast (Reproduced from (Cooper, 1840))

### 2.1.3 Microanatomy of breast tissues

The ductal network and milk cells are formed of epithelial cells that are cuboidal in shape and have a low cylindrical surface area (Vorherr, 1974; McManaman & Neville, 2003). Ductal epithelial cells contain fewer mitochondria, sparse endoplasmic reticulum, ribosomes and tonofilaments than their alveolar counterparts.

There are three major types of epithelial cells: (1) superficial (luminal) A-cells, (2) basal B-cells and (3) myoepithelial cells (see Fig. 2.6). Luminal A-cells are involved in milk synthesis and secretion during lactation and appear dark due to their abundance of robosomes. Basal B-cells are the most numerous and are clear and transparent structural elements of the epithelium. Current research also indicates that these clear cells are stem cells that differentiate into luminal and myoepithelial cells (Smith & Chepko, 2001; Gudjonsson et al., 2002). Myoepithelial cells are located around alveoli and the small excretory milk ducts. These cells act as contractile smooth muscle cells that eject milk from the alveoli and small milk ducts into the lactiferous ducts during the stimulus of suckling and the consequent release of oxytocin. To perform this function, myoepithelial cells have myofilaments in their sarcoplasm and branch around the alveoli in a star-like pattern.

The ductal and alveolar network is embedded in an extracellular matrix (stroma or ECM) of fat and fibrous connective tissues from the fascia mammae (see Fig. 2.6(d)). This extracellular matrix is a dense mesh of collagens, and glycoproteins that are secreted by the parenchymal cells. Collagens present in the matrix include Types I, III, IV, V, VI and I-trimer collagen. Glycoproteins in the ECM include laminin, fibronectin, vitronectin, thrombospondin tenascin, hyaluronan, and heparan sulfate proteoglycan. (Lochter & Bissell, 1995). The quantity and organisation of these collagens and glycoproteins in the ECM directly contribute to the mechanical behaviour of the breast.

### 2.1.4 Changes in breast anatomy

The breast undergoes significant morphological changes due to alterations in physiological conditions such as the menstrual cycle, pregnancy, and the onset of menopause. Pathological conditions such as breast cancer also cause morphological changes. This section provides a brief overview of these physiological and patholog-

(a)

(b)(c)

(d)

Figure 2.6: (a) Microanatomy of the milk producing alveolus showing the three different epithelial cell types and their surroundings. (b) An alveolus showing the two layers of luminal cells (inner layer) and myoepithelial cells (outer layer). (c) Topography of the starlike myoepithelial cells surrounding the alveoli and the minor ducts. (d) Micro anatomy of the breast stroma showing the fat (white cells) and fibrous components (pink fibres). (Reproduced from (Vorherr, 1974; Tot et al., 2002))

ical changes in breast anatomy.

### The ductal and alveolar networks

The proliferative phase of the menstrual cycle sees an increase in the mitotic rate and consequent proliferation of the alveolar cells induced by ovarian estrogens (Kopans, 2007; Vorherr, 1974). Mammary ducts become enlarged and the alveolar cells begin to secrete their contents into the lumen. In the luteal phase of the menstrual cycle, blood flow increases in the mammary glands which now exhibit increased tightness, fullness, and tension. Breast volume increases by 15 to 30  $cm^3$  during this time due to increased water retention and new formations of ductal and alveolar networks. Towards the end of the menstrual cycle tissues start to regress and lobuli become smaller and apoptosis of cells occurs (see Fig. 2.7).

Pregnancy induces a significant growth in the ductal-alveolar network. Within the first trimester of pregnancy, the breast exhibits an increase in the number of alveolar cells and the formation of new ductal networks. Glandular epithelial cells grow and invade connective tissues and replace fatty tissues in the connective matrix. During the second trimester, lobules increase in size as alveolar cells continue to proliferate and begin to store colostrum (form of milk. See Fig. 2.8). In the third trimester fat droplets begin to accumulate along with colostrum in the secretory cells. When lactation stops, an involution phase begins in the breast when the alveolar-ductal network starts to diminish to a less lobular morphology over a three month period.

The breast undergoes long-term involution over a woman's lifetime. As a woman ages, alveolar cell linings decompose and lobules shrink in size in a non-uniform fashion (see Fig. 2.9). Connective tissues are replaced by fat and parts of the ductal networks are destroyed as the ductal cells also undergo atrophy. Studies have shown that fibroglandular tissue content decreases with age, while fat content increases. This gradual change of breast structures does not seem to start at the onset of menopause but begins earlier in the thirties or forties and progresses at varying rates in individuals (Kopans, 2007).

(Kopans, 2007) provides a good overview of pathological conditions within the breast. Pathology is typically categorized by the level of the ductal network in which they occur. It is believed that most cancers occur at the terminal connection between

(a)

(b)

(c)

Figure 2.7: (a) At the beginning of the menstrual cycle, the lobules are small and contain minimum amount of secretion from the alveoli. (b) When alveoli secrete their contents the stroma is filled with fluid and is expanded. (c) During menstruation the myoepithelial cells are vacuolated and apoptosis begins. (Reproduced from (Tot et al., 2002))

Figure 2.8: A section of a lactating breast showing expanded alveoli filled with colostrum (white space). (Reproduced from (Mansel & Bundred, 1956)).

(a)

(b)

Figure 2.9: (a) shows a functioning lobule with alveoli and (b) shows an involuted lobule with very few milk producing units. (Reproduced from (Tot et al., 2002))

alveolar cells and the ductal network. As the name suggests, “ductal carcinoma in situ” (DCIS) appears on the inner linings of the ductal networks. It is believed that DCIS develops into the more lethal form of breast cancer, “invasive ductal carcinoma”, which invades the connective tissue network. Fibroadenomas are the result of an overgrowth of the connective tissue around the alveolar cells. The reader is referred to Kopans (2007) and Tot et al. (2002) for further details on the microstructure of diseased breasts.

### The extracellular matrix

Cell to cell and cell to ECM interactions enable the ECM to maintain mammary gland structure and function (Hansen & Bissell, 2000). The ECM undergoes remodelling during changes in physiological conditions such as the menstrual cycle, pregnancy and lactation. For instance, laminin, entactin, type IV collagen and heparan sulfate proteoglycan molecules are deposited in the matrix during proliferation of mammary ducts (during the proliferative phase of the menstrual cycle), while ECM proteases break down these molecules during an involution phase (towards the end of the menstrual cycle) (Lochter & Bissell, 1995; Ferguson et al., 1991). The quantity of ECM components also changes in disease states such as cancer. Current research indicates that cancerous growths cause a malfunction in the normal signalling pathways between the ECM and the parenchymal tissues of the breast (Hansen & Bissell, 2000; Paszek & Weaver, 2004). The reader is directed to Hansen & Bissell (2000), Paszek & Weaver (2004) and other relevant literature for more detailed information on changes in ECM composition.

## 2.2 Finite Elasticity Theory

With the anatomy described this section outlines the following four key relations that must be taken into account when modelling large deformations of breasts (Malvern, 1969; Atkin & Fox, 1980; Spencer, 1980):

1. Kinematics: This defines a set of equations which relate three-dimensional strain tensors to displacement gradients.
2. Stress equilibrium: A set of equations are derived from laws of conservation of linear momentum and angular momentum.
3. Boundary conditions: The external loads or displacements that are imposed on the body during deformation must be taken into account.
4. Constitutive relations: A set of equations relating the stresses to strains. These relations model the behaviour of the specific material of interest and are determined from experiments with a few theoretical restrictions imposed on them.

### 2.2.1 Kinematics

The kinematic equations describe the motion of a body subjected to loads and are outlined below.

#### Coordinate Systems

Consider Fig. 2.10. The body  $\beta_0$  has been subjected to a load and is now in a deformed state  $\beta_\alpha$ . The deformed state of the body is referred to as the *current configuration* and the original, undeformed state is referred to as the *reference configuration*. For these two configurations, large deformation mechanics uses two types of coordinate systems when analysing stresses and strains:

**Material Coordinates** A set of coordinates  $(X_1, X_2, X_3)$  is used to track each material point from the reference configuration to the deformed configuration. As the body deforms, the material coordinate axes deform with it, and hence the coordinate values of a material point do not change during the deformation. This material coordinate system is often called a *Lagrangian* description.

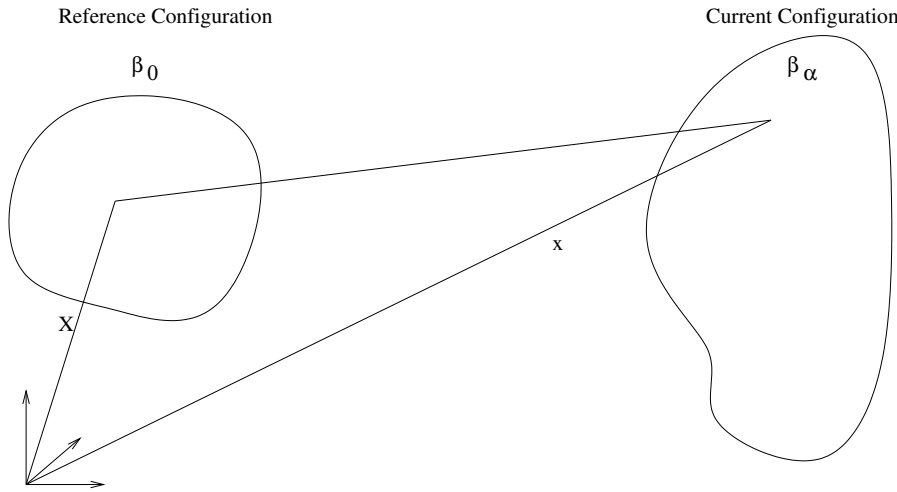


Figure 2.10: Body in reference and current configuration.

**Spatial Coordinates** A spatial coordinate system is often called an *Eulerian* description of a body's coordinates. A spatial coordinate system is a fixed coordinate system in space. When a body is represented by a global spatial coordinate system, the coordinates identify a specific position in space. Hence, if a body is in motion, a coordinate,  $(x_1, x_2, x_3)$ , associated with a material point  $\mathbf{p}$  at time  $t_0$ , may be associated with a different material point  $\mathbf{q}$  at time  $t_1$ .

The measure of strain requires a relationship between the spatial coordinates of material points in a deformed body and the material coordinates of the material points in the reference configuration. It is then possible to measure a change in the length of a material line segment using this relationship.

### The Kinematic Tensors

Let the positions of the material particles in the deformed state at time  $t$  be functions of their position in the reference configuration. In the case of quasi-static deformations, the relationship depends only on the material positions and not time. Therefore the relationship is defined by

$$\mathbf{x} = \mathbf{x}(\mathbf{X}) \quad (2.1)$$

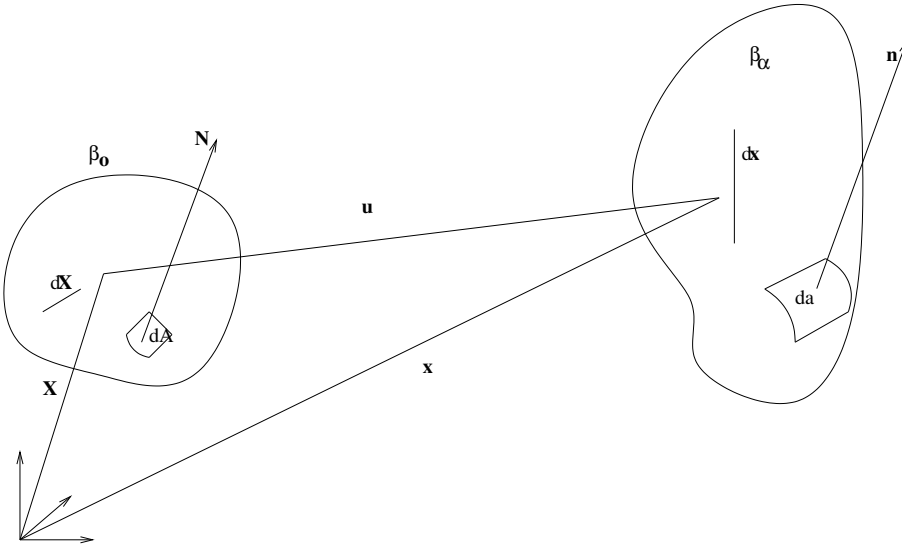


Figure 2.11: Deformation of line segment  $d\mathbf{X}$  to  $d\mathbf{x}$ .

Consider an infinitesimal line element  $d\mathbf{X}$  in the reference configuration being deformed into  $d\mathbf{x}$  in the current configuration (Fig. 2.11). A *deformation gradient tensor*  $\mathbf{F}$  relates the line element in the undeformed state to the line element in the deformed state by the relation  $d\mathbf{x} = \mathbf{F}d\mathbf{X}$ , where

$$\mathbf{F} = \frac{\partial \mathbf{x}}{\partial \mathbf{X}} \quad (2.2)$$

or using index notation,  $F_M^i = \frac{\partial x_i}{\partial X^M}$ , or as  $F_{iM}$  where  $i$  and  $M$  range over spatial and material coordinates, respectively. In addition to the mapping of line elements from the reference to the current configuration, the deformation gradient tensor allows for the mapping of differential volumes and areas as given by

$$\begin{aligned} dv &= \det(\mathbf{F})dV \\ &= JdV \end{aligned} \quad (2.3)$$

where  $J$  is the Jacobian of the deformation gradient tensor. The deformation gradient tensor represents the entire deformation, including rigid body motion and the strain, that the material experiences. In order to separate the rigid body motion from the deformation gradient tensor, a polar decomposition of the tensor results in  $\mathbf{F} = \mathbf{R}\mathbf{U}$  where  $\mathbf{R}$  is an orthogonal *rotation tensor* and  $\mathbf{U}$  is a symmetric tensor,

known as the *right stretch tensor*. The rotation tensor now describes the rigid body rotations and the right stretch tensor represents the material strain independent of rigid body motion. Another tensor that is independent of rigid body motions is the *right Cauchy Green tensor* or simply the *Green deformation tensor*,  $\mathbf{C}$  and can be calculated as follows:

$$\begin{aligned}\mathbf{C} &= \mathbf{F}^T \mathbf{F} \\ &= (\mathbf{R} \mathbf{U})^T \mathbf{R} \mathbf{U} \\ &= \mathbf{U}^T \mathbf{R}^T \mathbf{R} \mathbf{U} \\ &= \mathbf{U}^T \mathbf{U}\end{aligned}\tag{2.4}$$

In three-dimensions,  $\mathbf{C}$  is a 3x3 matrix, which has three scalar combinations of its components that do not change under coordinate transformations for a given body configuration. These are called the *principal invariants* and are given by:

$$\begin{aligned}I_1 &= \text{tr} \mathbf{C} \\ I_2 &= \frac{1}{2} [(\text{tr} \mathbf{C})^2 - \text{tr} \mathbf{C}^2] \\ I_3 &= \det \mathbf{C}\end{aligned}\tag{2.5}$$

When there is no motion or deformation, the deformation gradient tensor is the identity tensor  $\mathbf{I}$ , and hence the right Cauchy Green deformation tensor is  $\mathbf{I}$ . For convenience, *strain tensors* can be defined so that no motion or deformation yields the zero tensor  $\mathbf{0}$ . The *Green Strain tensor*,  $\mathbf{E}$ , satisfies this property and is defined as:

$$\mathbf{E} = \frac{1}{2}(\mathbf{C} - \mathbf{I})\tag{2.6}$$

### 2.2.2 Stress tensors for finite elasticity

Stress is typically the amount of force per unit surface area that the force is acting on. In large deformation mechanics, since the force and area can be measured in either the reference or the current configuration, three different measures of stress can be defined. As a stress tensor must obey the coordinate transformation laws required of a tensor, the components of a stress tensor are, in general, not physical components of stress.

### Cauchy stress tensor

The Cauchy stress tensor, with components  $\sigma_{ij}$ , refers to the force measured per unit area in the deformed configuration with respect to the deformed coordinate system. The first index identifies the direction of the normal vector  $\mathbf{n}$  of the surface on which the force  $\mathbf{p}$  is acting, and the second index identifies the direction of the force component.

### $1^{st}$ Piola-Kirchhoff stress tensor

This stress tensor, with components  $S_{Mj}$ , represents the force measured per unit undeformed area with respect to the deformed coordinate system. The upper case is used for the first index since the undeformed area is used in the calculation of the stress. As the force measured is that which is acting on the deformed surface, the second index is in lower case. This representation of stress proves to be useful when a natural zero stress reference state is known.

### $2^{nd}$ Piola Kirchhoff stress tensor

The  $2^{nd}$  Piola-Kirchhoff stress refers entirely to the reference configuration and is represented by components  $T_{MN}$ . The stress is the force measured per unit undeformed area, with the force being that which is acting on the undeformed area. This helps in the determination of constitutive models as a constitutive relation must be entirely independent of rigid body motion. As outlined by Malvern (1969) and Nash (1998), the relations between the second Piola Kirchhoff stresses and the other types of stress representations are summarized below in both tensorial and indicial notation:

$$\begin{aligned} \mathbf{S} &= \mathbf{TF}^T \boldsymbol{\Sigma} & \boldsymbol{\Sigma} &= \frac{1}{J} \mathbf{FS} &= \frac{1}{J} \mathbf{FTF}^T \\ S_{Mj} &= T_{MN} \frac{\partial x_j}{\partial X_N} & \sigma_{ij} &= \frac{1}{J} \frac{\partial x_i}{\partial X_M} S_{Mj} &= \frac{1}{J} \frac{\partial x_i}{\partial X_M} T_{MN} \frac{\partial x_j}{\partial X_N} \end{aligned} \quad (2.7)$$

### 2.2.3 Stress equilibrium and principle of virtual work

The equilibrium equations are derived from the following three conservation laws, which must be satisfied subject to any applied boundary conditions:

1. Conservation of mass requires that the mass of the body be the same in  $\beta_o$  and  $\beta_\alpha$ . This results in a relationship between the mass density ( $\rho_0$ ) in the reference state and the mass density ( $\rho$ ) in the deformed state:

$$\rho_0 = J\rho, \quad J = \det(\mathbf{F}) \quad (2.8)$$

2. Conservation of linear momentum requires that the time rate of change of linear momentum must balance all the forces that act on the body. This reduces to

$$\frac{\partial}{\partial X_M} \left( T_{MN} \frac{\partial x_j}{\partial X_N} \right) + \rho_0 b_j = \rho_0 f_j \quad (2.9)$$

where the entries of  $T_{MN}$  are calculated using a constitutive equation that relates the strains imposed on a body to the resulting stresses. The term  $b_j$  represents the components of the body forces and  $f_j$  represents the components of acceleration, which are zero for static problems.

3. Conservation of angular momentum requires that the time rate of change of moment of momentum of the body must balance the applied moments. This imposes a symmetry condition on the second Piola Kirchhoff stress tensor  $\mathbf{T}$ :  

$$T_{MN} = T_{NM}$$

All three conservation laws must be satisfied subject to a particular set of boundary conditions.

### Principle of virtual work

The principle of virtual work is an alternative form of expressing the stress equilibrium equations (2.9) in an integral or *weak* formulation.

Consider a body subjected to external surface traction forces,  $\mathbf{s}$ , and body forces,  $\mathbf{b}$ , which has reached a state of equilibrium. At this equilibrium state, if the body undergoes an arbitrary, infinitesimally small, virtual displacement  $\delta\mathbf{v}$  (not caused by prescribed external forces), virtual work is done by the surface tractions and body forces (product of force and displacement) to maintain the equilibrium position. Apart from the external virtual work, internal intramolecular forces inside the body also carry out virtual work. The body remains in equilibrium if the total virtual

work done by the internal and external forces sums to zero, resulting in the following equation (Malvern, 1969):

$$\delta W_{total} = - \int_S \mathbf{t} \cdot \delta \mathbf{v} dS + \int_{S_2} \mathbf{s} \cdot \delta \mathbf{v} dS = 0 \quad (2.10)$$

where the internal virtual work is that done by the internal stress vector,  $\mathbf{t}$ , inside the body and  $S_2$  is that part of the boundary without displacement boundary conditions imposed on it. Substituting Cauchy's formula ( $t_j^{(n)} = n_i \sigma_{ij}$ ) and noting that the virtual displacements can be written in component form as  $\delta \mathbf{v} = \delta v_j \mathbf{i}_j$ , equation 2.10 becomes:

$$- \int_S \sigma_{ij} n_i \delta v_j dS + \int_{S_2} \mathbf{s} \cdot \delta \mathbf{v} dS = 0 \quad (2.11)$$

Using Gauss's theorem, the surface integral on the internal stress distribution is converted to a volume integral, yielding

$$- \int_V \left[ \frac{\partial \sigma_{ij}}{\partial x_i} \delta v_j + \sigma_{ij} \frac{\partial \delta v_j}{\partial x_i} \right] dV + \int_{S_2} \mathbf{s} \cdot \delta \mathbf{v} dS = 0 \quad (2.12)$$

Expressing stresses in terms of the second Piola-Kirchoff formulation and substituting equation 2.9 into the volume integral, the principle of virtual work can be written as

$$\int_V \rho (b_j - f_j) \delta v_j dV - \int_V \frac{1}{J} T_{MN} \frac{\partial x_j}{\partial X_M} \frac{\partial \delta v_j}{\partial X_N} dV + \int_{S_2} \mathbf{s} \cdot \delta \mathbf{v} dS = 0 \quad (2.13)$$

To solve the equations of virtual work, it is necessary to evaluate the integral over the surface,  $S_2$ .

## 2.2.4 Boundary conditions

The equilibrium equations are typically solved with one or a mixture of the following general boundary conditions:

1. Displacement boundary conditions,  $\mathbf{x} = \bar{\mathbf{x}}$ , prescribed on the boundary  $\partial\Omega$ , a part of the deformed configuration  $\Omega$ . The overbar denotes a prescribed

quantity.

2. Surface traction boundary conditions,  $\mathbf{P}^{(\mathbf{N})} = \overline{\mathbf{P}^{(\mathbf{N})}}$  on  $\partial\Omega_p$ , where  $\mathbf{N}$  is the outward unit normal to  $\partial\Omega_p$  in the reference configuration.  $\mathbf{P}^{(\mathbf{N})}$  is the surface traction vector, defined as  $\mathbf{P}^{(\mathbf{N})} = \mathbf{N} \cdot \mathbf{T}$ .

### 2.2.5 Generalization for different coordinate systems

The kinematic tensors and stress equilibrium equations in the previous sections have assumed that only a rectangular cartesian coordinate system is used to identify the domain that they are being solved on. In the case of isotropic bodies, this specific coordinate system does not cause any problems. However, for anisotropic and heterogeneous materials, the orientation of the material axes may vary with location. This changing orientation is exhibited in the microstructure of the heart (Nash, 1998). Thus, it is more practical to define a set of material axes that are aligned with microstructural features of the material. The kinematic tensors and stress equilibrium equations can be re-written with respect to this new coordinate system (often called the material coordinate system). The reader is referred to Nash (1998) for details.

### 2.2.6 Constitutive relations

Now that the kinematic equations and the stress equilibrium equations have been formulated, a mathematical relationship must be developed between the stresses and strains within the body. The development of this relationship falls under the category of constitutive theory and the relationship is known as a *constitutive relation*.

The form of the constitutive relation is not universal as a constitutive relation is material behaviour specific. It describes the gross behaviour of a material under specific conditions of interest as it is impractical to attempt the modelling of the behaviour under all conditions due to the difficulty of the problem. Hence, it may be necessary to develop more than one constitutive relation for a material, if a variety of different conditions are of interest.

## General Characteristics

It must be decided if the body of interest is a solid, fluid or mixture of the two to determine the fundamental approach of the modelling process. For a solid, it must be determined if the material is elastic/inelastic, isotropic/anisotropic, linear/non-linear, and homogeneous/heterogeneous. A very brief description of some general characteristics is given below.

**Isotropy:** The response of a material to an applied load, relative to a prescribed configuration, is independent of the direction of loading.

**Transversely isotropic:** The response is independent of all directions transverse (perpendicular) to a single preferred direction.

**Orthotropic:** There are three preferred orthogonal directions. Application of equivalent loads in each of the three directions will result in a different response.

**Homogeneous:** The response to applied loads is independent of position within the body.

**Heterogeneous:** An inhomogeneous material with the response dependent on position within the body.

**Incompressible:** An Incompressible material preserves its volume under arbitrary loads.

As Humphrey (2002) states, it must be noted here that a material may be homogeneous in the reference configuration and heterogeneous after inducing applied loads; hence homogeneity must be specified with respect to a specific configuration. The same rule applies when identifying isotropy in a material because isotropic and anisotropic behaviours are the results of internal symmetries in the microstructure of a material, which may change with applied loads.

Incompressibility can be enforced using a kinematic constraint that is independent of the loads a body is subjected to. Humphrey (2002) states that most tissues consist largely of water, which is nearly incompressible. “But one ought to employ mixture or poroelasticity theories to account for solid-fluid interactions. Examples

include blood perfusion and the extruding or imbibing of fluid by a tissue as it deforms" (Humphrey, 2002). An example of the implementation of such a theory can be found in (Huyghe et al., 1991a) and (Huyghe et al., 1991b).

A class of constitutive relations can be postulated in which the stress is a function of the deformation gradient tensor:  $T_{ij} = f_{ij}(F_{mN})$ , where  $F_{mN}$  are the components of the deformation gradient tensor,  $T_{ij}$  are components of a stress tensor, and  $f_{ij}$  represent the functions. In order to conserve angular momentum,  $f_{ij} = f_{ji}$ . This formulation represents a behaviour known as *elasticity*. *Hyperelasticity* is the behaviour of a material when it is possible to define a single valued function, called a strain energy function, that is only dependent on the deformation gradient tensor (Atkin & Fox, 1980).

Inelastic materials can be *viscoelastic* by exhibiting behaviours of elasticity and viscosity. Unlike hyperelastic or elastic materials, viscoelastic materials undergo stress that is dependent on the strains and strain rates that the material has undergone throughout the deformation history (Lockett, 1972). Inelastic materials can also be *plastic* and undergo strains that are not dependent on stress after a limiting stress, called the yield stress, is exceeded. In the range of deformations that biological tissue undergo, plasticity does not usually play a role.

## Theoretical Framework

Once the general characteristics of the body have been identified, theoretical arguments regarding the form of the constitutive relation generally aid in the development of a specific law for a material behaviour. There are four principles in constitutive theory that must be satisfied during the development process (Humphrey, 2002; Malvern, 1969):

**Principle of Determinism:** This principle states that the material behaviour will be influenced by state of variables at the present and possibly in the past, but not on the future state of the variables.

**Principle of local action:** The behaviour of a particular material particle will not be influenced by state variables that are far away from the neighbourhood of the particle.

**Principle of Material frame indifference (objectivity):** This principle states that the constitutive relation must be independent of the frame of reference that is taken. The same material law must apply in all views that an observer may take.

**Principle of Equipresence:** This states that an independent variable assumed to be present in one constitutive equation of a material should be assumed to be present in all constitutive equations of the same material, unless its presence contradicts an assumed symmetry of the same material, or contradicts the principle of material frame-indifference, or some other fundamental principle

In the case of hyperelastic materials, the behaviour may be expressed in terms of a scalar potential,  $W$ , called a *strain-energy function*. In order that the constitutive relation satisfies the principle of objectivity, the strain energy function must be expressed in terms of the right Cauchy Green tensor ( $\mathbf{C}$ ) or Green's strain tensor ( $\mathbf{E}$ ). The second Piola-Kirchhoff tensor components may be defined in terms of the strain energy function as follows (Green & Adkins, 1970)

$$T_{MN} = \frac{1}{2} \left( \frac{\partial W}{\partial E_{MN}} + \frac{\partial W}{\partial E_{NM}} \right) \quad (2.14)$$

The strain energy function may be developed further by taking the general characteristics of the material into account. As isotropic materials do not have a preferred direction, the strain energy function is constant for all orientations of coordinate axes and thus can be a function of the principal invariants of  $\mathbf{C}$  (Spencer, 1980). An incompressible material will not change volume during deformations implying that the third strain invariant  $I_3 = \det(\mathbf{C}) = 1$ . Therefore, the strain energy function can be a function of the first two invariants alone. However, according to (Spencer, 1980), certain derivatives of the strain energy function tend to infinity in the limiting case of an incompressible material. Therefore it is more efficient to introduce a Lagrangian multiplier,  $\lambda$ , so that

$$W = \hat{W}(I_1, I_2) + \lambda(I_3 - 1) \quad (2.15)$$

This incompressibility condition gives rise to an internal hydrostatic pressure,  $p$ . Therefore, incorporating this Lagrangian multiplier formulation into equation (2.14)

gives

$$T_{MN} = \frac{1}{2} \left( \frac{\partial W}{\partial E_{MN}} + \frac{\partial W}{\partial E_{NM}} \right) - p C^{MN} \quad (2.16)$$

where  $C^{MN}$  are the contravariant components of the Cauchy Green deformation tensor. The relation,  $p = -2\lambda$ , is used to ensure that the additional components in the diagonal terms of the stress tensor are true hydrostatic stresses.

### Specific Functional Form

Once a general framework for the functional form of the material law has been determined, the specifics of the functional form must be determined. There are, in general, three ways of identifying a specific functional form for a particular material (Humphrey, 2002):

1. Theoretically, based on microstructural arguments
2. Directly from experimental data
3. Trial and error

Microstructural arguments have the highest chance of developing a constitutive relation that simulates reality with reasonable accuracy. However, the complexity of the microstructural events that occur during a deformation may prove to be too difficult to represent in a mathematical form and hence the last two methods are generally more widely used. Laws based on theoretical models may also add complexity to the solution of boundary value problems, typically introducing a large number of material parameters, which must be determined and thus slow down the solution process. In the case of rubber materials, a microstructural argument based on the long-chained molecular structure helped in the development of a purely entropic constitutive relation known as the neo-Hookean material law (Humphrey, 2002)

$$W = c_1(I_1 - 3) \quad (2.17)$$

where  $c_1 = nkT$  and  $n$  is the number of chains per unit volume,  $k$  is Boltzman's constant and  $T$  is the absolute temperature.

Experimental data fitting procedures are useful tools in modeling the gross behaviour of materials and have been used by Fung (1993), Huyghe et al. (1991a) and Pioletti & Rakotomanana (2000), for example, to model viscoelastic behaviour in soft tissue. Rivlin & Saunders (1951) conducted an extensive study on the material law for rubber and determined the Mooney-Rivlin material law for isotropic, incompressible hyperelastic materials:

$$W = c_1(I_1 - 3) + c_2(I_2 - 3) \quad (2.18)$$

where  $c_1$  and  $c_2$  are constants that must be determined from experiments on the particular material to be modeled.

Although the trial and error approach has a high potential of being unsuccessful, as long as the guesses of the specific form are done in an educated manner, it can provide reasonable constitutive relations.

## 2.3 Finite Elements for Finite Elasticity

Differential equations 2.9 outlined in Section 2.2.3 are nonlinear and do not generally have analytical solutions. The finite element method is typically used to solve these partial differential equations using their weak form in equation 2.13. This section outlines the finite element implementation of the finite elasticity theory that was used in simulating breast mechanics. The first section outlines the general technique behind the finite element method. Section 2.3.2 then briefly describes the implementation for finite elasticity. The reader is directed to (Zienkiewicz & Taylor, 2000b) and (Zienkiewicz & Taylor, 2000a) for an in-depth understanding.

### 2.3.1 The finite element technique

Consider a set of nonlinear differential equations,  $\mathbf{A}(\mathbf{u})$ , where  $\mathbf{u}$  is a set of unknown functions, that satisfies the following equations in a domain  $\Omega$ :

$$\mathbf{A}(\mathbf{u}) = 0 \quad (2.19)$$

A set of boundary conditions,  $\mathbf{B}(\mathbf{u})$ , are associated with the differential equations

on a boundary,  $\Gamma$ , of the domain,  $\Omega$ ; represented as

$$\mathbf{B}(\mathbf{u}) = 0 \quad (2.20)$$

The finite element technique involves the approximation of the unknown function by an approximation

$$\mathbf{u} \approx \hat{\mathbf{u}} = \Phi_n \hat{u}_n \quad (2.21)$$

$\Phi_n$  are called shape functions, used to approximate  $\mathbf{u}$  and  $\hat{u}_n$  are values of  $\mathbf{u}$  at  $n$  points in  $\Omega$ . The shape functions are typically defined locally for each element. The next step is to reformulate the set of differential equations in an integral form so that the equations can be satisfied element by element and hence as a whole. There are two procedures available to obtain the integral form - the weighted residuals method and the variational functionals method.

### Weighted residuals method

The set of differential equations, (2.19) and (2.20), can be reformulated in an integral form as

$$\begin{aligned} \int_{\Omega} \mathbf{v}^T \mathbf{A}(\mathbf{u}) d\Omega &= 0 \\ \int_{\Gamma} \mathbf{v}^T \mathbf{B}(\mathbf{u}) d\Gamma &= 0 \end{aligned} \quad (2.22)$$

where  $\mathbf{v}$  is a set of arbitrary functions same in number as the number in  $\mathbf{u}$ . This integral form ensures that the set of equations (2.19) are satisfied as long as equation (2.22) is satisfied for all functions  $\mathbf{v}$ .

Just as  $\mathbf{u}$  was approximated by equation (2.21),  $\mathbf{v}$  is approximated by

$$\mathbf{v} \approx \hat{\mathbf{v}} = \omega_n \hat{v}_n \quad (2.23)$$

Substituting equations (2.23) and (2.21) into equation (2.22) gives

$$\begin{aligned} \int_{\Omega} \omega_n \hat{v}_n^T \mathbf{A}(\Phi_n \hat{u}_n) d\Omega &= 0 \\ \int_{\Gamma} \omega_n \hat{v}_n^T \mathbf{B}(\Phi_n \hat{u}_n) d\Gamma &= 0 \end{aligned} \quad (2.24)$$

Since  $v_n$  are arbitrary, the only unknowns are the original set,  $\mathbf{u}$ . Therefore the

integral form of the original set of differential equations (2.19) and (2.20) is

$$\begin{aligned}\hat{v}_n^T \int_{\Omega} \omega_n \mathbf{A}(\Phi_n \hat{u}_n) d\Omega &= 0 \\ \hat{v}_n^T \int_{\Gamma} \omega_n \mathbf{B}(\Phi_n \hat{u}_n) d\Gamma &= 0\end{aligned}\quad (2.25)$$

There are a number of choices for the form of  $\omega$  and the reader is pointed to (Zienkiewicz & Taylor, 2000b) for further information. The simulations of breast mechanics have used the subset of finite element techniques known as the Galerkin finite element weighted residuals method. In this method,  $\omega$  is chosen to be the shape function used to approximate the unknowns,  $\Phi$ .

It can be shown that the second method of variational functionals provides the same integral formulation as that described using the principle of virtual work in Section 2.2.3 and is also the same integral formulation derived using the weighted residuals method.

### Additional constraints - Lagrange Multipliers

It may be necessary to satisfy equation (2.25) subject to a set of additional constraints. These constraints are usually added to the integral formulation via a Lagrangian multiplier formulation. Consider an additional set of differential equations constraining equation (2.19) in the domain  $\Omega$ , which are given by

$$\mathbf{C}(\mathbf{u}) = 0 \quad (2.26)$$

equation (2.25) now contains an additional integral to incorporate the constraints in equation (2.26)

$$\int_{\Omega} \omega_n \mathbf{A}(\Phi_n \hat{u}_n) d\Omega + \int_{\Omega} \lambda^T \mathbf{C}(\mathbf{u}) = 0 \quad (2.27)$$

where  $\lambda$  are a set of independent variables in the domain  $\Omega$  called Lagrange multipliers.

### 2.3.2 Implementation of finite elasticity

In the case of finite deformation theory, the unknowns are the increments to the undeformed coordinates,  $\mathbf{X}$ , which provide the deformed coordinates,  $\mathbf{x}$ , of the deforming body. The set of arbitrary displacements,  $\delta\mathbf{v}$ , are actually the virtual displacements discussed in Section 2.2.3 and the set of differential equations in equation (2.9) are the differential equations  $\mathbf{A}(\mathbf{u})$ .

This section describes the procedures implemented to solve equations 2.13. First, the shape functions used to approximate the displacement fields are described, and the following section describes a new set of material coordinates known as finite element coordinates to identify material points in the undeformed and deformed configurations. An overview is then given of the Gaussian quadrature scheme to approximate the integrals in equation (2.13). Finally, Newton's method is briefly described as it is used as the search method to solve the set of nonlinear equations.

#### Shape functions

Shape functions, or basis functions, allow for the description of quantitative fields of interest as a weighted sum of the field at specific points across the domain as in equations 2.21 and 2.23. There are a variety of shape functions that can be used to approximate the displacement field in solving the equations of finite elasticity. Typically, linear lagrange basis functions are used to describe this field. In this research both these and a higher order set of basis functions known, as cubic Hermite basis functions, were used.

**Linear Lagrange** The linear lagrange basis functions approximate the displacements by the weighted sum of the field values at two boundary points. Consider the line segment in Fig. 2.12 having a field,  $U$ , defined over it. The field over the segment between  $U_1$  and  $U_2$  can be interpolated with the linear basis functions as

$$U(\xi) = U_1(1 - \xi) + U_2\xi \quad (2.28)$$

with  $\xi$  being the coordinate space ranging from zero to one.

$$\begin{aligned} \Phi_1 &= (1 - \xi) \\ \Phi_2 &= \xi \end{aligned} \quad (2.29)$$

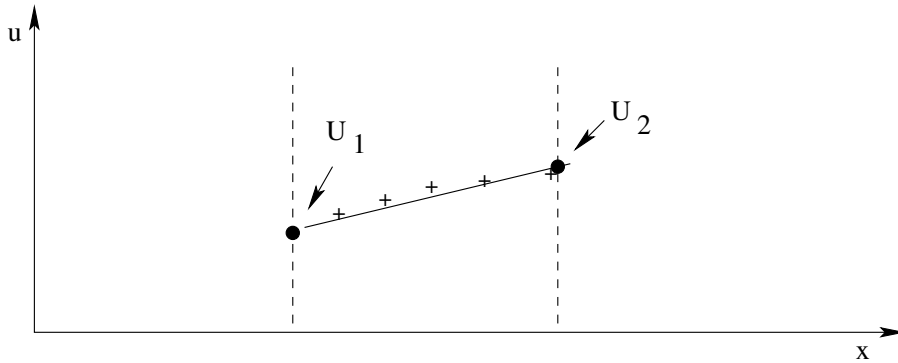


Figure 2.12: A line segment with a function  $u$  represented with field values  $U_1$  and  $U_2$  at the boundary points and linear basis functions.

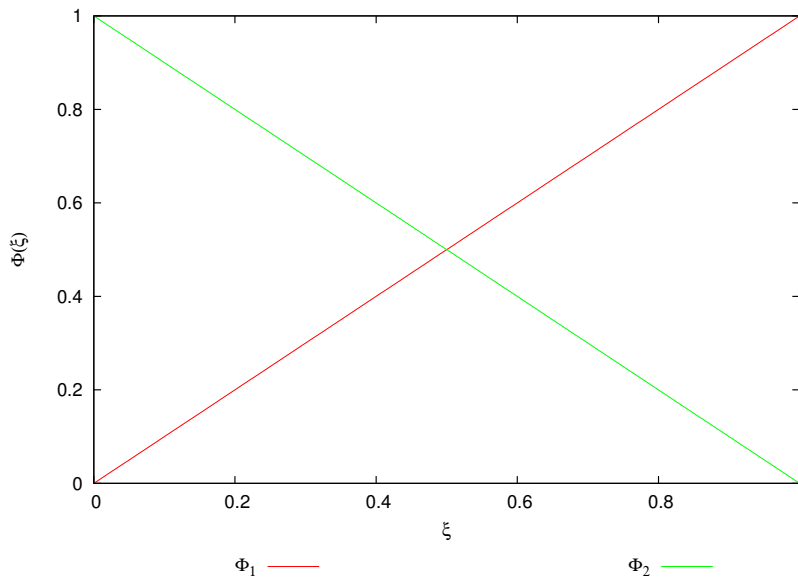


Figure 2.13: Linear Lagrange basis functions.

are the linear basis functions that weight the contribution of the boundary points (or nodes) depending on the position along the coordinate space  $\xi$  (see Fig. 2.13). when  $\xi = 0$ ,  $U = U_1$  and hence the first nodal parameter contributes entirely to the sum. As we move from left to right, the weight on  $U_1$  decreases while that on  $U_2$  increases until  $\xi = 1$  when all the contribution is from the function value at the second node. More complex functions can be approximated using linear basis functions by subdividing the domain into smaller segments across which a linear approximation captures the field more aptly.

**Cubic Hermite** Linear Lagrange basis functions are limited in that they only achieve  $C_0$  continuity. The cubic Hermite interpolation scheme uses the nodal values of the field as well as its first derivatives at two nodes, to provide  $C_1$  continuity. The basis functions are

$$\begin{aligned}\Phi_1^0(\xi) &= 1 - 3\xi^2 + 2\xi^3 \\ \Phi_1^1(\xi) &= \xi(\xi - 1)^2 \\ \Phi_2^0(\xi) &= \xi^2(3 - 2\xi) \\ \Phi_2^1(\xi) &= \xi^2(\xi - 1)\end{aligned}\tag{2.30}$$

and the interpolation of a field along a line segment is given by equation (2.31)

$$U(\xi) = \Phi_1^0 U_1 + \Phi_1^1 \left( \frac{\partial U}{\partial \xi} \right)_1 + \Phi_2^0 U_3 + \Phi_2^1 \left( \frac{\partial U}{\partial \xi} \right)_2\tag{2.31}$$

To make cubic Hermite basis functions more useful in practice, it is necessary to define a global derivative,  $\left( \frac{dU}{ds} \right)_N$ , of the field where  $s$  is the arc-length and  $N$  is the global nodal number. Then,  $\left( \frac{dU}{d\xi} \right)_n$  is calculated as follows

$$\left( \frac{dU}{d\xi} \right)_n = \left( \frac{dU}{ds} \right)_N \cdot \left( \frac{ds}{d\xi} \right)_n\tag{2.32}$$

where  $\left( \frac{ds}{d\xi} \right)_n$  is called the element scale factor, which scales the arc-length derivative of global node  $N$  to the  $\xi$ -coordinate derivative of element node  $n$ . This ensures that the global nodal derivative  $\frac{du}{ds}$  is continuous across element boundaries, rather than the elemental derivative  $\frac{du}{d\xi}$ .

Interpolation over two or three dimensions is done by using tensor products of the one-dimensional basis functions. For example, a three-dimensional field can be approximated using:

$$U(\xi_1, \xi_2, \xi_3) = \sum_{n=1}^N \sum_{m=1}^M \sum_{o=1}^O \Phi_n(\xi_1) \Phi_m(\xi_2) \Phi_o(\xi_3) U_{nmo}\tag{2.33}$$

### Finite element coordinate system

There are three sets of coordinate systems used in this thesis. The first is the rectangular cartesian coordinate system used to define the geometry of the breast in

spatial coordinates. There are two sets of material coordinate systems -  $\nu_\alpha$  system for describing the tissue material properties and a finite element coordinate system  $\xi_j$  used to describe the body in the undeformed and deformed coordinates. The finite element coordinates are a system of normalised elemental coordinates that are embedded in the body and deform with it. Therefore, the coordinates are not necessarily orthogonal. These coordinates can be mapped to the undeformed spatial coordinates of a body using the shape functions as shown below.

$$X_i = \Phi_n(\xi_1, \xi_2, \xi_3) X_i^n \quad (2.34)$$

The covariant base vectors and metric tensors are given in equation (2.35) for the undeformed ( $\mathbf{G}$ ) and deformed ( $\mathbf{g}$ ) configurations.

$$\begin{aligned} \mathbf{G}_M^\xi &= \frac{\partial X_k}{\partial \xi_M} \mathbf{g}_k^x \\ \mathbf{g}_M^\xi &= \frac{\partial x_k}{\partial \xi_M} \mathbf{g}_k^x \\ \mathbf{G}_{MN}^\xi &= \mathbf{G}_M^\xi \cdot \mathbf{G}_N^\xi = \frac{\partial X_k}{\partial \xi_M} \frac{\partial X_k}{\partial \xi_N} \\ \mathbf{g}_{MN}^\xi &= \mathbf{g}_M^\xi \cdot \mathbf{g}_N^\xi = \frac{\partial x_k}{\partial \xi_M} \frac{\partial x_k}{\partial \xi_N} \end{aligned} \quad (2.35)$$

### Approximating the integrals - Gaussian Quadrature

The volume and surface integrals in equation (2.13) cannot be always evaluated analytically as the equations are most often complicated and computationally intensive. Hence these integrals are usually approximated using the Gaussian Legendre quadrature scheme (Gaussian quadrature) of integration (Zienkiewicz & Taylor, 2000b). The scheme approximates an integral as the weighted sum of the function's value at specific points determined using a set of simultaneous equations. These points are called Gauss points and provide the best accuracy in approximating the integral: a polynomial of order  $2n-1$  can be exactly integrated given  $n$  Gauss points at which the function is evaluated. The integration of a one-dimensional function can be approximated using Gaussian quadrature as :

$$\int_0^1 f(\xi) d\xi \approx \sum_{i=1}^I w_i f(\xi^i) \quad (2.36)$$

where  $w_i$  is the weight for each Gauss point  $\xi^i$  in an  $I$  Gauss-point scheme. The Gauss Legendre quadrature scheme in two and three dimensions is a simple extension of the one-dimensional scheme as shown in equations (2.37) and (2.38)

$$\int_0^1 \int_0^1 f(\xi_1, \xi_2) d\xi_1 d\xi_2 \approx \sum_{i=1}^I \sum_{j=1}^J w_i w_j f(\xi_1^i, \xi_2^j) \quad (2.37)$$

$$\int_0^1 \int_0^1 \int_0^1 f(\xi_1, \xi_2, \xi_3) d\xi_1 d\xi_2 d\xi_3 \approx \sum_{i=1}^I \sum_{j=1}^J \sum_{k=1}^K w_i w_j w_k f(\xi_1^i, \xi_2^j, \xi_3^k) \quad (2.38)$$

where an  $I$  Gauss point scheme is used in the  $\xi_1$  direction, a  $J$  Gauss point scheme is used in the  $\xi_2$  direction and a  $K$  Gauss point scheme is used in the  $\xi_3$  direction.

### Galerkin finite element equations for finite elasticity

The finite element coordinates are a normalised set of coordinates so that  $0 \leq \xi_i \leq 1$ . The basis functions in Section 2.3.2 map the physical, spatial coordinates of a body into the finite element coordinate space. Hence, it is possible to transform the surface and volume integrals in equation (2.13) to the finite element coordinate space using the appropriate Jacobian. Equation (2.39) is the result of transforming equation (2.13) into the finite element space using the Jacobians  $\sqrt{\mathbf{G}^\xi} = \sqrt{\det(G_{ij}^\xi)}$  for the undeformed configuration volume integral and  $\sqrt{\mathbf{g}^\xi} = \sqrt{\det(g_{ij}^\xi)}$  for the deformed configuration surface integral.

$$\begin{aligned} \int_{S_2} s^j \delta v_j \sqrt{\mathbf{g}^\xi} d\xi_2 d\xi_1 &+ \int_V \rho_o (b^j - f^j) \delta v_j \sqrt{\mathbf{G}^\xi} d\xi_3 d\xi_2 d\xi_1 \\ &- \int_V T^{MN} F_M^j \frac{\partial \delta v_j}{\partial X_N} \sqrt{\mathbf{G}^\xi} d\xi_3 d\xi_2 d\xi_1 = 0 \end{aligned} \quad (2.39)$$

The virtual displacements  $\delta v_j$  are approximated using a set of shape functions as follows

$$\delta v_j = \Phi_n(\xi_1, \xi_2, \xi_3) \delta v_j^n \quad (2.40)$$

Equation (2.40) is substituted into equation (2.39) and each unknown virtual displacement parameter  $\delta v_j^n$  is considered in turn in equation (2.41).

$$\begin{aligned} \int_{S_2} s^j \Phi_n \sqrt{\mathbf{g}^\xi} d\xi_2 d\xi_1 &+ \int_V \rho_o (b^j - f^j) \Phi_n \sqrt{\mathbf{G}^\xi} d\xi_3 d\xi_2 d\xi_1 \\ &- \int_V T^{MN} F_M^j \frac{\partial \Phi_n}{\partial X_N} \sqrt{\mathbf{G}^\xi} d\xi_3 d\xi_2 d\xi_1 = 0 \end{aligned} \quad (2.41)$$

### Incompressibility constraint

As mentioned in Section 2.3.1, additional differential equation constraints can be incorporated via Lagrangian multipliers. Equation (2.41) is enough to solve for the deformed coordinates of a body with compressible mechanical behaviour. When the material is incompressible, an additional constraint must be incorporated to ensure that the third strain invariant,  $I_3$ , is 1. As mentioned in Section 2.2.6 it is difficult to ensure this constraint is exactly satisfied at every material point in the body. It is sufficient, however, to ensure that this constraint is satisfied in some average sense over a volume by using integral (2.42).

$$\int \int \int_{V_e} \left( \sqrt{I_3} - 1 \right) \Phi_n^p \sqrt{\mathbf{G}^\xi} d\xi_3 d\xi_2 d\xi_1 = 0 \quad (2.42)$$

where  $V_e$  is the domain of the elemental volume and  $\Phi_n^p$  are the basis functions used to approximate the hydrostatic pressure field.

Oden (1972) and others recommended that the basis functions used to approximate the hydrostatic pressure field be of a lower order than that chosen for the deformed coordinates to avoid numerical ill-conditioning and to be consistent when calculating stress components. This is because the strain energy function contributes to stress through the first derivatives of the displacement field while the hydrostatic pressure contributes directly as shown in equation (2.16). When the geometry is described using trilinear interpolation, an auxillary hydrostatic pressure parameter per element is introduced to satisfy the incompressibility constraint. When a tricubic Hermite interpolation is used to describe the geometry, a trilinear interpolation can be used to describe the hydrostatic pressure field. Therefore a hydrostatic pressure parameter is introduced at each node.

### Solving the equations - Newton's Method

A linearised system of equations can be obtained by reformulating equation (2.41) to be a set of residuals:

$$\mathbf{R}(\mathbf{x}) = \mathbf{0} \quad (2.43)$$

The aim is to find  $\mathbf{x}$  such that equation (2.43) is satisfied, given the undeformed coordinates,  $\mathbf{X}$ . This is a multi-dimensional root finding problem, which can be solved using the Newton Raphson technique (Press et al., 1992).

The method is derived from the Taylor series expansion of a function value at a point,  $\boldsymbol{\delta}$ , from the current point,  $\mathbf{x}$ . Consider the system of  $n$  nonlinear residuals  $R_i(\mathbf{x})$  with the current position in the parameter space being  $(\mathbf{x}_o)$  and the increment from the current position being  $\boldsymbol{\delta}$ . The 1<sup>st</sup> order Taylor series expansion of each of the equations is

$$R_i \mathbf{x}_o + \frac{\partial R_i}{\partial x_1}(\mathbf{x}_o)\delta_1 + \frac{\partial R_i}{\partial x_2}(\mathbf{x}_o)\delta_2 + \cdots + \frac{\partial R_i}{\partial x_n}(\mathbf{x}_o)\delta_n = 0 \quad (2.44)$$

This expansion can be reformulated to have  $R_i(\mathbf{x}_o)$  on the right hand side and can be set up in matrix form as

$$\mathbf{J}(\mathbf{x}_o)\boldsymbol{\delta} = -\mathbf{R}(\mathbf{x}_o) \quad (2.45)$$

$\mathbf{J}$  is the Jacobian (or element stiffness) matrix with the set of derivatives of the each of the  $n$  residuals with respect to the  $n$  solution degrees of freedom and the unknowns are the increments,  $\boldsymbol{\delta}$ , to the solution degrees of freedom for the next solution iteration. The elements of the Jacobian matrix can be calculated numerically using a finite difference approximation (or analytically if possible). For a one sided finite difference approximation, a derivative can be numerically calculated using

$$\frac{\partial R_i(\mathbf{x}_o)}{\partial x_j} = \frac{R_i(\mathbf{x}_o + \Delta \cdot \mathbf{e}_j) - R_i(\mathbf{x}_o)}{\Delta} \quad (2.46)$$

where  $\Delta$  is the perturbation applied to each of the unknowns,  $\mathbf{x}_o$  in turn.

The initial estimate of the deformed coordinates are the undeformed coordinates. Finite difference derivatives for each of the residual equations are calculated by perturbing each of the solution degrees of freedom by an amount  $\Delta$  using equation 2.46 to form the element stiffness matrix in equation 2.45. The increments,  $\boldsymbol{\delta}$ , are then found using direct solver techniques such as LU decomposition or iterative

solvers such as the Generalised Minimum Residual (GMRES) method. The above steps are repeated until a norm of the residuals is less than a specified tolerance. The residual norm used is the ratio of the total unconstrained residuals to the constrained residuals. The unconstrained residuals are associated with the degrees of freedom that do not have displacement boundary conditions applied. Constrained residuals are those residuals associated with degrees of freedom with displacement boundary conditions applied. Another norm used to determine convergence is the absolute sum of the solution increments in the increment vector,  $\delta$ . A solution is a converged solution if the ratio of unconstrained to constrained residuals and the sum of solution increments are less than a value of  $10^{-8}$ .

## 2.4 Biomechanical Properties of Breast Tissues

The organisation, composition and structure of the constituents of the breast (both gross and micro) directly contribute to the mechanical function of the breast. Investigations on the gross- and micro-anatomical structure of the breast have typically been conducted to better understand the morphology of breast pathologies for diagnosis and surgery (Kopans, 2007; Riggio et al., 2000). Interest in quantifying the mechanical properties of breast tissues has usually been motivated by research into identifying ways of diagnosing cancer (Samani et al., 2007; Krouskop et al., 1998; Wellman et al., 1999; Van Houten et al., 2003; Sarvazyan et al., 1995). To the author's knowledge, investigations have not been conducted to relate biomechanical properties of breast tissues to their microstructural organisation and composition. Nonetheless, the studies to date provide important information on the general characteristics of the gross structural components of the breast such as fat, fibroglandular tissues (fibrous connective tissue and the embedded parenchymal glandular components), and various pathological tissue types such as breast carcinomas and fibroadenomas. In this section these general mechanical characteristics are briefly discussed and the reader is directed to Appendix F for more details on the experimental techniques and constitutive relations developed in key studies on breast biomechanical properties and their relevance to developing finite element models of the breast.

Most of the studies to date have determined biomechanical properties of breast

tissues using uniaxial tension and compression tests on ex-vivo tissues samples (Samani et al., 2007; Krouskop et al., 1998; Wellman et al., 1999). In general, abnormal tissues are much stiffer than normal fat and fibroglandular tissues. For instance, Samani et al. (2007) found that fibroadenomas exhibited approximately twice the stiffness of fibroglandular tissues, while high-grade infiltrating ductal carcinomas (IDC) were thirteen times stiffer than normal fibroglandular tissues. Krouskop et al. (1998) showed that breast tissues exhibit a non-linear stress strain relationship and can be considered to be elastic as there were negligible viscoelastic effects observed when compression tests were done at different strain rates. In order to provide quantitative information on the mechanical properties, Table 2.1 shows a summary of the mean Young's moduli of 169 breast tissue samples that Samani et al. (2007) studied. Note that Young's moduli are not sufficient to characterise the nonlinear behaviour of breast tissues (see discussion in Appendix F).

Breast tissue type	Num. of samples	Young's modulus (kPa) mean $\pm$ STD
Normal fat	71	3.25 $\pm$ 0.91
Normal fibroglandular tissue	26	3.24 $\pm$ 0.61
Fibroadenoma	16	6.41 $\pm$ 2.86
Low-grade Infiltrating Ductal Carcinoma (IDC)	12	10.40 $\pm$ 2.60
Infiltrating Lobular Carcinoma (ILC)	4	15.62 $\pm$ 2.64
Ductal Carcinoma In Situ (DCIS)	4	16.38 $\pm$ 1.55
Fibrocystic disease	4	17.11 $\pm$ 7.35
Intermediate-grade IDC	21	19.99 $\pm$ 4.2
High-grade IDC	9	42.52 $\pm$ 12.47
Invasive mucinous carcinoma (IMC)	1	20.21
Fat necrosis	1	4.45

Table 2.1: Mean and standard deviation values of the calculated Young's modulus summarizing the tested 169 breast tissue samples (From Samani et al. (2007)).

Although Table 2.1 is typical of the general characteristics of the degree of stiffness across tissue types, the values are not typical. As discussed in Section 2.1, breast morphology varies with changing physiological conditions and age of a woman. Breast morphology is also highly variable across individuals. This morphological variation is reflected in the stiffnesses of the breast tissues as highlighted

by Van Houten et al. (2003). Fig. 2.14 clearly illustrates this variation in breast tissue mechanical properties with a plot summarising the stiffness of normal fat and fibroglandular tissues across a number of studies in the literature.

The variation in mechanical properties of breast tissues across individuals (and time for an individual) poses a major challenge in developing anatomically realistic individual-specific models of the breast. It is also unclear as to how much detail of the organisation of the breast tissue constituents (ECM and parenchyma) is necessary to create a reliable biomechanical model of the breast. Nevertheless, as will be outlined in the following section, previous studies show promise in the use of the finite element method to predict breast deformation and a research direction for this thesis is described in Section 2.6 that makes an important contribution towards developing a biomechanical model of the breast.

Figure 2.14: A bar graph showing the Young's modulus values for normal fat and normal glandular tissues compiled from various works. (Reproduced from (Van Houten et al., 2003)).

## 2.5 Previous Finite Element Models of Breast Biomechanics

The finite element method has proven to be a very useful method for modelling soft biological tissues, with models of the heart being developed from as early as 1972 (Gould et al., 1972). However, research into finite element modelling of breast biomechanics has only developed over the last decade. In recent years, models have predominantly been developed for image registration problems. This section provides an overview of breast biomechanics models published in the literature to date.

Yu-Neifert (1995) was one of the first to model breast tissue movement to determine the applicability of holographic interferometry in breast cancer detection. Holographic interferometry involves the use of holographic technology to create an interference pattern that is produced when a reference image (the breast in the reference state) and a deformed image (the breast under a certain load) are recorded on the same holographic film. Yu-Neifert created a three-dimensional finite element model of the breast to predict deformations under gravity loading conditions. Breast geometry was obtained from surface measurements using stereographs and the supine configuration was taken as the reference state. The model assumed that the normal, healthy breast was made of adipose tissue (fibrous and fatty tissue lumped into one material type) and skin. The adipose tissues were assumed to be homogeneous, isotropic and linearly elastic in the deformation range based on studies done on facial soft tissue. An indentor testing rig was built to estimate the Young's modulus of ex-vivo samples. Skin was also assumed to be linearly elastic and a Young's modulus value was chosen based on literature at that time. The deformations were modelled using finite deformation theory in ABAQUS<sup>2</sup> and validated by comparing measured displacement to model prediction of the most anterior point on the surface under two loaded configurations - prone with an error of 1.2% and upright with an error of 6%. Although the anterior point was predicted accurately, it is insufficient to conclude that the model is reliable. A more robust error measure, which compares model predictions and experimental data at more than one point, should have been utilised.

---

<sup>2</sup>commercial software package <http://www.hks.com/>

Kita et al. (1998) recognised the need for a model of deformations under mammographic compression when registering CC and MLO images of a patient's breast. They created a mathematical model of breast deformation based on four assumptions:

1. Cross section for compression<sup>3</sup> is deformed only in the plane by compression.
2. There is no deformation at the mid-plane between the plate and cassette.
3. Curves of the breast tissue deform uniformly, shrinking or stretching by a constant factor of its curvilinear coordinates.
4. Curves of breast tissue can be modelled by a quadratic equation.

The model was tested using real data and compared to predictions of location given by two radiologists. Although the model was not very accurate, it did show promising results that indicated a need for further development of mathematical models of the breast.

Azar et al. (2000) developed a more detailed finite element model of the breast to track internal tissues during MR image-guided needle biopsy procedures. The procedure involves imaging the breast without compression and then compressing the breast and using a finite element model to predict the position of a tumour in the compressed state. This helps the clinician to guide the needle to sample the right region of tissue. The model was more complex than the one by Yu-Neifert (1995) in a number of ways and treated the fibroglandular and fatty tissue as two separate tissue types (as opposed to one). The model was also more detailed as it used MR images to create hexahedral trilinear elements for internal tissues. Although it is known that breast tissues undergo large deformations, especially during compression, Azar did not use large deformation theory to model tissue displacements. Instead, the large deformations were divided into a number of smaller displacement steps, and each of the smaller steps were solved using small strain theory. This enabled the mechanics problem to be solved more quickly and made the model suitable for clinical use. The compression was simulated using displacement boundary conditions for nodes that were in contact with the compression plates. All internal tissues were assumed

---

<sup>3</sup>The cross section is that which is cut by the plane parallel to the compression direction and perpendicular to the chest wall

to be nonlinear, isotropic, incompressible and homogeneous, using material models developed by Wellman (1999) to characterise their mechanical behaviour. Wellman (1999) performed indentation experiments on ex-vivo samples of a variety of tissue types (fat, fibroglandular, and different types of carcinomas) and, to the author's knowledge, is the most widely cited work on breast tissue mechanical properties (see Appendix F for further details). Azar modified Wellman's representation of the mechanical response of fat to account for the effects of supporting tissues, which compartmentalise the fatty tissue and restrict its movement. Skin was not modelled because a sensitivity analysis had shown that it had minimal effect on the accuracy of the simulations. Three patients underwent the procedure with compressions in the order of 20% and a single landmark in each patient was tracked during the compression. Displacement differences<sup>4</sup> were 2.7 mm for a 7.2 mm lesion, 1 mm for a 5 mm lesion, and 7.3 mm for a 13 mm lesion respectively (an average 38% error as percentage of lesion size). This large error could be attributed to a number of possible sources, such as the use of small displacement theory to model large deformations. Small strain theory ignores the rotations that are typically present in nonlinear, large deformations.

Samani et al. (2001) was not focussed on computation speed as much as Azar and used finite deformation theory with contact mechanics to model breast compression. The model incorporated the properties of skin as well as other tissues (based on (Wellman, 1999)) but only a qualitative simulation of a breast compression was provided.

In contrast, Tanner et al. (2001) provided more quantitative information by presenting a method to assess the accuracy of biomechanical models in predicting deformation under compression. Images of the uncompressed and compressed breast were registered using landmarks and a non-rigid registration technique in order to estimate surface tissue displacements, which were used as boundary conditions in the model. A range of material constitutive relations (linear elastic to nonlinear elastic) from previous work in the literature were used to test the sensitivity of model predictions to the chosen material behaviour models. A variety of boundary conditions were also used for sensitivity analysis. The performance of the model

---

<sup>4</sup>difference in displacement of inclusion center of gravity (lesion, cyst or vitamin E pill), between model and experiment

was assessed by measuring the error in predicting the location of 12 landmarks from the uncompressed to compressed configuration. The average Euclidian distance between model predicted location and user-selected location on the compressed breast image was 6.4 mm. In addition, the Euclidean distance between the model predicted location and the location predicted by the non-rigid registration algorithm was also calculated to be 2.7 mm on average. The sensitivity analysis was useful in highlighting the important parameters for accurate model predictions. However, it is hard to identify the sources of error because of the complex interactions between the simulation parameters.

In the same year, Schnabel et al. (2001) validated the registration technique used in (Tanner et al., 2001) by registering images which were generated from finite element models that were assumed to simulate “gold standard” tissue displacements. MR images were used to create a finite element model which was then used to simulate tissue displacements that occur in a clinical setting. The predicted displacements could be used to create synthetic deformed images which were in turn registered to the original images using the non-rigid registration technique. Schnabel stated that the finite element models were used only to validate the registration algorithm and therefore the accuracy of the model in predicting tissue deformations was not essential. However, since the non-rigid registration algorithm was not restricted to physically plausible deformations, it is conceivable that a physically unrealistic deformation could still provide good results. Therefore, the validation method does not seem robust.

Ruiter et al. (2002) focussed on registration of X-ray to MR images of the breast to assist clinicians in collocation of tumours between mammograms and clinical MR data. A maximum registration error of 3 mm was considered to be acceptable as tumours above the size of 3 mm can be detected in MRI sequences. A total of 17 landmarks were tracked between uncompressed and compressed breast MR images and the model was used to simulate the deformation and track predicted landmark locations in the compressed breast. A variety of material models from the literature (skin was not included) and boundary conditions were applied to test the sensitivity of model accuracy to these parameters. A nonlinear heterogeneous model produced a mean error of 4.1 mm, while a linear elastic homogeneous model had a mean error of 3.7 mm in predicting tissue movement. A two-plate compression contact

boundary condition (simulates movement of top and bottom plates to compress breast) produced the best results with a 3.7 mm error. However, a similar study was published in (Ruiter et al., 2003), which showed that a linear elastic model produced average errors as high as 6.8 mm. Therefore, a nonlinear, neo-Hookean homogeneous model with an average error of 3.1 mm was chosen over the linear elastic model. These differing views highlight a need for a different approach to validating a breast biomechanics framework.

## 2.6 Thesis Research Proposal

Although the models published in the literature have been tested with clinical data, there are still a number of unanswered questions regarding the validity of the assumptions and modelling theories used. Due to the complexity of the interactions between different parameters in a finite element model of the breast (mechanical properties, tissue organisation and loading conditions), it is hard to determine the sources of error in model predictions. The research presented in this thesis was based on a different approach to previous studies in developing anatomically realistic models of the breast. It involved the use of controlled experiments on silicon gel phantoms and breasts of volunteers to systematically validate modelling assumptions and to identify and quantify sources of error in the modelling framework.

This thesis is structured to reflect the systematic approach in developing a breast biomechanics modelling framework. The research conducted in this dissertation is divided into two different parts and each part focusses on answering specific questions:

- Part II focusses on validating the mechanics modelling framework using silicon gel phantoms, and addresses the following four questions:
  1. How accurately can the deformed configuration of a homogeneous body be predicted under gravity loading, if its reference state, mechanical properties and boundary conditions have been accurately characterised? This is referred to here as the “forward problem”.
  2. How accurately can the reference configuration of a homogeneous body be predicted, given mechanical properties, boundary conditions and a set of

deformed configurations under different gravity loading conditions? This is referred to here as the “reverse problem”.

3. Can the interface between a thin membrane and the 3D constituents enclosed by the membrane be accurately modelled? (eg. skin enclosing internal breast tissue)
4. Is it possible to model a simple heterogeneous body consisting of two components, which occupy distinct regions in the volume? (eg. adjacent sections of fat and fibroglandular tissue)

Silicon gel phantoms provide the ability to answer these specific questions in a controlled manner because:

1. a custom designed mould used to make the gel enables the accurate representation of the reference state. The breast is almost always under the influence of gravity loading. To the author’s knowledge, all of the previous work took one of the deformed configurations as the modelling reference state. It is necessary to determine the importance of the accurate representation of the reference state for model predictions to be reliable.
2. it is possible to design the phantom to have a specific set of boundary conditions. Therefore any errors introduced by assumptions made on the attachment of the breast to the pectoral muscles and ribs can be experimentally quantified.
3. it is possible to impose a known set of loading conditions and control the types of deformations being imposed, to carefully identify sources of error.
4. it is possible to design the phantom to have varying degrees of heterogeneity. This enables the systematic incorporation of different types of tissue organisations (fat next to fibroglandular tissue, or skin-breast tissue interactions) for validation purposes. For example, attention can be given to the skin-breast tissue interface by creating a gel composite with a thin membrane (rubber for example) enclosing some homogeneous gel. When making such a composite, it is possible to specify the composite

geometry in the reference state. The composite can be stuck to a plate so that a fixed displacement boundary condition can be used. Specific types of loading conditions can be applied to independently estimate the mechanical properties of the individual constituents. With a well characterised set of loading conditions, boundary conditions, geometry and mechanical properties, the only unknown that can introduce a significant amount of error into model predictions is if the rubber-gel interface has not been modelled properly.

- Part III focusses on modelling the breast. While the silicon gel studies are important to validate individual modelling assumptions and parameters, it is important to keep the clinical application in mind. Research was conducted to answer four questions:
  1. How accurately can the geometry of the breast be represented for each individual by a finite element model using an automatic and efficient algorithm?
  2. Can the breast, in neutral buoyancy conditions, be considered as a representation of the reference configuration for predicting large deformations under gravity loading conditions?
  3. What errors are introduced if the prone gravity-loaded configuration is used as the reference state?
  4. Is a homogeneous model sufficient for the prediction of breast deformation under gravity loading conditions?

Validation of the biomechanics framework with controlled clinical experiments provides insights into the challenges of breast biomechanics. As will become clear at the end of this thesis, coupling silicon gel experiments with clinical experiments is a robust method of assessing the accuracy of modelling assumptions.

The proposed research of this thesis is necessary for providing clinicians with a software tool that accurately collocates tissue regions of interest across multiple images. The approach of this research is to develop a biomechanical model from

first-principles. The silicon gel and clinical experiments ensure that the modelling framework accurately simulates deformations of the breast that obey the laws of physics. While x-ray mammography is the main modality used for cancer diagnosis, MR imaging is becoming increasingly useful as an adjunct imaging modality for reliable diagnosis. MR images also provide better information regarding tissue distributions and are therefore more useful in assessing the performance of the modelling framework in tracking tissue deformations at this early stage of the project. Nonetheless, the knowledge gained and techniques developed while focussing on MR images will be very useful for predicting deformations in images from other modalities such as x-ray and ultrasound.

# **Part II**

## **Validation of the Biomechanics Modelling Framework**



# Chapter 3

## Forward Mechanics of a Homogeneous Body

As discussed in Section 2.5, there have been a number of methods used to model the deformations of breast tissue. Azar et al. (2000) justified that small strain theory helped to reduce the time of simulations. However, small strain theory ignores the nonlinear deformations that the breast undergoes and results in the accumulation of errors. Therefore, finite deformation theory is used in this thesis to accurately model the large deformations in the breast. A number of models using finite elasticity theory have already been published, but very few have conducted carefully controlled experiments to validate their basic framework. Small cuboid phantoms have typically been used to validate the framework, but these cannot represent the complexity of deformations undergone by breast tissues.

This chapter focuses on answering the following question:

**How accurately can the deformed configuration of a homogeneous body be predicted under gravity loading, if its reference state, mechanical properties and boundary conditions have been accurately characterised? This is referred to here as the “forward problem”.**

To answer this question, Section 3.1 first describes a validation of the modelling framework using an analytic solution to the passive inflation and axial extension of

a thick-walled cylinder. Section 3.2 describes the experimental framework developed to determine the accuracy of the modelling framework in predicting displacements of a custom built homogeneous phantom that is of a size and shape more representative of the breast. Section 3.3 describes the experiments that were conducted to address the above question.

### 3.1 Validation with an Analytic Solution

Rivlin (1950) developed an analytic solution for the general case of identifying the deformed state of a thick-walled cylinder made of Mooney-Rivlin material under pressure inflation, axial extension and torsion. In order to validate the finite element implementation of finite elasticity, pressure inflation and axial extension was simulated for a given reference state to obtain an analytic deformed state. The reader is directed to (Rivlin, 1950) for details on the derivation of the analytic solution procedure to this problem.

The analytic forward solution was generated using the parameters for the reference state and the applied boundary conditions shown in table 3.1. The analytic deformed state corresponding to these parameters has an internal radius,  $r_{int}$ , of 0.88 mm and an external radius,  $r_{ext}$ , of 1.23 mm. The analytic physical Green strains  $E_{rr}$ ,  $E_{\theta\theta}$  and  $E_{zz}$  were calculated at the undeformed radius  $R = 1.125$  for testing the accuracy of the model.  $r$  is the radial direction,  $\theta$  is the circumferential direction and  $z$  is the axial direction. The strains were -0.266, -0.131, and 0.945, respectively.

A finite element model of the reference state was created and the deformed state was predicted using the modelling framework. For a displacement converged model with eight circumferential elements, one axial element and two radial elements (16 tricubic-Hermite elements, 48 nodes, 1152 geometric degrees of freedom), the model predicted that the internal deformed radius,  $r_{int} = 0.8818$  mm and that the external deformed radius,  $r_{ext} = 1.23$  mm. The predicted deformed internal and external radii for three different refined geometries are shown in table 3.1. The physical Green strains  $E_{rr}$ ,  $E_{\theta\theta}$  and  $E_{zz}$  at the undeformed radius  $R = 1.125$  were predicted to be -0.267, -0.131, and 0.945, respectively in the solution converged model. This demonstrated that the basic finite element implementation of finite elasticity was

Parameter	Value
Internal undeformed radius $R_{int}$	1.0mm
External undeformed radius $R_{ext}$	1.5mm
Cylinder length $L$	1.0 mm
Mooney-Rivlin $c_1$	2.0 kPa
Mooney-Rivlin $c_2$	6.0 kPa
Axial extension ratio $\lambda$	1.7
Torsion angle $\theta$	0.0 radians
Internal pressure $P_{int}$	3.0 kPa
External pressure $P_{ext}$	0.0 kPa

Table 3.1: Parameters used for validation purposes using analytic solution for pressure inflation, and extension of a thick-walled cylinder

able to predict the deformed state accurately for this type of problem.

Refinement (circumferential x depth x radial)	$r_{int}$	$r_{ext}$
4x1x1	0.8809	1.2297
4x1x2	0.8807	1.2297
8x1x2	0.8818	1.23

Table 3.2: Deformed internal and external radii predicted for different mesh refinements of the reference state

## 3.2 Experimental Framework

Comparison with an analytic solution indicates that the finite element implementation of finite elasticity has been correctly programmed. However, it does not provide any indication of the accuracy of the method in predicting deformations of real objects. Experimental measurements and modelling assumptions inherently introduce error into model predictions. Therefore, in order to develop a reliable and accurate computational model of an object, it is important to systematically identify sources of error in a model and eliminate them (if possible). This section describes the experimental framework that was developed to validate modelling techniques for breast biomechanics and to identify sources of error in the modelling framework using silicon gel phantoms.

### 3.2.1 Modelling mechanical properties of silicon gel

All experiments on phantoms used Sylgard® 527 gel from Dow Corning, USA. The silicon gel is a two part mix with dielectric properties and therefore it can be imaged in an MRI machine. In order to model the large deformations of the silicon gel in the validation study, it was necessary to accurately identify its mechanical behaviour. This section shows the results of an experiment that was conducted to determine the best way to model the gel behaviour.

A tensile test was conducted on a cylindrical sample of silicon gel (with dimensions of 55 mm length and 15 mm diameter) to identify the material parameters that characterise the mechanical behaviour of the gel. The tensile testing rig (Fig. 3.1) consisted of a force transducer coupled to a displacement actuator that pulled the silicon gel sample. The measurements from the force transducer and displacement actuator were recorded on a force-displacement plot.

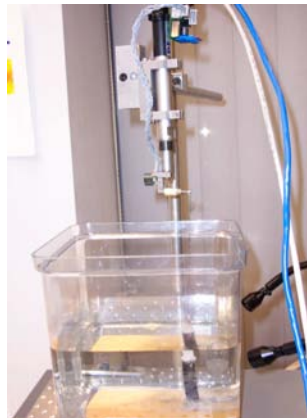


Figure 3.1: The tensile testing rig used to model the behaviour of the material. The density of the gel is similar to that of water and hence conducting the test under water minimised the effect of gravity.

The density of the gel is similar to that of water. Therefore the test was conducted under water to reduce the effect of gravity on the sample. This ensured that the experiment provided an estimate of the mechanical properties of the gel independent of gravity loading conditions. It was found that the gel behaved approximately linearly, as shown by the force-displacement plot in Fig. 3.2. As can be seen in this figure, a maximum displacement of 16 mm was achieved during the experiment.

The gel was assumed to be isotropic, incompressible and homogeneous. The incompressible material version of the neo-Hookean material law (equation (2.17)) was then fitted to the force-displacement data using a material parameter optimisation procedure in CMISS. Tricubic Hermite basis functions were used to describe the displacement field, while trilinear basis functions were used to describe the scalar hydrostatic pressure field (the incompressible elasticity theory). The bottom nodes in the model were fixed in all three directions to represent the gel being glued to the bottom-plate. The top nodes were then displaced by known increments in the vertical direction (as prescribed in the experiment) to a maximum displacement of 16 mm. The model then predicted the force required to stretch the gel. An optimisation procedure compared the predicted reaction force to that measured in the experiment. The objective was to find the optimal value of the material parameter that minimised the error between the predicted and measured forces. The optimisation procedure estimated the optimal neo-Hookean parameter to be 3.11 kPa.

This value was then used in a simulation of the experiment, to reproduce the experimental force-displacement graph of Fig. 3.2. The overlayed graph in Fig. 3.2 showed that the finite element model, with the estimated material parameter value of 3.11 kPa, was sufficient to reproduce the experimental observations.

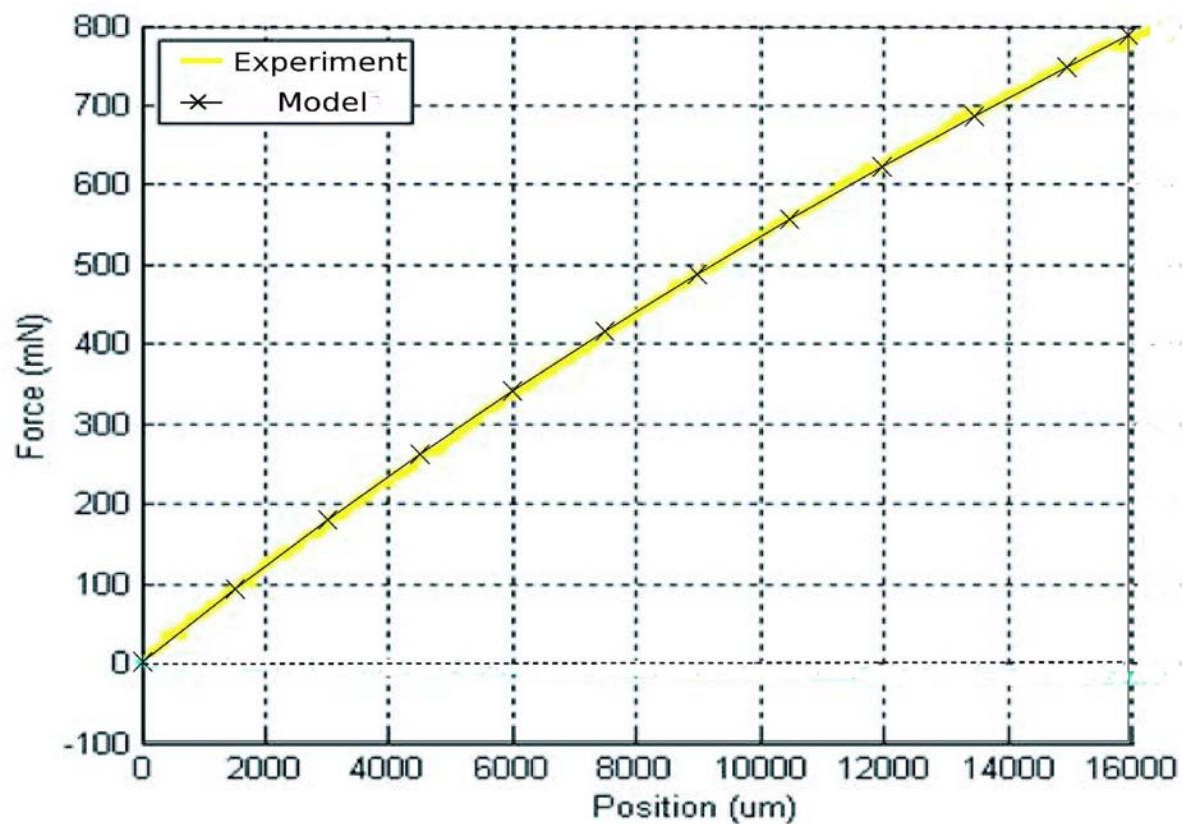


Figure 3.2: Force-displacement data experimentally recorded (yellow lines) and reproduced by CMISS (black lines with crosses) for the uniaxial extension of the silicon gel. The reproduced curve was obtained using estimated material parameter value of 3 kPa

The gel sample was then oriented as a cantilever beam as shown in Fig. 3.3. The estimated value of the material parameter from above was then used to simulate the deformation of the cylinder under gravity. One end of the cylinder was fixed in all three directions to represent the cantilevered end. A gravitational body force was then applied to simulate the cantilever deformation. The estimated value of the neo-Hookean parameter gave good predictions of the deformation of the cantilever beam (with maximum vertical displacement of approximate 28 mm) as can be seen in Fig 3.3.

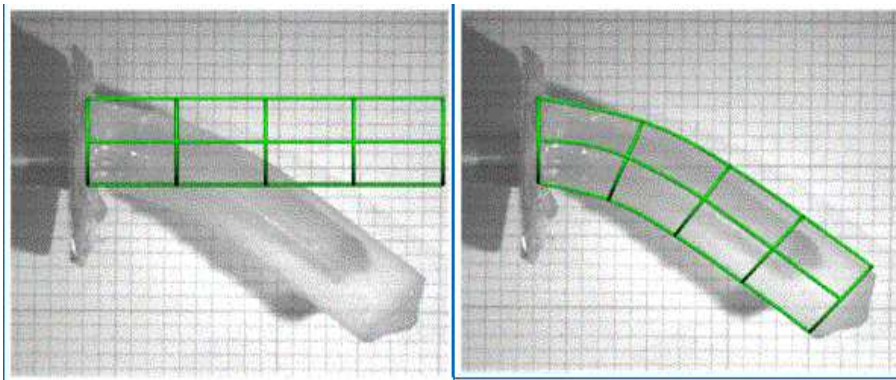


Figure 3.3: Comparison of finite element prediction of deformation of silicon gel under gravity. Thick lines show the finite element mesh created to simulate the problem using CMISS.

The neo-Hookean constitutive relation provided a good representation of the mechanical behaviour of the silicon gel under the above gravity loading conditions. Thus, the neo-Hookean constitutive relation was used to characterise the mechanical behaviour of the silicon gel phantoms. The value of the neo-Hookean parameter,  $c_1$ , for the phantoms were obtained through a nonlinear optimisation method using surface scans of the deformed shape. Typically, one deformed state (although more than one could be used) was used to optimise for the material parameter and the other four orientations in Fig. 3.5 were used to measure the accuracy of the model in predicting deformations. It should be noted that the mechanical properties of the gel were primarily determined by the ratio of the two liquid components (called Part A and Part B) used to make the gel. Part B is the catalyst that increases the number of chains and thus the stiffness of the gel, formed by the Part A component. The gel mechanical properties vary with each mixture that is made, and therefore

the material parameter,  $c_1$ , had to be identified for each mixture.

### 3.2.2 Phantom geometry and boundary conditions

Previous studies such as (Azar et al., 2000) and (Samani et al., 2001) performed validation experiments on cubical phantoms much smaller in size compared to a typical breast. In order to validate the performance of the modelling framework in predicting breast tissue movement under gravity loading conditions, in the author's belief, it was important to create a phantom that could simulate the types of deformations imposed on the breast. Therefore, a specialised mould for a phantom was designed (see Appendix A for design details) such that the gel could undergo deformations that more closely represented those experienced by the breast. The mould was made of two subunits of the design shown in Fig. A.1. Fig. 3.4 shows the mould and the silicon gel phantom that was cured in it. An obvious shape for the mould would have been hemispherical, but this flat-sided design was chosen with future silicon gel experiments in mind. For example, a validation exercise in mind for the future is to determine the best way to model the skin-breast tissue interface (see Chapter 5). A hemispherical mould geometry would make it difficult to enclose the gel with a thin membrane since it would create folds in the membrane. The mould in Fig 3.4(a) would make it easier to cover the gel with a thin flat membrane.

The boundary conditions were kept simple at the base of the phantom by curing the gel on a paper covered perspex plate. Curing the gel with the plate screwed to the mould, allows for the gel to bond to the acrylic in what is believed to be a stress-free state. Fixed displacement boundary conditions could therefore be applied to the nodes on the base of the mould. The mould represents the shape of the gel phantom in the reference state. As the mould was custom built, it was straightforward to create a model of the undeformed reference state using the mould dimensions (Fig. 3.4(c)). In contrast, the reference state of the breast (with no loads applied) is not available as gravity loading is always present. Chapter 4 addresses the problem of identifying the reference state from a given set of deformed states under different gravity loading conditions.

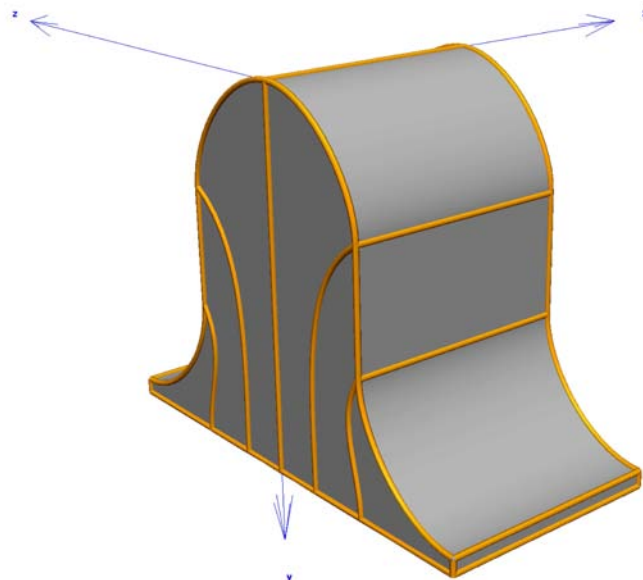
### 3.2.3 Applying loading conditions

In order to test the accuracy of the model in predicting deformations under gravity loading, six different loading conditions were applied. The orientations of the phantom under these loading conditions are given in Fig. 3.5. The phantom was positioned in these orientations by placing the base of the gel on inclined wedges constructed from perspex material using a CNC milling machine. To ensure that the gel was at the right orientation, the inclined planes and gel were placed on top of a custom built leveling base with vertically adjustable feet.



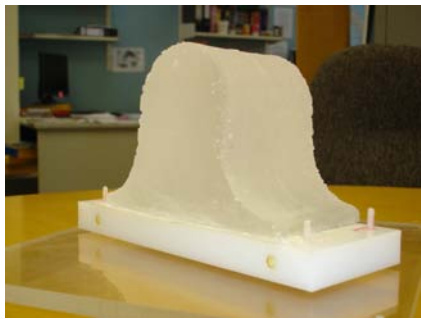
(a) Mould

(b) Gel phantom

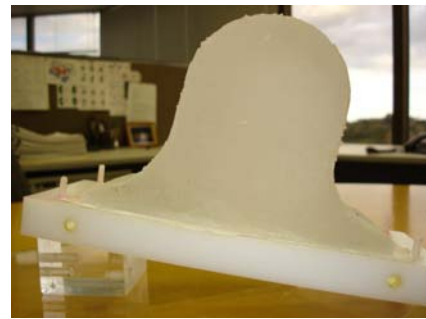


(c) Model of phantom

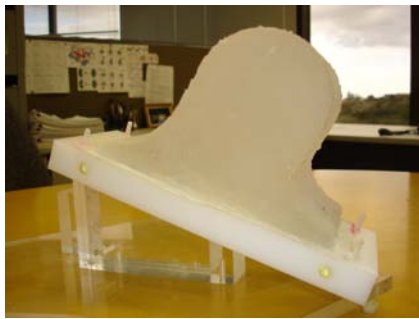
Figure 3.4: Mould, gel and model. The coordinate axes were given anatomical labels similar to those used for the breast: x-axis is medio-lateral (ML), y-axis is antero-posterior (AP) and z-axis is supero-inferior (SI).



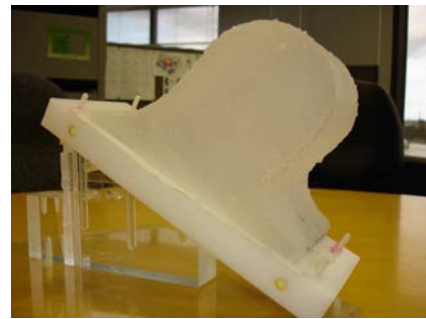
(a) 0 degrees (Supine)



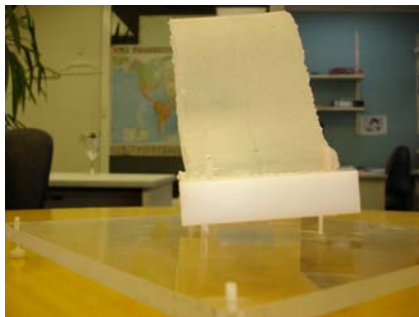
(b) 10 degrees Supero-Inferior (10 SI)



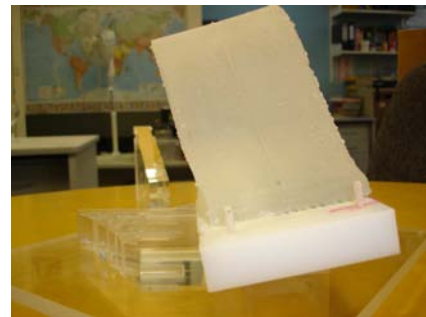
(c) 20 degrees Supero-Inferior (20 SI)



(d) 30 degrees Supero-Inferior (30 SI)



(e) 5 degrees Medio-Lateral (5 ML)



(f) 10 degrees Medio-Lateral (10 ML)

Figure 3.5: Orientation of gel under different gravity loading conditions. The gel placed on the flat end was called the supine position to mimic a person lying on their back. The anatomical axis references (for example 10 SI, 5 ML, etc.) indicate the axis about which the base plate is tilted.

### 3.2.4 Displacement convergence analysis of phantom model

It is important to perform a displacement convergence analysis to determine the resolution of the model that provides an accurate prediction of the deformed configuration for the particular loading conditions of interest (gravity, in this case).

For this purpose, the displacements of the gravity loaded gel phantom were recorded from simulations at fifteen points within the model (Fig. 3.6). The displacement accuracy is important near regions of high curvature and therefore a number of the material points in this neighbourhood were analysed. These points are also expected to compress due to the loading conditions imposed. In order to also analyse the areas of tensile strain, additional points near the midsection of the phantom were chosen. The simulations predicted deformations under gravity loading with the 30 SI loading vector  $[0, -8.4957, 4.9050]$  (see Fig. 3.5 for loading vector terminology). This loading produced the deformation shown in Fig. 3.6.

The Euclidean displacements that each data point underwent during the deformation was calculated for each mesh resolution. The RMS error between successive refinements were then recorded (plotted in Fig. 3.7) and the mesh resolution corresponding to 4200 degrees of freedom (Fig. 3.8) was chosen as a sufficient resolution. This mesh consisted of 96 tricubic Hermite elements (4 elements medio-lateral, 4 elements antero-posterior and 6 elements supero-inferior) and 175 nodes. This displacement converged mesh was used in subsequent work on validating the modelling framework using the silicon gel phantoms.

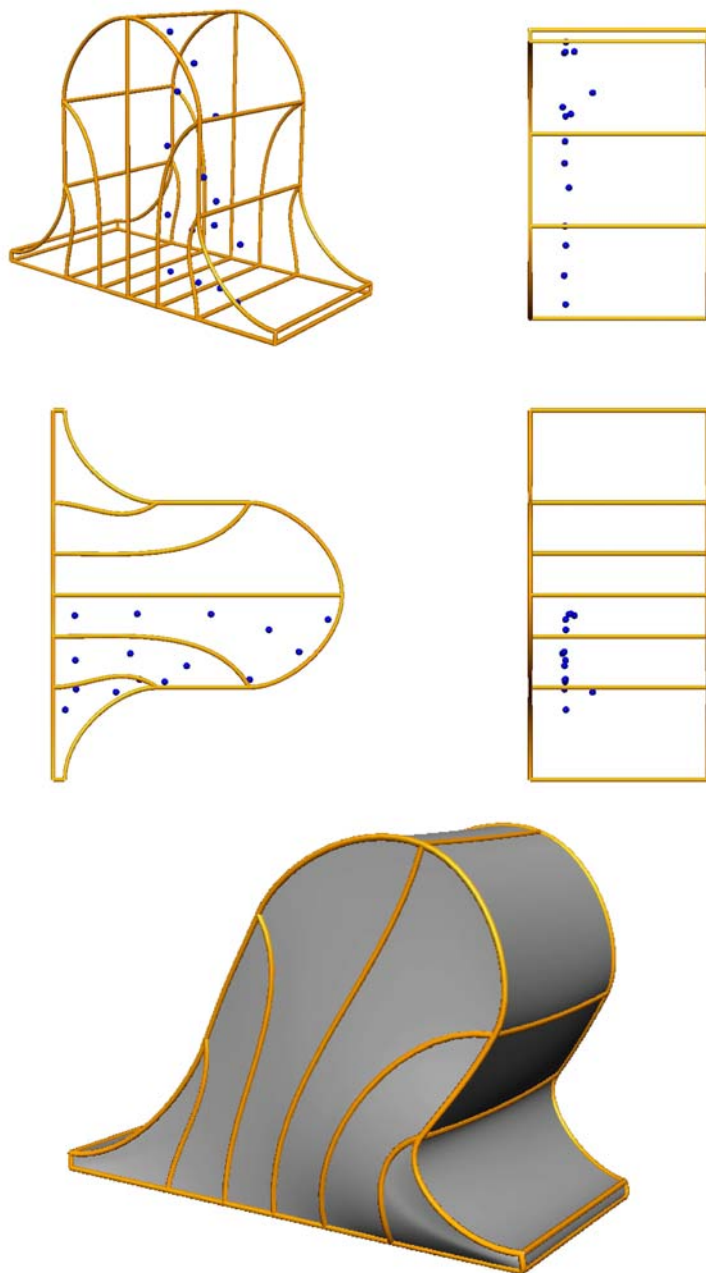


Figure 3.6: (top) Three-dimensional view of initial phantom model and data points at which strains were calculated. (bottom) Predicted mode of deformation using 30 SI gravity loading condition

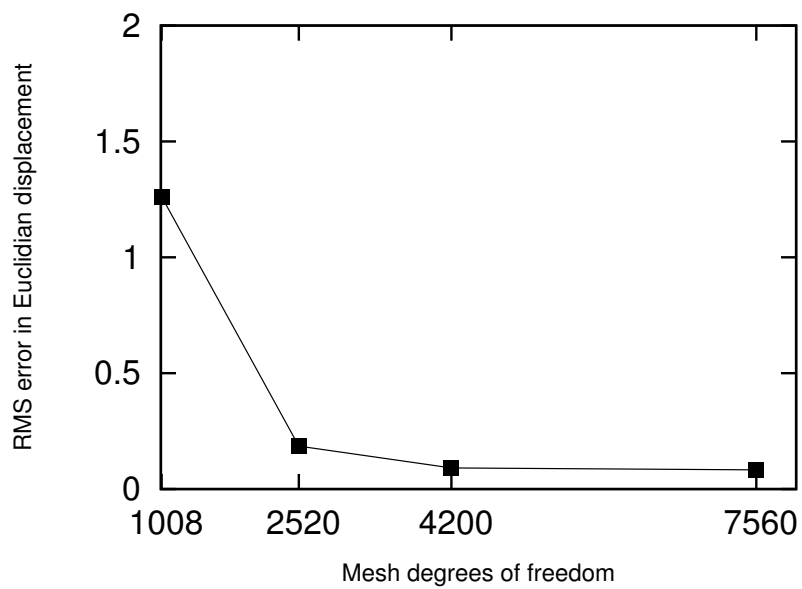


Figure 3.7: Graph showing the convergence of RMS error in displacements of points inside mesh (Fig 3.6) with increasing resolution.

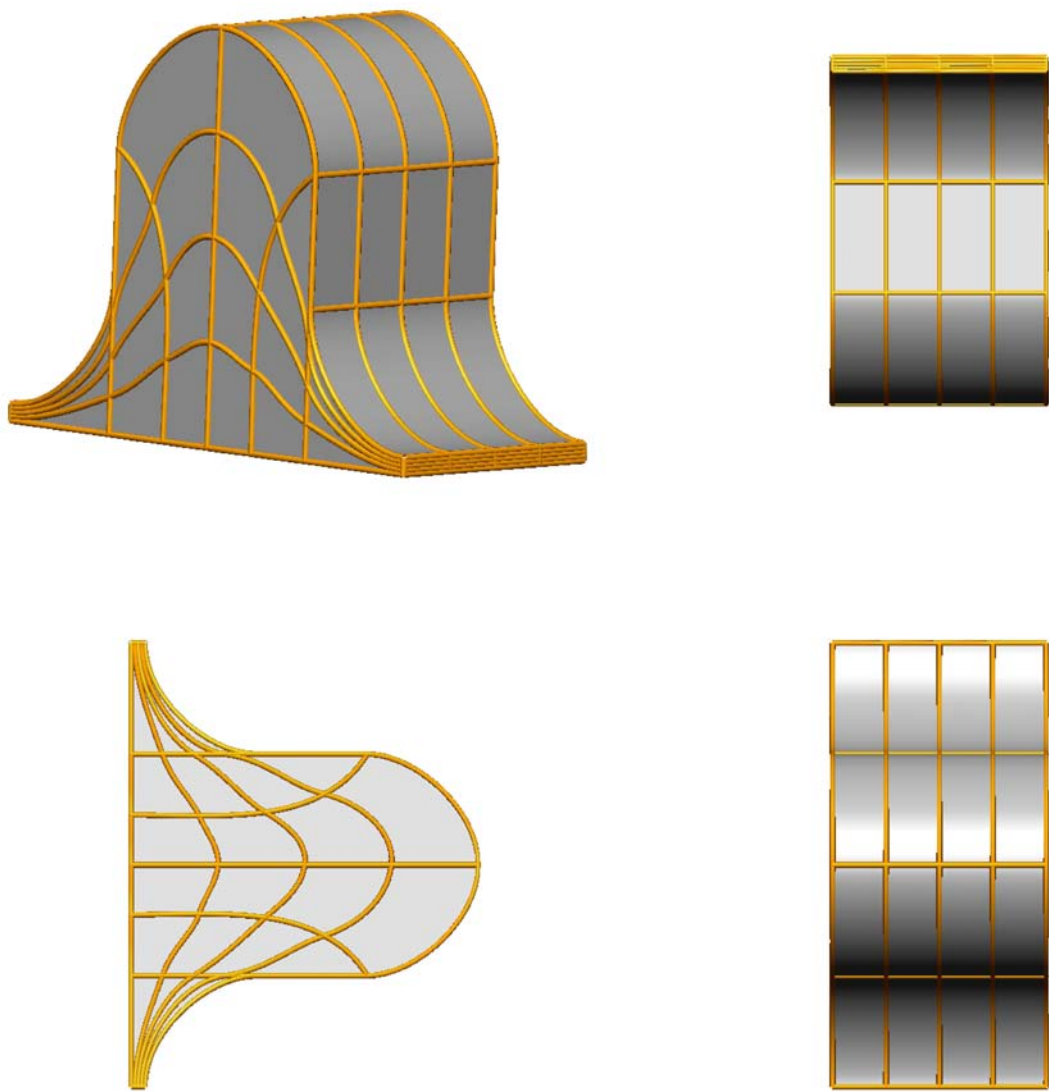


Figure 3.8: Mesh resolution (with 4200 degrees of freedom) chosen for this study.

### 3.3 Validation Experiments

Two sets of validation studies were conducted on two separate gel phantoms. A first set of studies used x-ray images of one phantom to validate the finite element model. However, the study produced some contradictory results and indicated large errors in model predictions of large deformations. Sources of error were identified and then a second set of experiments used MR images of a gel phantom to perform the validation study. This section outlines the methods and results obtained from the MR imaging study (with improvements on the x-ray study) to validate the basic finite elasticity framework for modelling the deformations of a homogeneous body under gravity loading conditions. The x-ray study is described in Appendix B to illustrate the importance of silicon gel studies to identify sources of error in a model.

#### 3.3.1 Validation method

In order to quantify the accuracy of the modelling framework in predicting deformations of the phantom, two forms of experimental measurements were obtained - surface deformations and internal marker movement.

##### Surface deformation tracking

A simple measure of prediction accuracy was made by comparing predicted and experimental recordings of the surface deformations of the homogeneous gel. The deformed surface was recorded using a Polhemus Fastscan laser scanner<sup>1</sup>. The error between the predicted deformed surface and the recorded surface data was calculated by projecting the data points onto the model using the closest orthogonal projection approach described in (Nielsen, 1987). The length of the data projection vectors from data point to element coordinates represents the error in model predictions. The root mean squared error (RMSE) of the data projection vectors was calculated as a measure of the error in predicting surface deformations.

---

<sup>1</sup><http://www.polhemus.com/>

### Internal marker movement

Although surface deformation tracking provides a good indication of the model accuracy, it is important to quantify the error of the model in predicting internal tissue movement. This is important as the overall aim is to track internal regions of tissue across multiple imaging modalities. Also, with heterogeneous tissue distributions, different regions inside the breast will deform differently.

Silicon gel appears as a grey object under MRI when using a T2 weighted sequence. Six internal markers were embedded in the gel by inserting high density polyethylene cylindrical rods (2 mm long and 2 mm radius) into the gel during the curing process. Since the rods were relatively small compared to the dimensions of the gel, it was assumed that any localised stiffening in the neighbourhood of the rods was negligible, and that the assumption of material homogeneity was still appropriate. The mould was imaged (3D imaging sequence with 0.6 mm x 0.6 mm x 0.6 mm resolution) in a 1.5 T Siemens MR scanner to obtain the internal marker positions (polyethylene appears as a black spot in the grey gel image) in the undeformed state (Fig. 3.9(a)). The MR images of the homogeneous silicon gel are not hampered by the distortion effects typically present in x-ray images (see Appendix B), thus the absolute spatial coordinates of the internal markers could be obtained from the MR images without further calibration. The marker boundaries were segmented from the images using intensity thresholding to create a data set representing each marker. The center of mass of each data set was calculated and incorporated in the model of the reference state. MR images were then obtained with the gel at different orientations with respect to gravity to measure the deformed configuration locations of the internal markers. The marker coordinates calculated from the MRI of the deformed states were then compared to predicted marker coordinates by simulating the deformation using the reference state model. The Euclidean distance between predicted and measured locations was used as a quantification of prediction error.

MR images of the gel were obtained in two gravity loaded orientations (Figures 3.9(b) and 3.9(c)) to obtain the deformed locations of the internal markers. The gel was laser scanned in the orientations in Fig. 3.5 and the 30 SI configuration was used to determine the mechanical properties of the gel phantom. An optimisation procedure was set up with the 30 SI deformation to determine the value of  $c_1$  for the neo-Hookean material relation using the 30 SI deformed data set. The objective

function of the optimisation procedure was to minimise this RMS error with the optimal  $c_1$  value found using the following steps:

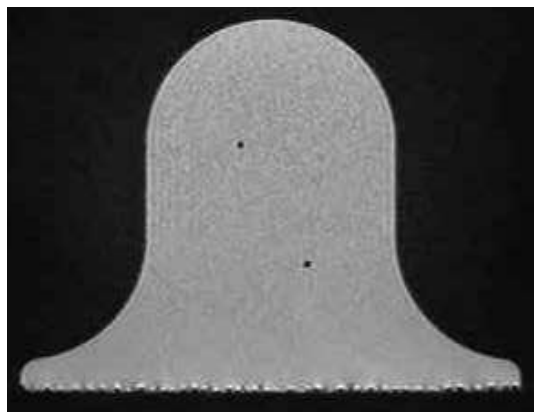
1. The mesh in Fig. 3.8 was deformed in the 30 SI configuration with an initial estimate of the  $c_1$  value.
2. The RMS projection error between the 30 SI deformation data set and the predicted deformed surface of the mesh was calculated.
3. The initial estimate of  $c_1$  was perturbed and the model was re-solved. The new RMS error with the new predicted deformed configuration was calculated.
4. A finite difference derivative of the objective function with respect to  $c_1$  was calculated using the RMS errors and  $c_1$  values in steps 2 and 3.
5. This derivative provided a search direction for the next estimate of the material parameter value.
6. Steps 1-5 were repeated until the RMS error was minimised, yielding an optimal  $c_1$  value.

### 3.3.2 Validation results

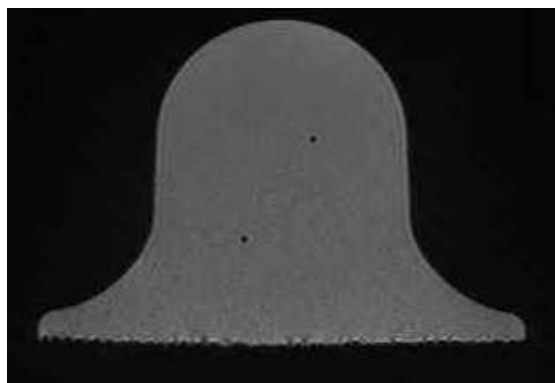
The optimal neo-Hookean material parameter was found to be  $c_1 = 0.61$  kPa for this experiment. The quantitative errors in tracking internal markers and surface deformations are given in Table 3.3 and a visual representation of the model prediction are given for the 20 SI configuration in Figures 3.10 and 3.11.

Deformation	10 ML	5 ML	10 SI	20 SI	30 SI	Supine
Max Ext Rat.	1.5	1.3	1.2	1.3	1.4	1.2
Max Displ.	50 mm	23 mm	18 mm	34 mm	52 mm	11 mm
Surface RMSE	1.36 mm	1.65 mm	1.21 mm	1.47 mm	1.74 mm	1.48 mm
Int. Mk 1 ED				2.09 mm		1.01 mm
Int. Mk 2 ED				2.05 mm		1.4 mm
Int. Mk 3 ED				2.08 mm		1.04 mm
Int. Mk 4 ED				1.76 mm		0.69 mm
Int. Mk 5 ED				2.11 mm		0.34 mm
Int. Mk 6 ED				1.72 mm		0.37 mm

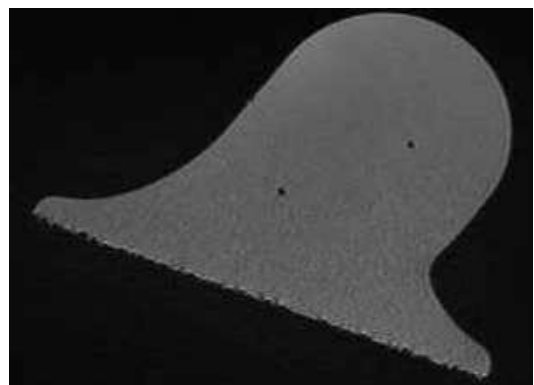
Table 3.3: Root-mean-squared errors (RMSE) in tracking surface deformations and Euclidean distance (ED) between predicted and measured internal marker positions for the silicon gel phantom imaged using MRI. The maximum extension ratios were chosen from a list of extension ratios calculated at all the Gauss points in the mesh. The maximum displacements were chosen from a list of the displacements of all the nodes in the silicon gel model. These values are given to provide an indication of the amount of deformation under the different loading conditions.



(a) Reference configuration



(b) Supine configuration



(c) 20 SI configuration

Figure 3.9: MRI of gel in the reference, supine and 20 SI configurations. The black spots are polyethylene markers inside the gel. Note that the markers shown in (a) are not the same as the markers in (b) and (c)

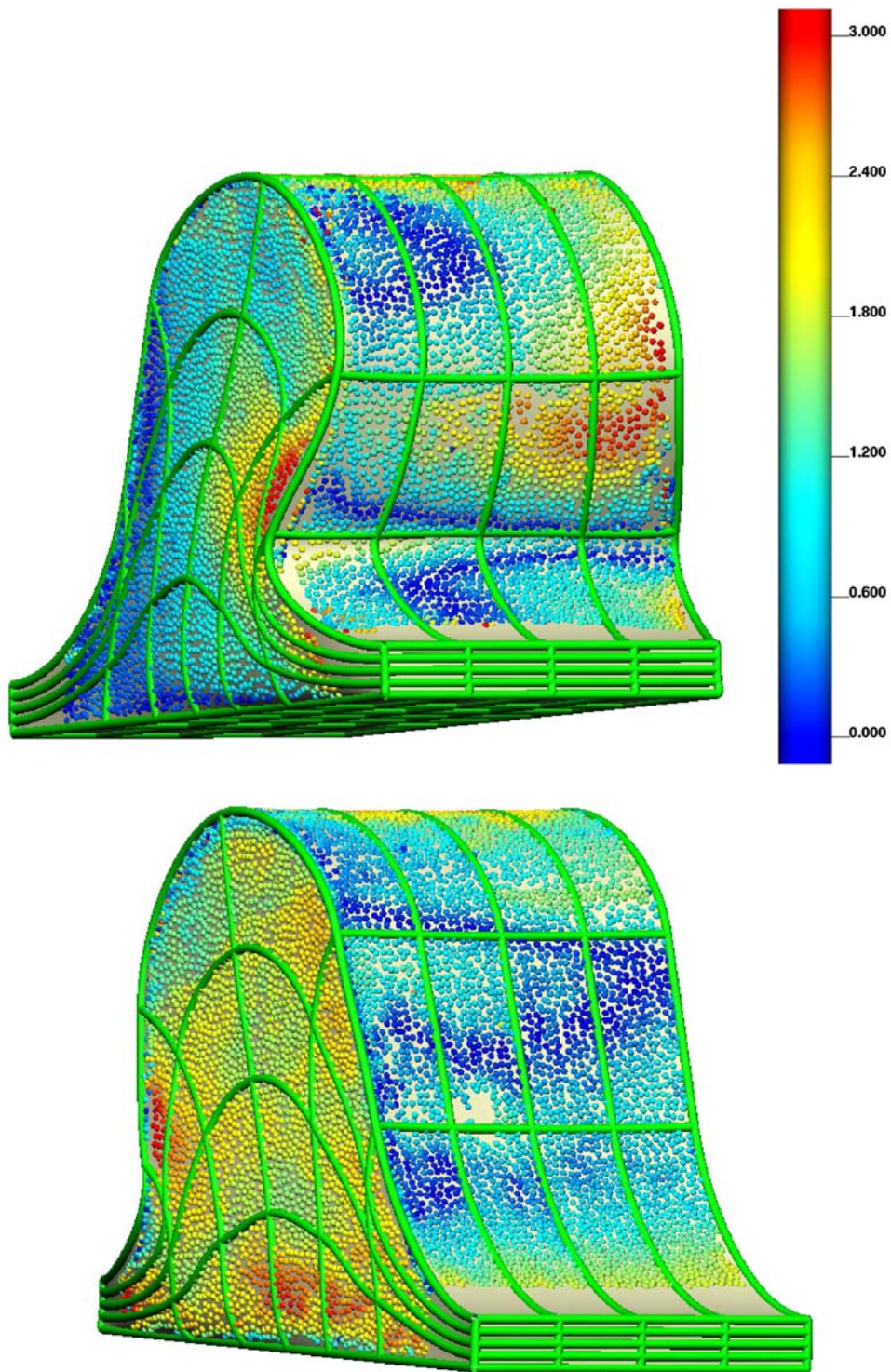


Figure 3.10: Visual representation of surface deformation matching accuracy with an RMS error of 1.47 mm. The spheres represent the surface data points obtained using the laser scanner with the colour map showing the individual error magnitude, in millimeters, associated with each data point.

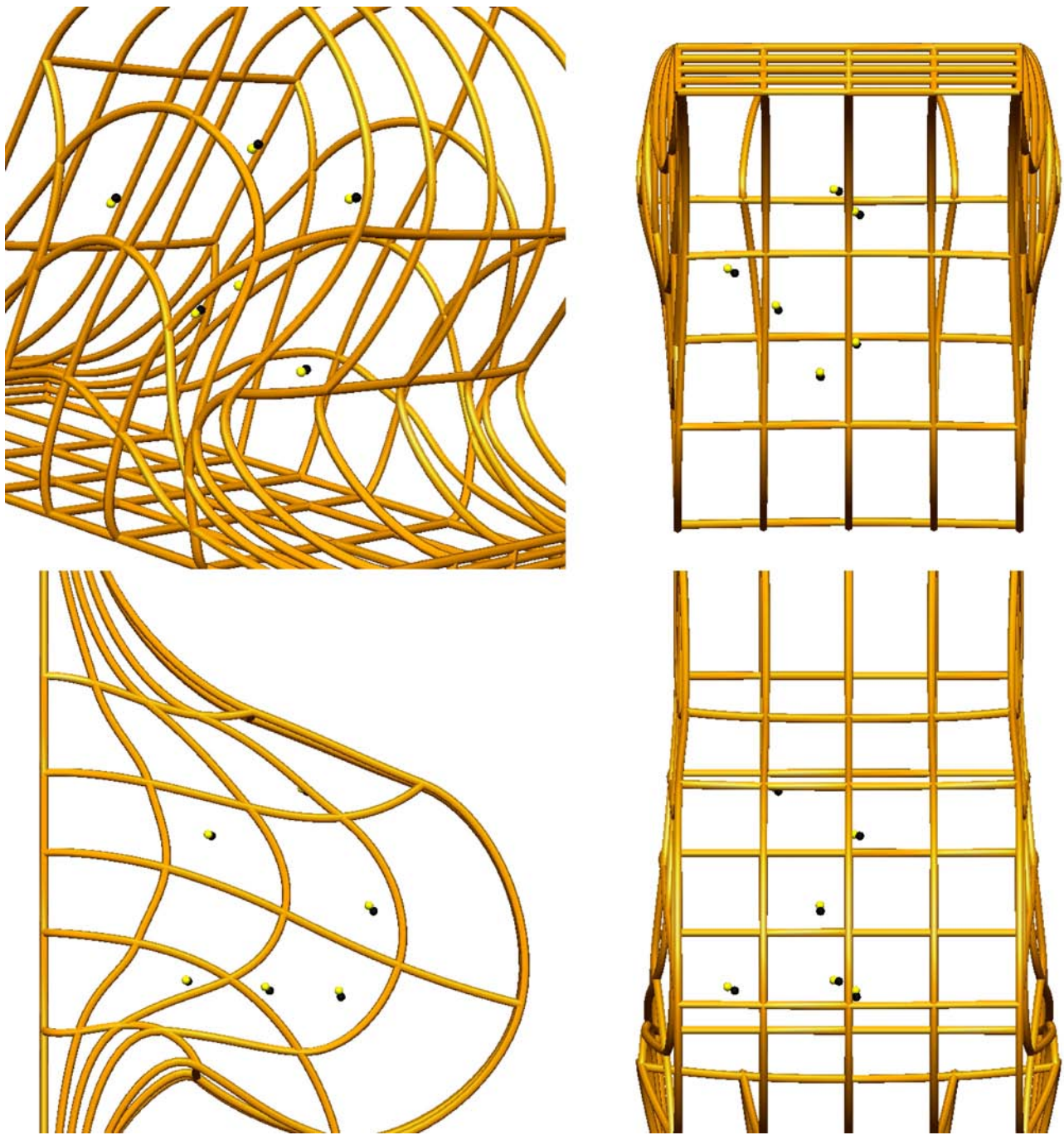


Figure 3.11: Visual representation of the internal marker tracking accuracy for 20 SI deformation. The yellow spheres represent actual locations and the black spheres represent predicted locations of the internal markers. The internal marker location errors ranged from 1.76 mm to 2.11 mm

### 3.3.3 Discussion

The results show that the finite element model of the silicon gel phantom provides reliable predictions of the deformations under different gravity loading conditions. The surface deformation prediction error is reasonably consistent across the deformed states, and the error in predicting the internal marker locations is also reasonably consistent for a specific deformation. The magnitude of the errors are lower than the acceptable error of 3 - 5 mm in localising the position of a lesion in an MR image, based on its known position in two standard mammograms and vice versa (Ruiter & Stotzka, 2006).

It should be noted that the measured accuracy in model predictions is limited by the methods used to quantify it. A major source of error is the resolution of the Polhemus scanner in recording the deformed surface. In order to quantify the accuracy of the laser scanner, the surfaces of a rigid block were scanned. The volume of the rigid block was calculated based on the recorded surface data cloud and compared to its actual volume. There was a 3.6% error in the volume of the block. This could account for the inaccuracies in the material parameter fitting procedure (1.74 mm RMSE in predicting 30 SI deformation, which was used to estimate the mechanical properties). The limitations in accuracy enforced by the scanner is shown by the consistency of surface RMS errors of the model in predicting surface deformations (see Table 3.3).

The size of the markers also limits measurable accuracy as they do not really represent material particles of the homogeneous gel. An improvement can be made to the current experimental technique by mixing many more (in the order of hundred) smaller internal markers (in the order of microns) into the silicon gel before letting it cure. A more robust method of estimating the accuracy would be to use cross-correlation to measure the similarity between an MR image of the internal marker locations with a model-produced image containing predicted internal marker locations. However, as the gel takes approximately 3 hours to cure, markers have sufficient time to sink to the bottom or float to the top of the gel. This could make the gel properties heterogeneous, as the markers may produce trails and disturb the homogeneity of the gel. Therefore challenges lie ahead in identifying materials that will be of approximately the same density as the silicon gel.

### 3.4 Conclusion

How accurately can the deformed configuration of a homogeneous body be predicted under gravity loading, if its reference state, mechanical properties and boundary conditions have been accurately characterised? This is referred to here as the “forward problem”.

A finite element model of a homogeneous body can reliably predict surface deformations with an average RMS error of  $1.5 \text{ mm} \pm 0.2 \text{ mm}$ , and track internal marker locations with an average error of  $1.4 \text{ mm} \pm 0.7 \text{ mm}$ . This result can be used as a reference to compare against errors in predictions of more complex models of breast deformation that will be developed.

# Chapter 4

## Reverse Mechanics of a Homogeneous Body

Chapter 3 quantified the error of the modelling framework in predicting the deformed configuration of a homogeneous body by applying gravity loading conditions to the reference configuration. However, all images of the breast are obtained under gravity loading conditions (mammography adds compressive loads as well). Therefore, any finite element geometry created from a set of breast images will represent a deformed configuration of the breast. Prediction of large deformations is a non-linear problem, making it necessary to calculate the stress free reference state of the breast in order to provide reliable predictions of breast deformation under a variety of loading conditions. To date, no model published in the literature has addressed this aspect of breast modelling.

This chapter focuses on answering the following question:

**How accurately can the reference configuration of a homogeneous body be predicted, given mechanical properties, boundary conditions and a set of deformed configurations under different gravity loading conditions? This is referred to here as the “reverse problem”**

In answering this question, a new technique of determining the reference state was developed and implemented as described in Section 4.1. In Section 4.2, the

implementation was first tested using the analytic solution to the passive inflation and extension of a cylinder described in Section 3.1. The accuracy of the method is then quantified and its use in breast modelling is discussed in Section 4.3.

## 4.1 Directly Calculating a Reference State - The Reverse Method

Previously published methods to solve the reverse problem have focused on reformulating the finite elasticity theory in terms of the Eulerian frame of reference (Govindjee & Mihalic, 1996, 1998). However, examination of the finite element implementation of the finite elasticity equations shows that it is possible to compute the reference state by redefining the knowns and unknowns in the problem definition for the Lagrangian formulation.

Consider again the finite elasticity Equations (2.13). For the forward problem,  $\mathbf{X}$  are known and  $\mathbf{x}$  are unknown. In order to find the values of the unknowns using Newton's method, finite difference derivatives of the residuals are calculated with respect to each of the unknown solution degrees of freedom ( $\mathbf{x}$  in this case). These derivatives are used to construct the linear system of equations that are solved to determine the solution parameter increments (see Section 2.3.2).

On the other hand, for the reverse problem,  $\mathbf{x}$  can be considered as known, and  $\mathbf{X}$  the unknowns. Therefore, Equation (2.13) can be rewritten as:

$$\mathbf{R}(\mathbf{X}) = \mathbf{0} \quad (4.1)$$

The aim is to find  $\mathbf{X}$  such that equation (4.1) is satisfied. Given an initial estimate of the parameters of the reference state,  $\mathbf{X}_0$ , an improved estimate of the reference state,  $(\mathbf{X}_0 + \delta_{\text{undef}})$  can be found using:

$$\mathbf{J}(\mathbf{X}_0)\delta_{\text{undef}} = -\mathbf{R}(\mathbf{X}_0) \quad (4.2)$$

Then the Jacobian matrix consists of first derivatives of the finite elasticity residuals with respect to the parameters of the reference state, which are computed as:

$$J_j^i(\mathbf{X}_0) = \frac{\partial R_i(\mathbf{X}_0)}{\partial X_j} = \frac{R_i(\mathbf{X}_0 + \Delta \cdot \mathbf{e}_j) - R_i(\mathbf{X}_0)}{\Delta} \quad (4.3)$$

where  $\Delta$  is the perturbation applied to each of the unknowns,  $\mathbf{X}_0$  in turn.

An appropriate initial estimate of the parameters of the reference state are parameters of the deformed state. The boundary conditions on the reference state are applied as if the forward problem was being solved. The solution procedure is equivalent to that for the forward problem with the only difference being that the parameters of the reference state are varied to satisfy the conventional equilibrium equations. A flow chart is given in Fig. 4.1 to provide an outline of the algorithm.

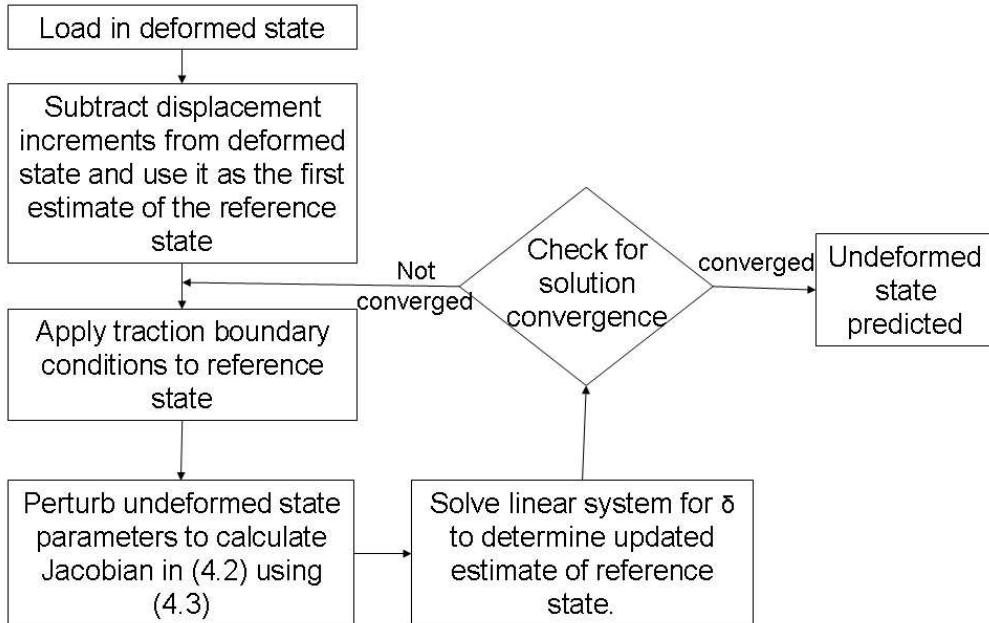


Figure 4.1: Algorithm to solve for the reference state, given a deformed state and loading conditions

The shape functions and interpolation schemes used to solve the forward problem are maintained from the forward to reverse problems. There is no change in strategy required for numerical integration. The primary difference is to calculate the Jacobian matrix via perturbations of the parameters of the reference state (rather

than the deformed state).

This method provides a simple way of predicting the reference state. Finite element modelling packages, whether in-house or commercial, typically choose either the Eulerian or Lagrangian formulation of the equilibrium equations. CMISS<sup>1</sup> uses the Lagrangian formulation and would require substantial effort in order to implement the Eulerian formulation to solve the reverse problem due to the size of the software code. Since the proposed method simply modifies the formulation of the Jacobian stiffness matrix, the method is straightforward to implement in an existing finite element package that uses the Lagrangian formulation.

## 4.2 Validation with an Analytic Solution

In order to determine the theoretical validity of the reverse method, the deformed state for pressure inflation and axial extension of a thick-walled cylinder was calculated analytically from a given reference state using the parameters in Table 3.1, as described in Section 3.1. The analytic deformed state corresponding to these parameters has an internal radius,  $r_{int} = 0.88$  mm and an external radius,  $r_{ext} = 1.23$  mm. A finite element model of this deformed configuration was created and the reference state was computed using the reverse method with  $\Delta$  in Equation (4.3) equal to  $1 \times 10^{-4}$ .

For a solution converged model with eight circumferential elements, one axial element and two radial elements (16 tricubic-Hermite elements, 48 nodes, 1152 geometric degrees of freedom), the reverse method predicted that the internal undeformed radius,  $R_{int} = 1.00$  mm and that the external undeformed radius,  $R_{ext} = 1.50$  mm. A range of values of  $\Delta$  from  $1 \times 10^{-8}$  to 1.0 were then used to see the effect of the size of the finite difference interval on prediction accuracy. All values from  $1 \times 10^{-2}$  and smaller computed  $R_{int} = 1.00$  mm and  $R_{ext} = 1.50$  mm. This demonstrated that the reverse method was able to predict the reference state accurately.

The mesh took seven Newton-Raphson iterations to reach a converged solution. More elements were necessary in the circumferential direction to accurately represent the circular geometry in rectangular Cartesian coordinates. Fig. 4.2 shows the convergence rate of the simulation in predicting the reference state.

---

<sup>1</sup><http://www.cmiss.org>

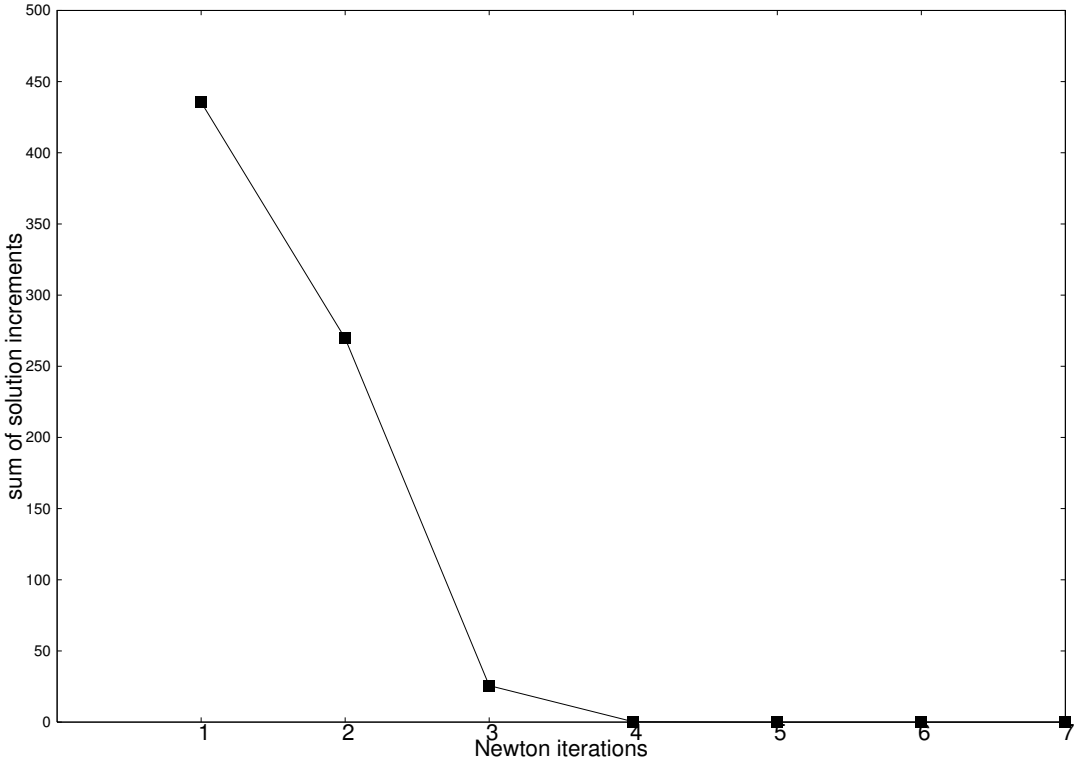


Figure 4.2: Convergence rate of reverse method.

### 4.3 Validation with an Experiment

The experimental framework provides a way to quantify the error in predictions of the reference state using the reverse method. From Section 3.3, the reference configuration, six deformed configurations, the mechanical properties, loading conditions and boundary conditions were known. A finite element model of a deformed configuration was created from the 30 SI deformed gel surface measurements. The neo-Hookean model of the mechanical properties, boundary conditions and loading conditions that were used in predicting the deformed configuration were then used to predict the reference configuration.

A surface data set was produced using the reference model used in Section 3.3. The error between the predicted reference surface and the actual reference surface was calculated by projecting the synthetically created reference configuration data points onto the predicted reference state surface configuration. The root mean

squared error (RMSE) of the data projection vectors was calculated as a measure of the error in predicting the reference configuration.

With regards to the internal markers, the center of mass coordinates of the markers in the deformed configurations were incorporated into the corresponding fitted deformed meshes and their locations in the reference state were predicted. The marker coordinates calculated using MRI in the reference state were then compared to the predicted marker coordinates. The Euclidean distance (ED) between predicted and measured locations was used as a quantification of prediction error.

### 4.3.1 Validation results

The RMS errors in fitting finite element models to the six deformed configuration surface data clouds is given in Table 4.1. Fig. 4.3 shows the fitted model for the 20 SI deformation. The quantitative errors in tracking internal markers and surface deformations are give in Table 4.2 and a visual representation of the model prediction is given for the 20 SI configuration in figures 4.4 and 4.5.

Deformation	10 ML	5 ML	10 SI	20 SI	30 SI	Supine
Surface RMSE	0.51 mm	0.6 mm	0.4 mm	0.67 mm	0.56 mm	0.64 mm

Table 4.1: Root-mean-squared errors (RMSE) in fitting finite element model surfaces to laser scanned surface deformation data.

Deformation	10 ML	5 ML	10 SI	20 SI	30 SI	Supine
Max Ext Rat.	1.5	1.3	1.2	1.3	1.4	1.2
Max Displ.	50 mm	23 mm	18 mm	34 mm	52 mm	11 mm
Surface RMSE	1.1 mm	1.4 mm	1.1 mm	1.3 mm	1.5 mm	1.21 mm
Int. Mk 1 ED				2.22 mm		1.04 mm
Int. Mk 2 ED				2.19 mm		1.24 mm
Int. Mk 3 ED				2.2 mm		0.87 mm
Int. Mk 4 ED				1.88 mm		0.81 mm
Int. Mk 5 ED				2.67 mm		0.36 mm
Int. Mk 6 ED				1.86 mm		0.35 mm

Table 4.2: Root-mean-squared errors (RMSE) in matching the reference configuration surface and Euclidean distance (ED) between predicted and measured internal marker positions for the silicon gel phantom imaged using MRI. The maximum extension ratios were chosen from a list of extension ratios calculated at all the Gauss points in the mesh. The maximum displacements were chosen from a list of the displacements of all the nodes in the silicon gel model. These values are given to provide an indication of the extent of deformation under the different loading conditions.

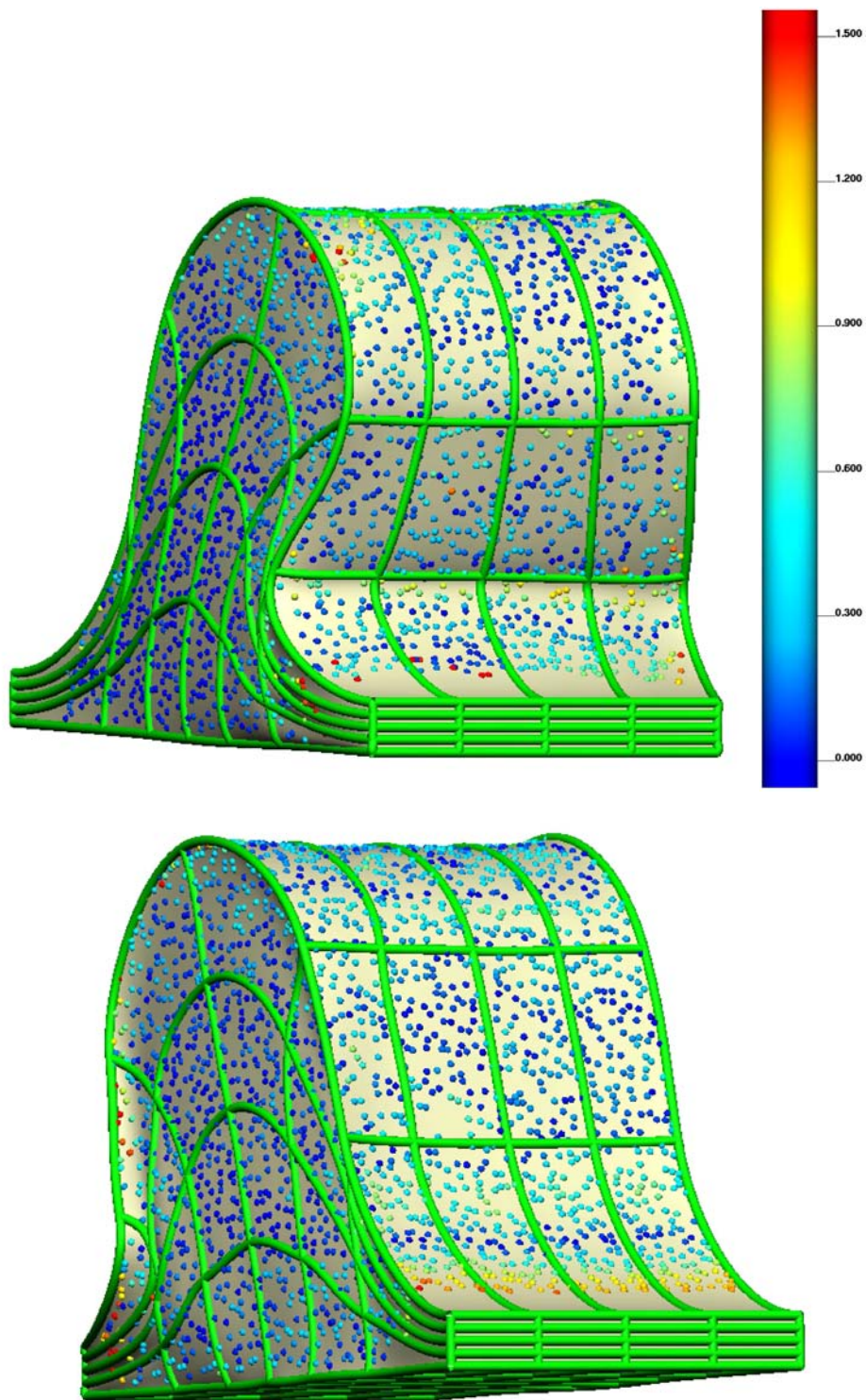


Figure 4.3: Finite element model fitted to data from 20 SI deformation with an RMS error of 0.67 mm. The spheres represent the surface data points obtained using the laser scanner with the colour map showing the individual error magnitude, in millimeters, associated with each data point

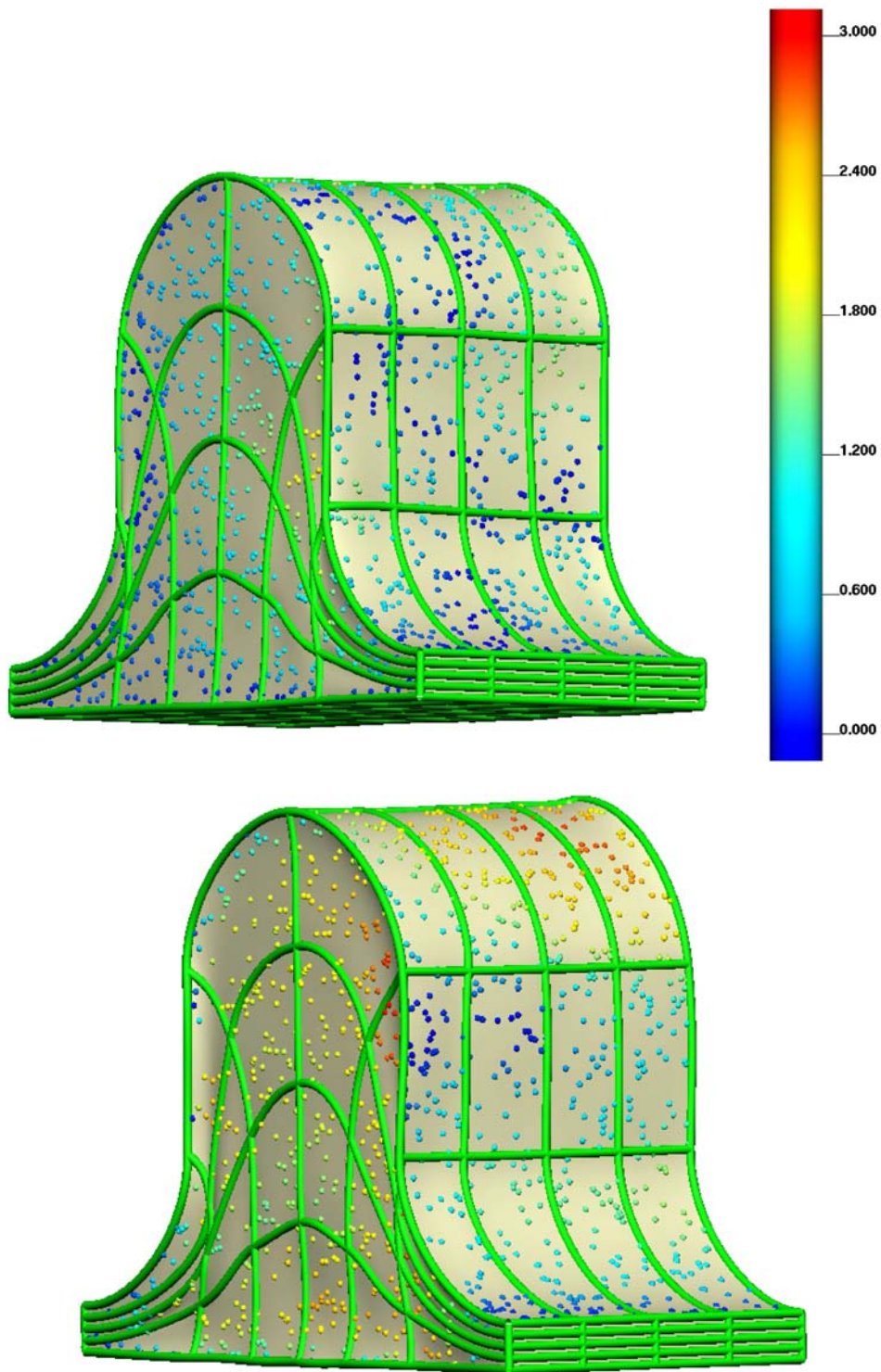


Figure 4.4: Reference configuration surface matching accuracy from the 20 SI deformation with an RMS error of 1.3 mm. The spheres represent the surface data points of the true reference state (obtained from the mould) with the colour map showing the individual error magnitude, in millimeters, associated with each data point

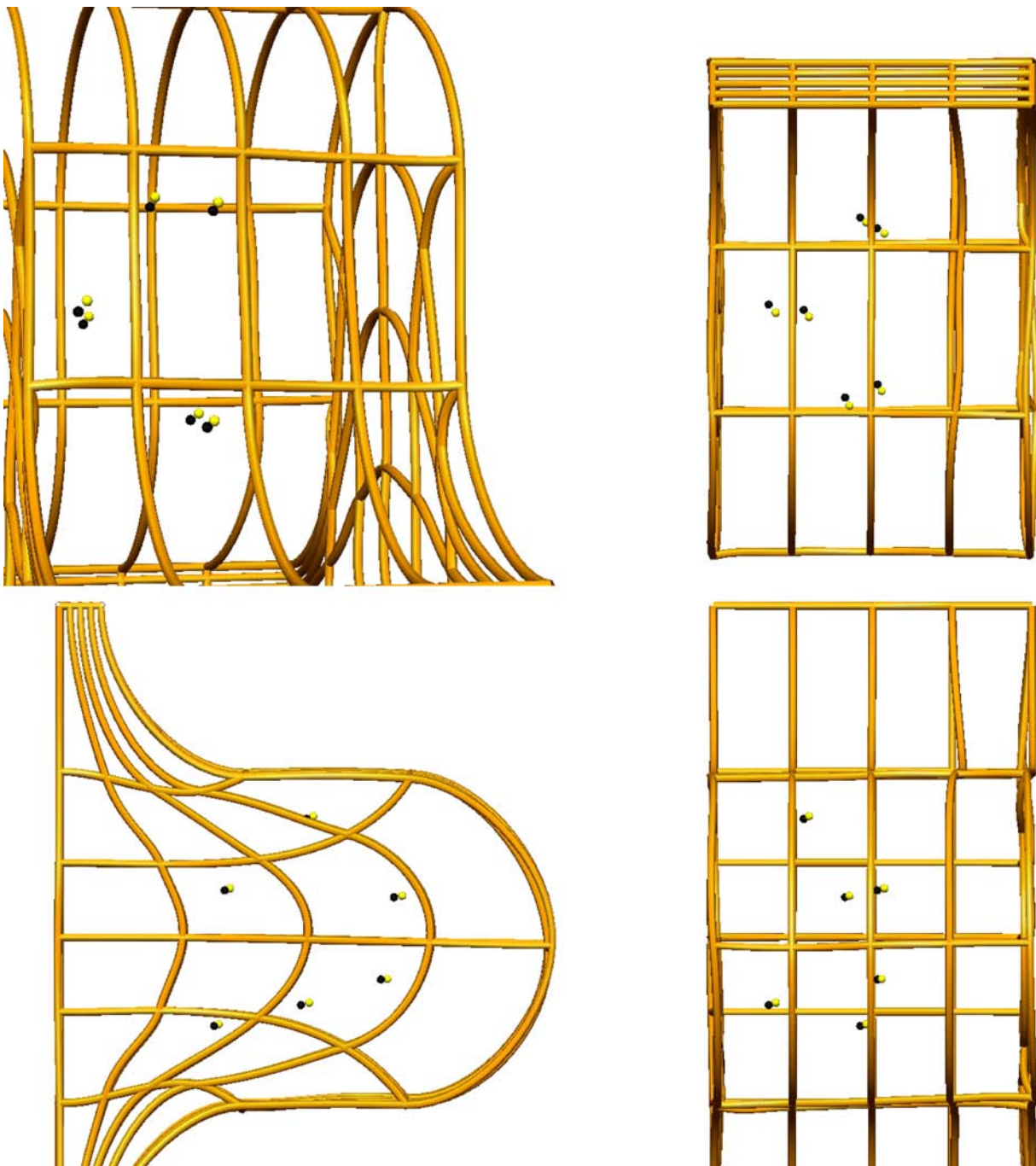


Figure 4.5: Internal marker tracking accuracy for 20 SI deformation. The yellow spheres represent recorded marker locations (from MRI) and the black spheres represent predicted locations of the internal markers in the reference state. The internal marker location errors ranged from 1.86 mm to 2.67 mm.

### 4.3.2 Discussion

The experimental results show that a finite element model of the silicon gel phantom can reliably predict the reference state using deformed configurations under different gravity loading conditions. The surface predictions are consistently of the same order across the different deformations. The errors in predicting the internal marker locations in the reference state are below the acceptable error of 3 - 5 mm in localising the position of a lesion in an MR image, based on its known position in two standard mammograms and vice versa (Ruiter & Stotzka, 2006). The internal marker localisation errors are also reasonably consistent for an individual deformation.

As discussed in Section 3.3.3, the accuracy in predicting the reference configuration is limited by the size of the markers and the accuracy of the laser scanned data. Note that these inherent errors in experimental measurements cause the reverse method to predict slightly different reference configurations from different deformed configurations. To illustrate this issue, Fig. 4.6 illustrates surface data sets of two predicted reference configurations using two deformed configurations of the silicon gel phantom. It is clear from the figure that the two data sets do not match. This discrepancy in these predicted reference configurations is potentially more pronounced for more complex systems such as the breast, due to the heterogeneity and complex loading conditions during diagnostic procedures.

One approach to resolving this issue would be to optimise for a single reference state using multiple deformed configurations, rather than directly calculating it from a single deformed configuration (as above). This method was implemented in the modelling framework and is referred to here as the reverse optimisation method. However, preliminary results show that the current implementation is computationally too expensive for breast modelling applications. Further details on the current reverse optimisation implementation and the preliminary results are given in Appendix C.

Nonetheless, the reverse calculation method demonstrated above is a novel technique for determining the reference state of a body and the results from the validation studies in Sections 4.2 and 4.3 have shown that predictions are reliable. Further studies should compare the efficiencies and accuracies of reverse optimisation methods to determine a tractable method for reliable and efficient predictions of breast

deformation in a clinical setting. The issues described above do not impede further research with the reverse method. In fact, the reverse method can provide insight into a number of aspects pertaining to breast biomechanics. Therefore, the reverse method is used in this thesis to determine the reference state of a body.

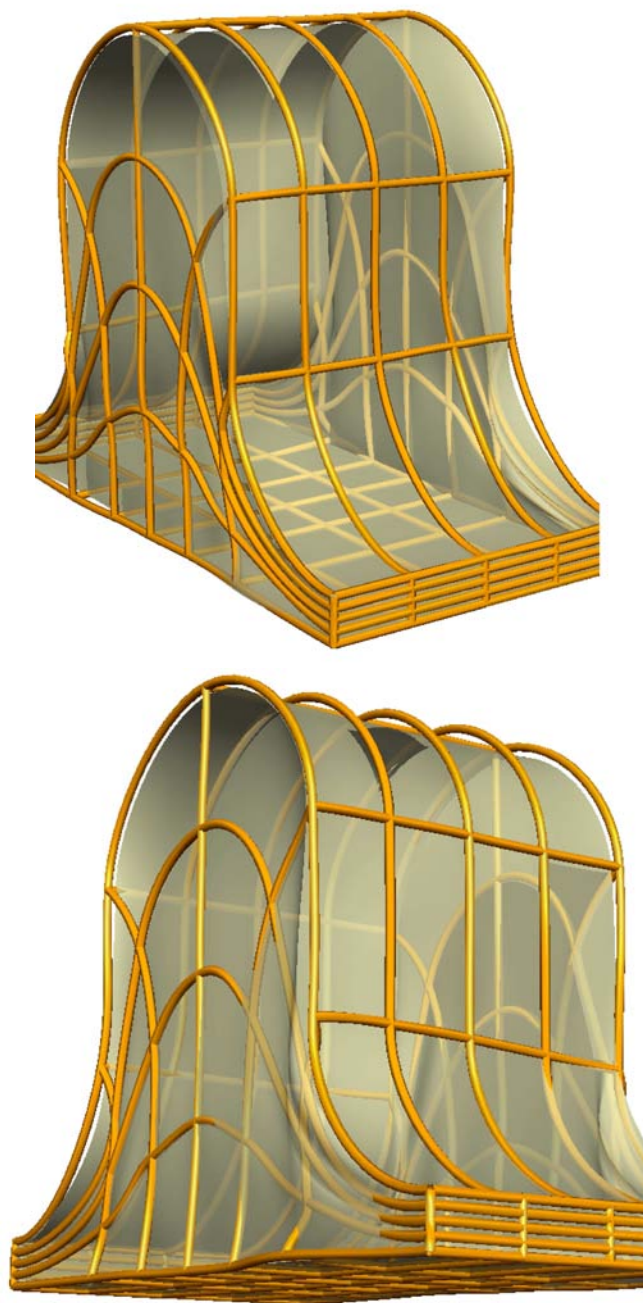


Figure 4.6: Two predicted reference state surface data sets using the reverse method. The gold lined mesh was obtained from the predicted reference state for deformed configuration 10 ML. The cream coloured surface configuration was obtained from the predicted reference state for the 30 SI deformed configuration.

## 4.4 Conclusion

How accurately can the reference configuration of a homogeneous body be predicted, given mechanical properties, boundary conditions and a set of deformed configurations under different gravity loading conditions? This is referred to here as the “reverse problem”.

A finite element model of a homogeneous body can reliably predict the reference configuration surface with an average RMS error of  $1.3 \text{ mm} \pm 0.1 \text{ mm}$ , and track internal marker locations to the reference state with an average error of  $1.5 \text{ mm} \pm 0.8 \text{ mm}$ . This result can now be used as a reference against which the performance of breast mechanics models can be assessed in the future.

# Chapter 5

## Forward Mechanics of a Heterogeneous Body

Chapters 3 and 4 were focused on validating a mathematical modelling framework in predicting deformed and reference configurations of a homogeneous, isotropic body under gravity loading conditions. However, as described in Section 2.1, the breast is heterogeneous, consisting of fatty and glandular tissue, enclosed by a fibrous layer of tissue called the fascia mammae. The gross anatomy is rather organised and anisotropic, with the lactiferous ducts placed in a radial pattern. Coopers ligaments connect the posterior part of the breast to the skin layer, providing a direction of increased stiffness in order to suspend the breast.

Some previous studies in the breast biomechanics field have modelled this heterogeneous structure. In the case of internal breast tissues, different constitutive relations have typically been assigned to elements in the model, based on the type of tissue they enclosed (Ruiter & Stotzka, 2006; Tanner et al., 2006; Samani et al., 2001; Azar et al., 2000). Each tissue type (fat, fibroglandular and tumour) was modelled as being isotropic, incompressible and homogeneous. Linear, piecewise linear, and nonlinear constitutive relations as proposed by a number of researchers (Krouskop et al., 1998; Samani et al., 2001; Azar et al., 2001; Wellman, 1999) were used to simulate breast deformation under gravity and compressive loading conditions. Azar (2001) attempted to incorporate the effects of Cooper's ligaments by using a piecewise linear constitutive relationship, designed to match the stiffness of glandular tissue at large strains.

The skin was modelled either as two-dimensional or thin three-dimensional elements enclosing internal breast tissues and exhibiting a linear elastic mechanical behaviour. Yu-Neifert (1995) used the traditional method of adding an extra three-dimensional layer of elements adjacent to the three-dimensional volume elements of breast tissue. The elements shared nodes with the three-dimensional breast tissue elements, representing a tight coupling at the interface (3D-3D coupling). Samani et al. (2001) modelled the skin as two-dimensional membrane elements, but it is not clear as to how they were coupled to the three-dimensional volume elements of breast tissue. Ruiter (2003); Ruiter & Stotzka (2006) were the only studies that performed numerical experiments to compare between different interface modelling techniques. The effects of 3D-3D coupling and tied contact coupling (where contact mechanics is used to model the interface) on breast deformation prediction were compared using MR images of the deformed state of the breast.

However, complex interactions between the different parameters in the model make it hard to discern the sources of error in model predictions. To the author's knowledge, no experimental study has been conducted to validate the modelling techniques used to represent the mechanical interactions between different types of tissues. This chapter describes the first set of experiments to validate methods of modelling heterogeneity.

Silicon gel phantom experiments were first conducted to validate a model of the interface between a thin rubber membrane and a thick volume of silicon gel in Section 5.1. This composite was designed with the skin-breast tissue interface in mind. The experiment was conducted to answer the following question:

**Can the interface between a thin membrane and the 3D constituents enclosed by the membrane be modelled accurately? (eg. skin enclosing internal breast tissue)**

As will become clear in Section 5.1, this work highlighted the need for validating models of heterogeneity by assigning different material properties to different elements. This would test the accuracy of the model in representing the interface between fat and fibroglandular tissue for example. Therefore, a validation study was conducted to answer another question:

**Is it possible to model a simple heterogeneous body consisting of two components, which occupy distinct regions in the volume? (eg. adjacent sections of fat and fibroglandular tissue)**

The results of this particular study are shown in Section 5.2 and the findings from these studies are discussed in Section 5.3. This chapter is focused on the validity of modelling techniques in representing the interface between different types of tissue, therefore the constitutive models or experimental techniques used to characterise the mechanical behaviour of breast tissues (fat, fibroglandular and skin) are not of immediate importance. However, the reader is directed to Appendix F for an overview of the literature on constitutive relations for breast biomechanics.

## 5.1 The Interface between Skin and Breast Tissue

Initially, it was assumed that the interface between skin and breast tissue could be represented as a thin membrane (skin) attached (tight coupling) to the thick internal breast tissue. Due to the infancy of recent studies that investigate the through-thickness properties of the skin (Hendriks et al., 2006), an assumption was made that the skin has the same mechanical properties through its different layers. With these assumptions, experiments were designed to answer the first question:

**Can the interface between a thin membrane and the 3D constituents enclosed by the membrane be modelled accurately?**

### 5.1.1 Validation experiment

A composite silicon gel/membrane cuboid phantom (see Fig. 5.1) was constructed to validate and determine the best way of modelling the interface. The silicon gel used was the same as in previous studies (here the dimensions were 58 mm x 25 mm x 25 mm), and the membrane was a silicon sheet from Jehbco Silicones<sup>1</sup> (0.4 mm

---

<sup>1</sup>[www.jehbco.com.au](http://www.jehbco.com.au)

thickness).

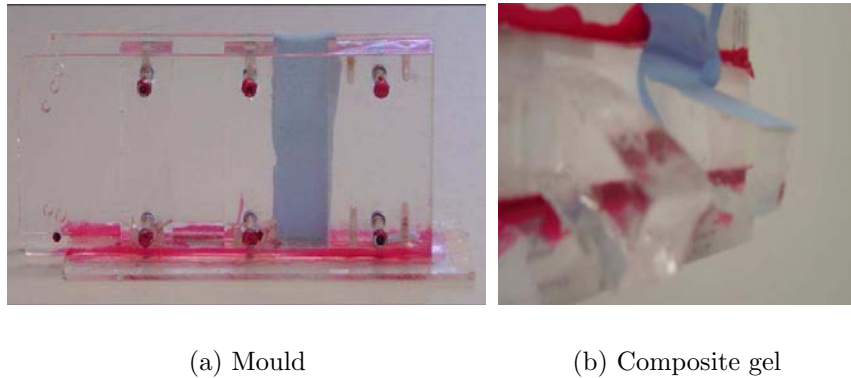


Figure 5.1: Mould and composite phantom used to validate interface models

It was assumed that the mechanical behaviour of the composite was a combined effect of the independent mechanical properties of its two components. This is a standard assumption made in the literature, and is the basis for many ex-vivo experimental studies that focus on estimating the mechanical properties of each tissue type independently (see Appendix F for details).

The silicon sheet is an isotropic, homogeneous material. The mechanical properties of the sheet were determined independently using the 2D multiaxial experimental and modelling techniques developed by Kvisttedal (2004). Membrane theory was used to model the deformations of the rubber sheet and the experimental measurements of force and displacement were used to estimate the mechanical properties. The reader is referred to (Oden, 1972) for further details on the specific membrane theory used to model rubber deformation. It was found that the material could be modelled using the neo-Hookean constitutive relation, with the parameter value  $c_1$  of 703.4 kPa. An independent estimate of the mechanical properties of the rubber was also obtained using a crude uniaxial extension experiment, which estimated that  $c_1$  was 560 kPa. Considering the simplicity of the latter uniaxial experiment, we were confident that the material parameter estimation using membrane theory and the multiaxial extension equipment provided reliable results.

As in Section 3.2.1, the silicon gel was modelled as a neo-Hookean solid. In order to estimate the mechanical properties of the gel, an experiment was first conducted to

test the hypothesis that two gels made from the same mix have the same mechanical properties. The experiment validated the hypothesis and therefore, a homogeneous gel was made from the same mix as that for the composite. The  $c_1$  parameter value of the silicon gel in the composite was assumed to be the value (1.3 kPa) estimated using the cantilevered beam setup (Fig. 5.1) of the homogeneous gel.

The deformed surface configuration of the composite was then laser scanned in the cantilever setup in Fig. 5.1 to use for the validation and comparison study of the different techniques of modelling the interface.

As will become clear, it was necessary to compare results of simulations from CMISS and a commercial package called ABAQUS. As ABAQUS does not use cubic-Hermite basis functions to represent the geometry, the models used to predict the deformation of the composite were represented using trilinear meshes for direct comparison between CMISS and ABAQUS results.

Two techniques were used to model the interface between the gel and the membrane in Fig. 5.1. A description of the techniques and their performance in predicting the deformation of the composite are given in the following sections.

### 5.1.2 3D-3D tight coupling

The first is the standard technique of modelling each material as a set of three-dimensional elements. One set of material properties are assigned to a group of elements representing the gel, and another set are assigned to the group of elements representing the membrane. The three-dimensional finite elasticity equations are solved on all the elements. This technique is referred to as “3D-3D tight coupling” in this thesis.

The cantilever set up was modelled using trilinear elements representing the geometric degrees of freedom, and a piecewise constant interpolation for the hydrostatic pressure in the elements. The gel and membrane composite model was subject to gravity loading conditions, with fixed displacement boundary conditions acting on all the nodes on the cantilever end.

A displacement convergence analysis was first conducted to identify the mesh resolution required to provide reliable predictions. Fig. 5.2 shows data points in the model at which displacements were recorded for successive resolutions during the

convergence analysis. The Euclidean displacements that each data point underwent during the deformation was calculated for each mesh resolution. The RMS error in displacements between successive refinements were then recorded (plotted in Fig. 5.3) and the mesh corresponding to 1500 degrees of freedom (Fig. 5.4) was chosen as the best resolution. This mesh consisted of 324 trilinear elements and 500 nodes.

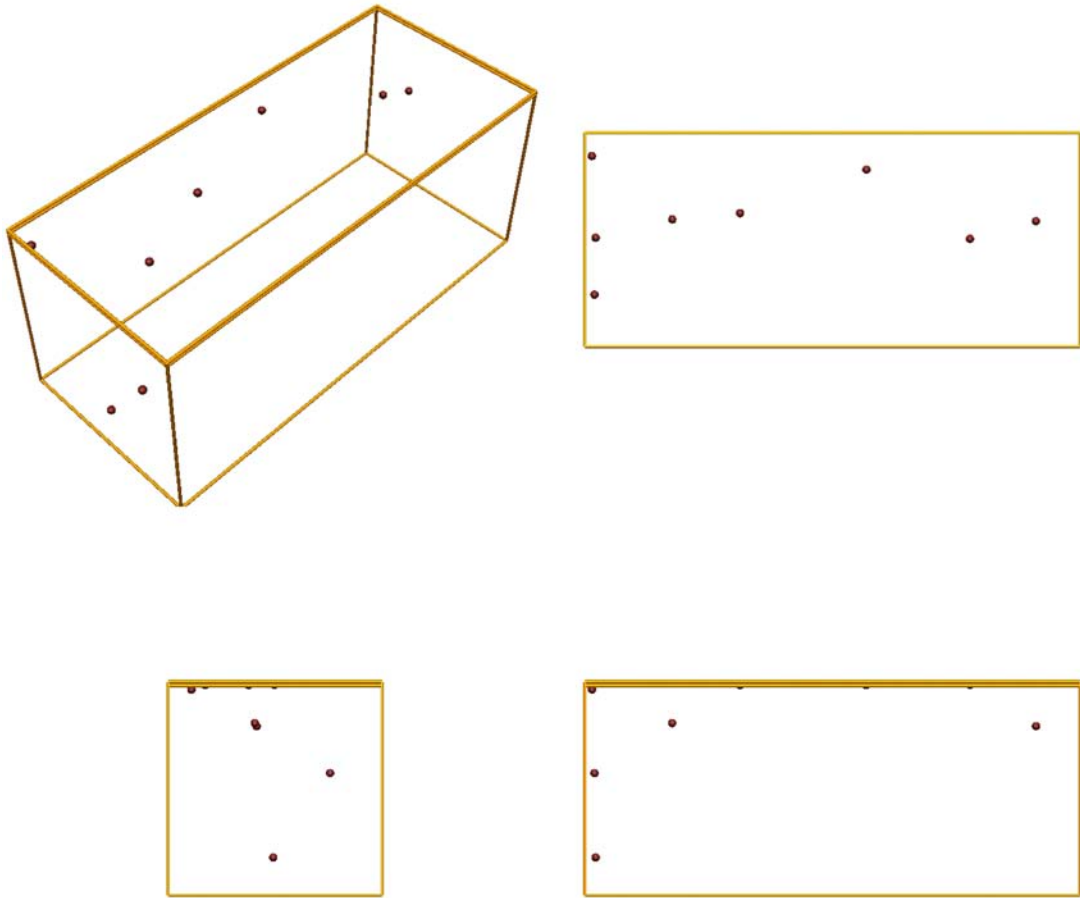


Figure 5.2: Data points at which displacements are recorded for convergence analysis.

Fig. 5.4 shows the model predictions using the displacement converged model. Clearly, the **3D-3D tight coupling model of the interface did not match the experimentally observed deformations.**

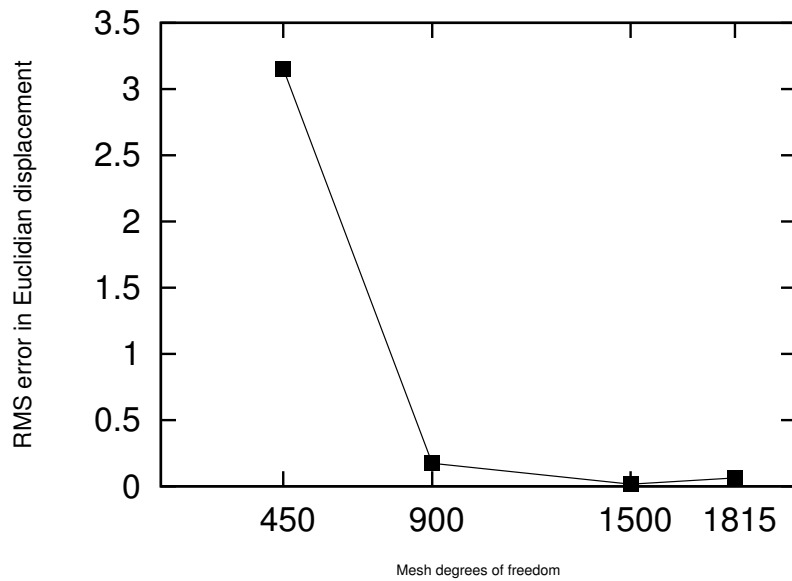


Figure 5.3: Model convergence of RMS error in displacements of selected points inside the mesh (Fig 5.2) with increasing mesh resolution.

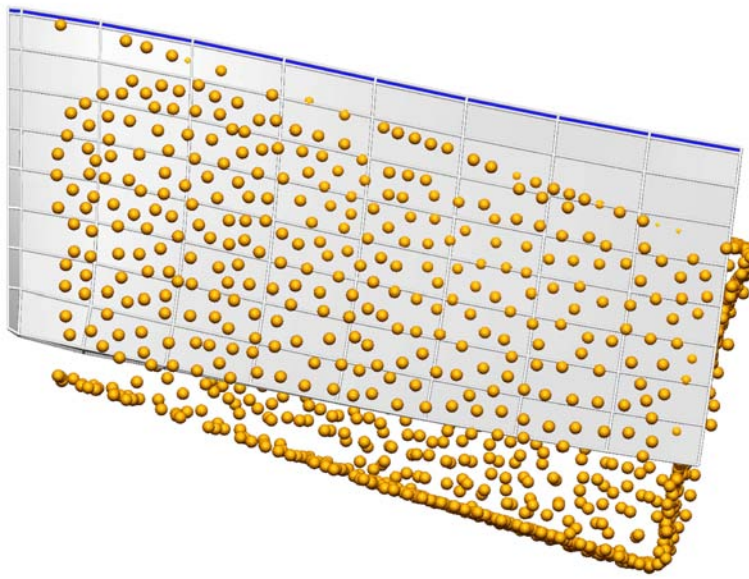


Figure 5.4: Comparison of model prediction (shaded) to experimental data (gold spheres). The top elements (dark blue) represent the rubber membrane, and the gray elements represent the gel.

### 5.1.3 2D-3D tight coupling

In another method of modelling the interface, the membrane is represented as a set of two-dimensional elements and a specialised form of finite elasticity theory, known as membrane theory is solved on them. This method is called “2D-3D tight coupling” in this thesis. These two-dimensional elements are coupled to the three-dimensional gel elements (on which the standard 3D finite elasticity equations are solved) to represent the interactions between membrane and gel. Elements are assigned a set of material properties, based on the material they represent. This method was implemented in CMISS with the original intention of reducing the size of the problem of modelling the skin-breast tissue interface, which could be important for a highly refined internal breast tissue model. Reduction was anticipated due to the use of a two-dimensional, rather than three-dimensional theory to model the skin.

As in Section 5.1.2 the gel and membrane composite model was subject to gravity loading conditions, with a fixed displacement boundary condition on all the nodes at the cantilever end. The results of a displacement convergence analysis with the same selected points in Fig. 5.2 are illustrated in Fig. 5.5.

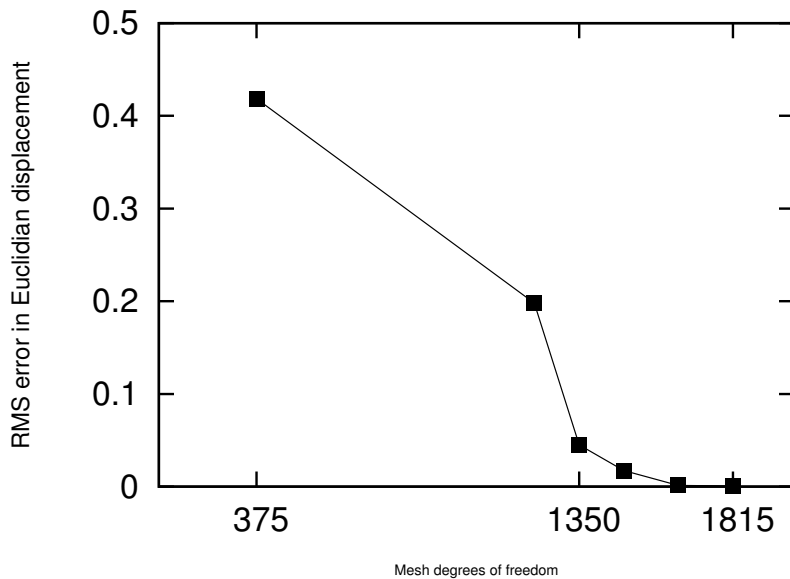


Figure 5.5: Model convergence of the RMS error in displacements of selected points inside the mesh (Fig 5.2) with increasing mesh resolution.

Fig. 5.6 shows the model predictions using a displacement converged model consisting of 450 nodes and 324 elements (1350 degrees of freedom). As can be seen from the figure, **a 2D-3D tight coupling model of the interface also does not match experimentally observed deformations.**

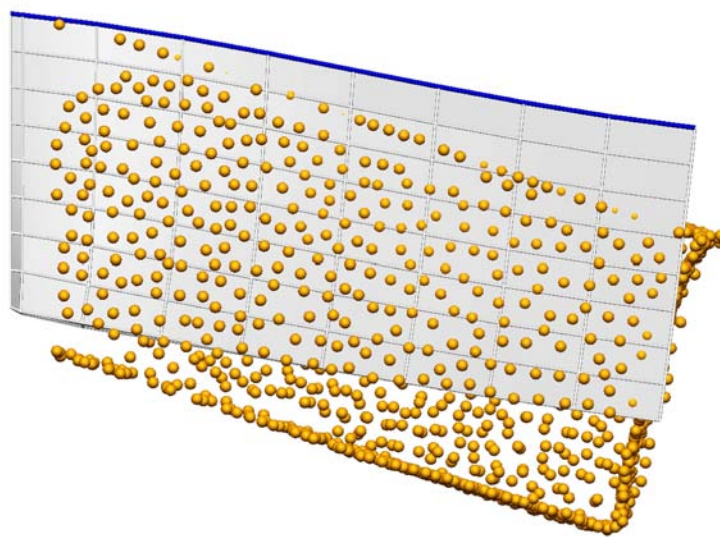


Figure 5.6: Comparison of model prediction (shaded) to experimental data (gold spheres). The top lines (blue) represent the rubber membrane as two-dimensional elements, and the gray elements represent the gel as three-dimensional elements.

### 5.1.4 ABAQUS

Since both 3D-3D tight coupling and 2D-3D tight coupling did not match the experimental data, it was important to check these results using an independent software package. ABAQUS is a well-known commercial package used by a number of researchers in the breast biomechanics field (Yu-Neifert, 1995; Samani et al., 2001; Ruiter & Stotzka, 2006). In this thesis, ABAQUS/CAE v 6.5.1 was used for comparison with results from CMISS.

The composite was modelled in ABAQUS as two three-dimensional solids constrained to have their surfaces at the interface to be tied together during deformation. Enforcement of this constraint was assumed to be appropriate due to the tight attachment between membrane and gel. For a comparison of the predictions between ABAQUS and CMISS, the vertical displacement of the node shown in Fig. 5.7 was obtained from both simulations. CMISS predicted a vertical displacement of 11 mm and ABAQUS predicted a vertical displacement of 12.1 mm, while the experimental vertical nodal displacement was 18.8 mm. This difference between model predictions from both software packages and actual deformations indicated that the errors were probably less to do with bugs in implementation, but more to do with fundamental theoretical and experimental oversight.

The discrepancy between CMISS and ABAQUS predictions was at first difficult to understand, considering the fact that both models were conceptually identical. This indicated that the methods of modelling heterogeneity were different between the two packages. Indeed, further investigations indicated that formulation of finite elasticity in ABAQUS is different from CMISS (see Appendix D for further details).

With the 3D-3D tight coupling and the 2D-3D tight coupling models in CMISS not matching the experimental data, four questions remained unanswered:

1. Do the mechanical properties of the constituents change when made into a composite?
2. Are the interface models tested in this thesis adequate?
3. Are the mismatches symptoms of numerical problems in the models, due to the thin elements (membrane) directly adjacent to thick (gel) elements?
4. Are the mismatches symptoms of numerical problems in the models, due to

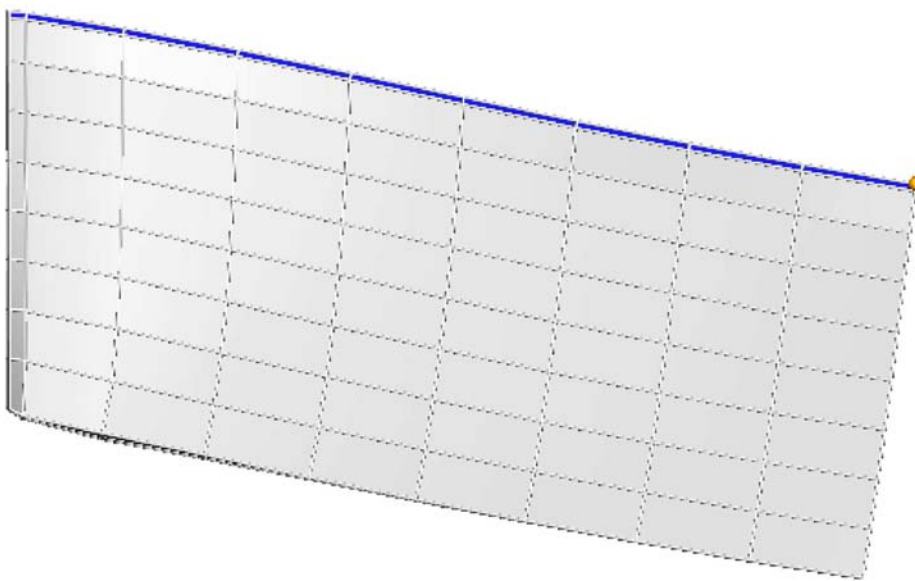


Figure 5.7: Node used to compare between ABAQUS and CMISS shown as a gold sphere.

very stiff materials (membrane stiffness of 701 kPa) adjacent to very soft materials (gel stiffness of 1.3 kPa)?

Questions 3 and 4 were first addressed by constructing a composite in which the constituents were of more similar proportions such that the stiffnesses were approximately 2-to-1 in ratio. The design of such a silicon gel phantom, and modelling of the deformations of such a composite, would effectively mimic the interface between fat and fibroglandular tissue and is described in the following section.

## 5.2 The Interface between Fat and Fibroglandular Tissues

This validation exercise was conducted to answer the following question:

Is it possible to model a simple heterogeneous body consisting of two components, which occupy distinct regions in the volume? (e.g. adjacent

sections of fat and fibroglandular tissue.)

### 5.2.1 Validation experiment

A two-component silicon gel composite was constructed, with each component being of approximately equal size. The composite was made by first pouring a silicon gel mix with the neo-Hookean material parameter  $c_1 = 2.89 \text{ kPa}$ . Once the gel cured, and while still in the mould, an equal amount of another mix with  $c_1 = 1.43 \text{ kPa}$  was poured and cured on top. The material parameters were again assumed to be the same as those estimated on separate homogeneous cuboid samples made from the same mixes. The composite was 60 mm x 25 mm x 25 mm in size. The composite was again subject to gravity loading conditions in a cantilever set up.

### 5.2.2 3D-3D tight coupling

A displacement converged trilinear model (see Fig. 5.8 and Fig. 5.9 for details on convergence analysis) consisting of 320 elements, and 495 nodes (1485 degrees of freedom) was subjected to gravity loading conditions in a cantilever set up. A fixed displacement boundary condition was imposed on the nodes along the cantilever end and the top half of elements were assigned a  $c_1$  value of 1.43 kPa, while the bottom half of elements were assigned a  $c_1$  value of 2.89 kPa consistent with the individual cuboids in the composite. As shown in Fig. 5.10, the model still did not match the experiment.

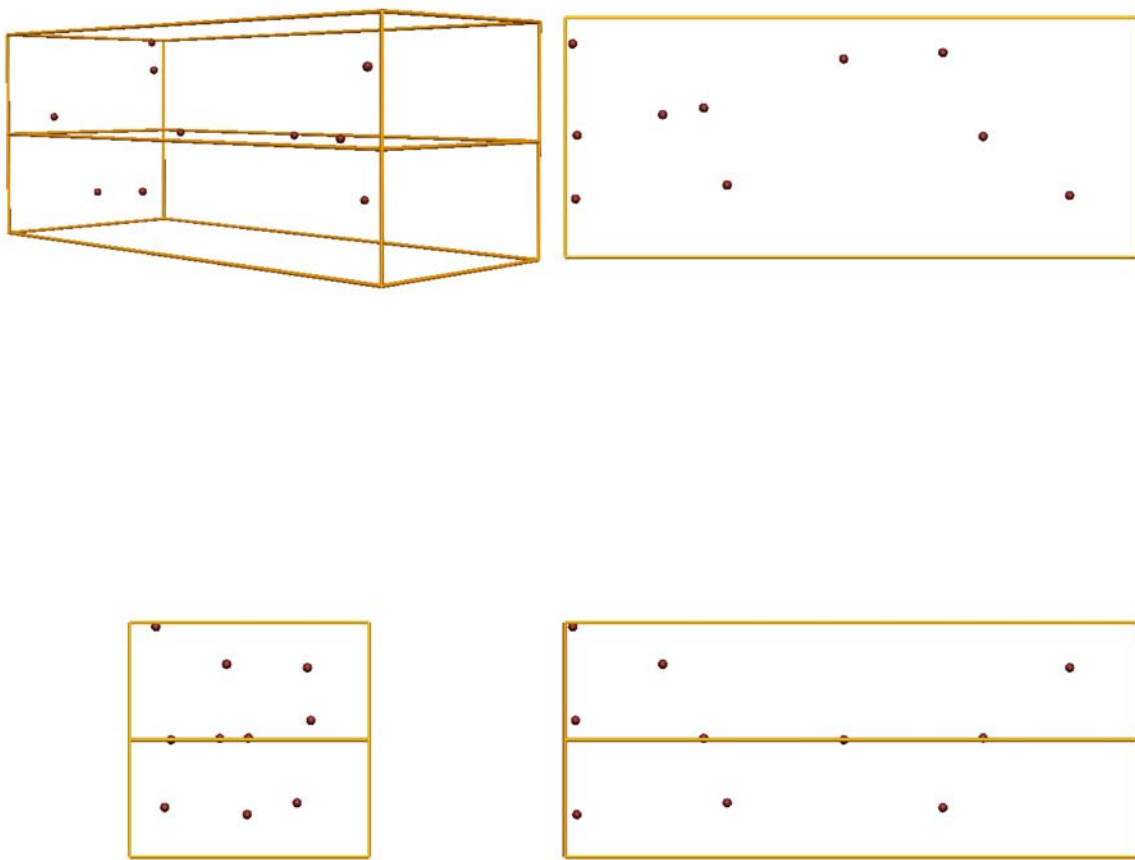


Figure 5.8: Data points at which displacements are compared for convergence analysis.

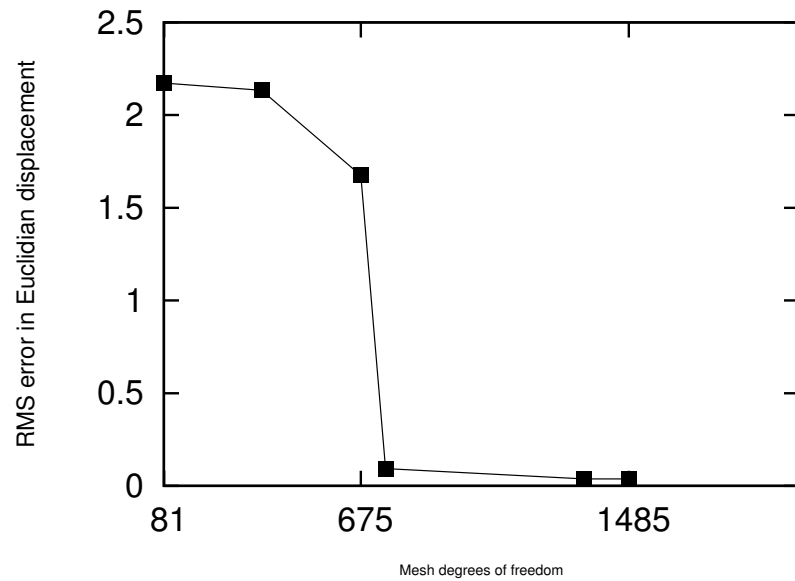


Figure 5.9: Model convergence of RMS error in Euclidean displacements of selected points inside the mesh (Fig 5.8) with increasing mesh resolution.

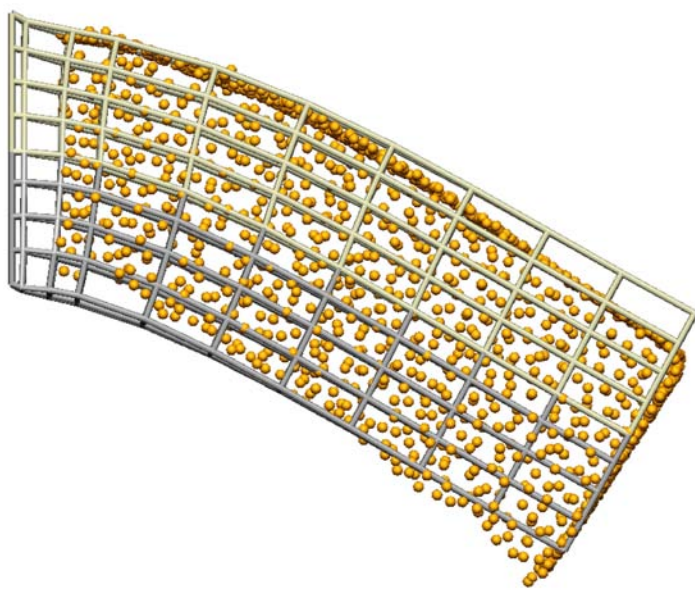


Figure 5.10: Comparison of model prediction (lines) to experimental data (gold spheres). Upper elements (cream lines) represent gel with  $c_1 = 1.43$  kPa, and the lower elements (grey lines) represent gel with  $c_1 = 2.89$  kPa.

### 5.3 Discussion

The validation studies presented in Sections 5.1.1 and 5.2.1 show significant differences in current methods of modelling heterogeneous bodies compared to experimental results. Careful consideration must be given to address the two remaining unanswered questions:

1. Do the mechanical properties of the constituents change when made into a composite?
2. Are the interface models tested in this thesis adequate?

It was assumed that the neo-Hookean material parameter values for the constituents can be obtained from independent measurements using gels made from the same mixes as those in the composite. However, it is possible that the mechanical properties of the constituents are different when made into a composite. In this case, perhaps, the mechanical properties of the constituents should only be determined using experiments on the composite itself.

Apart from the adequate characterisation of the mechanical behaviour of the constituents, consideration must be given to the theoretical accuracy of the types of interface models used in literature. 3D-3D tight coupling is a standard technique used to model heterogeneous bodies. However, it should be noted that this technique is questionable. Considering the heterogeneous silicon gel in Fig. 5.10, it is clear that displacement continuity must be enforced, as the components are tightly bonded to each other. However, strain continuity should not be enforced in all directions. It is important to enforce strain continuity in the plane of the interface to maintain compatibility of the surfaces. However, strain continuity should not be enforced in the direction normal to the interface plane. This can be understood by considering the case of the interface between a very stiff steel cube and very soft rubber cube. If one traverses straight through the heterogeneous body from the soft rubber into the hard steel, larger normal strains in the rubber material would be observed compared to that in the steel. Thus, at the interface between the rubber and steel, a discontinuity in strain would be anticipated. Therefore enforcing strain continuity normal to the interface plane would over-constrain the real behaviour. Further studies are needed to determine whether contact theory as used by Ruiter

& Stotzka (2006), would adequately account for this issue.

These additional studies would resolve the issues regarding heterogeneity modelling. The systematic approach taken in this study highlights the need for a combination of silicon gel phantom studies and clinical validation work. Although this work has raised additional questions, rather than provide conclusive answers, this validation exercise will be of benefit to the wider field of biomechanics.

## 5.4 Conclusion

The following two questions were addressed:

1. **Can the interface between a thin membrane and its enclosed constituents be modelled accurately?**
2. **Can a simple inhomogeneous body consisting of two components, which occupy distinct regions in the volume be modelled accurately? (eg. fat and fibroglandular tissue adjacent to each other)**

The validation studies in this chapter raised questions regarding the current methodology of modelling heterogeneities. It is questionable whether 3D-3D tight coupling models the interface between two distinct bodies. An interface between the two bodies should enforce strain continuity in the plane of the interface, whilst allowing strain discontinuity normal to the interface plane. Additional research is required to determine the correct way to model the interface. When characterising the mechanical behaviour of the constituents, a variety of experiments should be conducted to ensure that a wide range of strains are being represented. In addition to characterising the individual components of the composite independently, material testing must also be conducted on the composite itself. This will verify that the mechanical properties of the constituents do not change when made into a composite.

# Part III

## Modelling the Breast



# Chapter 6

## Modelling Breast Geometry

The research presented in Part II focussed on the development of the modelling framework and its validation for modelling large deformations using silicon gel phantoms. While the silicon gel experiments are important to measure the accuracy of specific modelling features, the silicon gel phantoms were not intended to represent the breast. It is important to combine silicon gel phantom studies with clinical validation studies on breasts of volunteers to develop a reliable software tool that can assist clinicians in tracking tumours across multiple imaging modalities.

In order to model the mechanics and predict the displacements of breast tissues, the first step is to create finite element geometries that capture the gross anatomical structure as accurately as possible. This chapter focusses on answering the following question:

**How accurately can the geometry of the breast be represented for each individual by a finite element model using an automatic and efficient algorithm?**

To this end, an automatic procedure was developed to create individual-specific finite element models of the breast. Firstly, an overview of previous representations of breast anatomy found in the literature is provided. A detailed description of the methods used for this thesis are then provided from segmentation to geometric fitting. Examples are provided to illustrate the performance of the techniques used. The chapter concludes with some insight into future areas of development.

## 6.1 Background and Previous Work

One of the earliest biomechanical models of the breast was developed by Yu-Neifert (1995). A two-component model of skin and adipose tissue was constructed by fitting trilinear elements to experimentally measured breast surface geometry. Other research groups have since extended these ideas. Azar et al. (2000) distinguished adipose tissue from fibroglandular tissue, by manually segmenting the different tissues, using contours to follow the breast boundary. The contours were used to create trilinear volume elements for biomechanics simulations. The segmented data was then used to assign material properties to each of the elements. In parallel, other researchers such as Wu & Sullivan (2001) and Tanner et al. (2001) used marching cubes algorithms and intensity thresholding techniques to create tetrahedral elements to model breast geometry with heterogeneous properties.

However, tetrahedral elements are known to cause computational problems during mechanics simulations (Samani et al., 2001). Samani et al. (2001) developed a mesh generation technique with virtually minimal user input called *transfinite interpolation mesh generation*. The method uses a third-order polynomial to fit to the chest wall boundary, and quadratic polynomials to fit to the breast surface. The images are segmented into different tissue types using standard thresholding techniques, and elements are created for each image slice and stacked together to provide a three-dimensional mesh. This method produced a mesh with 2280 elements and 2590 nodes using a clinical image dataset (Samani et al., 2001). A similar technique was also used by Ruiter (2003) using approximately 350 quadrilateral elements to perform simulations within a reasonable amount of time. One drawback of the previous mesh generation techniques is the large number of elements needed to capture the anatomical detail available in the images. MR images needed to be down-sampled in resolution to control the number of elements used in Samani's and Ruiter's work.

The Bioengineering Institute (University of Auckland) has developed techniques using hexahedral volume elements with cubic-Hermite basis functions to capture the anatomical detail of a number of organs of the human body from the heart to lungs to the musculoskeletal system (Fernandez et al., 2004). Cubic Hermite interpolation enforces  $G_1$  (first derivative) continuity, and the higher degrees of freedom enable the representation of anatomical detail very accurately with fewer elements than those

which use lower order basis functions. This thesis uses the techniques developed in (Nielsen, 1987) to develop finite element geometries of the breast.

Although Cooper (1840) provided a detailed study on breast tissue organisation and structure, it is not clear if such high detail is necessary for accurate predictions of breast tissue movement. As a first step, it was decided to not incorporate the spatial organisation of the internal tissues (fat, fibroglandular and cancerous tissues) in great detail, but to apply elemental or regional variation of material type within the mesh to take this heterogeneity into account (see Appendix E for details on regional variation of material types). To the author's knowledge the use of cubic-Hermites and regional variation of tissue types are novel contributions to the field of breast biomechanics. However, Chapter 5 highlighted the lack of understanding about the correct way to model the spatial organisation of heterogeneity. Hence, this chapter only focussed on capturing the overall shape of the breast by capturing the skin and muscle surfaces. The following sections describe the mesh generation procedure that was developed to model breast geometry and to customize it to each individual.

## 6.2 Creating Individual-Specific Models

The variability in breast geometry and anatomy means that creating finite element geometries suitable for numerical computations can be a manually intensive procedure. An automated mesh generation procedure would reduce the time to create a model suitable for biomechanical analysis. This would not only help in the research phase of the project, but would also be useful in the clinical setting where a medical practitioner could be spending time on analysing results from simulations and comparing them to mammograms.

To this end, an automatic mesh generation procedure was developed to create individual-specific models of the breast which are useful for finite element computations. The procedure involves fitting the front surface of a generic mesh to a segmented dataset of the skin, and then the back surface to a dataset of the muscle. The fitting procedure uses a least squares approach to fit the faces of the volume elements to the data points representing the anatomy. The aim is to minimise the RMS distance of the orthogonal projection of the data points onto the surfaces being

fitted. This section describes the different steps that are taken to model the gross anatomical structure of the breast.

### 6.2.1 Tissue segmentation and digitisation

For this thesis, clinical magnetic resonance (MR) images of the breast of ten individuals (lying prone) were obtained from Dr. Ruth Warren at Cambridge University, U.K.<sup>1</sup> There were at least three sets of MR images taken for each individual, one in each of the three directions: sagittal, coronal and transverse. There were two sets of coronal images taken for each individual. The first set was before injection of gadolinium, which is a contrast agent used to distinguish tissue types more clearly for MRI. The second set of coronal images were obtained by acquiring images at seven different time points after injection of gadolinium. The number of images varied for each direction as the offsets between images were different. In the sagittal and coronal directions, the images were taken with a 3mm slice thickness giving a total of 60 images per set. The transverse direction images had a much larger slice thickness and hence there were very few images in this direction.

The images of an individual were loaded into CMISS for manual segmentation of the different tissues. There is a considerable amount of human judgement involved in this segmentation process, but it typically takes less than a day to perform for one patient. Hence, the automation of the segmentation procedure is not under investigation for the time being, but it would be straightforward to implement it at a later stage. The digitising process effectively creates a plane of data for each of the MR images where the user can then assign data points by clicking on areas of interest using the mouse. Once these planes are assembled together with the slice thickness taken into account, a 3D data set is generated. By outlining the skin in each of the 60 sagittal images and combining the data, a digitised 3D representation of the exterior of the breast consisting of a dense set of data is obtained. A 3D representation of the individual components of the breast can be created by choosing only to outline the specific area with the data points. Skin and muscle data were segmented from each of the image sets. For some cases, attempts were made to capture other areas such as the fibroglandular and fatty tissue (see Fig. 6.1 and Fig. 6.2).

---

<sup>1</sup>Dr. Warren obtained a Local Regional Ethics Committee approval for use of the images in this thesis.

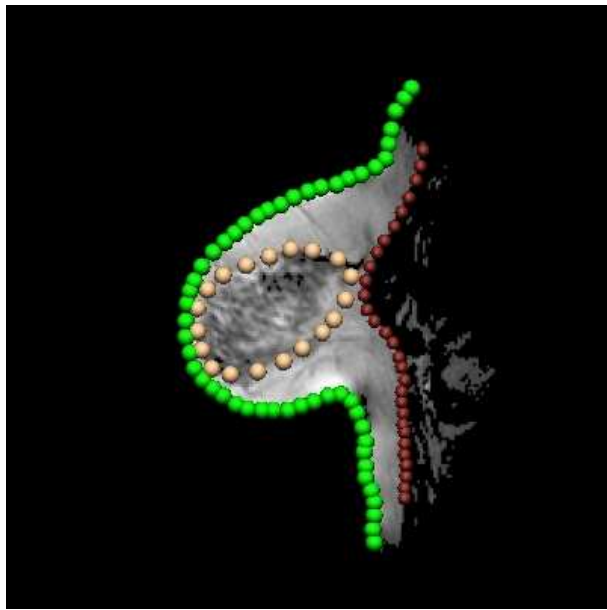


Figure 6.1: Segmenting different tissue types. Green data points represent the skin. The muscle boundary is segmented with brown data points. The boundary between fat and fibroglandular tissue is segmented using yellow data points

Some of the anatomical structures were not always easily distinguishable from others in the MR images. In the case of fibroglandular tissue, some images of the breast portrayed cross-linking and intertwining of the fibrous tissue which could not be easily represented. In cases where the fibroglandular tissues were easily distinguishable, they were digitised. The digitisation of the muscle also proved to be rather difficult and a subjective choice was required during the segmentation stage.

Out of the ten individual sets, six of them were digitised. The sagittal images were most useful due to the clearly defined anatomical boundaries. As a result, sagittal images were mostly used to digitise the breast components such as the skin, fat, muscle and fibroglandular areas. From the other image views, only the skin layer is clearly defined. The four image sets that were not digitised contained geometric irregularities and were not suitable for this study.

The face-fitting algorithm developed by Nielsen (1987) was then used to fit external faces of hexahedral tri-cubic Hermite elements to geometric boundaries (the skin and the muscle surfaces) and is described in the following sections.

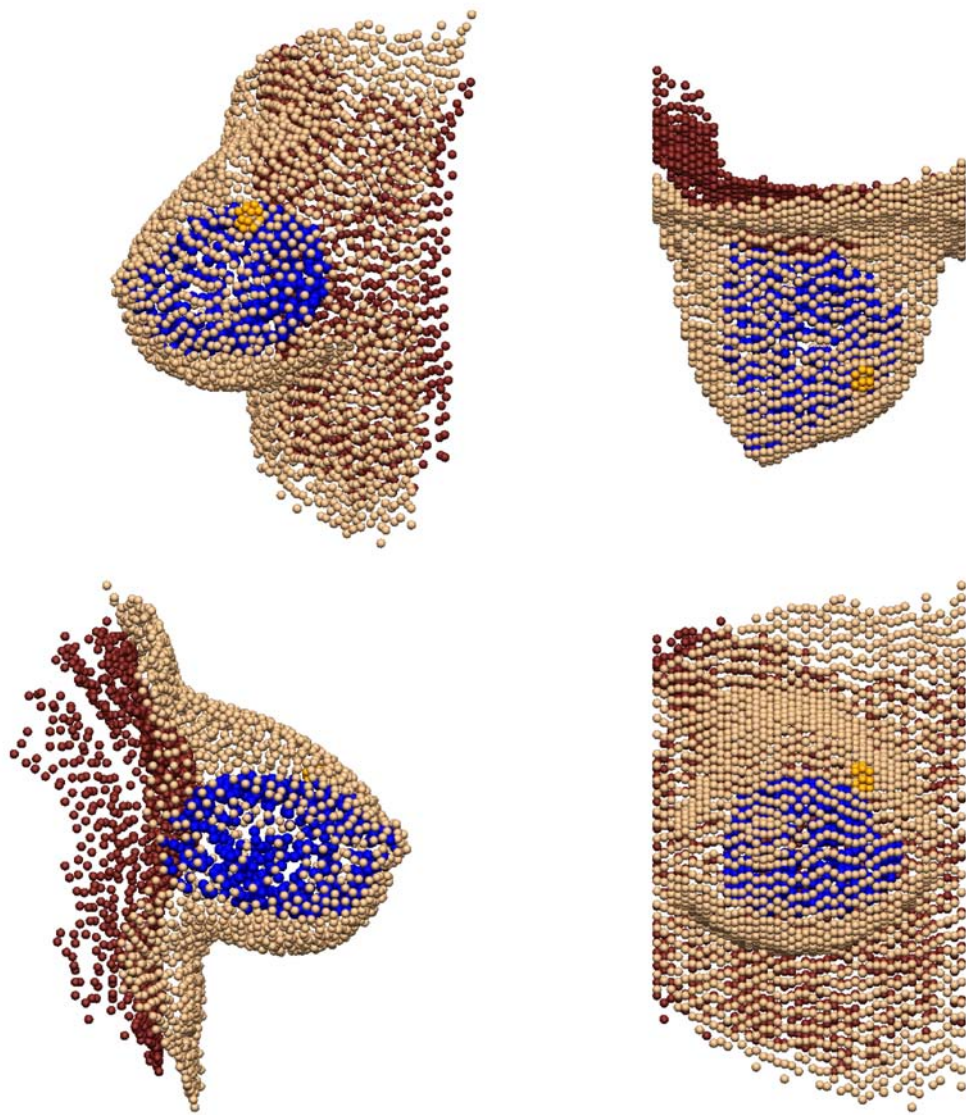


Figure 6.2: 3D digital representation of the various breast tissue components obtained from manual segmentation. The blue coloured data points represent the interface between fibroglandular and fatty tissue, the orange spheres represent the segmented vitamin E tablet, the maroon points represent the muscle boundary, and the light brown points represent the skin surface.

### 6.2.2 Initial geometry

It is critical to construct an initial geometry that is reasonably close to the contours of the data set. Lack of a good initial mesh can lead to distorted surfaces and can also result in distorted volume elements with large aspect ratios. These badly shaped elements can lead to numerical problems when solving large deformation mechanics problems.

All meshes were created in the 3D torso right handed coordinate system: - the  $x$  axis goes across the chest (medio-lateral, from right to left), the  $y$  axis traverses antero-posterior, and the  $z$  axis is directed in the infero-superior direction (see Fig. 6.3(a)). Similarly, the element coordinate system was constructed such that  $\xi_1$  was medio-lateral,  $\xi_2$  was infero-superior and  $\xi_3$  was antero-posterior. A number of attempts were made to create an initial mesh that would conform to the skin datasets in Fig. 6.2 and provide the best fit with reasonably shaped volume elements.

In the first instance, a mesh was created by defining a simple four element (2x2x1) mesh (2 elements in  $\xi_1$ , 2 elements in  $\xi_2$  and one element through  $\xi_3$ ). The digitised individual data set was then used to determine the overall height and width of the model. These values were then used to determine the gross dimensions of the 2x2x1 mesh. The middle node was translated to the location of the nipple (Fig. 6.3(a)). This mesh was then refined twice in the  $\xi_1$  and  $\xi_2$  directions to give an 8x8x1 (64 element) mesh (Fig. 6.3(b)). This degree of refinement was necessary to ensure that the model accurately represented the skin surface.

However, the surface fitting algorithm did not produce the adequate results. The resulting fitted mesh provided a good representation of the data (Fig. 6.4(a)), but the volume elements were distorted, with large aspect ratios (Fig. 6.4(b)). This was mainly due to having too many degrees of freedom in the fitting problem, and because the degrees of freedom in the third dimension (in the antero-posterior direction) were not part of the surface fit.

On examining the data, it was clear that the distortion of the volumes was due to the high curvature in the surface that the initial mesh element faces had to conform to. Therefore, another initial mesh was created, with fewer elements, but with a better representation of the degree of curvature in the geometric data (Fig. 6.5). This mesh provided good results with only twenty four elements used to model the geometry, and was therefore the mesh used for face fitting of breast geometries.

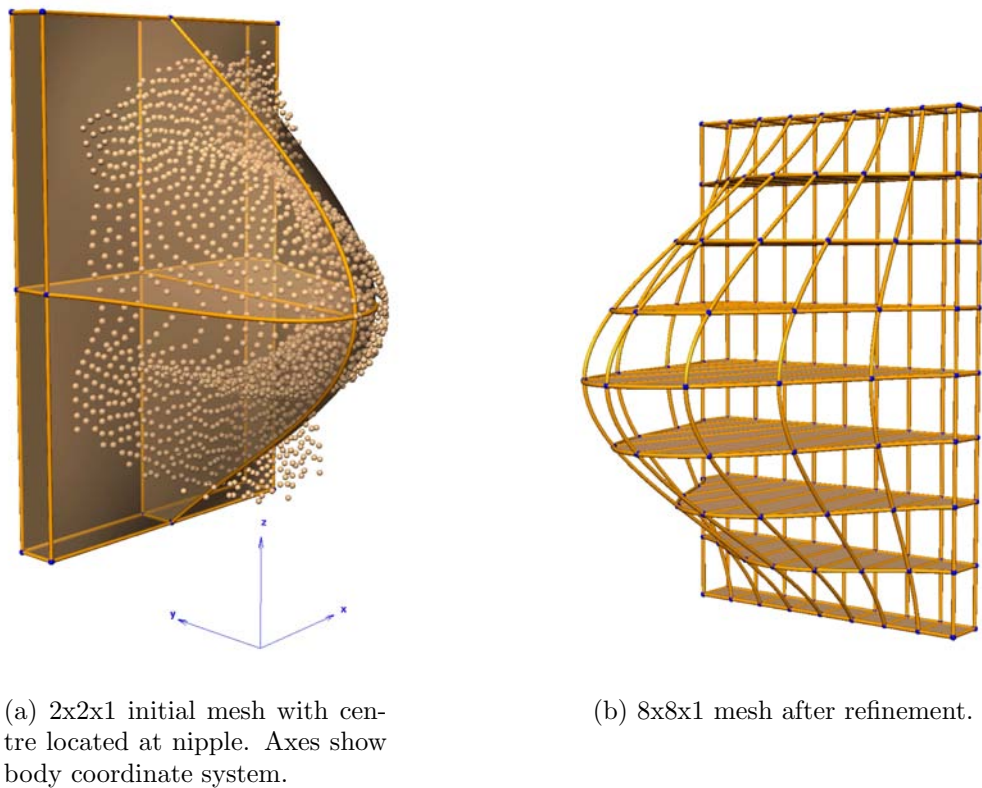
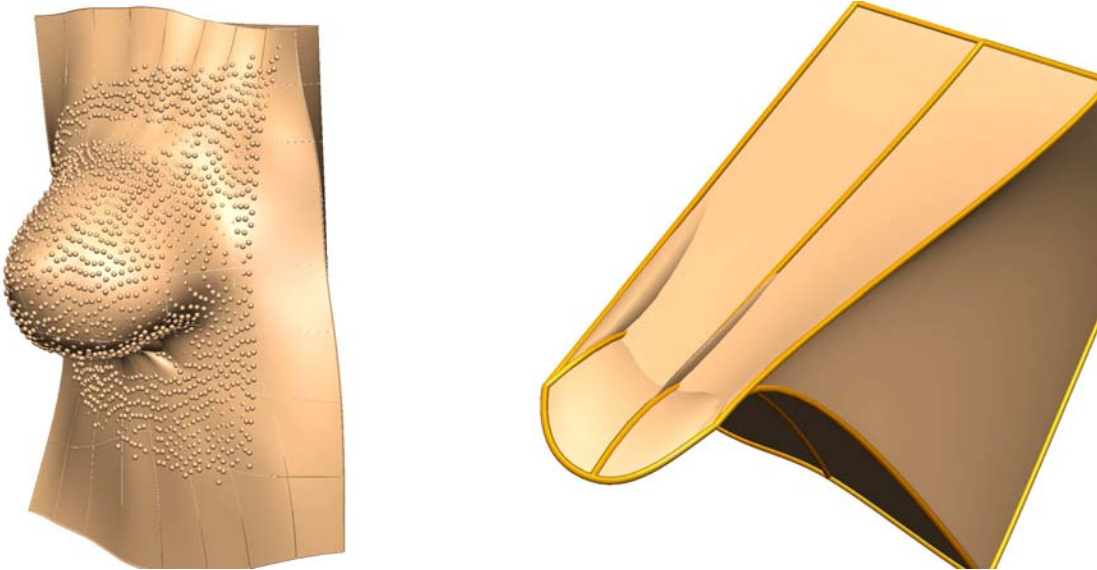


Figure 6.3: First attempt at creation of initial mesh specific to each individual.



(a) fitting result using first  
initial mesh.

(b) Two distorted volume elements in the fit-  
ted mesh

Figure 6.4: Surface fitted initial mesh showing distorted volume elements.

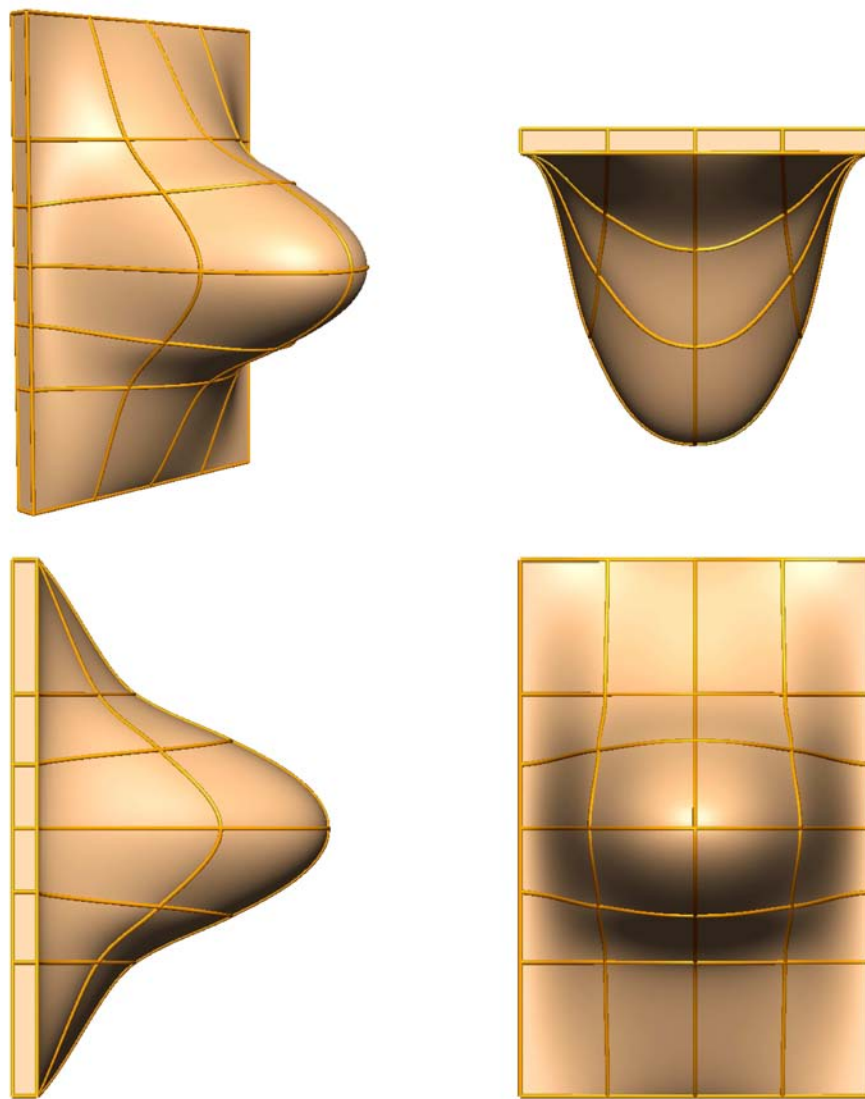


Figure 6.5: The initial mesh used to model breast geometry.

### 6.2.3 Automatic model generation

An automated procedure was developed in order to quickly create customized finite element models for individuals. The method is a six-stage process involving surface fitting of the skin and muscle after scaling and repositioning of the initial and intermediate meshes. The procedures are outlined in this section and the code given in Appendix G.

#### Stage 1: Scaling and repositioning the initial mesh (Automatic)

As discussed above, the shape of the initial mesh plays a critical role in the quality of the surface fitting results. The initial mesh created in Fig. 6.5 required rescaling as there is a lot of variation in breast size across individuals. It is also necessary to reposition the initial mesh to the region of the data as each individual is not in the same position in the MRI scanner. Therefore, code was written to determine the geometric dimensions of the skin data set. The ratio between the initial mesh size and the data set size was used to scale the model, and the model was repositioned to the middle of the data cloud. Fig. 6.6 shows the resulting initial mesh after running the code using the data set shown in Fig. 6.2.

#### Stage 2: Further customisation (Automatic)

In some cases, stage 1 was still not sufficient to produce an initial mesh that was adequate for the main surface fitting algorithm. Fig. 6.7 shows the new initial mesh after scaling and repositioning the model in Fig. 6.5 for one of the image data sets used in this study. The data points are still too far away from the surfaces to be fitted accurately. In this case the initial mesh could be customised further to follow the curvature of the data more closely before the main surface fitting procedure is conducted.

To fix this problem, seven skin segmented MR image slices were chosen at approximately equally spaced intervals from the image set. The nodes of the skin surface on the mesh were then automatically moved to match the contour of the segmented skin data of the chosen image slices as shown in Fig. 6.8. This additional customisation produced a better initial mesh for the end result of creating an accurate individual specific finite element model of the breast.

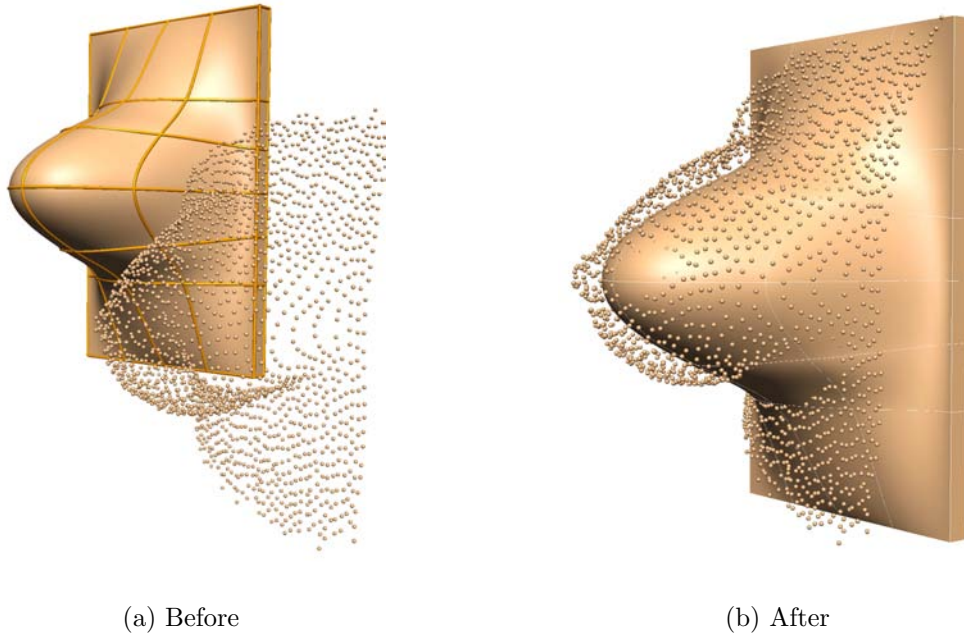


Figure 6.6: Scaling and translation of the initial mesh to the skin data cloud

### Stage 3: Modelling the skin contour (Automatic)

The fitting procedure was run on the initial mesh in Fig. 6.8, and took six iterations to stretch out the surfaces to fit the data. This ensured a gradual arrival at the optimal fit with the best projections of data points onto the surfaces. As discussed in Section 2.3.2, arc-lengths are typically used as scale factors for cubic-Hermite basis functions. In this fitting problem, the scale factors were set to unity to obtain direct control over the derivatives at nodes. This was necessary to adjust the derivatives in the antero-posterior direction and is explained in Section 6.2.3. Therefore, updates of scale factors are not necessary in this fitting procedure.

### Stage 4: Repositioning the skin fitted mesh (Automatic)

Comparing Figures 6.9(a) and 6.9(b) it is clear that the nodes on the front edges of the mesh have moved in the antero-posterior direction during the fitting procedure. In order to fit the back face to the muscle, it is necessary to modify the back face to provide a good initial mesh for muscle surface data fitting. Due to the proximity of the muscle data cloud to the skin data cloud (Fig. 6.2), it is possible for the back

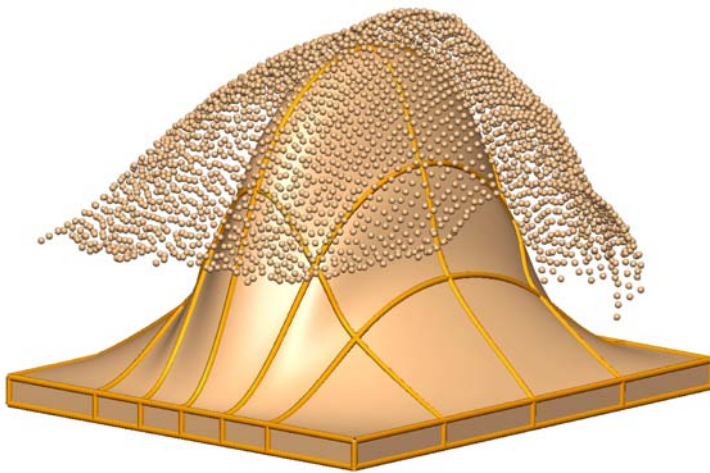


Figure 6.7: The new mesh for a particular image set, showing that the scaling and repositioning was not sufficient to produce a good initial mesh.

face nodes around the edges to move too close to the front face nodes around the edges of the model. Hence, it would be ideal to fix the edge nodes from moving in the antero-posterior direction during the fit. However, for gravity loading problems, mass is an important factor during simulations and hence the nodes cannot be fixed in their current position. Therefore, code was written to move the edge nodes closer to the front edge nodes they connect to, resulting in an arbitrarily chosen thickness of 5 mm around the edges of the model. The rest of the nodes on the back surface of the model were also moved automatically to be closer to the muscle data set. The data point in the muscle data set which was furthest away from the skin data set was first found. The nodes of the back surface were then moved to be 20 mm away from this muscle data point. This provided a good initial mesh for muscle data fitting (shown in Fig. 6.10).

### Stage 5: Modelling the muscle contour (Automatic)

The modified mesh was then fitted to the muscle data cloud. The back face was fitted over five iterations and the results are shown in Fig. 6.11.

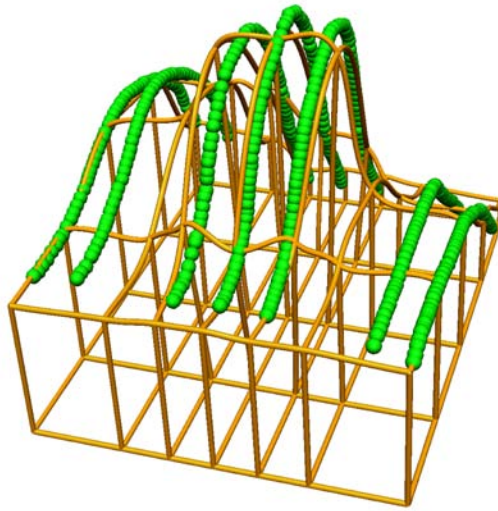


Figure 6.8: Further customisation of the initial mesh. The green spheres represent the segmented skin contours in the seven slices of the MR image set chosen. The mesh nodes were moved in the antero-posterior direction (y coordinate) to follow the contour of these data points.

### Stage 6: Adjusting derivatives through the thickness (Manual)

Since the derivatives in the antero-posterior direction are not in the fitting procedures for both skin and muscle, the resulting volumes after the fitting procedures can still be distorted, as illustrated in Fig. 6.12(a). This problem can be eliminated by ensuring that the derivatives in the  $\xi_3$  direction are normal to the plane in which the node lies. The normal is the cross product of the derivatives at the node in the  $\xi_1$  and  $\xi_2$  directions. By using unit scale factors for the cubic-Hermite interpolation it is possible to directly set the  $\xi_3$  derivatives to the normal. Code was written to calculate the unit normal to the plane in which the node lies. However, it was not easy to determine the magnitude of the normal that would make the mesh suitable for biomechanics simulations. Hence, at this stage, this part is done manually (see Section 6.3 for possible solutions to this problem). The resulting mesh from modifying these derivatives is shown in Fig. 6.12.

### 6.2.4 Fitting Results

The procedure described in Section 6.2.3 was applied to the MR image sets of the six individuals that were digitised. The RMS errors following the fitting procedures for skin and muscle contours are given in Table 6.1. The table also shows the total time it took on a Pentium IV desktop PC to create the individual-specific models. Fig. 6.13 shows the surface geometries of the different individuals, illustrating the ability of the code to fit a model to a wide range of shapes. Muscle data was not digitised for the sixth individual since only coronal images were available for segmentation. Thus, the muscle fitting error was not available.

Individual	Skin	Muscle	Breast size	Total Time
1	1.18 mm	1.27 mm	210x90x130	5 min 36s
2	1.49 mm	1.15 mm	225x117x135	6 min 3s
3	1.84 mm	1.78 mm	178x117x156	5 min 50s
4	1.74 mm	1.83 mm	250x108x98	5 min 23s
5	1.49 mm	1.57 mm	205x126x84	6 min 8s
6	0.99 mm	N/A	148xN/Ax123	2 min 43s

Table 6.1: RMS errors and time for geometric fitting of skin and muscle surfaces of the finite element model to skin and muscle from MR images of breasts from six individuals.

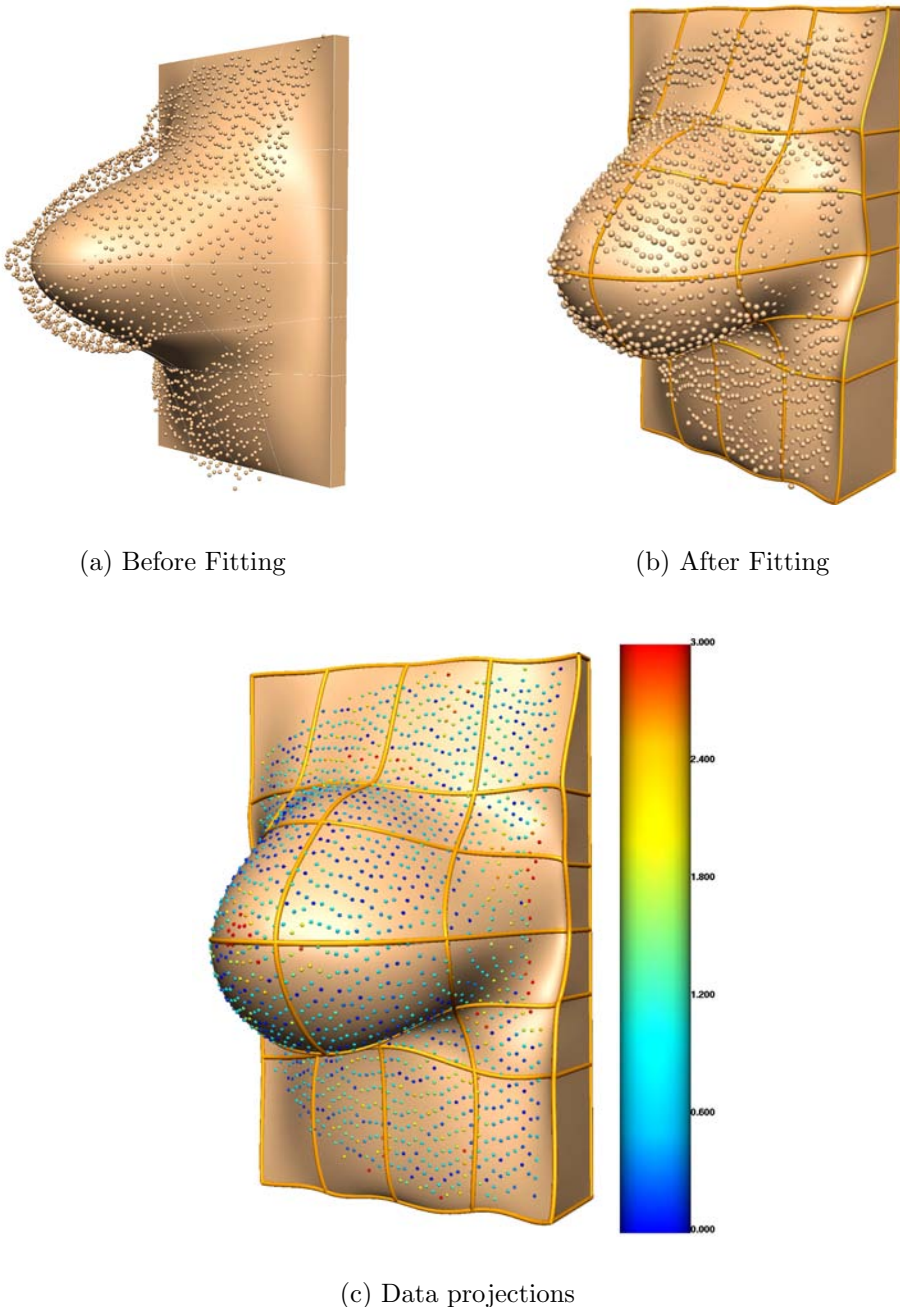


Figure 6.9: Fitting results. (a) and (b) showing the mesh before and after fitting the surfaces to the skin data set. (c) final data projections showing quality of fit with an RMS error of 1.18 mm. The spheres represent the skin surface data segmented from the MR images with the colour map showing the individual error magnitude, in millimeters, associated with each data point

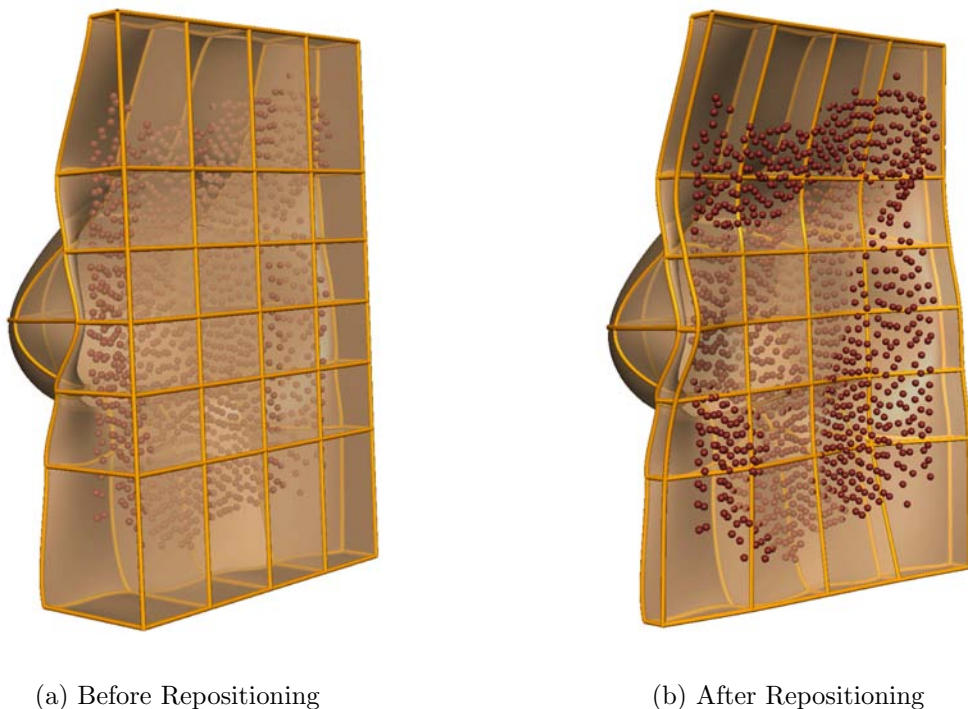


Figure 6.10: Repositioning of the mesh. (a) showing mesh before repositioning of back face nodes. (b) showing the result of moving the back nodes closer to the muscle data set.

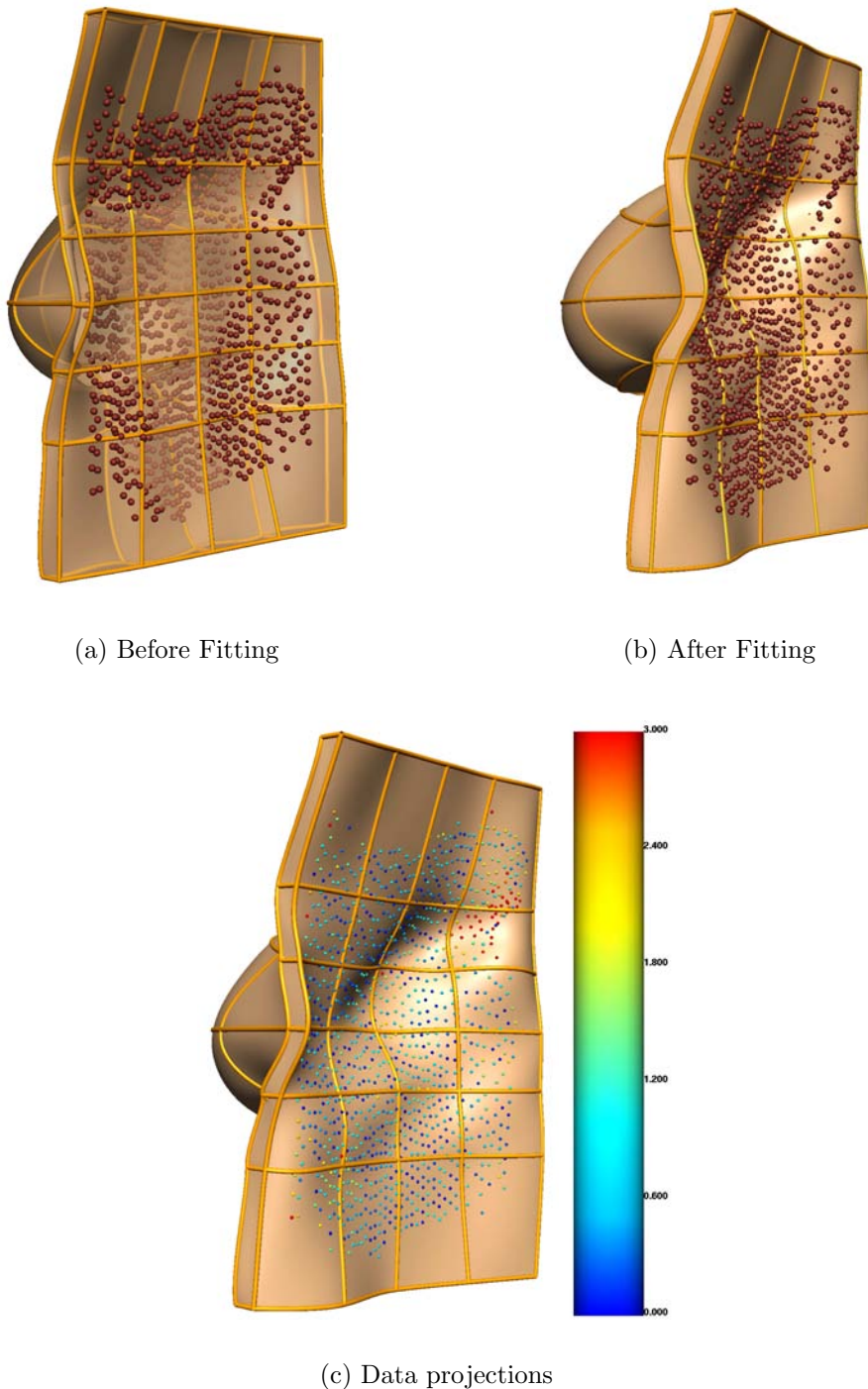
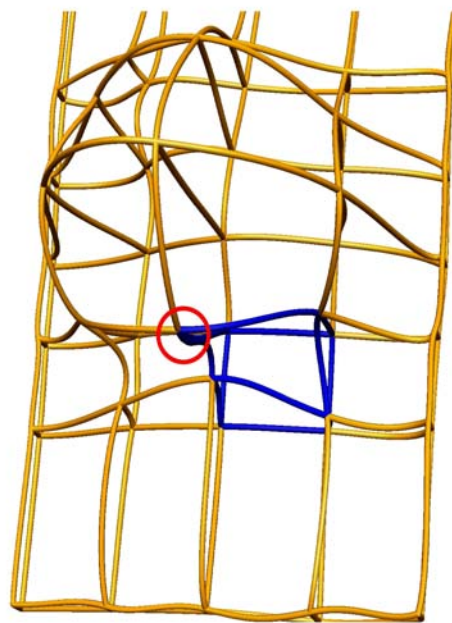
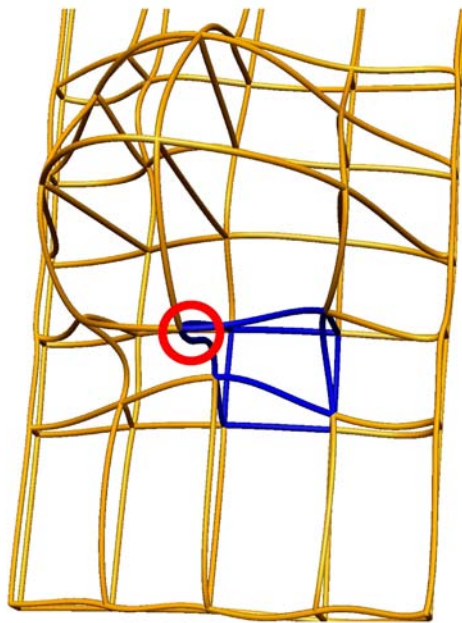


Figure 6.11: Fitting results. (a) and (b) showing the mesh before and after fitting the surfaces to the muscle data set. (c) showing final data projections showing quality of fit with an RMS error of 1.27 mm. The spheres represent the muscle surface data segmented from the MR images with the colour map showing the individual error magnitude, in millimeters, associated with each data point



(a) Before fixing derivatives



(b) After fixing derivatives

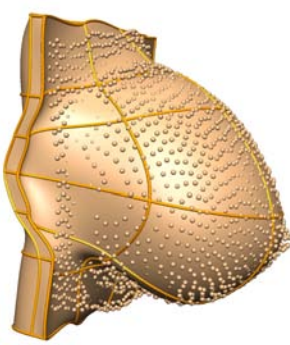
Figure 6.12: Recalculating  $\xi_3$  derivatives changes the shape of the volume (in blue for example) to be less distorted, making the model usable for large deformation mechanics problems



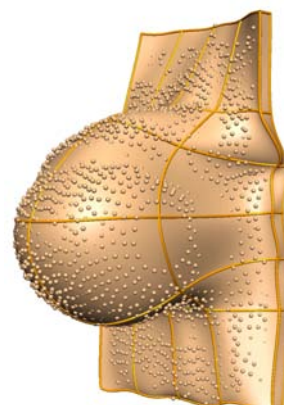
(a) Individual 1



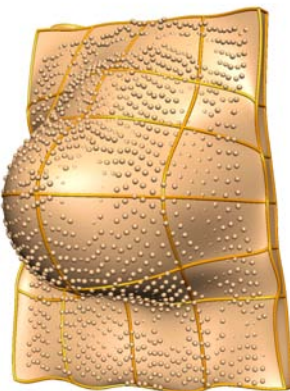
(b) Individual 2



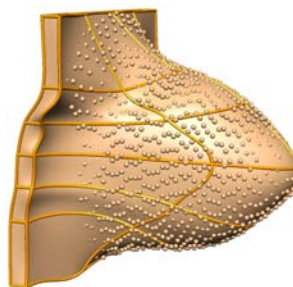
(c) Individual 3



(d) Individual 4



(e) Individual 5



(f) Individual 6

Figure 6.13: Final breast surface geometry for each individual following the fitting procedure

## 6.3 Discussion

The results in Table 6.1 show that the semi-automatic model generation code performs well with a wide range of breast geometries. The times show that the code is quick and that once the adjustment of derivatives in the antero-posterior direction is automated, it could be used effectively in the clinical setting.

This requirement to manually adjust the derivatives is because the fitting algorithm only fits the surfaces of the hexahedral mesh and does not incorporate the parameters of the elements in the third dimension. One possible solution would be to incorporate a 3D fitting constraint in the algorithm. The objective function could be modified such that the volumes of the hexahedral element do not collapse to zero, invert or distort.

It is also important to have an even distribution of data points across the surfaces to be fitted. The lack of an even distribution is typically addressed by the use of Sobolev smoothing. However, the Sobolev weights can still prove to be insufficient to avoid element volume distortion. Future work should also ensure that the skin and muscle contours are easily identifiable in the image sets, and that the tissues can be segmented to produce an even distribution of data across fitting surfaces.

In the process of ensuring that there is an even distribution of segmented data points, work must be conducted to identify best ways to automatically segment the different tissues. There are a vast number of image segmentation techniques which could be tried and tested for optimal performance with breast images.

## 6.4 Conclusions

**How accurately can the geometry of the breast be represented for each individual by a finite element model using an automatic and efficient algorithm?**

An algorithm was developed to rapidly create individual-specific finite element geometries of the breast with an average RMS error of  $1.46 \text{ mm} \pm 0.32 \text{ mm}$  in representing skin, and an average RMS error of  $1.52 \text{ mm} \pm 0.3 \text{ mm}$  in representing muscle. Aside from the areas for further improvement described in the discussion, this method was used for modelling breast geometries. Chapter 7 shows the results of

a large deformation mechanics study using a customised model of a breast from one volunteer. This automatic model generation technique was used to rapidly create finite element models of the breast under different gravity loading conditions.

# Chapter 7

## Modelling Breast Mechanics - The Clinical Setting

In order to validate the modelling framework for breast mechanics, it is necessary to design a set of experiments on volunteers, similar to the silicon gel phantom studies. This chapter describes the development of a new clinical experimental plan (Section 7.1) in order to address three questions:

- Can the breast under neutral buoyancy conditions be considered as a representation of the reference configuration for predicting large deformations under gravity loading conditions?
- What errors are introduced if the prone gravity-loaded configuration is used as the reference state?
- Is a homogeneous model sufficient for the prediction of breast deformation under gravity loading conditions?

Based on images from Section 7.1, Section 7.2 describes studies that were conducted to address these issues. This is followed by a discussion in Section 7.3 of the results of this study and highlights future directions in both the modelling and the experimental objectives.

## 7.1 Clinical Experimental Plan

Experimental protocols were developed to obtain two types of breast MR images. Section 7.1.1 first describes the development of tools to obtain MR images of the breast under a variety of gravity loading conditions. Section 7.1.2 then describes the design of a water container to obtain the images of the breast under neutral buoyancy for its potential use as a reference state of the breast.

### 7.1.1 Imaging the breast under gravity loading conditions

Orienting a woman in different positions produces large deformations of the breast. A wide range of deformations are required for a robust validation of the finite element modelling framework in a clinical setting. A standard breast MR coil consists of a flat or curved base to support the woman and the breasts hang freely through two slots for imaging (Fig. 7.1). Standard breast coils do not provide the flexibility of changing the orientation of the subject to be imaged because the coil apparatus must remain flat on the table. The slots may also be in contact with the breast during the imaging process, typically resulting in complex contact loading conditions being applied to the breast.

In order to provide different orientations with respect to the direction of gravity, whilst keeping the breast in a freely hanging state, a set of polystyrene boards were created to position volunteers in five different orientations:

1. prone (face down) with the breasts hanging freely.
2. 11.5 degrees head up. The volunteer is in a prone position with their back arched slightly upwards, such that the head is raised.
3. 11.5 degrees head down. The volunteer is in a prone position such that the back is arched slightly downwards. Head and feet are directed towards the bed, whilst the bottom is raised.
4. 11.5 degrees right shoulder down. The volunteer is positioned prone with their upper part of the body is rotated about the supero-inferior axis.
5. supine (face up) with arms slightly away from the torso to avoid contact with the breasts.



Figure 7.1: A typical breast coil used for MR imaging of the breast.

Fig. 7.2 shows the polystyrene boards that were made for the imaging procedures. Four of each board were made to provide flexibility to fit large breasts by stacking the boards to provide a bigger separation between MR machine bed and the breasts. Boards were also made without the holes to give more support to the lower part of the body (Fig. 7.3).

With the exception of the supine position, all other orientations were obtained with the volunteer lying on their stomach to reduce the motion artefacts due to breathing. Sufficient image quality was obtained by placing the polystyrene boards on a spine coil on the MR machine bed. All images were T2 (TE=102, TR=6560) weighted with iPAT<sup>1</sup> turned on for faster image acquisition, and had 512x512 pixel dimensions with a 350x350 mm field of view and 2.5 mm slice thickness through the supero-inferior direction. The MR sequence typically took five and a half minutes

<sup>1</sup>iPAT: “integrated Parallel Acquisition Techniques” is a faster way of scanning by acquiring phase encoding lines in parallel.

to acquire each image set.

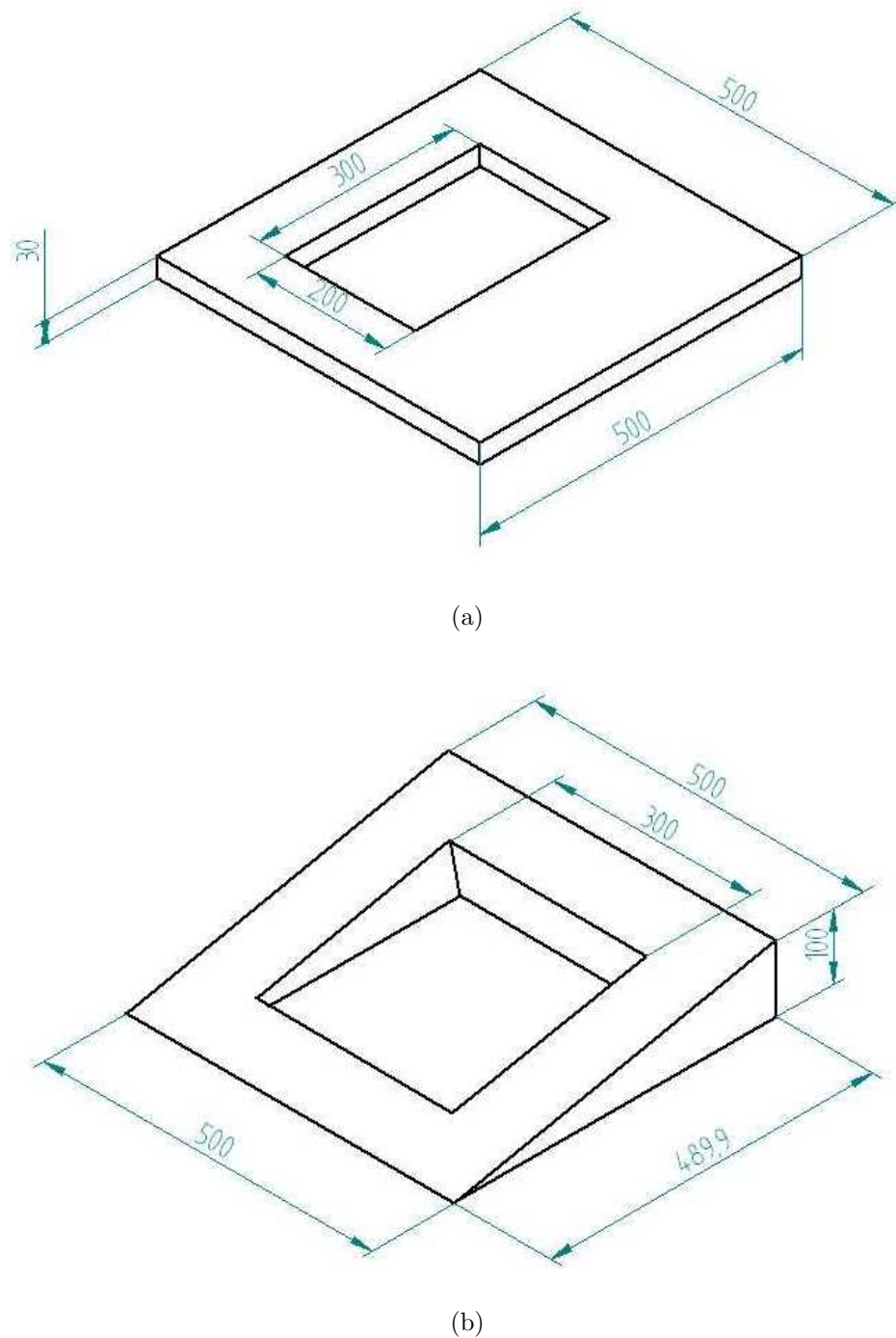


Figure 7.2: (a): Polystyrene board with hole to position breasts in prone position with no contact. (b) Polystyrene board with a 11.5 degree incline.

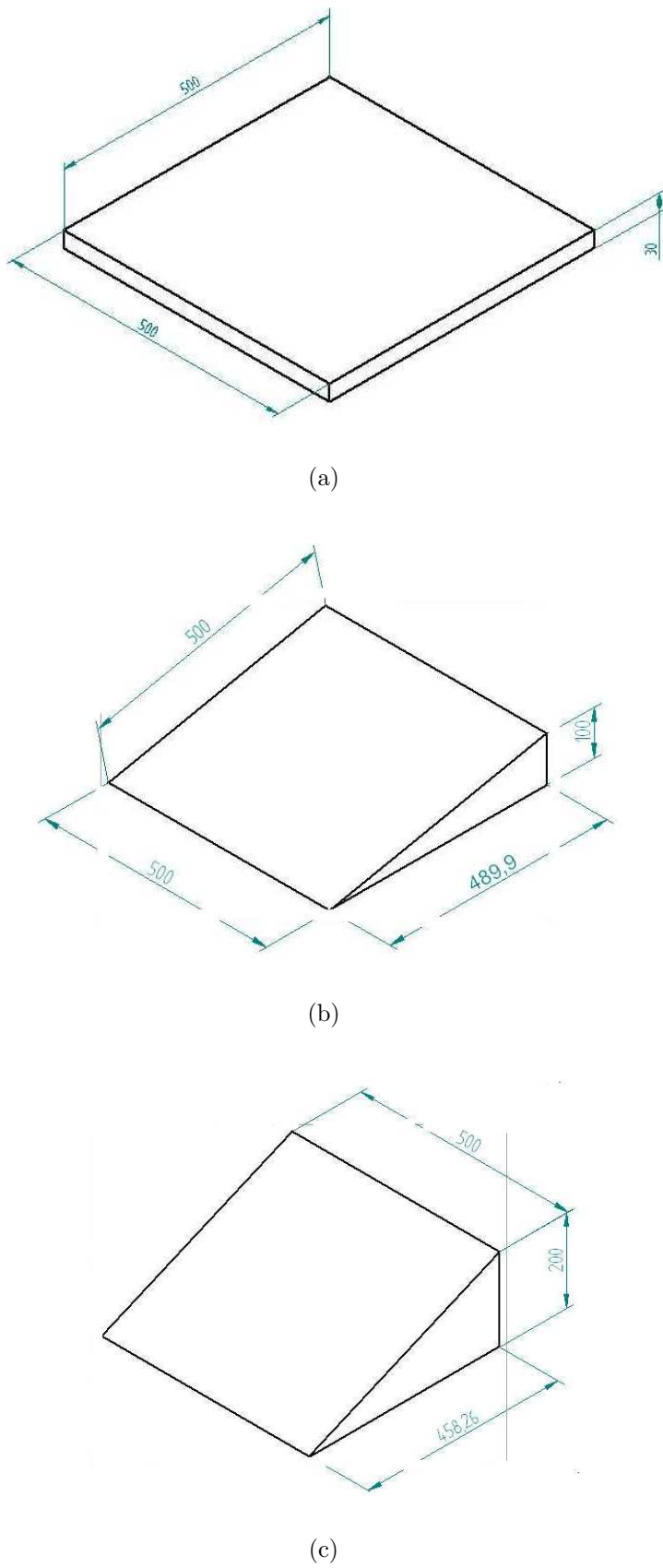


Figure 7.3: Polystyrene boards used to support the lower half of the volunteer's body

### 7.1.2 Imaging the breast in neutral buoyancy

As described in Chapter 4, all images of the breast are taken under gravity loading conditions. Therefore, any models created from these images represent deformed configurations of the breast. Chapter 4 presented a novel technique to determine the reference state of a body from a deformed configuration given mechanical properties of the material and the loading conditions applied to obtain that deformed configuration. A validation study conducted with a homogeneous silicon gel phantom showed that the method accurately predicted the known reference configuration.

It is important to have a reliable representation of the reference configuration for predicting large deformations of the breast. The reference state influences model predictions due to the nonlinear nature of the finite elasticity equations. Although the validation result in Chapter 4 is promising, it is important to perform a similar validation exercise using clinical data to ensure that the method is reliable in a clinical setting.

Given that soft biological tissues consist primarily of water, immersing the breast in water causes it to be in an almost neutral buoyancy state, thus it assumes a shape to reflect this change in loading conditions. A hypothesis was made that the images of the breast in neutral buoyancy provide a good representation of the breast in the reference state. To test this hypothesis, a water container was designed to fit around the breast of a volunteer, for imaging the breast in neutral buoyancy. The device was designed and developed with the help of Ms. Angela Lee during an undergraduate research project as part of the Biomedical Engineering Degree at the University of Auckland (Lee, 2006).

#### Water container design

The surface configuration of the breast of a mannequin was first scanned using a laser scanner. A computer model of a 200 mm diameter cylinder was then superimposed on the data (see Fig. 7.4). Data points on the mannequin surface that intersected with the cylinder opening were identified and plotted to determine the profile that should be cut at one end of the cylinder in order to comfortably fit on the torso (Fig. 7.5). The intersection of the cylinder opening to a volunteer's MR dataset was also obtained and plotted. However, due to the lack of data near the arms of the

volunteer, only a partial profile could be obtained (see Fig. 7.5).

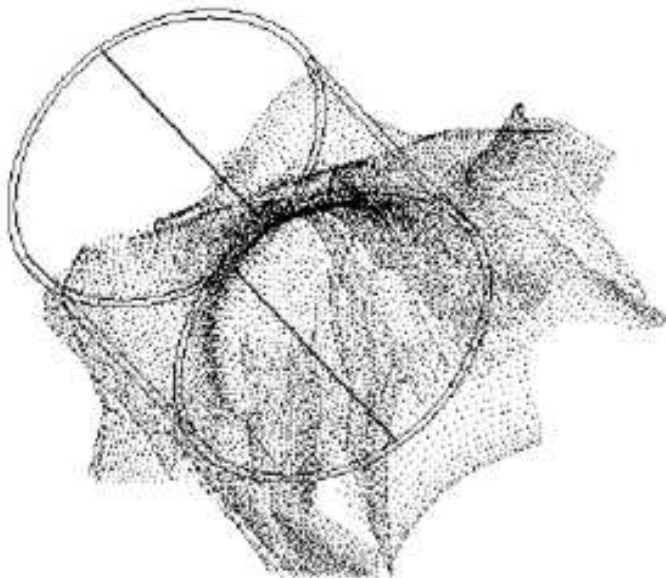


Figure 7.4: Overlay of cylinder on surface of mannequin breast.

The profiles exhibited a close resemblance to a sine curve. It was found that the best fit to the chest was obtained using a profile with a functional expression  $(11.5\sin 2\theta)(2.5 + \sin(\theta + \pi/4))$  on a 180 mm diameter cylinder. This profile was cut out of one end of the cylinder, and the other end was sealed with a wooden board. A rubber seal was then fitted to the profile end to provide a more comfortable fit for the volunteer and to prevent leakage of water (see Fig. 7.6(a)). The cylinder was placed in a plastic container to catch any water spill over. A polystyrene slab with a 10 degree incline was attached to the base to make it easier to position the breast inside the container whilst the volunteer lay prone on the polystyrene boards (Fig. 7.6(b)).

Images were then obtained with the cylinder filled with water as shown in Fig. 7.7. A comparison of the prone breast (left breast in Fig. 7.7) to the neutrally buoyant breast (right breast in Fig. 7.7) shows that the effect of the water on breast shape is significant, and thus warranting an investigation on the possible use of the image set as the reference configuration of the breast.

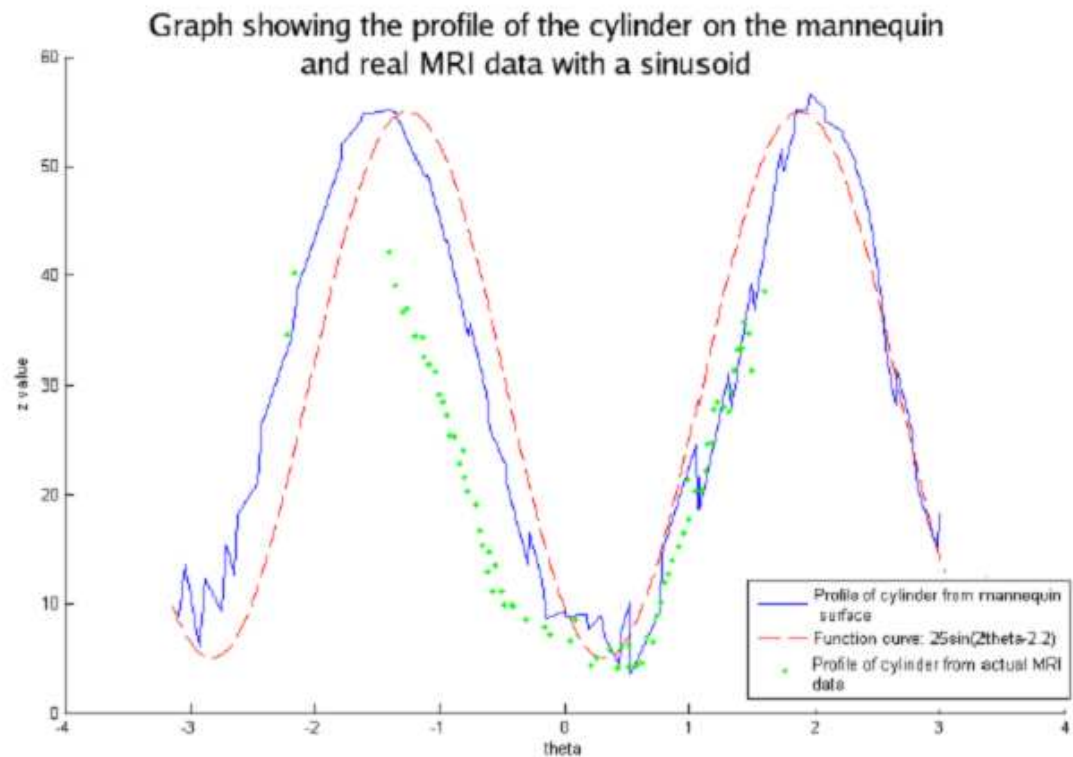
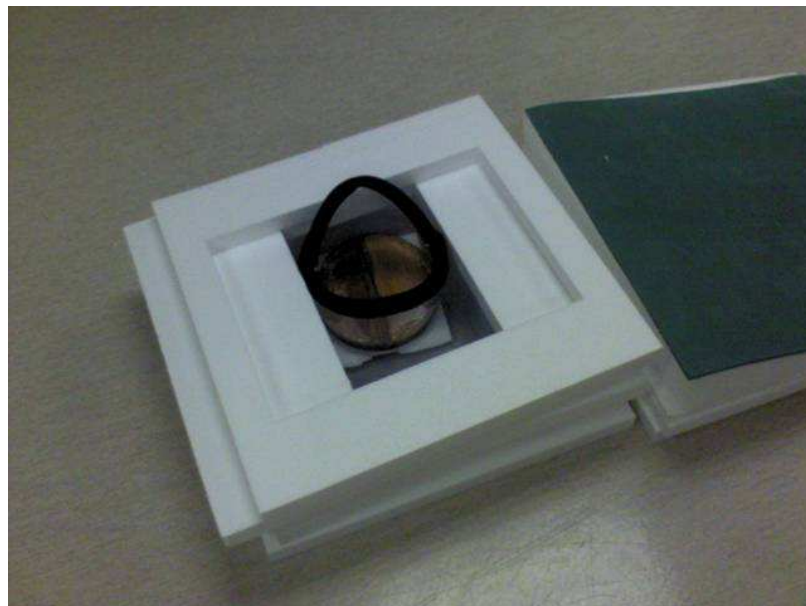


Figure 7.5: Profile of points on mannequin and MR dataset that intersect with the cylinder opening.



(a)



(b)

Figure 7.6: (a): Cylinder used for neutral buoyancy imaging. Plastic container used to catch water spill over. Polystyrene attached to base to make it easier to position the breast inside the container. (b) cylinder and polystyrene bed on which the volunteer is positioned

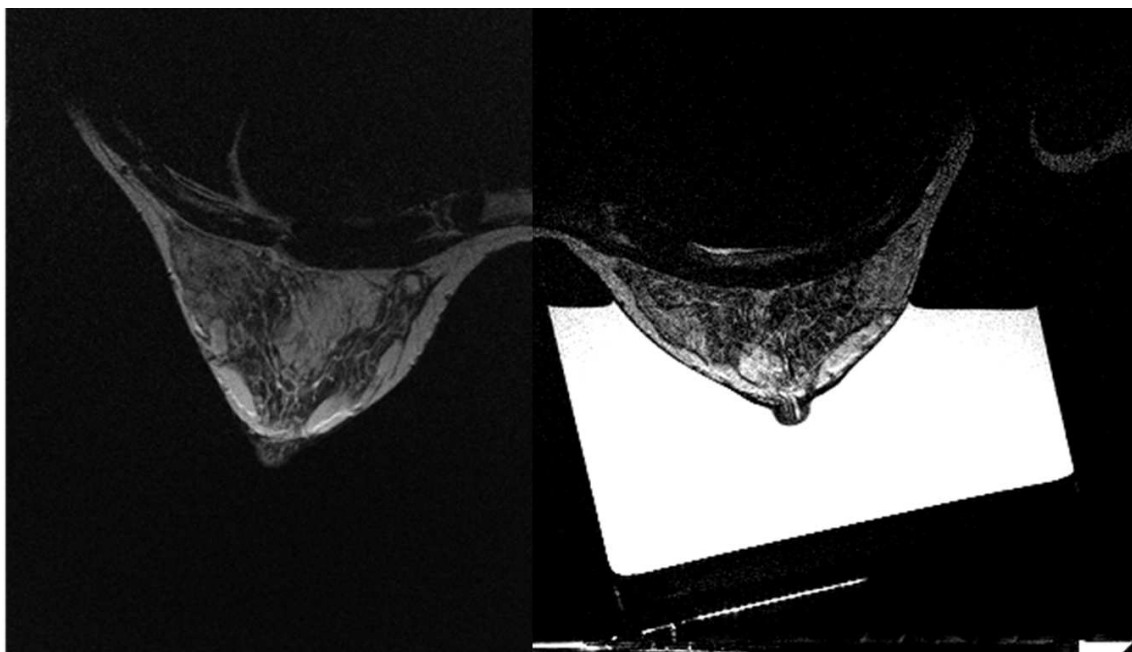


Figure 7.7: Image of the breast in neutral buoyancy. The left image is of the left breast in the prone position. The right is the image of the right breast in neutral buoyancy. The white block represents the water bath.

## 7.2 Modelling the Clinical Experiments

The neutral buoyancy and gravity loading images obtained with the experimental plan described in the previous section are the first of their kind. The images provide a rich set of information on breast deformation that can be used to test the modelling framework. This section outlines three preliminary studies that were conducted using breast images of one volunteer under gravity and neutral buoyancy conditions to address the three questions that were stated at the start of this chapter.

Section 7.2.1 describes the development of a homogeneous model of the breast to simulate the neutral buoyancy to gravity loaded deformations. Section 7.2.2 then assesses the accuracy of the reverse solution technique described in Chapter 4 in predicting a reference state, by using the computed reference configuration (rather than the neutral buoyancy configuration) to predict the deformations of the breast. Previous studies in the literature such as Ruiter et al. (2003); Samani et al. (2001); Azar et al. (2000); Yu-Neifert (1995) used one of the deformed configurations (typically the prone gravity-loaded state) as the reference state. Section 7.2.3 looks at the effect of using a deformed configuration as the reference state (rather than the neutral buoyancy configuration or the computed reference configuration) on the accuracy of model predictions.

### 7.2.1 Neutral buoyancy to gravity loading - a homogeneous model

A homogeneous model of the breast of one volunteer was developed to predict the deformations of the breast from the neutral buoyancy configuration to the prone, gravity loaded configuration. The neutral buoyancy and prone image data sets were taken at different times and therefore at different positions relative to the MR scanner coordinate system. Hence the neutral buoyancy datasets were first aligned to the prone datasets by identifying the sternum in both image sets and finding the transformation matrix that provided the best alignment of this anatomical landmark. The transformation matrix was then applied to the skin, and bone datasets from the neutral buoyancy images. A generic finite element model of the breast was fitted (using techniques in Chapter 6) to the skin (with an RMS error of 0.78 mm) and chest surfaces (with an RMS error of 1.2 mm) of the neutral buoyancy images as

shown in Fig. 7.8.

The neutral buoyancy configuration was assumed to represent the reference state of the breast and a fixed displacement boundary condition (tissue firmly attached to the chest wall) was assumed to be valid at the bone-breast tissue interface. The pectoral muscles were incorporated in this study as a part of the breast tissue because it is unclear as to what the appropriate boundary conditions are at the chest wall. With the breast tissue assumed to be isotropic, homogeneous, and incompressible, a neo-Hookean constitutive relation was used to describe the mechanical properties in the model. The geometric coordinates were described using a tricubic-Hermite interpolation and the hydrostatic pressure field was described using a trilinear interpolation function.

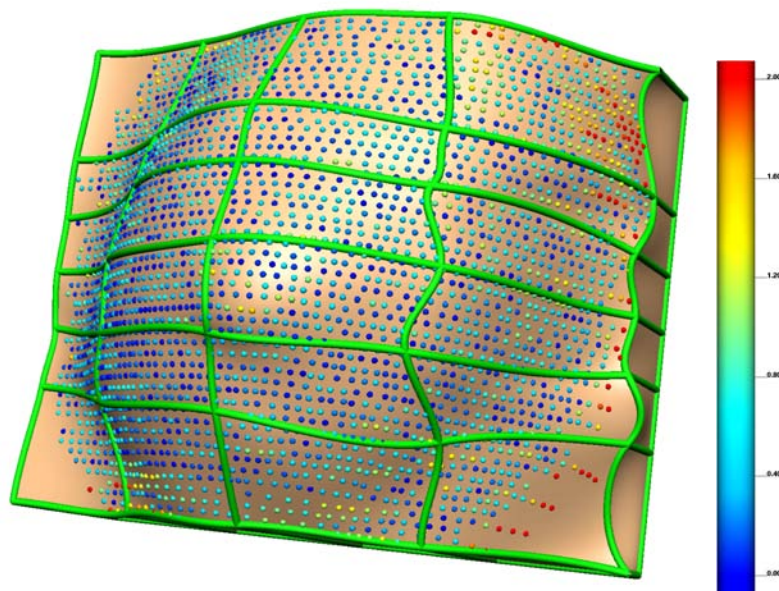
A displacement convergence analysis was first conducted by refining the 24 element fitted tricubic-Hermite mesh to ensure that the model predictions were reliable with the given assumptions. Fig. 7.9 shows the seven data points in the model at which displacements were recorded for successive refinements during the convergence analysis. The Euclidean displacements that each data point underwent during the deformation was calculated for each mesh resolution. The RMS errors between successive refinements were then recorded (plotted in Fig 7.10) and the mesh corresponding to 5184 degrees of freedom (Fig. 7.11) was chosen as the best resolution. This mesh consisted of 112 tricubic Hermite elements (7 elements medio-lateral, 8 elements supero-inferior and 2 elements antero-posterior) and 216 nodes.

The mesh in Fig. 7.11 was then used to predict the deformed configuration of the breast under gravity loading conditions in the prone position. The accuracy of the model prediction was quantified by comparing the manually segmented prone configuration of the breast skin to the model predicted skin configuration. The segmented points were projected onto the deformed surface of the model, and an RMS error was calculated as explained in Section 3.3.1. The model predictions matched the experimental data best with the neo-Hookean material parameter  $c_1 = 0.08 \text{ kPa}$ , with an RMS error of 5.03 mm (Fig 7.12).

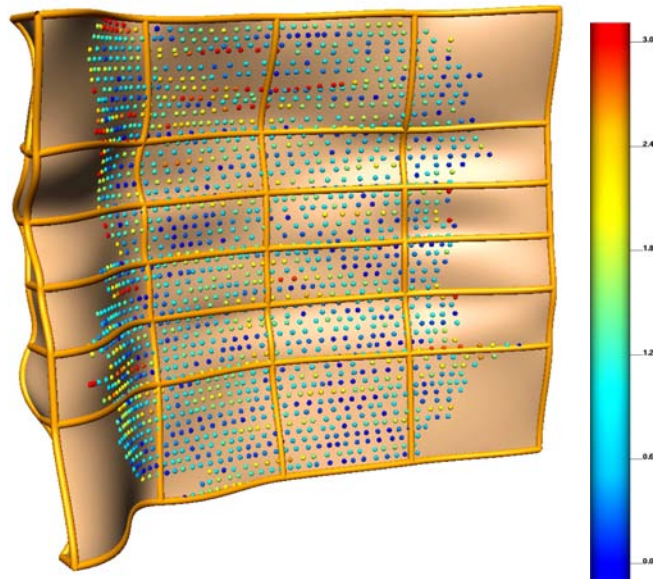
It is encouraging to note that the model matches the maximum displacement of the tip of the breast (shown in Fig. 7.12). The model surface contour is similar in shape to the contour followed by the experimental data. However, Fig. 7.13 shows that the model does not accurately capture the regional deformations (5.8 mm RMS

error in surface matching data point contour). The model was also used to predict the deformations of the breast in the four other orientations for which images were obtained (Fig 7.14 - Fig. 7.17), once again showing that the preliminary model is capable of capturing gross characteristic contours of the breast. However, it still needs improvement to provide more regional accuracy.

One possible source of error is the use of the neutral buoyancy configuration as the reference configuration of the breast. As mentioned earlier, the breast was not completely immersed in water. In order to determine if the major source of error was in using neutral buoyancy configuration as a reference, a further set of simulations were conducted using a theoretically accurate reference configuration. This configuration was obtained using the prone gravity loaded image set and the reverse method described in Chapter 4. Its effect on model predictions is given in the following section.



(a) anterior (skin) surface



(b) posterior (muscle) surface

Figure 7.8: Generic breast mesh fitted to the skin and bone surface data points from neutral buoyancy images with RMS errors of 0.78 mm and 1.2 mm respectively. The spheres represent the skin and bone surface data points obtained from the MR images with the colour map showing the individual error magnitude in millimeters, associated with each data point

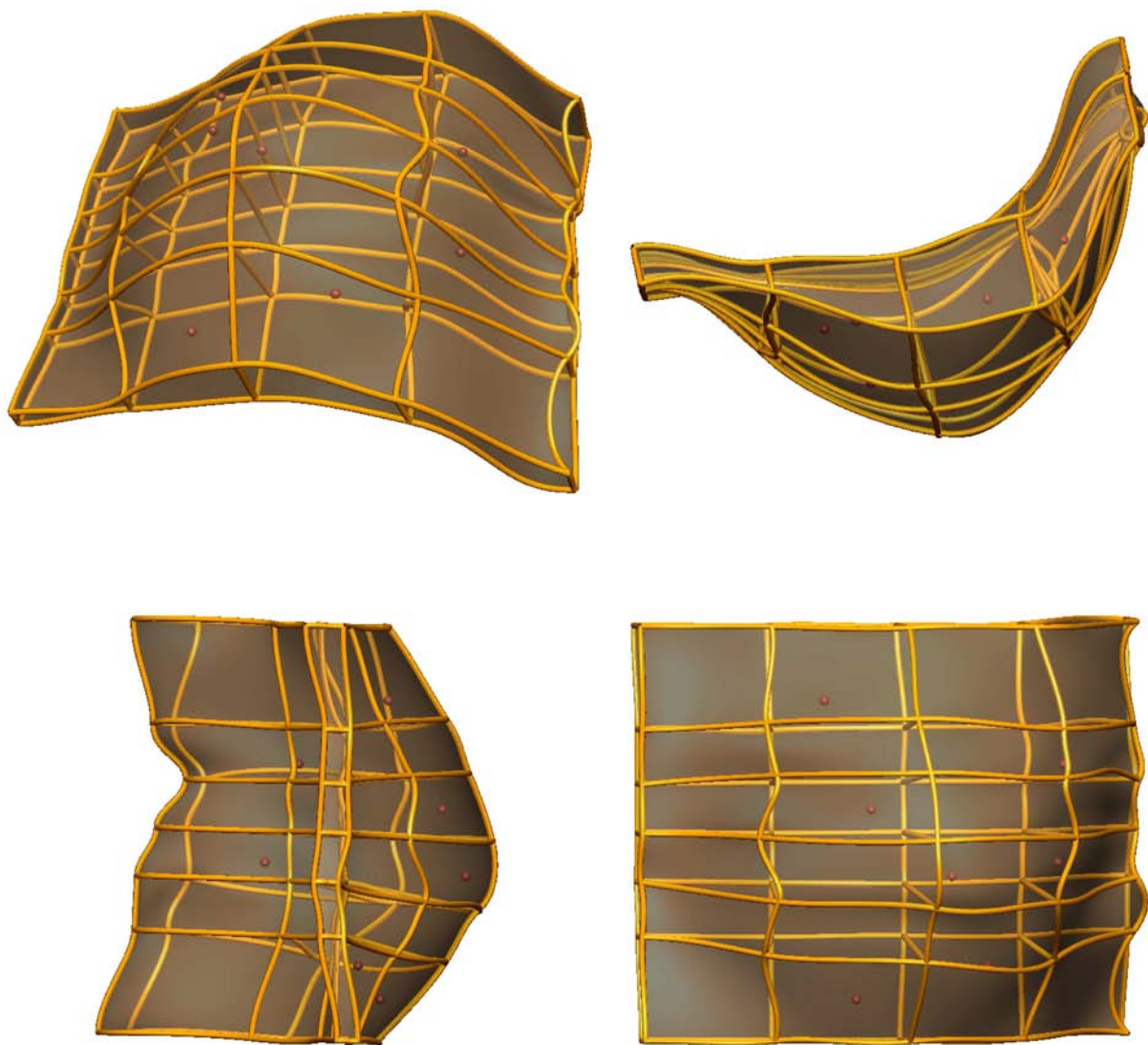


Figure 7.9: Data points at which displacements are recorded for convergence analysis.

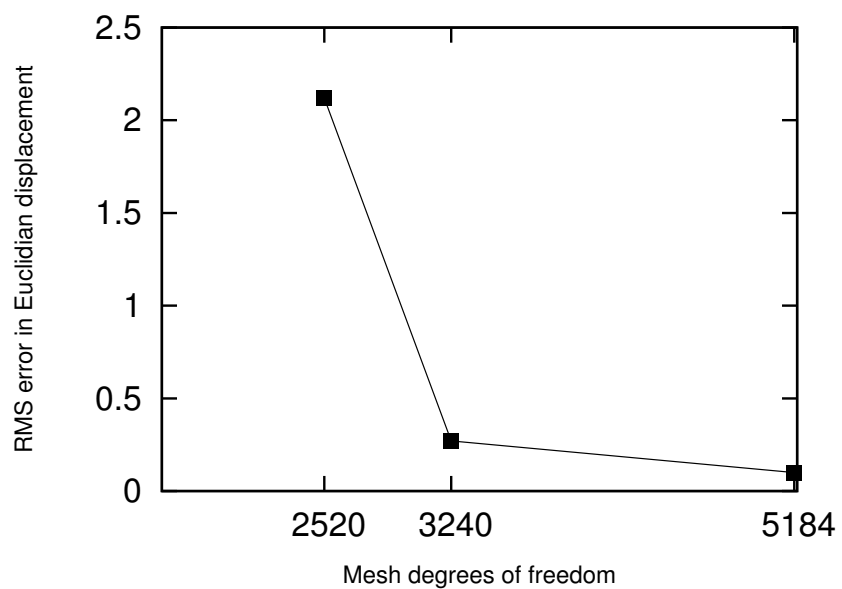


Figure 7.10: Convergence of RMS error in Euclidean displacements of selected points inside the model (Fig 7.9) with increasing mesh resolution.

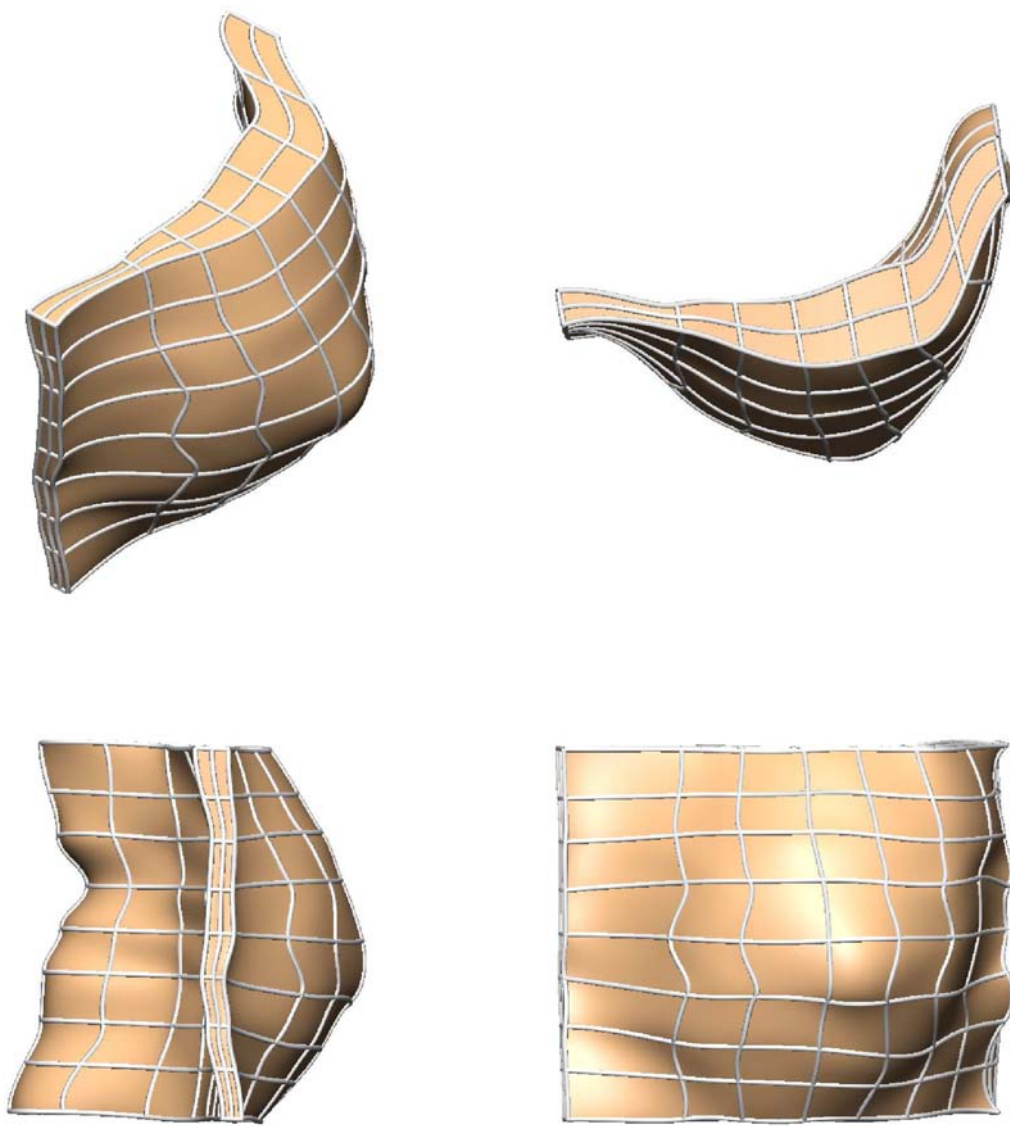


Figure 7.11: Mesh resolution (with 5184 degrees of freedom) chosen for this study.

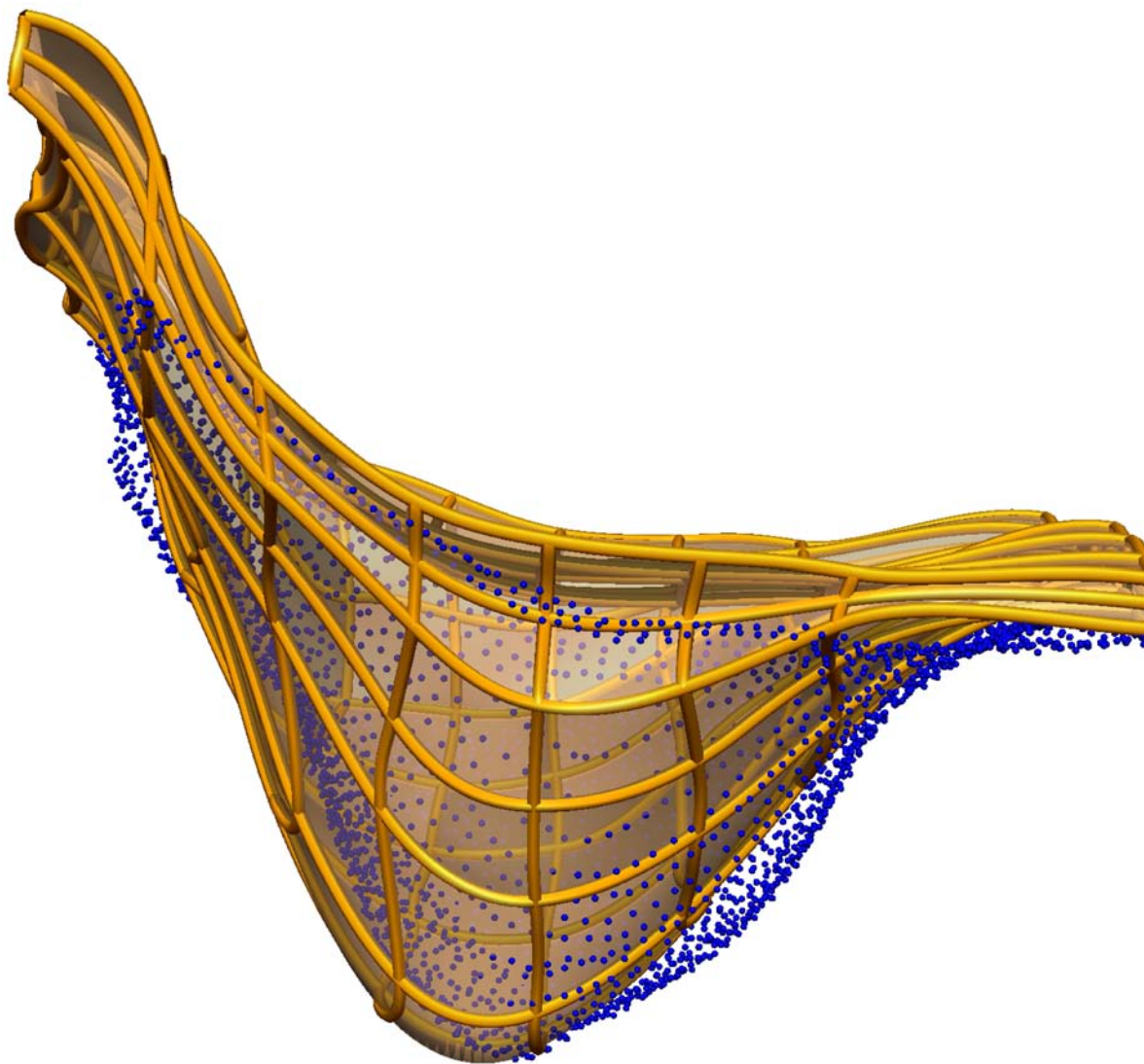


Figure 7.12: Comparison of model prediction (lines, surfaces) to experimental data (blue spheres) for the prone orientation.

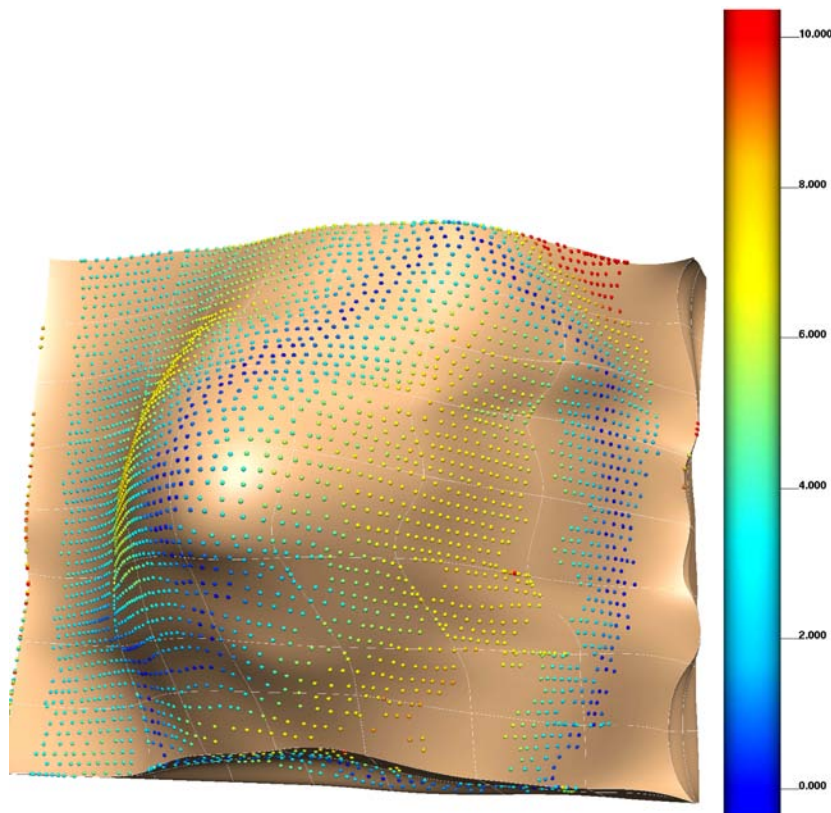


Figure 7.13: Comparison of model prediction to experimental data in the prone orientation with an RMS error of 5.08 mm. The spheres represent the skin surface data points obtained from the prone gravity loaded MR images with the colour map showing the individual error magnitude, in millimeters, associated with each data point.

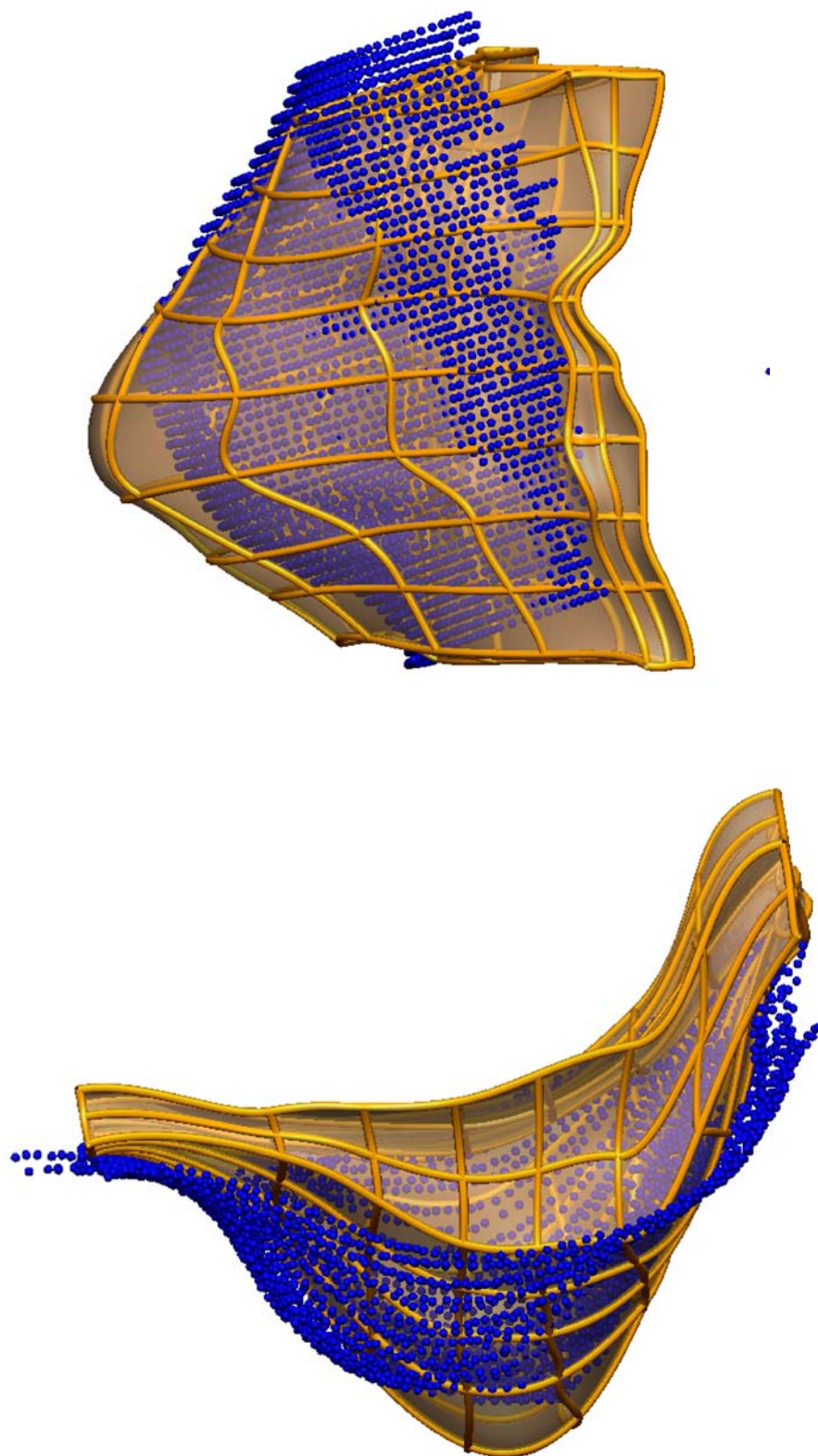


Figure 7.14: Comparison of model prediction (lines, surfaces) to experimental data (blue spheres) with volunteer arched upward in MR machine with an RMS error of 5.99 mm.

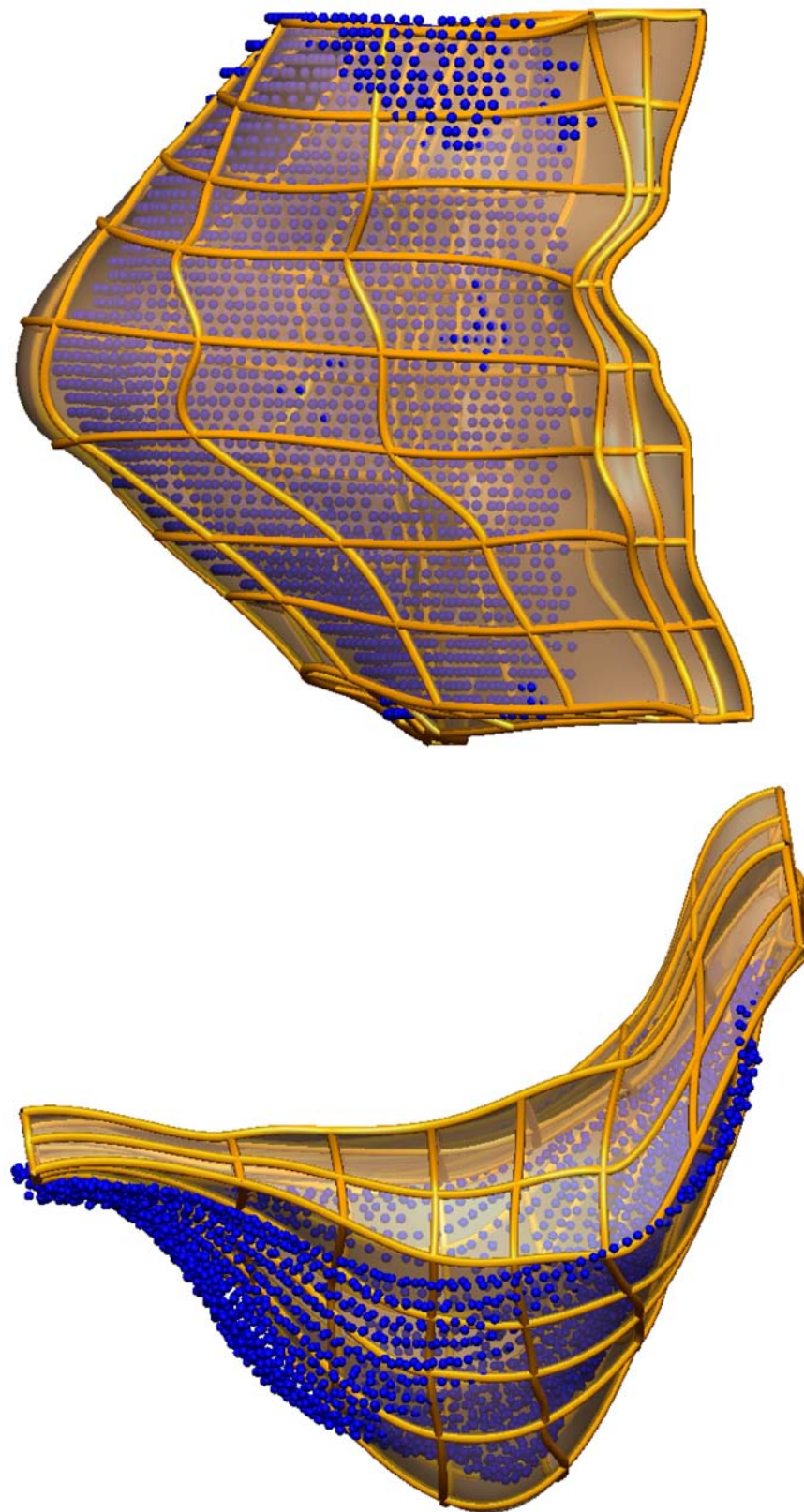


Figure 7.15: Comparison of model prediction (lines, surfaces) to experimental data (blue spheres) with volunteer arched downward in MR machine with an RMS error of 4.84 mm.

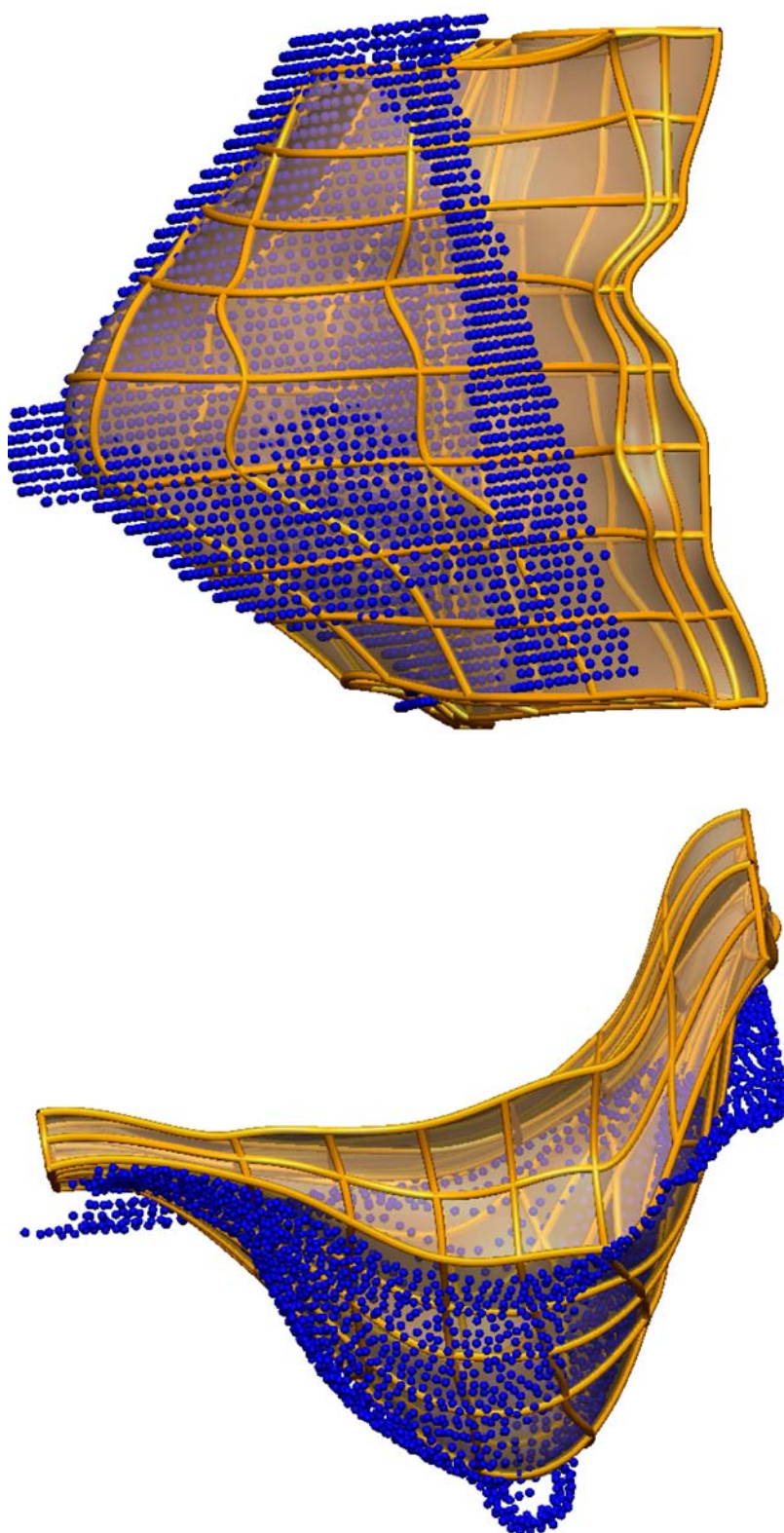


Figure 7.16: Comparison of model prediction (lines, surfaces) to experimental data (blue spheres) with volunteer oriented with the right shoulder down. The RMS error was 4.86 mm.

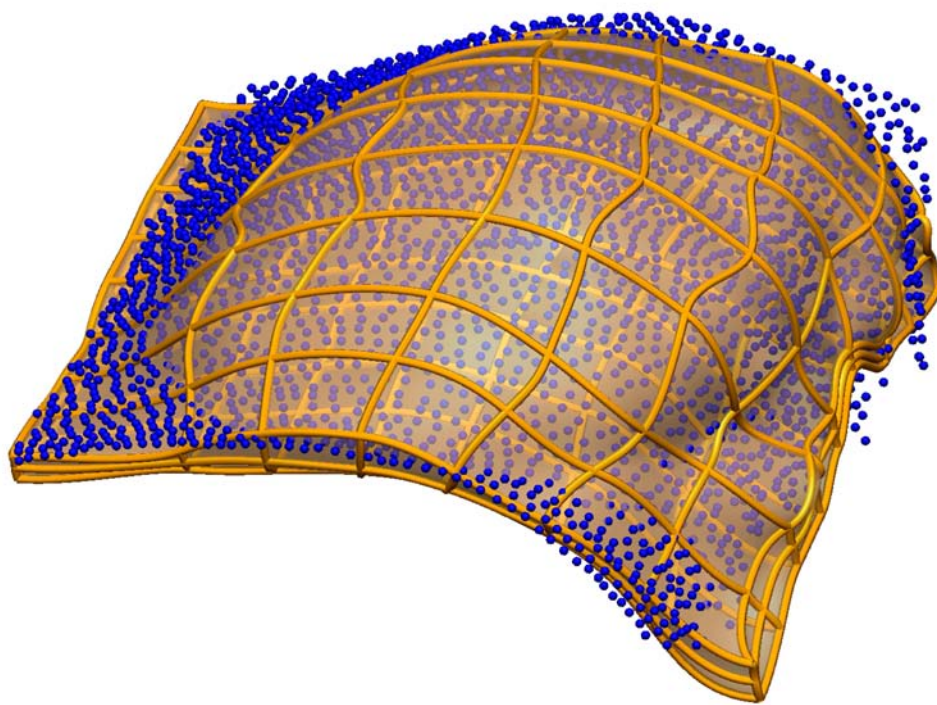


Figure 7.17: Comparison of model prediction (lines, surfaces) to experimental data (blue spheres) in supine position with an RMS error of 7.37 mm.

## 7.2.2 Using the reverse method

In this study, a model of the breast was first fitted to the skin (with an RMS error of 0.6 mm) and chest surfaces (with an RMS error of 1.0 mm) of the prone (gravity-loaded) position image set (Fig 7.19). The reference configuration of the breast model was then estimated using the reverse calculation method described in Chapter 4 applying the same kinematic boundary conditions as used in Section 7.2.1. The mesh was refined in the same manner as for the forward modelling study in the previous section to ensure reliable displacement converged model predictions.

The value of  $c_1$  in the neo-Hookean constitutive equation was chosen, with the objective of minimising the error in predicting breast deformation in the “head up” orientation. This optimisation process involved the calculation of the reference configuration from the fitted prone gravity loaded model, using an initial guess of the  $c_1$  value. The calculated reference configuration was then subjected to the “head up” gravity loading condition, and following the model solution, the RMS error in capturing the breast skin surface in this configuration was calculated. A finite difference derivative of the RMS error objective function with respect to the material parameter was then obtained after perturbing  $c_1$  slightly (by 0.0001 kPa), repeating the above computations and forming the numerical gradient. The derivative was used as a search direction for a value of  $c_1$  that minimised the RMS error in predicting the “head up” configuration. A summary of this material parameter optimisation algorithm is shown in the flow chart in Fig. 7.18.

The optimal  $c_1$  value was 0.1 kPa, predicting the “head up” deformation with an RMS error of 3.8 mm (Fig 7.20). The resulting theoretical reference configuration was also used to predict the deformations in the other three orientations (see Fig. 7.22 - Fig. 7.24). The figures show that the current model requires refinements for more accurate predictions and is discussed in Section 7.3.

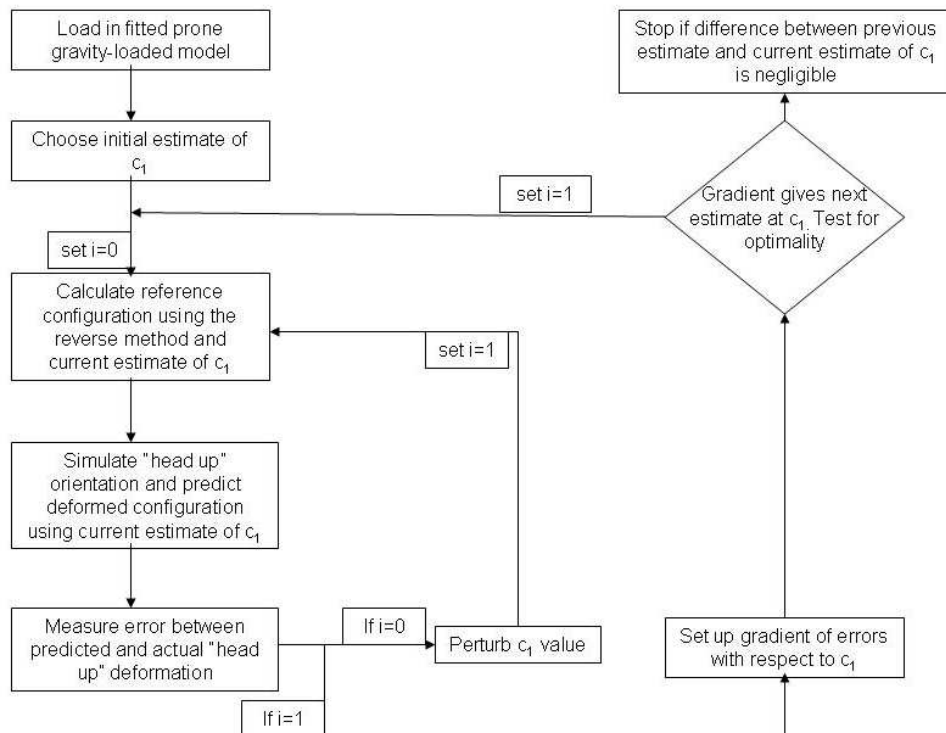
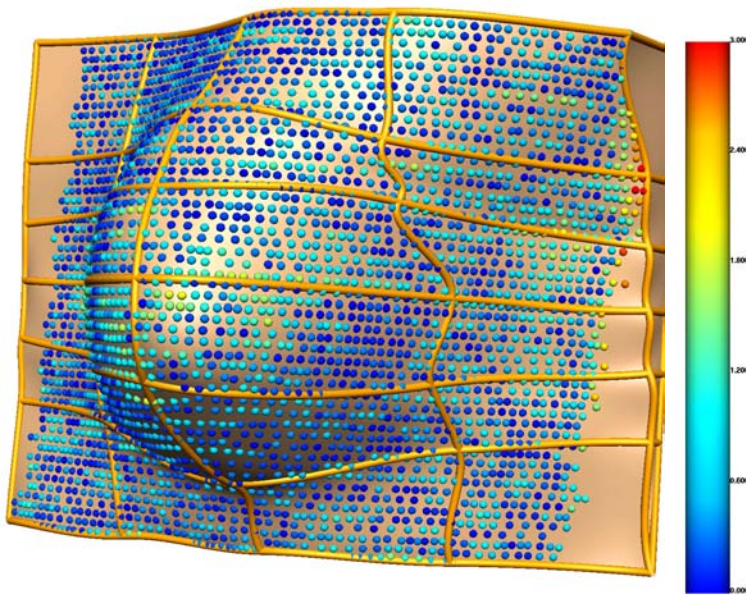
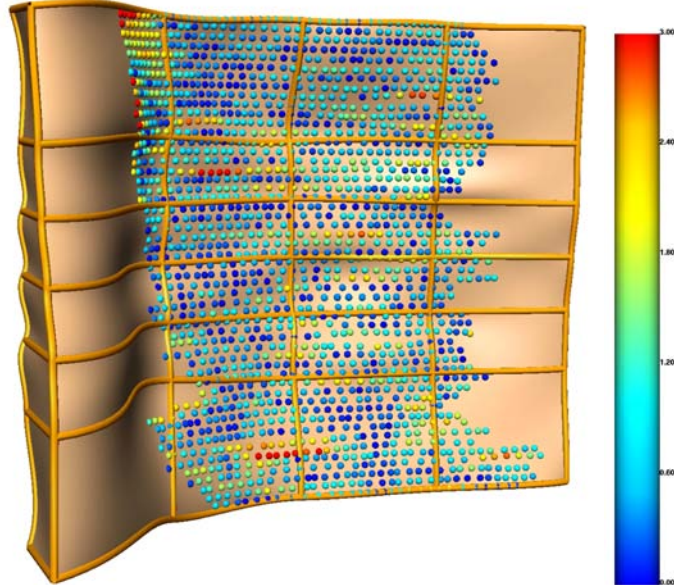


Figure 7.18: Flow chart of the material parameter optimisation algorithm to characterise the mechanical behaviour of the breast.



(a) anterior (skin) surface



(b) posterior (muscle) surface

Figure 7.19: Generic mesh fitted to the skin and bone surface data points from prone gravity-loaded images with RMS errors of 0.6 mm and 1.0 mm respectively. The spheres represent the skin and bone surface data points obtained from the MR images with the colour map showing the individual error magnitude in millimeters, associated with each data point

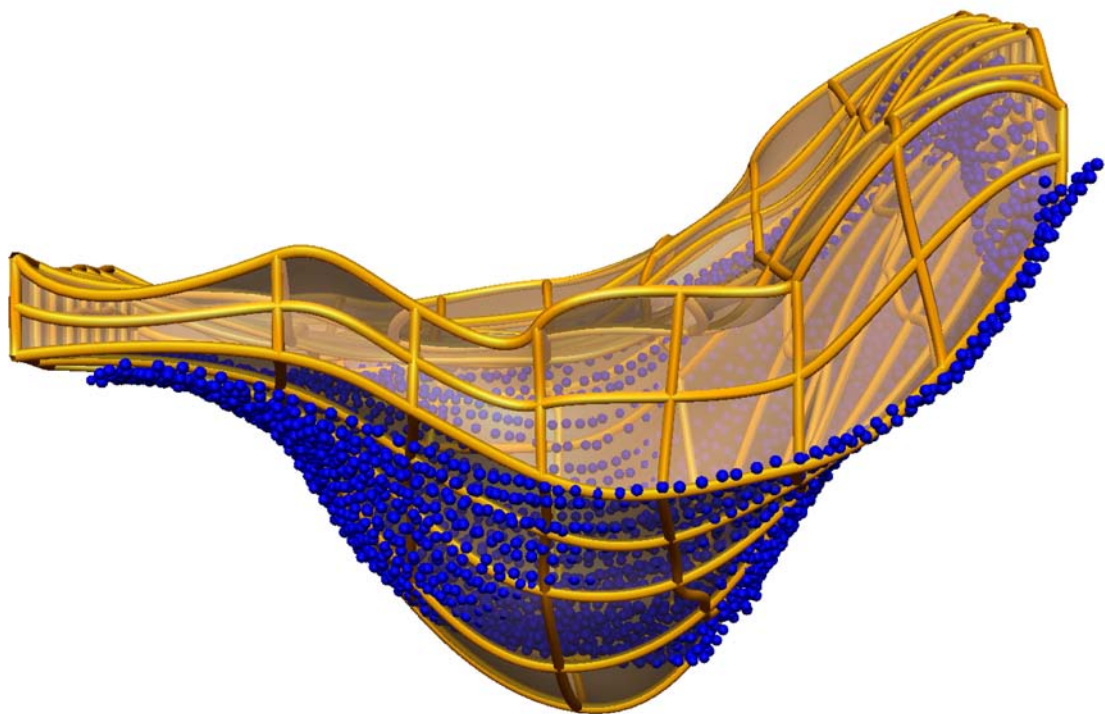


Figure 7.20: Comparison of model prediction from computed reference configuration to experimental data with volunteer in “head up” position in MR machine (blue spheres).

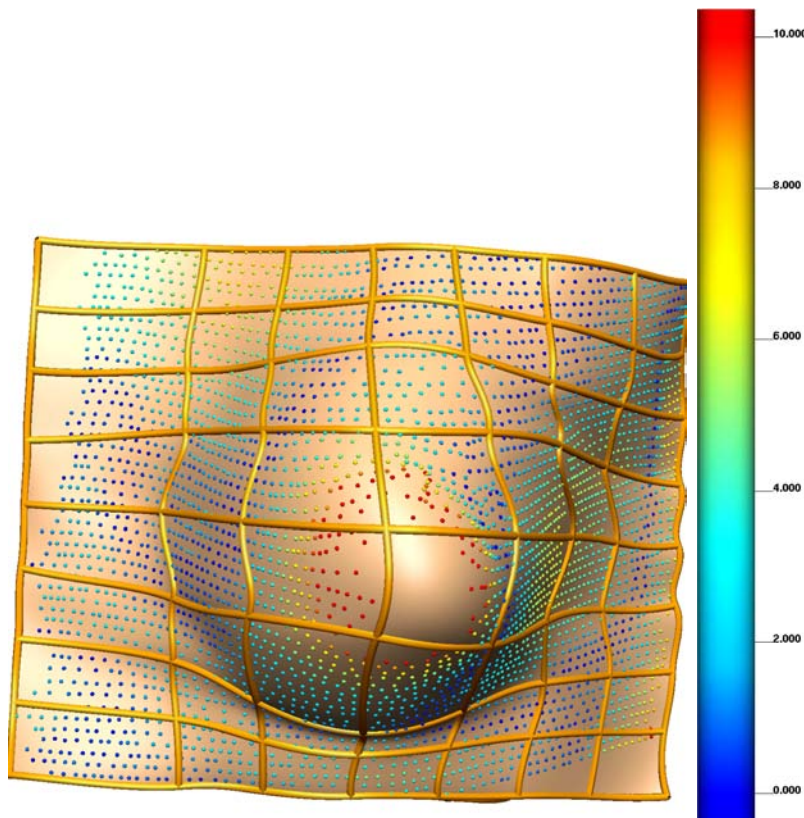


Figure 7.21: Comparison of model prediction (lines, surfaces) to experimental data (blue spheres) in the “head up” orientation with an RMS error of 3.8 mm. The spheres represent the skin surface data points obtained from the “head up” gravity loaded MR images with the colour map showing the individual error magnitude, in millimeters, associated with each data point.

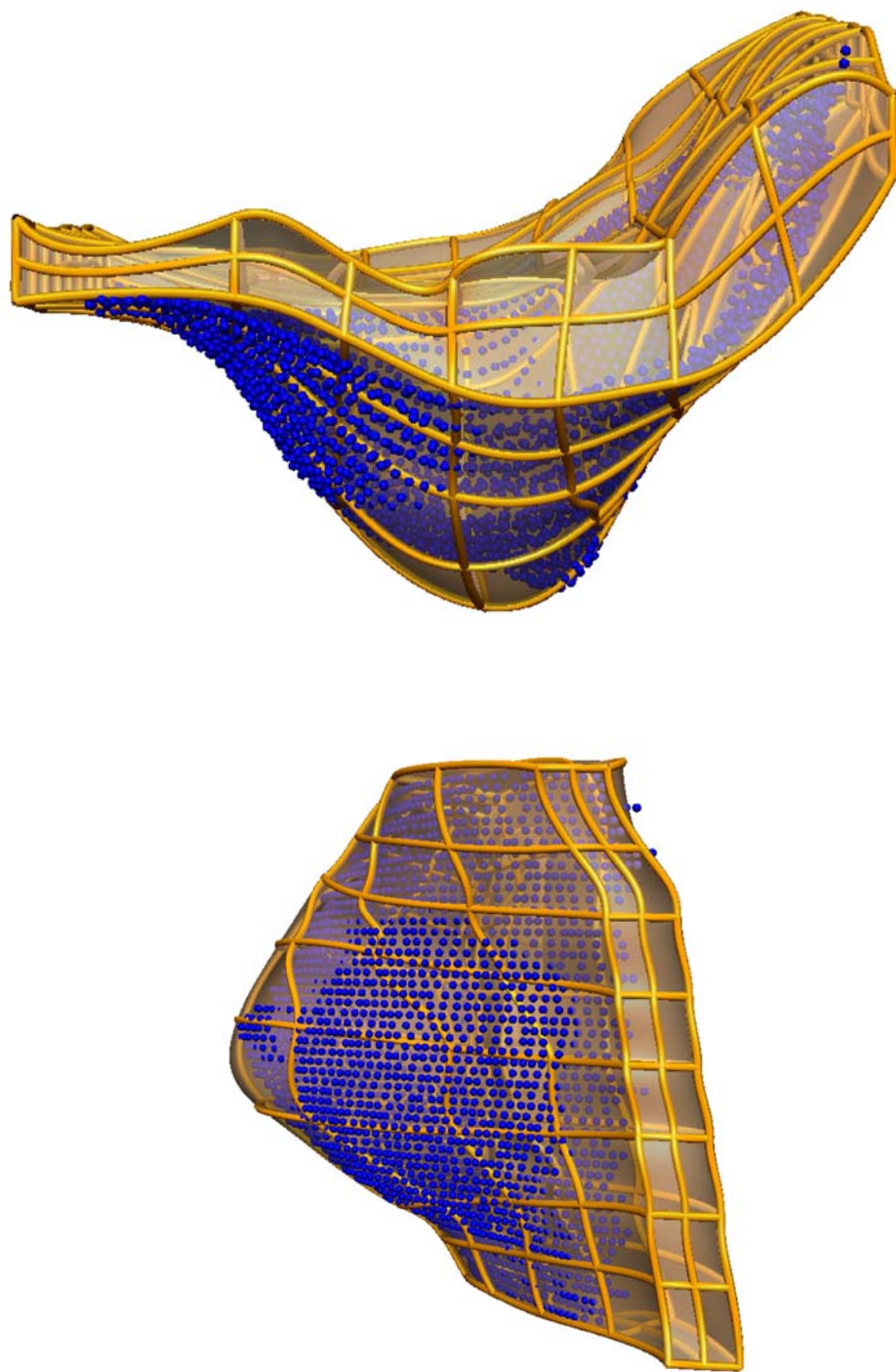


Figure 7.22: Comparison of model prediction (lines, surfaces) from computed reference configuration to experimental data (blue spheres) with volunteer arched downward in MR machine with an RMS error of 3.5 mm.

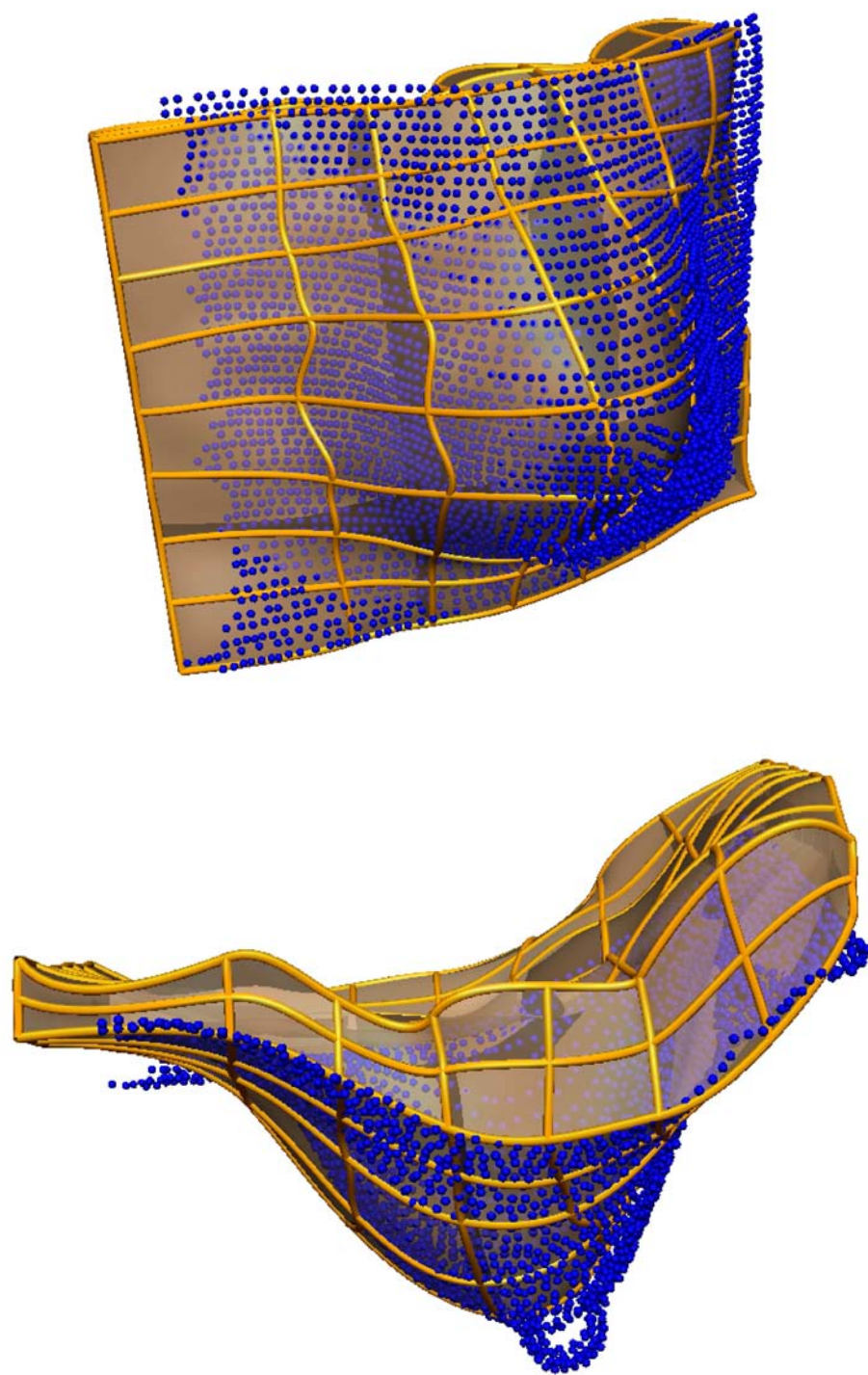


Figure 7.23: Comparison of model prediction (lines, surfaces) from computed reference configuration to experimental data (blue spheres) with volunteer oriented with the right shoulder down, with an RMS error of 4.7 mm.

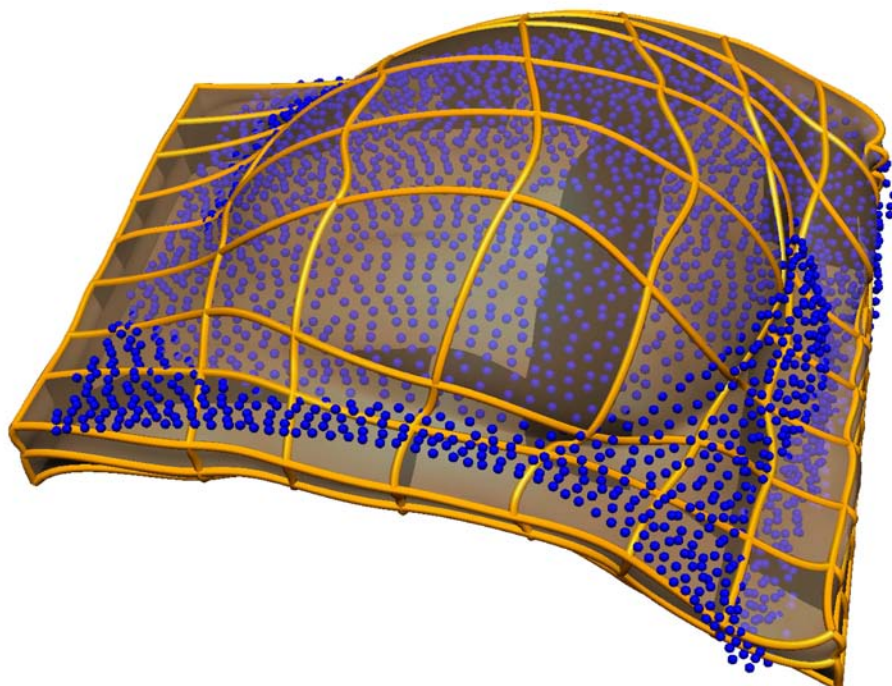


Figure 7.24: Comparison of model prediction (lines, surfaces) from computed reference configuration to experimental data (blue spheres) in supine position with an RMS error of 9.1 mm.

### 7.2.3 Using the prone gravity-loaded configuration

This study was conducted to determine the effect of using the prone gravity-loaded configuration as the reference state (rather than the neutral buoyancy configuration or the computed reference state) on the accuracy of predicting the four other gravity-loaded configurations.

The prone gravity-loaded model used in the previous section was subjected to the “head up” gravity load with the same kinematic boundary conditions that were used in Sections 7.2.1 and 7.2.2. The value of  $c_1$  in the neo-Hookean constitutive equation was chosen, with the objective of minimising the error in predicting breast deformation in the “head up” orientation. The accuracy of the model prediction was quantified by comparing the manually segmented head up configuration of the breast skin to the model predicted skin configuration. The segmented points were projected onto the deformed surface of the model, and an RMS error was calculated as explained in Section 3.3.1. The model predictions matched the experimental data best with the neo-Hookean material parameter  $c_1 = 50$  kPa, with an RMS error of 3.97 mm (shown in Fig 7.25 and 7.26). The model was also used to predict the deformations of the breast in the three other orientations for which images were obtained (shown in Fig. 7.27-7.29).

The figures illustrate that the model seemingly predicts the deformations of the breast in the “head up” and “head down” orientations more accurately than the deformations of the “right down” or supine deformations. This bias in accuracy is mainly because of determining the  $c_1$  value of the neo-Hookean constitutive relation using the “head up” deformed configuration. Note that the  $c_1$  value of 50 kPa in this study is very high compared to 0.08 kPa or 0.1 kPa in the previous two studies. This high stiffness restricts the model to predict very small displacements from the initial prone-gravity loaded reference configuration. The “head up” and “head down” configurations involve a smaller alteration (compared to the supine or “right down” configurations) in the way the volunteer is positioned in the MR scanner. Therefore, the predicted deformed configurations appear to capture the breast deformations in these two orientations with the same order of accuracy as the models in the previous two studies that used a neutral buoyancy configuration or a computed reference configuration as the reference state. However, the model predictions are clearly incorrect for the “right down” and supine configurations.

When comparing the supine configurations predicted in the three studies presented in this chapter (see Figs. 7.17, 7.24 and 7.29), it is clear that the supine configuration in this study is unrealistic. The same conclusion can be arrived at if the “right down” configurations are compared (see Figs. 7.16, 7.23 and 7.28). This indicates that the use of the prone gravity-loaded configuration introduces additional errors into model predictions and that a better estimate of the reference configuration than the prone gravity-loaded configuration is required for accurate prediction of breast deformation under a variety of gravity loading conditions.

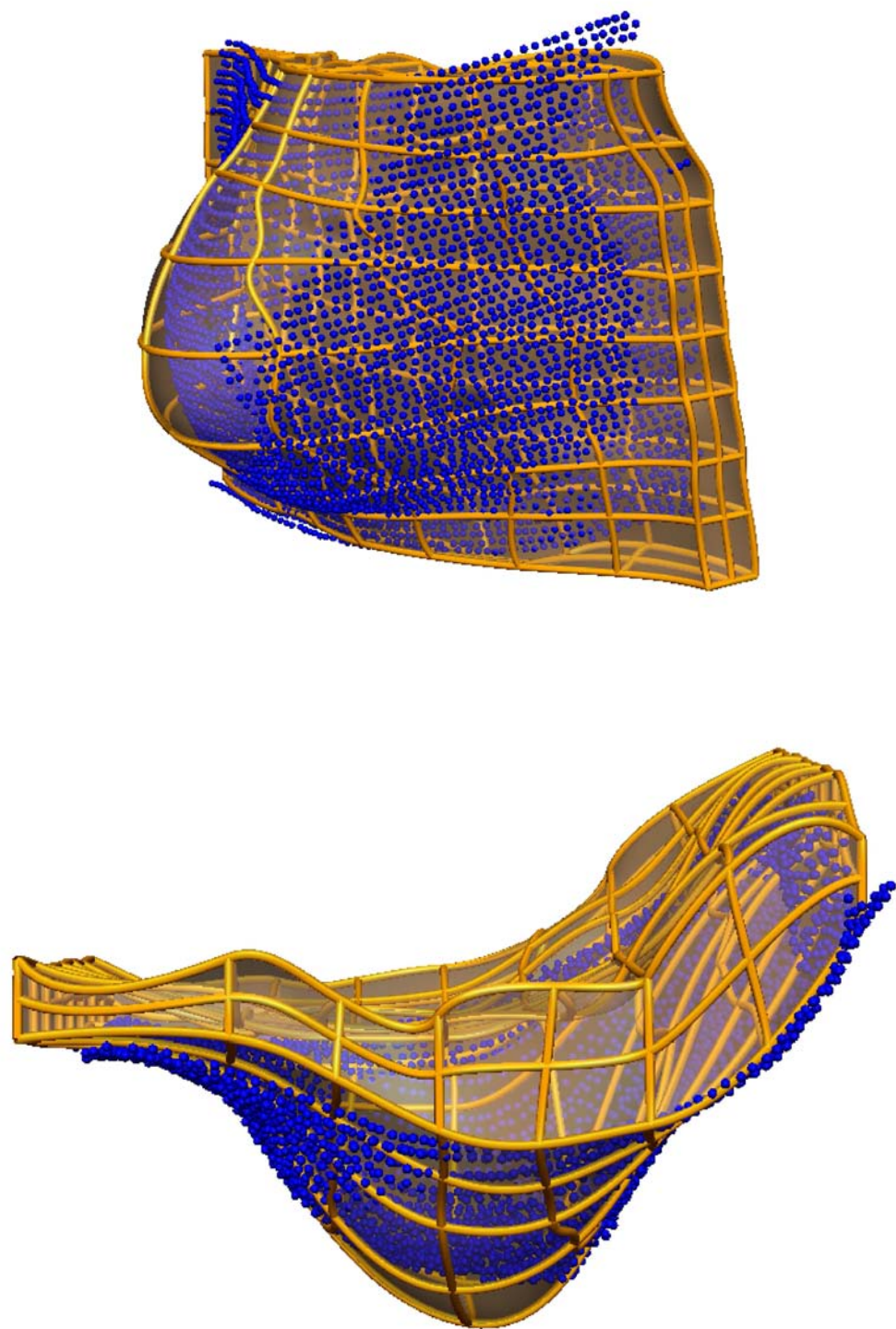


Figure 7.25: Comparison of model prediction (lines, surfaces) from the prone gravity-loaded configuration to experimental data (blue spheres) with volunteer in “head up” position in MR machine (blue spheres).

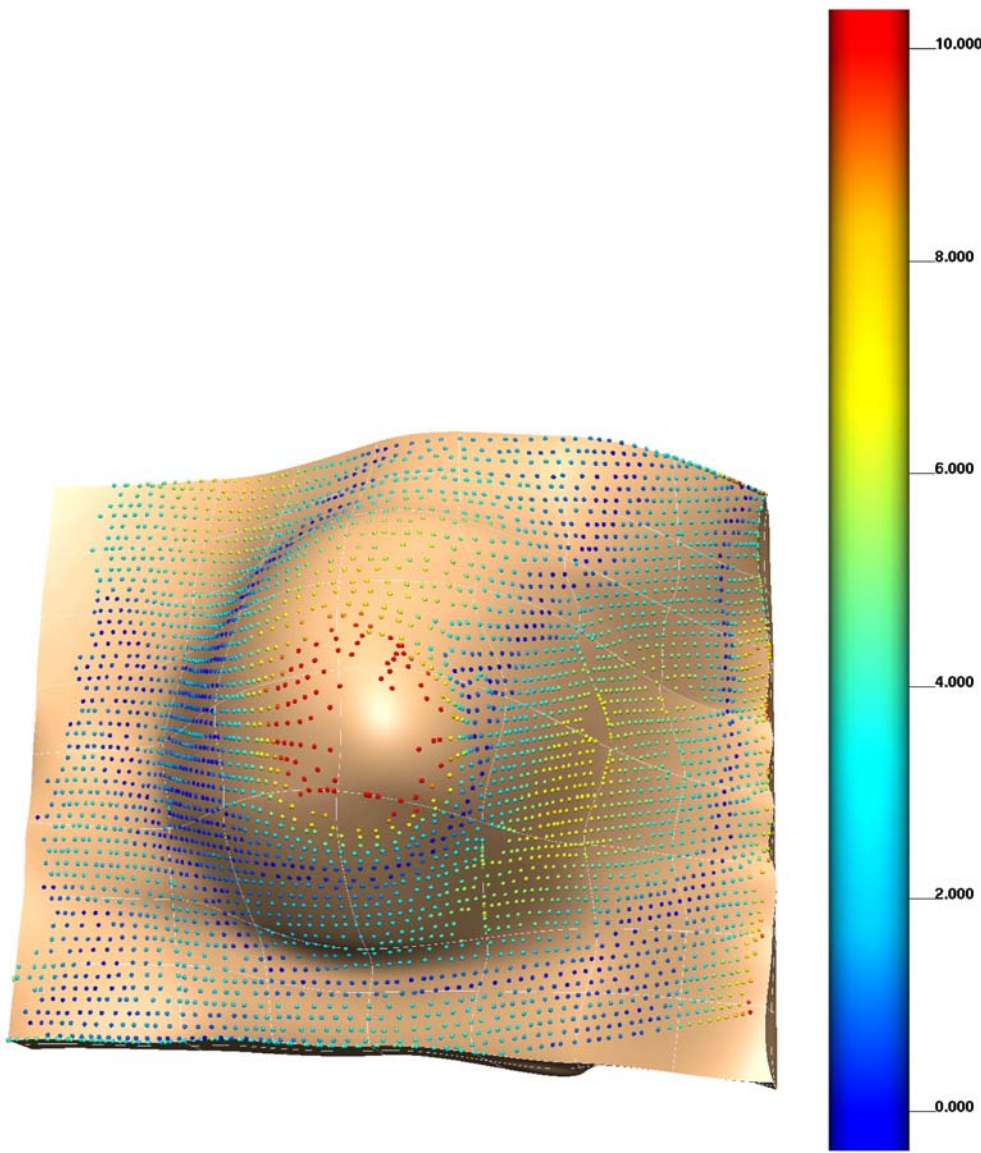


Figure 7.26: Comparison of model prediction (lines, surfaces) to experimental data (blue spheres) in the “head up” orientation with an RMS error of 3.97 mm. The spheres represent the skin surface data points obtained from the “head up” gravity loaded MR images with the colour map showing the individual error magnitude, in millimeters, associated with each data point.

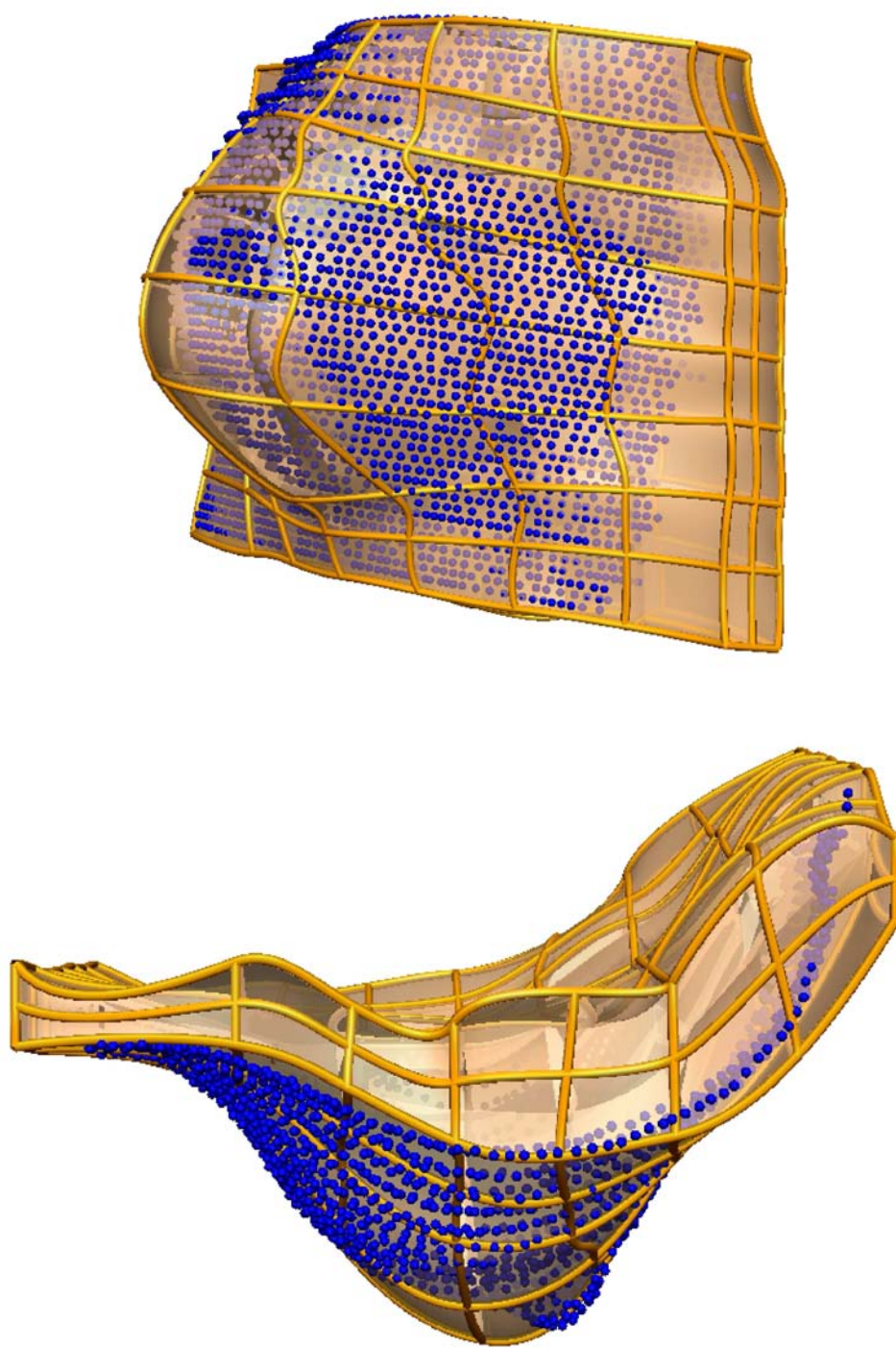


Figure 7.27: Comparison of model prediction (lines, surfaces) from the prone gravity-loaded configuration to experimental data (blue spheres) with volunteer arched downward in MR machine with an RMS error of 3.8 mm.

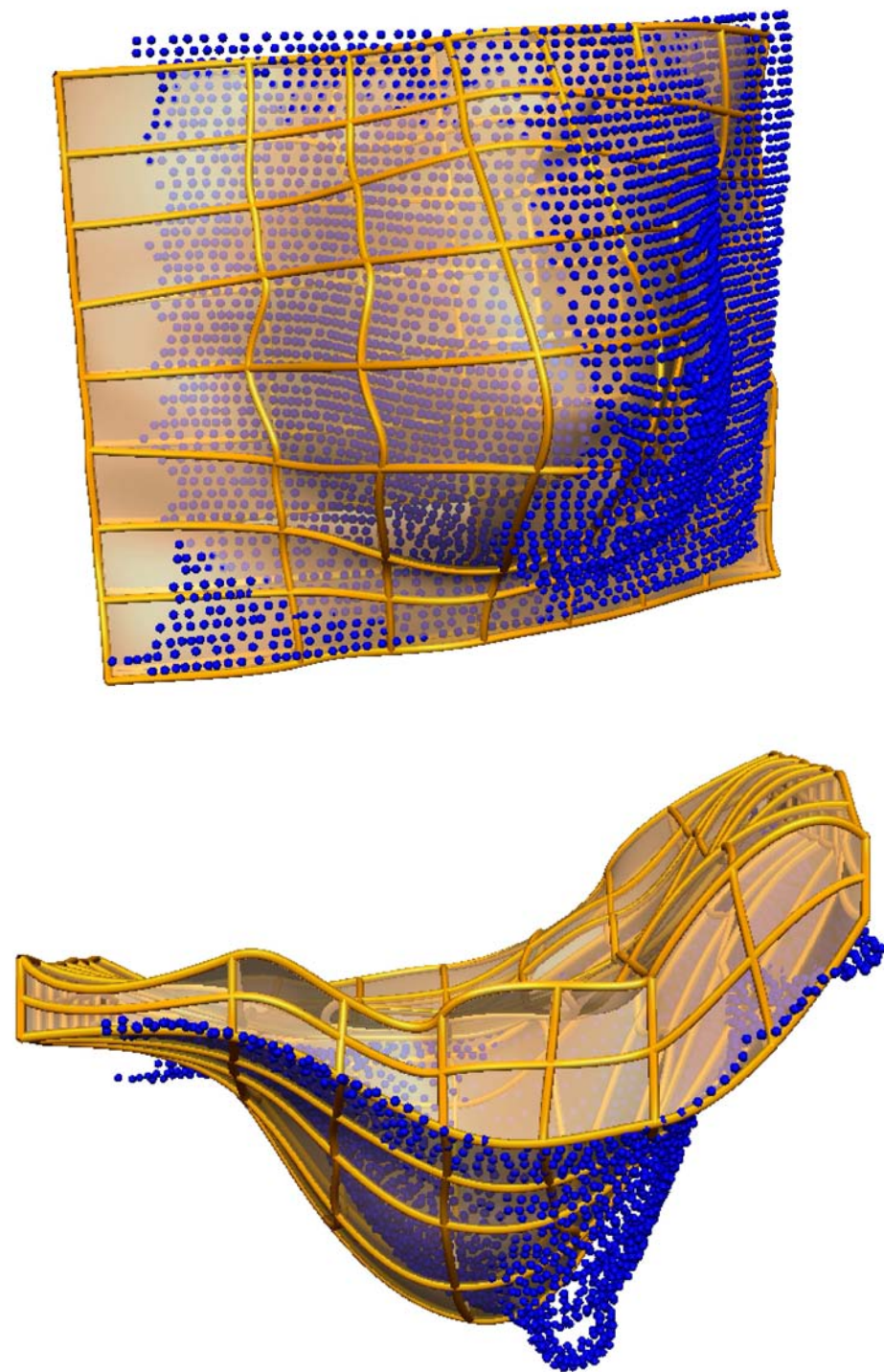


Figure 7.28: Comparison of model prediction (lines, surfaces) from the prone gravity-loaded configuration to experimental data (blue spheres) with volunteer oriented with the right shoulder down, with an RMS error of 6.5 mm.

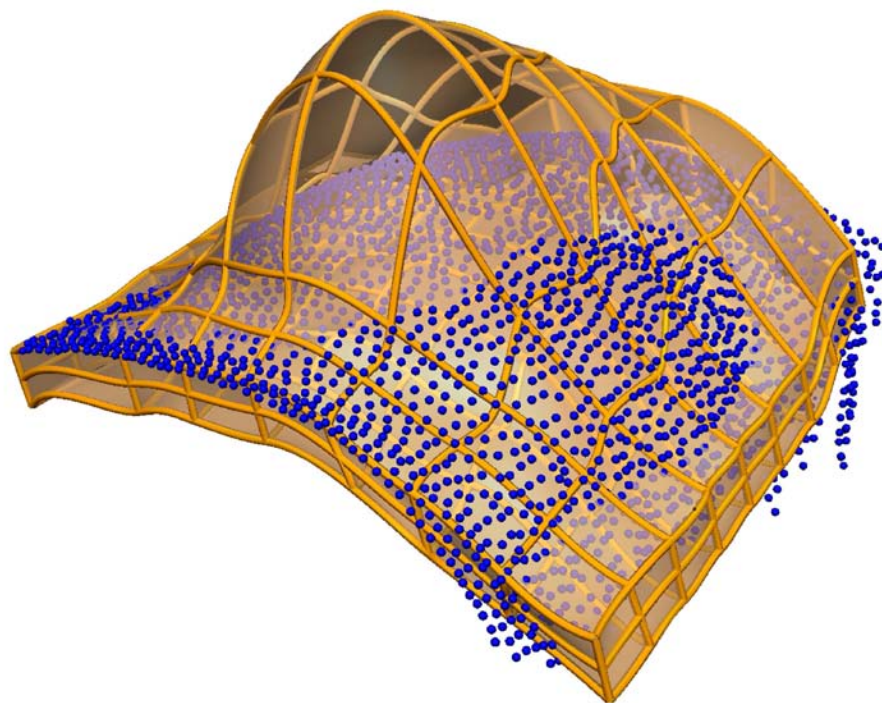


Figure 7.29: Comparison of model prediction (lines, surfaces) from the prone gravity-loaded configuration to experimental data (blue spheres) in supine position with an RMS error of 11.4 mm.

### 7.3 Discussion

The studies in this chapter have shown that a homogeneous model can reproduce gross deformation characteristics, however the models do not accurately reproduce regional deformations. The models that used the neutral buoyancy configuration or the computed reference configuration as the reference state performed better at predicting breast deformations than the model that used the prone gravity-loaded configuration as the reference state. This is particularly clear when comparing the supine configuration predictions. This indicates that an accurate representation of the reference configuration is important for model predictions, an aspect of breast modelling that has been overlooked by previous researchers.

However, these results are preliminary and a number of improvements need to be made to both the experimental and modelling frameworks for a robust validation of a computer model for predicting breast deformation. In terms of the model, possible sources of error are:

1. As each image set was obtained with the volunteer in a different orientation, image sets must be aligned to each other in a common coordinate system. In this chapter, the alignment method was rudimentary by matching the orientation of the sternum. Future studies should involve the acquisition of more rigid landmarks with the images and more advanced rigid-body registration techniques should be used.
2. The current model does not take into account the spatial distribution of fat and fibroglandular tissue, only describing the mechanical behaviour with one material parameter  $c_1$  in the homogeneous model. The accuracy of the computed reference configuration (obtained in Section 7.2.2) in predicting regional breast deformation in the “head up” orientation may possibly be improved by introducing heterogeneity into the model.
3. It is not clear as to how the breast tissue is attached to the chest and pectoral muscles. Thus, the validity of applying fixed displacement boundary conditions at the chest nodes in the model must be tested.

Apart from improving the model, there is further room for improvement in the experimental aspects of this study.

1. While acquiring the neutral buoyancy images, it became clear that further improvements need to be made to the design of the container. The profile of the cylinder opening needs to be re-designed to ensure better contact between cylinder and torso. A future design should also minimise the height of the cylinder as the current design reduced the amount of space available for positioning the volunteer comfortably in the MRI machine.
2. Fig. 7.7 shows that the breast was not fully immersed in water. Full immersion will be important for a better representation of the reference state of the breast, as the breast is partially under gravity loading in the current image set. This drawback was once again due to the lack of full contact between breast and cylinder, and an improved design that takes this into account will solve the problem of partial submersion.
3. One disadvantage of using the polystyrene boards was the tendency for parts of the body to stick to the polystyrene. The volunteer also experienced some discomfort as the imaging progressed, as the support near the breast hole was not strong enough and not ergonomic. The skin in contact with the board had a tendency to stretch over time as there was still small movement due to breathing.
4. The wedging of the cylinder (as in Fig. 7.6(a)) and repositioning of the patient meant that prone and neutral buoyancy image sets could not be directly compared without an alignment step. This is difficult when there are very few landmarks present. Vitamin tablets that were placed on the breast melted in the warm water during neutral buoyancy imaging. Holes, sealed with rubber bungs, have now been drilled out of the cylinder to provide a drainage system. Therefore, once a neutral buoyancy image set is acquired, the water can be drained out of the holes to obtain a prone image set while the volunteer is lying in the same position as the neutral buoyancy case.
5. Due to the size of the cylinder and the size of the water catchment container, it was difficult to position the volunteer such that one breast could be imaged in the prone gravity loaded position and the other could be imaged in neutral buoyancy. The lip of the water catchment container rubbed against the prone

breast, and therefore, future developments should ensure that nothing is in contact with this breast.

With these improvements taken into account, future validation experiments will provide more conclusive answers regarding the accuracy of the modelling framework in predicting breast deformations.

## 7.4 Conclusions

This chapter addressed the following questions:

- **Can the breast under neutral buoyancy conditions be considered as a representation of the reference configuration for predicting large deformations under gravity loading conditions?**
- **What errors are introduced if the prone gravity-loaded configuration is used as the reference state?**
- **Is a homogeneous model sufficient for the prediction of breast deformation under gravity loading conditions?**

A new experimental plan was developed to acquire images of the breast in gravity loading and neutral buoyancy conditions. A homogeneous model of the breast of a volunteer was created using prone gravity-loaded and neutral buoyancy images. Preliminary results of simulations indicate that a homogeneous model does not accurately predict regional breast deformation. The results also indicated that an accurate representation of the reference configuration is necessary for accurate model predictions. However, the results did show promise in the performance of the modelling framework since gross features of the breast shape observed in the clinical images were also observed in the model. Additional improvements to the model will improve the accuracy of the model in providing predictions of breast deformations that are useful for the clinical setting.

# **Part IV**

## **Thesis Review**



# **Chapter 8**

## **Conclusions and Future Work**

The overarching aim of the breast biomechanics modelling research project is to develop a software tool that helps clinicians align points within the breast across multiple imaging modalities. This thesis focussed on the development of anatomically realistic finite element models of breast deformation under gravity loading conditions. These predictions are of potential use in the clinical setting for tracking internal tissue movement between MR imaging procedures (where the patient is oriented in the prone position) and biopsies (where the patient is oriented in the supine position).

This thesis adopted a systematic approach to develop a biomechanical model of the breast. Attention was firstly given to develop experiments on silicon gel phantoms in order to validate individual modelling techniques that make up the modelling framework, and secondly to develop an experimental plan on breasts of volunteers to validate the models for use in the clinical setting.

The experimental data from both sets of experiments are important contributions of this thesis to the field of breast biomechanics. The data were used to address specific questions, which are summarised here in the order they were presented in this thesis.

### **8.1 Silicon Gel Studies**

Experiments were first conducted on homogeneous silicon gel phantoms. Chapter 3 showed that a finite element model of a homogeneous body can reliably predict

surface deformations with an average RMS error of  $1.5 \text{ mm} \pm 0.2 \text{ mm}$ , and track internal marker locations with an average error of  $1.4 \text{ mm} \pm 0.7 \text{ mm}$ . A novel technique known as the reverse method was then developed and implemented in the modelling framework to be able to answer this question (see Chapter 4). The validation experiment showed that a finite element model of a homogeneous body can reliably predict the reference configuration surface with an average RMS error of  $1.3 \text{ mm} \pm 0.1 \text{ mm}$ , and track internal marker locations to the reference state with an average error of  $1.5 \text{ mm} \pm 0.8 \text{ mm}$ .

Experiments were then conducted on two-part composite phantoms to quantify the accuracy of the modelling framework in prediction deformations of heterogeneous bodies (see Chapter 5). However, the results indicated that the standard technique of modelling heterogeneity (assigning elements with different mechanical properties to represent the different tissues they contain) needs further validation and possible improvement. The current hypothesis is that at the interface between two different types of materials, the model should enforce strain continuity in-plane, but allow for discontinuity through the plane, moving from one tissue type to another. However, with current techniques, trilinear elements do not enforce any strain continuity in any direction and tricubic-Hermite elements enforce continuity in all directions.

## 8.2 Clinical Studies

These studies first focussed on developing an efficient way of accurately representing the breast shape of an individual. A new algorithm has been developed to rapidly create individual specific finite element geometries of the breast with an average RMS error of  $1.46 \text{ mm} \pm 0.32 \text{ mm}$  in representing skin, and an average RMS error of  $1.52 \text{ mm} \pm 0.3 \text{ mm}$  in representing muscle.

This semi-automatic algorithm was then used with neutral buoyancy breast images and a variety of gravity loaded breast images of a volunteer, previously unavailable, to determine the best estimate of the reference configuration of the breast. The validity of using a homogeneous model to predict breast deformations was also investigated. Results indicated that a homogeneous model is insufficient to accurately predict breast deformation under gravity loading. The results also indicated that using the prone gravity-loaded configuration as the reference state (as done by

previous studies in the literature (Ruiter et al., 2003; Azar et al., 2000; Yu-Neifert, 1995)) introduced additional errors compared to using the neutral buoyancy configurations or the theoretically computed reference state. This indicated that the identification of an accurate representation of the reference configuration for reliable predictions of breast deformations under gravity loading should not be overlooked in future studies. It was encouraging, however, that the homogeneous model was able to predict the gross shape of the breast in the different gravity loading conditions when using the neutral buoyancy configuration as a reference state, and when using the theoretical reference state (computed using the reverse method). These results indicate that further investigation is warranted to consider the use of breast biomechanical models in tracking internal tissue movement across multiple imaging modalities.

### 8.3 Future Work

This thesis has highlighted a number of important avenues of research, which should be pursued to achieve the overarching aim.

- The validation of techniques to model heterogeneity using silicon gel composites is of immediate importance due to its necessity for modelling heterogeneities in the breast. The techniques must be validated for a variety of loading conditions to ensure that they are robust and reliable for the wider field of biomechanics modelling.
- The silicon gel studies validated the modelling framework by tracking the movement of small plastic rods in the gel, across different gravity loaded configurations. A more robust method of validation could involve cross correlation techniques to track smaller particles than those used in this thesis (the rods are approximately 2 mm in length and radius). Development of a cross-correlation measure of error could also be very useful in validating the modelling framework in predicting breast deformation. Malcolm et al. (2002) illustrates the use of such a technique in tracking speckle patterns on the surface of a deforming membrane.

- As indicated in Chapter 6, the breast tissues were manually segmented from breast MR images for generating individual specific finite element geometries. A completely automated mesh generation procedure is possible, provided that more image processing techniques are used to segment the different tissue types. The procedure should also ensure that volumes are not distorted by using positive-volume-preserving constraints. The image processing techniques could also be used to align the different image sets of the breast to a common coordinate system. This is necessary as each image set is obtained with the volunteer in a different orientation (as discussed in Chapter 7).
- The silicon gel experiments provided control over the types of boundary conditions that needed to be applied to test specific aspects of the modelling framework. However, the nature of the boundary loads in the breast are unknown. Imaging studies must be conducted to first determine the characteristics of the interface between the pectoral muscles and the internal breast tissues. These studies should then be coupled with silicon gel phantom studies to determine the best way to model the breast near the chest wall.
- More focus should be given to the characterisation of mechanical properties of breast tissues. As discussed in Appendix F, very few studies have been conducted to characterise the mechanical properties of the breast in-vivo under a wide range of strains and loading conditions. Chapter 7 indicated at a possible method of obtaining material parameters of internal breast tissue by optimising for the neo-Hookean material parameter value using different gravity loaded configurations of the breast. Additional work must be conducted to determine the viability of this approach in characterising mechanical properties of breast tissues for each individual.
- Research must also be conducted towards the final goal, by developing and validating non-rigid registration algorithms that incorporate the finite element model to ensure that only physically plausible configurations are considered.

## 8.4 List of Publications

A list of publications that have been presented in journal articles and conference proceedings, related to the work conducted in this thesis, are shown below.

### Articles

- **V Rajagopal**, J H Chung, D P Bullivant, P M F Nielsen and M P Nash, Finite elasticity: determining the reference state from a loaded configuration, *Intl. J. for Numerical Methods in Engng* (under second review) 2007
- **Vijay Rajagopal**, Jae-Hoon Chung, Ruth Warren, Ralph Highnam, Martyn Nash, Poul Nielsen. Finite Element Modelling of Breast Biomechanics: Predicting the Effects of Gravity. In *MICCAI 2006 Workshop on Computational Biomechanics for Medicine*.
- Jae-Hoon Chung, **Vijay Rajagopal**, Poul Nielsen, Martyn Nash. A Biomechanical Model of Mammographic Compressions, Biomechanics and Modelling in Mechanobiology (in press) 2006.
- Jae-Hoon Chung, **Vijay Rajagopal**, Poul Nielsen, and Martyn P Nash. Computational modelling of the breast during mammography for tumor tracking. In *SPIE Medical Imaging 2005*, vol 5746, pages 817-824, Feb 2005.
- Pras Pathmanathan, David Gavaghan, Jon Whiteley, Mike Brady, Martyn P Nash, Poul M F Nielsen, and **Vijayaraghavan Rajagopal**. Predicting tumour location by simulating large deformations of the breast using a 3D finite element model and nonlinear elasticity. In *Lecture Notes in Computer Science*, vol 3217, pages 217 - 224, Sep 2004. *Medical Image Computing and Computer Assisted Intervention*.

### Abstracts

- **Vijayaraghavan Rajagopal**, Poul M F Nielsen, and Martyn P Nash. Finite Element Modelling of Breast Biomechanics: Directly Calculating the Reference State. In the *28<sup>th</sup> Annual International Conference of the IEEE Engineering in Medicine and Biology Society*, New York, U.S.A, Aug 2006.

- **V Rajagopal**, Y Kvistedal, J Chung, M P Nash, P M F Nielsen. Modelling the Skin-Breast Tissue Interface. In the 5<sup>th</sup> World Congress of Biomechanics, Munich, Germany, July 2006
- **V Rajagopal**, Y Kvistedal, J Chung, M P Nash, P M F Nielsen. Coupling skin to internal breast tissue for finite element modelling of breast biomechanics. In the 3<sup>rd</sup> European Medical and Biological Engineering Conference, Prague, Czech Republic, Nov 2005
- **Vijayaraghavan Rajagopal**, Jae-Hoon Chung, Martyn P Nash, and Poul M F Nielsen. Finite element modelling of breast biomechanics: Finding a reference state. In the 27<sup>th</sup> Annual International Conference of the IEEE Engineering in Medicine and Biology Society, Shanghai, China, Sep 2005
- **Vijayaraghavan Rajagopal**, Poul M F Nielsen, and Martyn P Nash. Development of a three-dimensional finite element model of breast mechanics. In the 26<sup>th</sup> Annual International Conference of the IEEE Engineering in Medicine and Biology Society, San Francisco, U.S.A, Sep 2004.
- Jae-Hoon Chung, **Vijay Rajagopal**, Poul Nielsen, and Martyn P Nash. Computational modelling of the breast under mammographic compression for tumour tracking. In Industrial Mathematics Initiative 2004, Daejong, South Korea, Aug 2004.
- Jae-Hoon Chung, **Vijay Rajagopal**, Poul Nielsen, and Martyn P Nash. Finite element model of breast compression during mammography. In Canadian Medical and Biological Engineering Society 2004, Quebec, Canada, Sep 2004.
- Jae-Hoon Chung, **Vijayaraghavan Rajagopal**, Poul M F Nielsen, and Martyn P Nash. Modelling mammographic compression of the breast with applications to tumour tracking. In New Zealand Biomedical and Medical Societies Conference, Queenstown, NZ, Nov 2004.
- **Vijay Rajagopal**, Poul M F Nielsen, and Martyn P Nash. A 3d finite element model of the breast to study breast cancer. In WC2003 World Congress on Medical Physics and Biomedical Engineering, Sydney, Australia, Aug 2003.

# **Part V**

## **Appendices**



# **Appendix A**

## **Phantom Mould Design**

This appendix consists of the designs of the components of the silicon gel phantom mould described in Chapter 3. The materials used for each part and their quantities are given with each draft drawing sheet. The dimensions are all in millimeters.

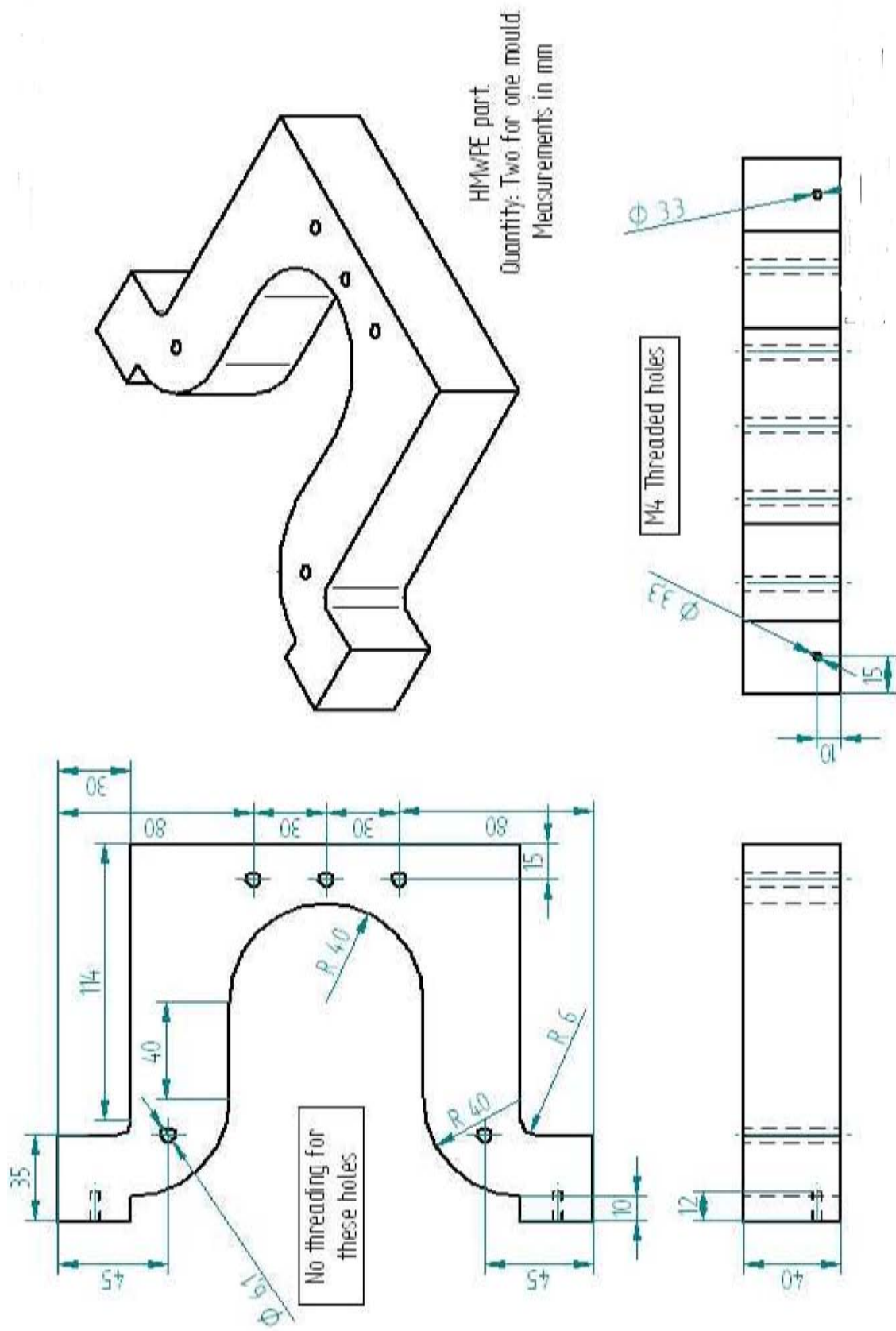


Figure A.1: Draft view of mould created for phantom studies

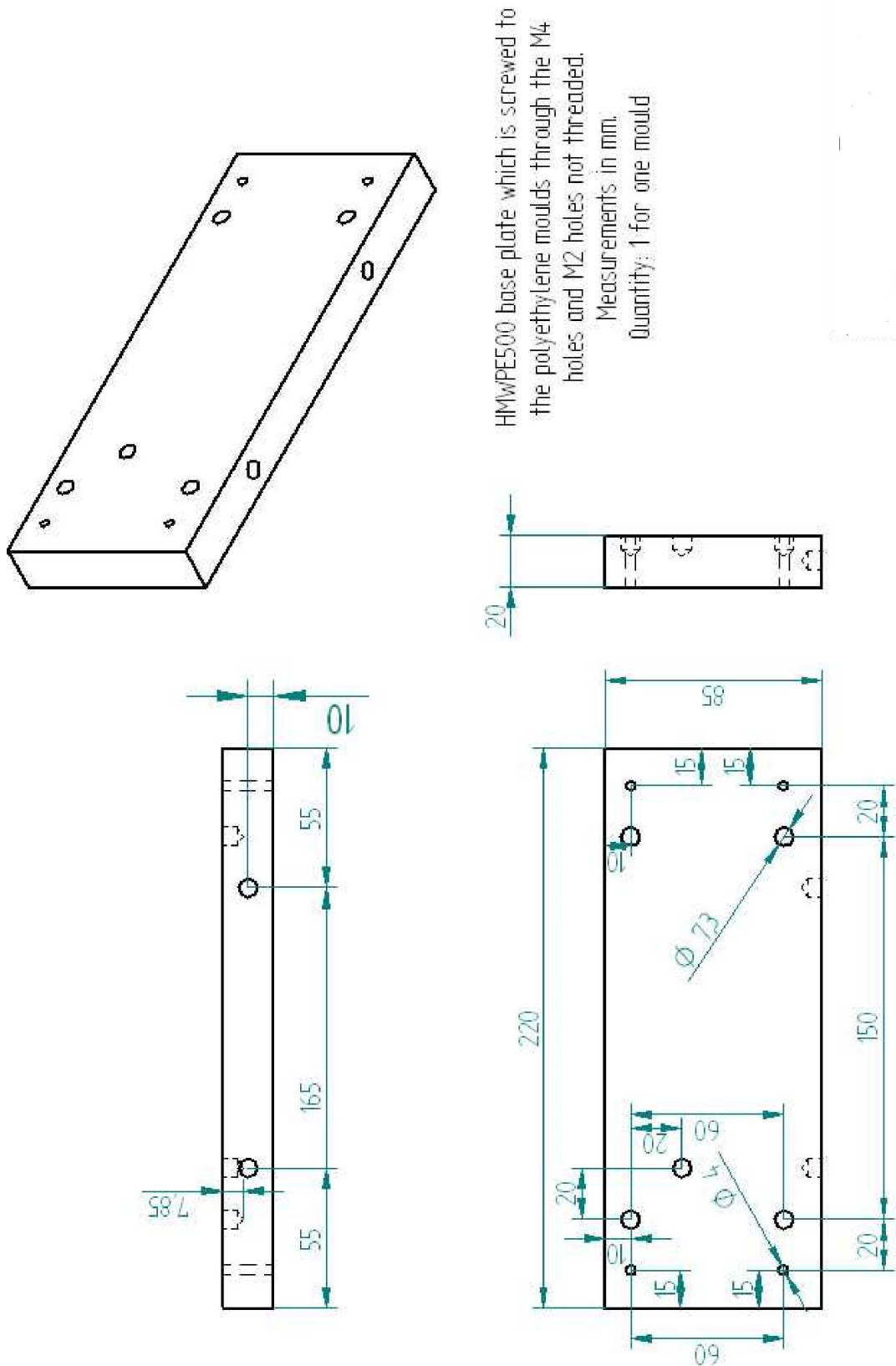


Figure A.2: Base plate of mould

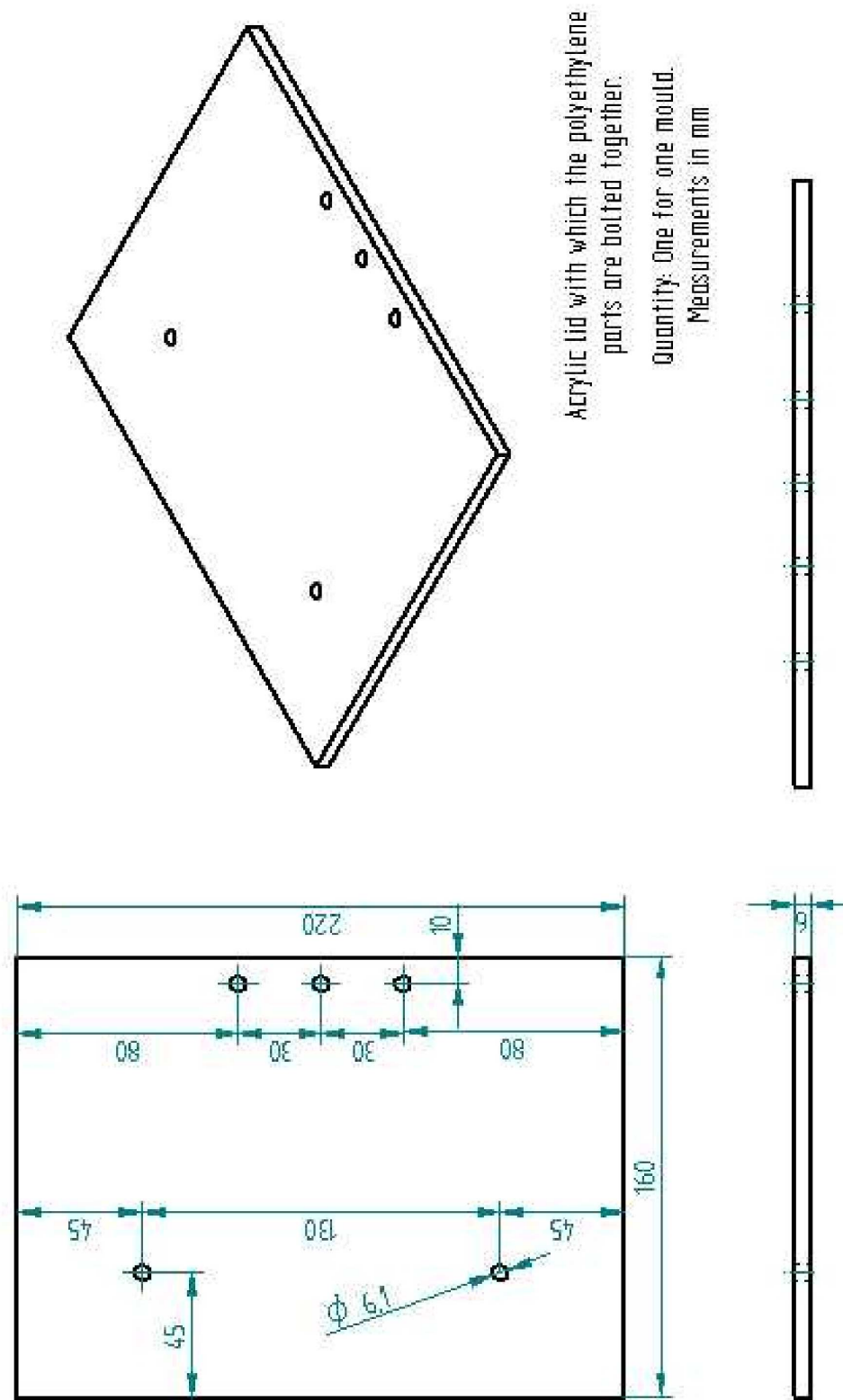


Figure A.3: Bottom lid of mould

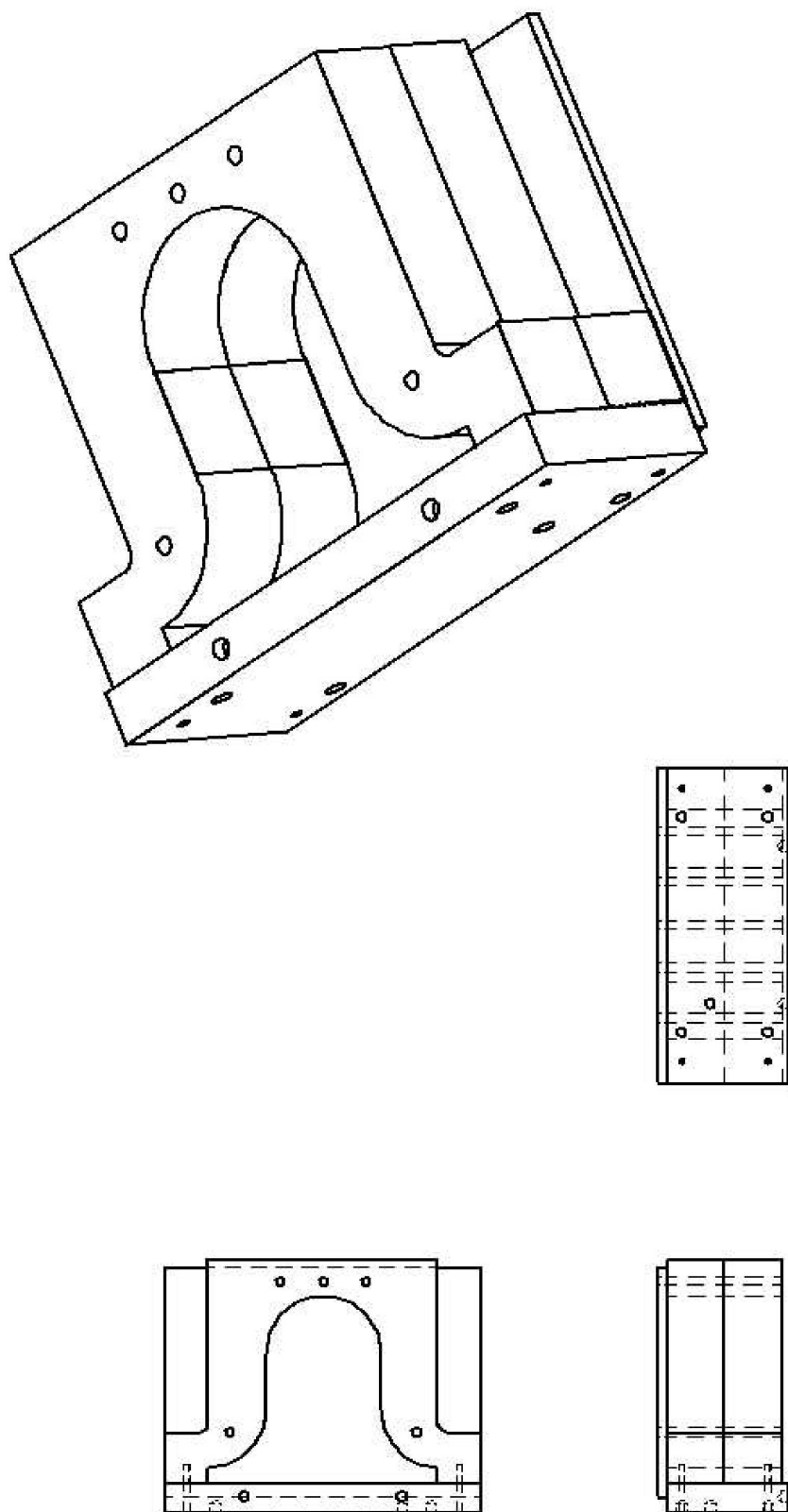


Figure A.4: Assembly of the parts into the mould



# Appendix B

## Model Validation Using X-Ray Images

Before quantifying the error of the modelling framework in predicting the deformations of the homogeneous gel using MR images in Chapter 3, x-ray imaging was used to validate the modelling framework. However, the results produced large errors in model predictions. Nevertheless, the study emphasises the importance of silicon gel phantom studies in identifying sources of error, and therefore is described in this appendix.

### B.1 Methods

Two internal markers were created in a silicon gel phantom by injecting a radio-opaque substance (Gastrograffin), which is visible under x-ray imaging. This was done while the gel was still in the mould, and the mould and gel were x-rayed to obtain the internal marker positions in the undeformed state. The gel was taken out of the mould and oriented at different angles (Table B.1) to the direction of gravity. These different gravity loaded deformed states were laser scanned to record the deformed surface configurations (five different deformed states were obtained). The gel was also x-rayed in two of these orientations (30 SI and Supine) to obtain the deformed locations of the internal markers. Three ball bearings were glued to the posterior plate on which the gel was fixed to provide a system of global coordinates to which the internal marker locations could be referred.

### B.1.1 X-Ray Distortion and Biplane Registration

X-ray images contain geometric image distortions such as pincushion distortions, and S-shaped warping (Onnasch & Prause, 1992). Pincushion distortions occur from the mapping of the electrons from the curved input screen of the image intensifier to the flat output screen. The mapping causes larger object magnification at the periphery of the image than at the center, resulting in the pincushion effect. Spiral distortions occur due to the magnetic field component parallel to the image intensifier affecting the radial electron velocity in the image intensifier which causes the rotation of the image. Translation of the image occurs when the transversal magnetic field component acts on the longitudinal electron velocity. Therefore, it is necessary to remove these distortion effects by determining an undistortion transformation matrix based on distortions on a grid. A clear perspex grid was imaged under the x-ray machine used for this study and figure (B.1) shows that there is virtually no distortion effect visible on the x-ray image. Therefore, no distortion correction was needed for the validation study.

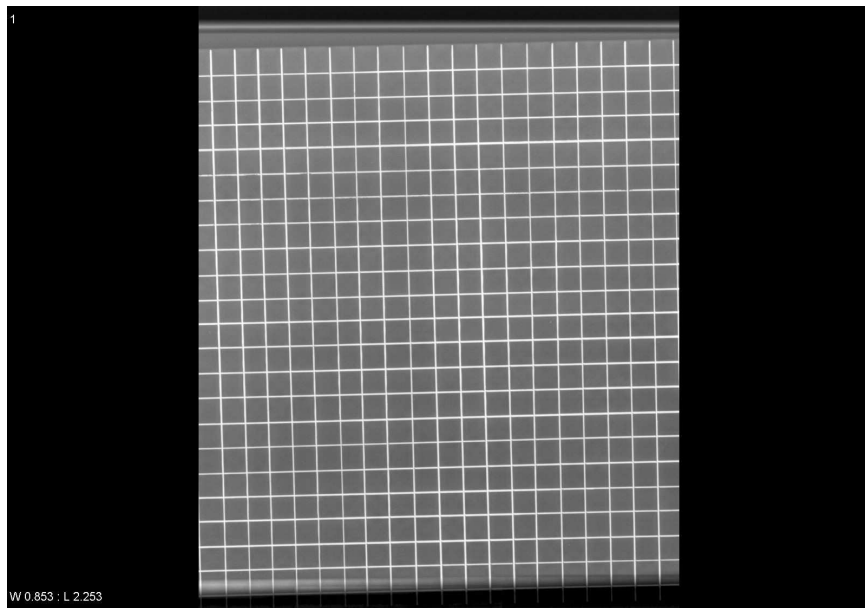


Figure B.1: X-ray image of a acrylic grid. No distortion visible

Two x-ray images were needed (biplane) to determine the three-dimensional location of the internal markers in the gel phantom. To perform biplane registration,

a perspex phantom consisting of 48 lead spheres glued to its surface was imaged from two orthogonal views (forty five degrees to the left and right from center) (Fig. B.2) (Cheng et al., 2005). These stereo-graphic views and true coordinates obtained using the FARO arm, were then used to reconstruct the three-dimensional coordinates of the spheres and a calibration matrix that can be used to reconstruct the three-dimensional coordinates of the internal markers in the gel phantom using bi-plane images of the gel taken in the same manner as for the perspex phantom. The registration work is based on the epipolar geometric technique reviewed by Zhang (1998).

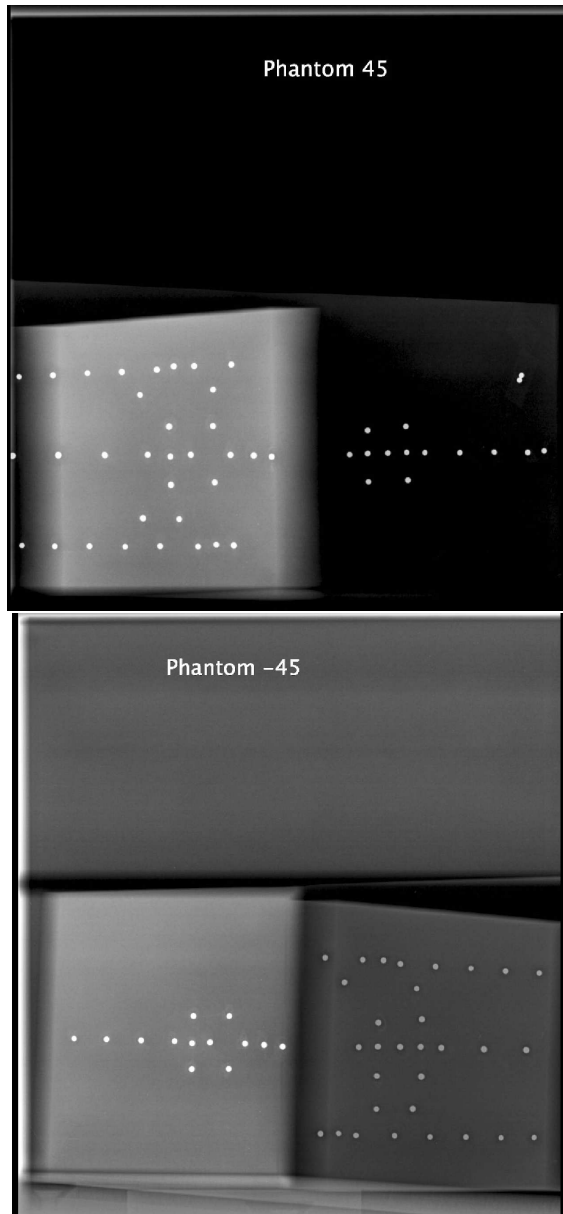


Figure B.2: Acrylic phantom and its x-ray images taken from orthogonal views.

## B.2 Results

The material parameter,  $c_1$ , in the neo-Hookean strain energy function, was found to be 1.38 kPa. The supine deformation and 30 degree supero-inferior (30 SI) deformation were x-rayed (Fig. B.3) to record the location of the internal markers in the deformed states. The locations of two internal markers were recorded and compared to the predicted locations of the model. The errors in tracking the internal markers and surface deformations are given in Table (B.1). Visual representations of the errors in tracking the markers and surface deformations for the supine deformation are given in Figs. B.4 and B.5, respectively.

Deformation	10 ML	20 ML	20 SI	30 SI	Supine
Surface RMSE	0.86 mm	0.67 mm	0.92 mm	0.92 mm	0.75 mm
Int. Mk. 1 RMSE				2.8 mm	3.1 mm
Int. Mk. 2 RMSE				3.1 mm	3.4 mm

Table B.1: Root-mean-squared errors (RMSE) in tracking surface deformations and Euclidean distance between predicted and measured internal marker (Int. Mk.) positions for a silicon gel phantom imaged using x-ray. ML: medio-lateral tilt (degrees), SI: supero-inferior tilt (degrees).

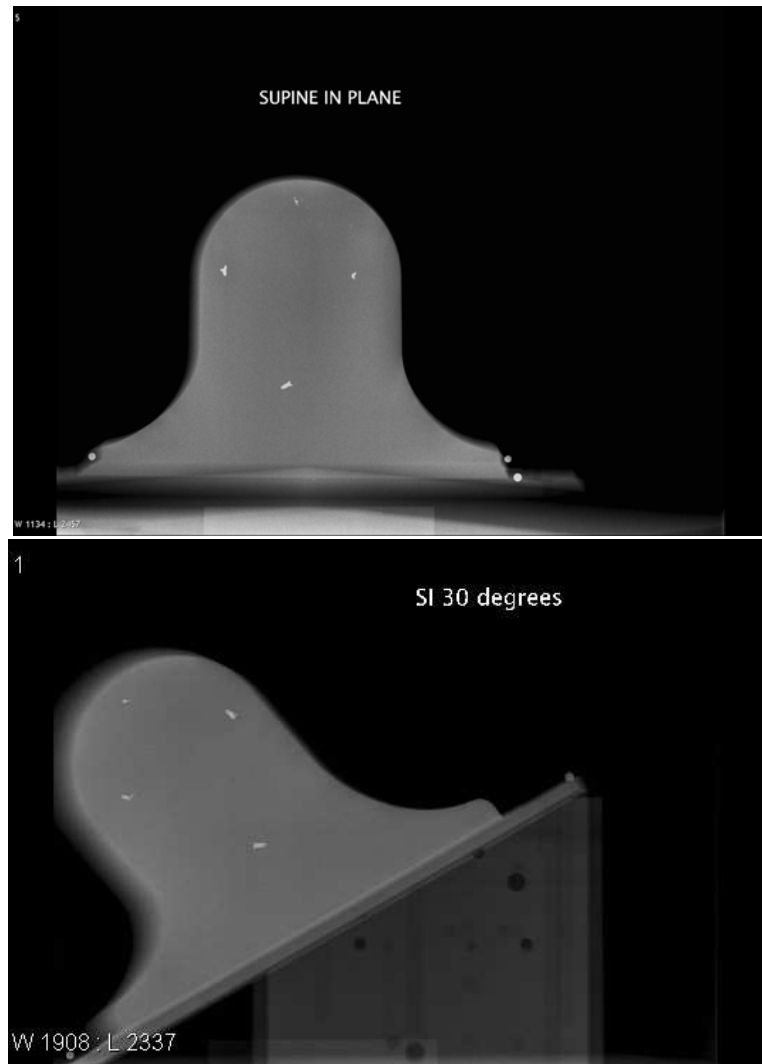


Figure B.3: X-ray images of the gel phantom used to measure internal marker tracking errors. White spots in the x-ray images represent Gastrograffin markers inside the gel.

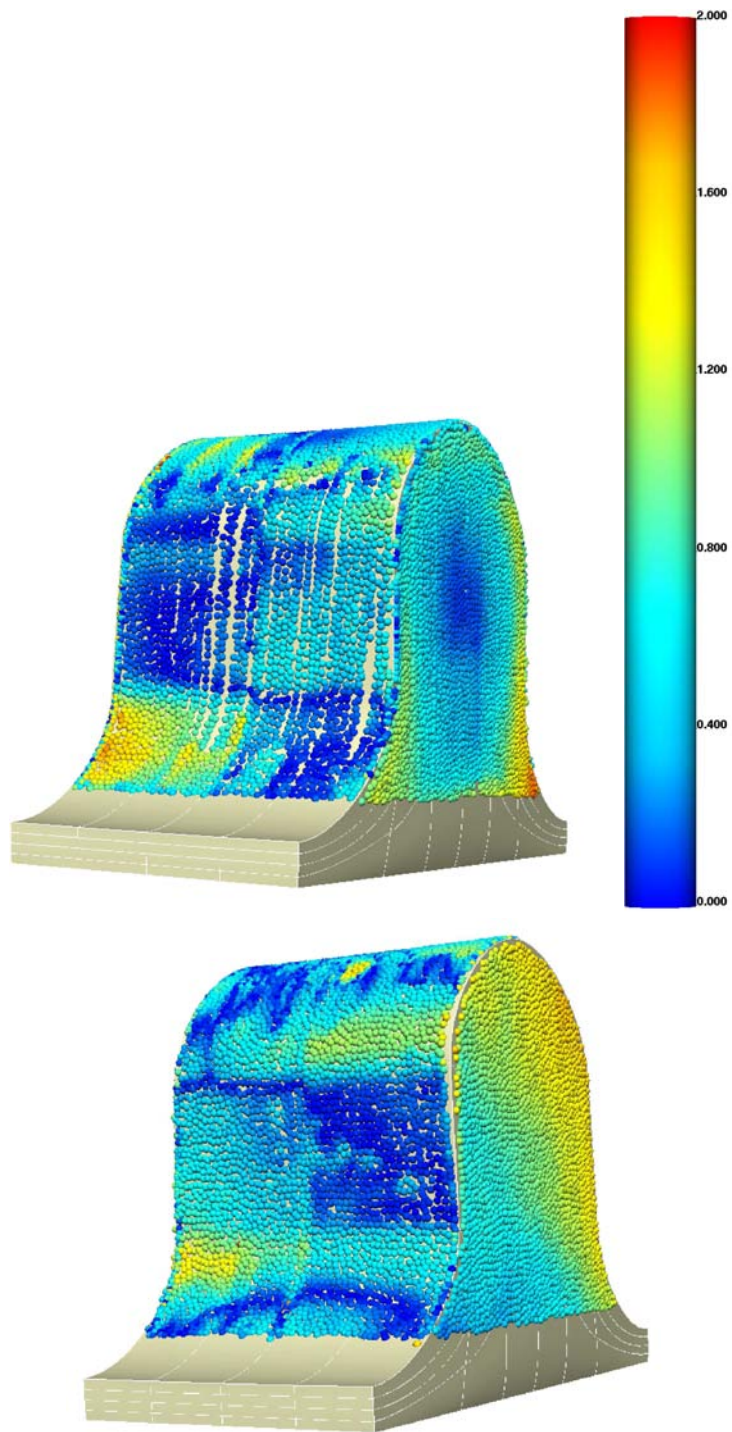


Figure B.4: Visual representation of surface deformation matching accuracy in the supine configuration with an RMS error of 0.75 mm. The spheres represent the surface data points obtained using the laser scanner with the colour map showing the individual error magnitude, in millimeters, associated with each data point.

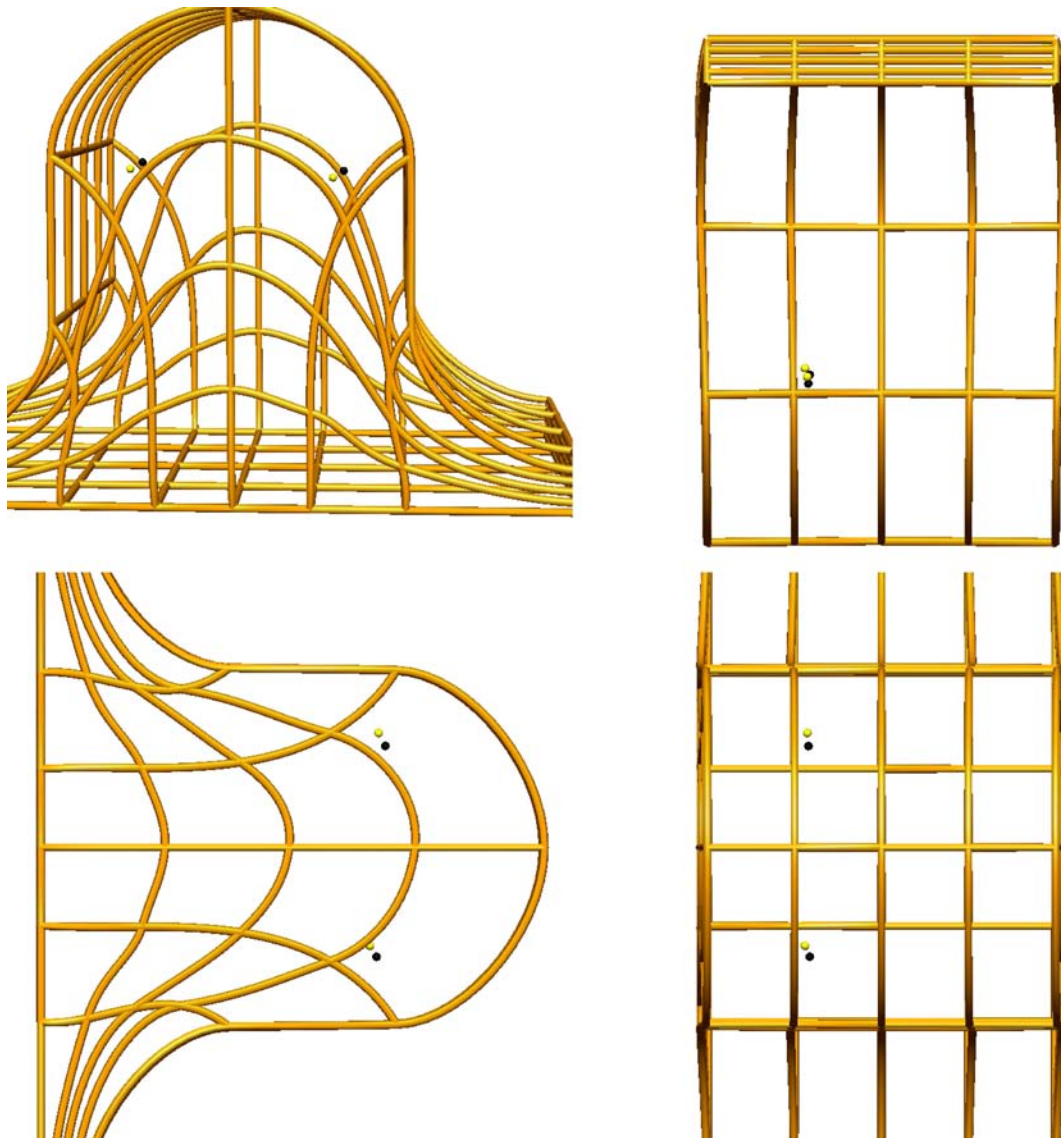


Figure B.5: Visual representation of the internal marker tracking accuracy for the supine deformation. The yellow spheres represent actual locations and the black spheres represent predicted locations of the internal markers.

### B.3 Discussion

The validation study is a well-controlled method of determining sources of error in a model prediction. The relatively high internal marker tracking error using x-ray images could be an accumulated result of a number of sources of error. The reconstructed location of the ball bearings on the posterior plate had an estimated error of 2 mm. The gel's homogeneity and small error in matching surface deformations also made it difficult to interpret the amount of error that the model contributed. This study implied that the three-dimensional coordinate reconstruction had a critical impact on internal marker location prediction. MR imaging eliminates issues of distortion effects present in x-ray images. In future studies, improvements will be made in three-dimensional localisation of internal markers during the x-ray imaging experiments. It should be noted that this study provides an important example of how it is possible to identify sources of error in model predictions by matching surface deformations and tracking internal marker locations using silicon gel phantoms, for which all model parameters are well determined.



# Appendix C

## The Reverse Optimisation Method

The reverse method (described in Chapter 4) is a reliable way of determining a reference state of a body. However, multiple variations (albeit with small differences) of the reference state will be predicted for each fitted deformed configuration model. Hence, a nonlinear optimisation algorithm (referred to as “the reverse optimisation method” in this thesis) was developed to compute a reference state from a set of deformed states obtained by applying different gravity loading conditions. This appendix outlines the algorithm and presents results of a preliminary study that was conducted to test its performance.

With the reference configuration formulation outlined in section 2.2.3 an iterative method of estimating the reference state is proposed, given one or more deformed configuration measurements. Consider a finite element model consisting of  $n$  degrees of freedom. From Fig. C.1:

1. Fit a finite element model to a deformed configuration.
2. An initial estimate of the reference state is obtained by using the reverse method and a fitted model of one of the deformed configurations.
3. Each degree of freedom (out of the  $n$  in total) of current reference state is perturbed.  $i$  in Fig. C.1 identifies a particular degree of freedom.
4. Predictions of the deformed configurations are made from the perturbed reference configuration using the standard forward mechanics techniques described in Section 2.3.2 and Chapter 3.

5. The errors in predicting the available deformed configurations is calculated.
6. The errors before and after perturbation of the  $i^{th}$  degree of freedom are used in a one-sided finite differencing scheme to estimate the rate of change of error with respect to the degree of freedom.
7. Steps 3 to 6 are repeated for each degree of freedom of the reference configuration until  $i = 1 \dots n$ . Then, the gradients of errors are set up in a matrix of the rates of change of error with respect to each reference configuration degree of freedom. This matrix of gradients provides the search direction for the next estimate of the reference state.
8. The optimal reference state is determined in an iterative fashion, and the search stops when the errors in predicting the available deformed configurations are minimised.

By using multiple deformed states in this procedure, one single reference configuration can be determined and used to reliably predict the deformed states for other loading conditions.

## C.1 Preliminary Study

After implementing the reverse optimisation algorithm, a preliminary investigation was conducted to test the accuracy of the method in optimally identifying a reference state for the simplest case of only using one deformed configuration. A data cloud of the five surfaces of a cuboid was generated as shown in Fig. C.2(a). The cuboid was created using trilinear basis functions, with four elements along its length. A cantilever beam deformation was simulated by fixing the  $x, y$  and  $z$  coordinates of one face and applying gravity loading downwards. The material behaviour was described by the neo-Hookean law. This constitutive equation accurately captured the deformations imposed on the silicon gel (see Section 3.2.1). The material location of the data points were calculated in the undeformed and tracked to the deformed state to give a deformed state data cloud as in Fig. C.2(b). The undeformed model was slightly perturbed by running a simulation where the deformed state of Fig. C.2(b) was the reference state and gravity loading was applied in the opposite

direction (upwards). This perturbed configuration was used as the initial estimate of the known undeformed state is shown in Fig. C.2(c). This was because the reverse method would produce the correct reference configuration as we are dealing with synthetic data. The reverse optimisation method was then used with this initial estimate to determine the best reference state for the synthetic deformed configuration data cloud.

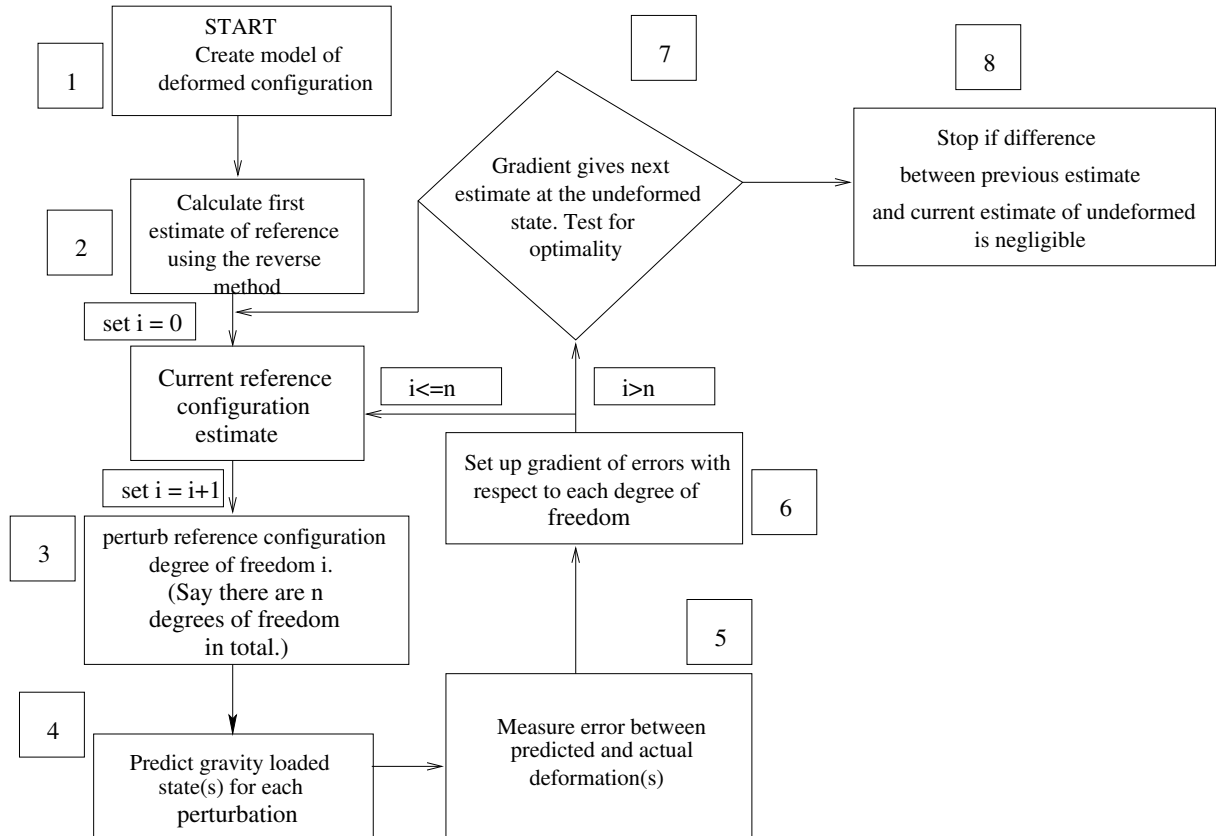


Figure C.1: The reverse optimisation method: Proposed method of estimating the reference state.

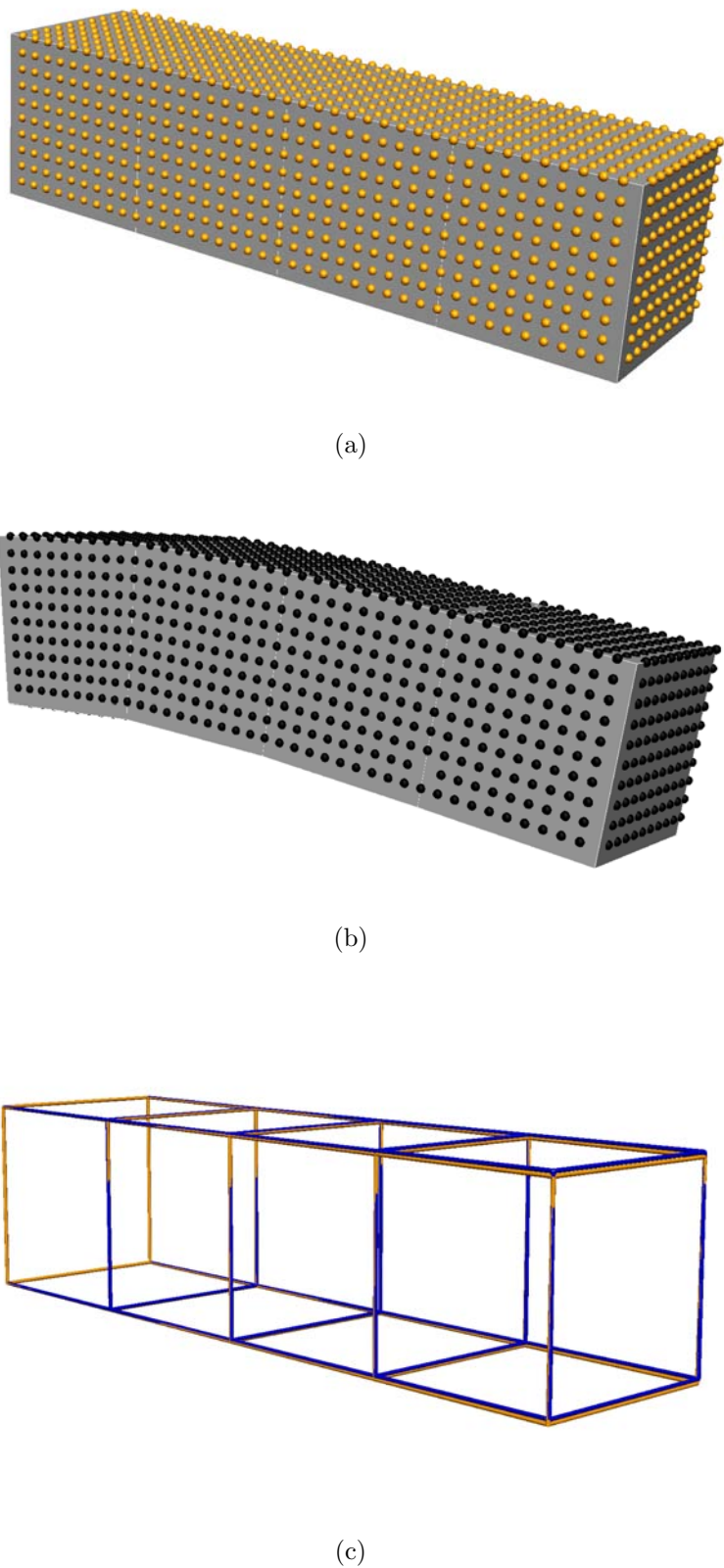


Figure C.2: (a): Undeformed state and data cloud. (b): Predicted deformed state and tracked data cloud (c): undeformed state (gold lines), and initial guess at undeformed state (blue lines overlayed on undeformed)

## C.2 Results

With three coordinates per node, and sixteen free nodes in the mesh, the nonlinear optimisation algorithm took thirteen iterations (search directions) to find the forty eight optimal values for the data projection errors to be minimised. The optimal solution was found to be very accurate with the relative difference between an optimised and actual undeformed variable value in the order of  $10^{-5}$ .

## C.3 Discussion

Typically, finite elasticity problems involve either

1. estimation of the deformed configuration (standard forward mechanics problem) given the undeformed state and material properties
2. or the estimation of material properties given the deformed state and the undeformed state (material parameter estimation).

The proposed method determines the undeformed state given material properties and deformed geometries. However, in the clinical setting, neither the material properties nor the reference state of the breast are known. This iterative method could be extended to estimate material properties along with the reference state. Due to the large deformations in the breast for small changes in patient orientation, it is possible to obtain a rich set of deformed configurations by placing the patient in different orientations with respect to the direction of gravity (see Chapter 7 on obtaining gravity loaded configurations of the breast). Thus, given a set of deformed configurations under known loading conditions, it would be possible to characterise the rest of the unknown parameters that are necessary to model breast biomechanics.

However, the major obstacle in extending this algorithm is the computation time it takes to find the optimal solution. Table C.1 shows the total time that was taken to find the reference state (geometry in Fig. C.1) as the number of unknowns (degrees of freedom) in the problem increased. The first five simulations in the table were run on trilinear meshes successively refined along the length of the geometry, while the last simulation was run on a single tricubic-Hermite element. As shown in the table, there is an increase in computational time with increasing degrees of freedom. The

time it takes to find the reference configuration of the cubic-Hermite mesh makes this optimisation technique currently impractical for breast modelling.

Deg of freedom	Objtve func	SQP Iter	Func evals	Func calls	Total time
12	3.5e-7	5	5	65	20 s
24	6.6e-7	9	14	350	2 min 51 s
36	7.1e-7	11	11	407	4 min 37 s
48	7.6e-7	7	24	1176	17 min 16 s
156	6.6e-7	44	172	27004	15 h 10 m 47 s

Table C.1: Performance of the reverse optimisation method in estimating the reference configuration with increasing degrees of freedom.

There are a number of possible avenues for reducing the computational time:

- One obvious avenue involves parallelisation of steps 3 to 6 in Fig C.1. The forward mechanics simulations for each of the perturbations in step 3 can be conducted in parallel on separate processors. In the ideal situation, n processors would be used for n degrees of freedom.
- The projection of the deformed configuration data points on the predicted deformed surfaces (step 5) is a time consuming step. This is because the algorithm to find the closest approach is an iterative process. In the current implementation of optimising for the reference state, all data are projected after every forward mechanics simulation. Investigations should be conducted to determine if it is possible to only re-project data points in the neighbourhood of the perturbed degree of freedom. This is based on the assumption that the perturbation of a degree of freedom, only affects the coordinates of a small neighbourhood of degrees of freedom in the predicted deformed configuration.
- Construction of the global stiffness matrix for forward mechanics simulations takes a large proportion of the total time. Investigations should be conducted to determine if the entire stiffness matrix must be recomputed at every step. Time could be saved by recomputing only the entries that are affected by a perturbed degree of freedom in the optimisation algorithm.

- The optimisation algorithm is currently based on the sequential quadratic programming algorithm (NPSOL). Research must be conducted on the efficiency of the algorithm compared to other techniques which are available.

The investigations should be conducted initially using silicon gel phantoms to find the optimal technique for practical use. These avenues of improvement have a potential to make the optimisation algorithm viable for clinical application and should be investigated in future work.

## Appendix D

# Comparing ABAQUS and CMISS Simulations

Discrepancies, shown in Chapter 5, between 3D-3D tight coupling model in CMISS and the tied surface constraint, 3D-3D model in ABAQUS indicated possible differences in implementations of models of heterogeneity between ABAQUS and CMISS. This appendix describes the study that was conducted to assess the validity of this hypothesis.

As a first step, predicted deformations of a one-element homogeneous cube under displacement boundary conditions were compared between CMISS and ABAQUS.

A one-element unit cube was subjected to a uniaxial extension of 0.5 mm by applying a displacement to the front face as shown in Fig. D.1. The back face was fixed from displacing in direction “1”. Similarly, the side face nearest to the viewer was fixed from displacing in direction “3”, and the bottom face was fixed from displacing in direction “2”. This meant that, after applying the displacements, the top face is free to move in direction “2” and the side face farthest from the viewer is free to move in direction “3”. The neo-Hookean material constitutive relation with  $c_1 = 1$  kPa was used to characterise the mechanical behaviour of the element. As can be seen in Fig. D.2, both CMISS and ABAQUS predict identical deformed configurations, with deformed nodal coordinates being identical.

A further simulation was done to test the modelling frameworks when the strains in the element are a little more inhomogeneous. This inhomogeneity was achieved by displacing only the top two nodes at the free end by 0.5 mm as in Fig. D.3. The

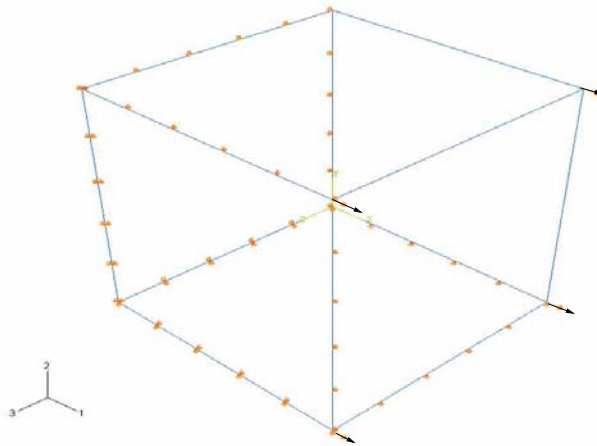


Figure D.1: First one-element unit cube problem set up for comparison between CMISS and ABAQUS. The arrows represent the nodes on which a displacement of 0.5 mm is set. Gold coloured markers represent the application of zero displacement boundary conditions on specific degrees of freedom of the cube.

rest of the problem was kept the same and the deformed states predicted by the two packages are given in Fig. D.4. The figure shows a significant difference between the predicted deformed states of ABAQUS and CMISS. The top right hand node on the farthest face from the viewer was predicted to have displaced a distance of 0.28 mm in direction “2” by ABAQUS, and 0.22 mm by CMISS.

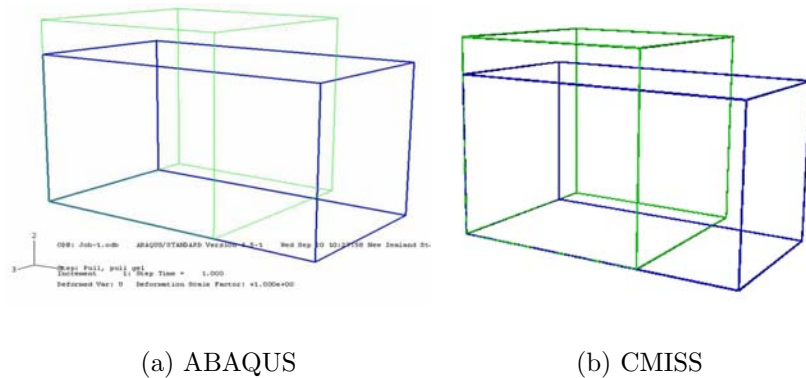


Figure D.2: Comparison of deformed state (blue lines), predicted from the reference state (green lines) using ABAQUS and CMISS. The prediction is for the problem in Fig D.1.

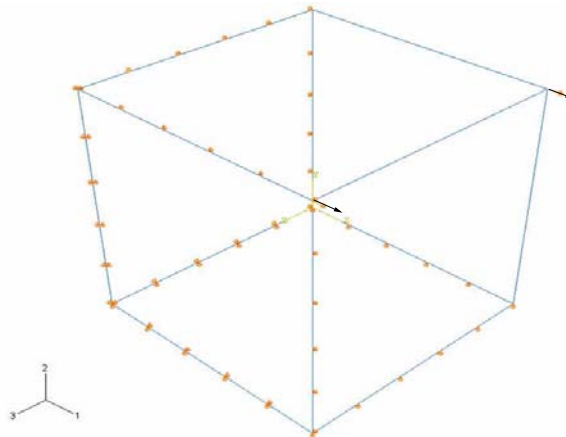


Figure D.3: Second one-element unit cube problem set up for comparison between CMISS and ABAQUS. The arrows represent the nodes on which a displacement of 0.5 mm is set. Gold coloured markers represent the application of zero displacement boundary conditions on specific degrees of freedom of the cube.

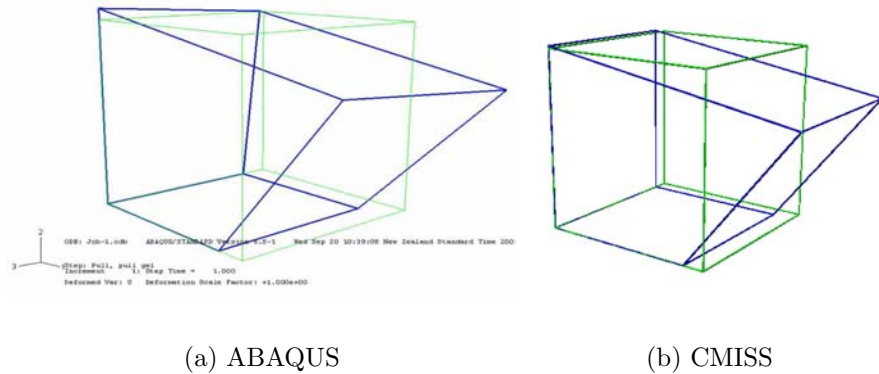


Figure D.4: Comparison of deformed state (blue lines), predicted from the reference state (green lines) using ABAQUS and CMISS. The prediction is for the problem in Fig D.3.

This discrepancy between ABAQUS and CMISS should theoretically not be present if both packages used the same implementation of finite elasticity theory. Such discrepancies cannot be overlooked as numerical error due to their size-approximately 20% relative error between CMISS and ABAQUS. This error would result in unreliable predictions of tissue deformation, and could be potentially harmful to a breast cancer patient in a clinical setting.

Matlab code was also written separately to obtain a more independent judgement on the accuracy of the software packages. Both the Lagrangian and Eulerian formulations of the finite elasticity equations matched the CMISS modelling package. The ABAQUS theoretical and user manuals were enquired and indicated that rates of deformation were used to model finite elastic theory. This is different from CMISS, which uses deformation itself to describe finite elasticity theory. As detailed information on the implementation of finite elasticity in ABAQUS is hard to obtain, it was not possible to further investigate the source of error between ABAQUS and CMISS. Since CMISS is an in-house software package, with enough transparency to check the implementation, we have confidence in the CMISS results.



## Appendix E

# Defining Constitutive Models in CMISS Using CellML

The neo-Hookean constitutive relation was the only relation used to describe material behaviour in this thesis (Chapters 3, 5). Even in Chapter 5, the materials used to create an heterogeneous phantom could be characterised with the neo-Hookean relation, with different  $c_1$  values.

However, it is likely that different constitutive relations will be used to describe the different properties of different breast tissues. CMISS is used extensively at the Bioengineering Institute for a wide variety of applications. A fairly recent development was its extension to allow for easy importability of cellular models for electromechanics simulations in the heart (Nickerson, 2005). This extension was also created to define different cellular models at different locations in the heart. This existing feature provided an excellent base to define constitutive relations in CellML format and to also have the ability to define different material relations at different locations in a finite element geometry.

The existing framework requires the user to define the constitutive equation in CellML by writing out the six expressions for the change in the strain energy function with respect to each Lagrangian strain -  $\frac{\partial W}{\partial E_{11}}$ ,  $\frac{\partial W}{\partial E_{22}}$ ,  $\frac{\partial W}{\partial E_{33}}$ ,  $\frac{\partial W}{\partial E_{12}}$ ,  $\frac{\partial W}{\partial E_{23}}$ ,  $\frac{\partial W}{\partial E_{13}}$ .

For example Mooney-Rivlin constitutive equation, which is given by:

$$W = c_1(I_1 - 1) + c_2(I_2 - 1) \quad (\text{E.1})$$

was defined using CellML with the equations:

$$\begin{aligned}\frac{\partial W}{\partial E_{11}} &= 2c_1 + 4c_2(E_{22} + E_{33}) + 4c_2 \\ \frac{\partial W}{\partial E_{22}} &= 2c_1 + 4c_2(E_{11} + E_{33}) + 4c_2 \\ \frac{\partial W}{\partial E_{33}} &= 2c_1 + 4c_2(E_{11} + E_{22}) + 4c_2 \\ \frac{\partial W}{\partial E_{12}} &= -4E_{12}c_2 \\ \frac{\partial W}{\partial E_{13}} &= -4E_{13}c_2 \\ \frac{\partial W}{\partial E_{23}} &= -4E_{23}c_2\end{aligned}\tag{E.2}$$

The input data into the CellML routine are the Lagrangian strains, and the output data are the deviatoric components of the 2nd Piola Kirchhoff stress tensor. The strain and stress tensors are evaluated at Gauss points in a finite element, and therefore a CellML file type is defined at each Gauss point as well. The definition of CellML models is not restricted by element boundaries and therefore it is possible to specify a regional variation of mechanical properties in a body by assigning different CellML models at different spatial locations. Although not used in this thesis, this feature has been used by other researchers in defining constitutive relations for passive mechanics such as orthopaedic research Shim et al. (2006) and is an important contribution to the IUPS Physiome project.

Further work must be conducted to find the optimal combination of mesh resolution and spatial resolution of the definition of CellML models. After performing such investigations, it is anticipated that this technique will enable detailed models to be represented with a smaller number of elements than with the existing technique, which restricts material property assignment within element boundaries.

# Appendix F

## A Review on Characterising Mechanical Properties of Breast Tissues

Breast biomechanics is a relatively new field of research. There have been only a few studies focussing on the mechanical properties of breast tissues. The focus of this thesis was on validating individual aspects of the modelling framework, and the determination of suitable constitutive models for breast tissue mechanics was set aside for future work. However, in order to survey the current state of breast mechanics research, a literature review was conducted on methods and models used to characterise the mechanical behaviour of breast tissues. This appendix provides a summary of some of the important work conducted by previous researchers in this area.

### F.1 Yu-Neifert (1995)

As mentioned in Section 2.5, Yu-Neifert (1995) developed one of the first predictive models of breast deformation. As part of this research, an indenter test method was developed to test the mechanical properties of the internal breast tissues. The tissue was assumed to be an isotropic, composite material (fibrous connective tissue embedded in an adipose tissue matrix) and an effective Young's Modulus was estimated using the equation  $E_e = E_f V_f + E_m V_m$  where  $V_f$  and  $V_m$  are the ratios of the matrix

and adipose components and  $E_m$  and  $E_f$  are the Young's moduli of the components. Mechanical tests involved indentation of roughly cylindrical tissue samples (25 mm radius, 70 mm height) contained in a plexi glass container (50 mm internal diameter, 62 mm outer diameter and 75 mm height), under a 150 mm diameter plexi glass indenter rod. Force was applied using weights, and the displacements were measured using a video camera. Possible viscoelastic effects were also considered by measuring the position of the indenter right after indentation and 10 minutes after the first recording, with the indenter in the same position. Viscoelastic effects were observed to be negligible as the indenter did not move from its set position in the ten minutes of loading. A contact mechanics model of the indentation experiment was used to estimate the mechanical properties of the tissue samples, assuming that they were linearly elastic in what was considered to be the physiological range of 10% strains. The Young's modulus was estimated to be 400 Pa, but this estimate was not sufficient to accurately predict the deformations of the breast from supine to prone positions.

## **F.2 Krouskop et al. (1998)**

Although Yu-Neifert's breast mechanics model was one of the first in the field, characterisation of the mechanical properties of the breast tissues have been investigated for a while longer. Studies on breast tissue mechanical properties have been conducted, independent of breast deformation model development, to use tissue elasticity as a way to characterise tissue type. These studies were conducted to assess the performance of a field of research called elastography for cancer detection Sarvazyan et al. (1995). Elastography consists of applying a small quasi static compressive force to a tissue and estimating the local axial motions (from images) by means of a correlation technique. These motion estimates represent displacements and are used to estimate a strain field on an image called an elastogram. The strain distribution is related to stiffness distribution (via constitutive relationships of the different tissues) that highlights the relative stiffness of the various tissues. Krouskop et al. (1998) highlights the major findings of the research in terms of breast tissue mechanical properties in recent years.

Krouskop *et al* subjected excised, homogeneous breast tissue (fat, glandular,

fibrous, intraductal carcinoma and infiltrating carcinoma) samples (15 mm radius, height less than a quarter of the diameter) to compression loading at three different strain rates (0.1 Hz, 1.0Hz and 4.0 Hz) to quantify the elastic moduli of the tissues and examine their viscoelastic nature. The tissues were sinusoidally compressed with a 10 N load cell on an INSTRON machine (indenter diameter of 4.83 mm), with a strain range of 10% from a precompressed position (5% and 20% precompression levels). The tissue samples were assumed to be incompressible, linearly elastic (in the 10% strain range at each precompression level) and isotropic and a mathematical model of the experiment was developed to estimate the Young's moduli using the experimental data.

The following observations were made from this study:

1. The elastic modulus of fat was nearly constant (average stiffness of 20 kPa) over a large range (30%) of applied strain.
2. Glandular tissue exhibited a non-linear behaviour, becoming stiffer as the strain is increased. It was also much stiffer (average stiffness of 28 kPa at 5% precompression and 48 kPa at 20% precompression) than fatty tissue at all strains.
3. Fibrous tissue also exhibited nonlinearity with an average stiffness of 96 kPa at 5% and 218 kPa at 20% precompression.
4. Intraductal carcinomas had an average stiffness of 22 kPa at 5% and 291 kPa at 20% precompression levels, while infiltrating carcinomas had an average stiffness of 106 kPa and 558 kPa at 5% and 20% precompression levels.
5. Breast tissue can be considered to be elastic as there were negligible viscoelastic effects observed at different strain rates.

### F.3 Wellman (1999)

Wellman et al. (1999) is one of the most cited bodies of work on constitutive model development for breast tissues (Azar et al., 2000), (Samani et al., 2001), (Ruiter et al., 2002). The thesis from which this work was published, was focussed on developing a hand held scanning device with a distributed pressure sensor and a magnetic

position tracker. This device could then be used by a clinician to palpate the breast surface to identify palpable breast lumps and estimate the pressure distribution across the breast surface using constitutive models of breast tissue that related the local compressive strains to a stress.

The experimental studies involved a compression/punch indentation device developed to obtain force-displacement curves for uniaxial compression and punch indentation. The device consisted of a 4mm diameter flat-bottomed punch and its position and force applied were measured using a linear potentiometer and uniaxial load cell. Breast tissue samples were resected to a minimum of 10mm by 10mm and a thickness of 2mm. The samples were preconditioned using a 2N load cell 10 times and the small load restricted strains to less than 10%. Tests were also conducted with different rates of strain to test for the effects of viscoelasticity. The tissue samples were assumed to be isotropic, homogeneous and incompressible and exponential curves of the form  $\sigma_n^* = \frac{b^*}{m^*} (e^{m^* \epsilon_n} - 1)$  were fitted to the stress-strain curves recorded from the experiments.

The conclusions made in this study were very similar to those made by Krouskop et al. (1998), with gross observations such as negligible viscoelastic effects, linear response of fat and nonlinear response of glandular tissues and carcinoma. The average Young's moduli estimated with the experimental data at 10% strain for fat, glandular tissue and ductal carcinoma were 10 kPa, 88 kPa and 640 kPa respectively.

## **F.4 Williams (2000)**

Williams (2000) performed one of a few in-vivo compression experiments on the human breast in the literature to characterise the mechanical behavior of normal breast tissues. The experiment consisted of compressing the breast using a custom built compression device and RF coil that imposed medio-lateral compression (taken to be the y-direction. x-direction was supero-inferior and z-direction was antero-posterior) at varying degrees to produce different deformed breast MR images. The compression device consisted of top and bottom plates, with the bottom consisting of a single surface coil to obtain the MR images. The top plate was moved along posts to provide varying degrees of compression to the breast. Force sensors (measuring forces only normal to sensing area) were stuck underneath the top plate and their

readings were recorded when they came in contact with the breast.

The force readings were converted to axial stress using  $\sigma = Force/Area$  where the area is the cross-sectional area of the sensor. A maximum of six sensors were used in the compression studies, however, due to breast shape and restrictions imposed on placement of the sensors due to the compression device and MR machine, reliable readings on the breast surface were only available at two or three points. The sensors were aligned linearly along the supero-inferior direction, and due to the lack of sufficient information on the force distribution across the breast surface, a quadratic interpolation scheme was used to estimate the distribution using the two or three points at which force was measured.

To estimate strains, it was necessary to track line segments between the “undeformed” and deformed states. The rib cage, fatty tissue, boundaries between glandular and fatty tissue and the nipple were used to define internal tissue landmarks as they were easily distinguishable. Distances between landmarks between undeformed and deformed images were used to estimate strains. External landmarks were also placed (nail polish with metallic material) to act as external material points that can be tracked on the MR images.

The following assumptions were made in the stress-strain analysis:

1. The compression plates imposed uniaxial compression. This would mean that the breast was assumed to be freestanding and not rigidly attached or confined.
2. The plates were assumed to introduce very little friction. Finite slipping of the plates due to underlying fatty tissue was unaccounted for.
3. There was a uniform distribution of force across each line segment. This assumption was verified by placing additional force sensors at the bottom plate when compressing a breast phantom. One human breast contained force sensors at the bottom plate as well. The sensor readings showed similar values and therefore, the assumption was acceptable.
4. The tissue was assumed to be homogeneous.

Line segments were characterized as either adipose or fibroglandular tissue. If a segment composed at least 50% of the glandular tissue, then it was modelled as glandular. Other segments were modelled as adipose tissue. Only segments

classified as glandular were used for stress-strain analysis. This was because of the homogeneity assumption that was made. However, one patient consisted mostly of fatty tissue and therefore their measurements were used to characterise fatty tissue.

The stress-strain data (measured and interpolated) was then used to fit polynomials using a least-square polynomial technique. It was noted that there was non-zero stress at zero strain as the body weight and gravity was introducing stress - the breast was still in a deformed state under gravity loading. The compression experiment was conducted on three patients - A,B, and C. Patient B's breast had mostly adipose tissue and was therefore used to characterise fatty tissue mechanical behaviour. Patient A and C's breast were used to characterise glandular tissue behaviour alone, with the polynomial fitting the data from patient C best. Further, material parameters for four tissue models in literature were determined using a nonlinear curve fitting technique on the experimental data - Mooney-Rivlin (Rivlin, 1950), Ogden (Twizell & Ogden, 1983), Blatz (Fung, 1977) and Vito (Vito, 1973).

## **F.5 Discussion**

The studies described above represent the main techniques used to date for characterisation of mechanical properties of breast tissues. Additional studies based on similar techniques have been conducted in recent years. Han et al. (2003) performed ultrasonic indentation tests on breast tissues in-vivo consisting of a force sensor and an optical tracking system integrated to an ultrasound system. A demonstration of the technique was conducted by testing the mechanical properties of breast tissue of one volunteer, which showed that the material behaves nonlinearly, as previously established by (Krouskop et al., 1998) and (Wellman, 1999). Samani & Plewes (2004) conducted indentation experiments imposing 10% strains at 0.1 Hz and unlike Krouskop et al. (1998), fitted the entire nonlinear behaviour of the tissues using a polynomial in terms of the strain invariants ( $I_1$  and  $I_2$ )  $U = \sum_{i+j=1}^N C_{ij}(I_1-3)^i(I_2-3)^j$ .

The material parameters were estimated using an optimisation technique coupled with a nonlinear finite element model of the indentation experiments.

The mechanical properties estimated by the different studies have a wide range due to the variety of tests conducted and the fact that inter-patient variability is

known to be high. A large number of previous studies have only been concerned with estimating Young's moduli because they were interested only in relative stiffness values for characterisation of tissues for cancer detection. However, when developing a model to predict breast deformation under gravity it is important to incorporate the entire nonlinear range of mechanical behaviour of the breast tissues due to the large deformations imposed under different gravity loading conditions (see Chapter 7). It is possible to test and characterise the mechanical properties of the breast tissues more accurately in-vivo, than to test excised tissues as tissue interactions are taken into account during an in-vivo study.

The study conducted by Williams (2000), although in-vivo, requires further extensions for more accurate characterisation of mechanical properties. One extension would be to remove the quadratic interpolation scheme to create more data. The assumption of homogeneity was made to simplify the test, but removing the assumption has the potential of characterising the mechanical properties of the tissues more accurately.

With the limitation of (Williams, 2000) in mind, the work conducted by (Krouskop et al., 1998), (Wellman, 1999) and (Samani & Plewes, 2004) provide the best data on breast tissue mechanical properties in the current literature. Although Krouskop et al. (1998) was only interested in extracting Young's moduli, the experiments in this work provide the best data for characterisation of mechanical properties due to the large strain range (30%) to which the tissue samples were imposed. Samani & Plewes (2004) emphasised on characterising the entire nonlinear behaviour of the breast tissues, but restricted the data to under 10% strains, which was the same case for the study by (Wellman, 1999). Future studies on characterisation of mechanical properties of breast tissue should ensure that the nonlinear behaviour of the tissues are captured and possibilities for in-vivo mechanical testing must be conducted (see Chapter 8 on future work).



# Appendix G

## Automatic Generation of Breast Geometries

The following sections provide the CMISS command files that were used to generate individual-specific finite element geometries shown in Chapters 6 and 7. The details of the algorithms contained in this code are described in Chapter 6.

### G.1 Scaling and Repositioning the Initial Mesh

```
#####
#COM FILE: MoveInitMesh.com
#Author: Vijay Rajagopal
#Description: Moves the initial mesh and scales it to the skin data cloud
#####

#load perl libraries for CMISS
use CmUtils
use CmUtils::File::Ipnode
use CmUtils::File::Ipdata
use CmUtils::Objects::NodeGroup
use CmUtils::Objects::Field
use CmUtils::Objects::Node
use CmUtils::Vector
```

```
#skin data file to use
$skinFile = "Skin"

#initial mesh file name
$meshFile="poulBreastRef_unit"

#store node number of the nipple node on the initial mesh and the
# middle node on the back (muscle) face of the mesh
$nippleNode=5;
$midChestNode=12;

#dimensions of the initial mesh
$initDimX = 166;
$initDimY = 130;
$initDimZ = 160;

fem def para;r;surface_fitting
fem def coord 3,1
fem def data;r;$skinFile
$dgroup = readIpdata("$skinFile");
$numNodes = $dgroup->numberOfNodes();

#store data file's x,y,z values in arrays
for($i=1;$i<=$numNodes;$i++)
{
    $node = $dgroup->getNode($i);
    $nodeVals = $node->getValuesHash();
    $X[$i] = $nodeVals->{coordinates}{x}[0]{value};
    $Y[$i] = $nodeVals->{coordinates}{y}[0]{value};
    $Z[$i] = $nodeVals->{coordinates}{z}[0]{value};

}
#find the nipple data point - one with the smallest y value.
```

```
#(positive y is from nipple to chest)

for($i=1;$i<=$numNodes;$i++)
{
$node = $dgroup->getNode($i)->getValuesHash();
$Y = $node->{coordinates}{y}[0]{value};
if($Y == min(@Y))
{
$node = $dgroup->getNode($i)
$nodeVals = $node->getValuesHash();
#store coordinates of data point that we shall take to be extreme nipple point
$NippleX = $nodeVals->{coordinates}{x}[0]{value};
$NippleY = $nodeVals->{coordinates}{y}[0]{value};
$NippleZ = $nodeVals->{coordinates}{z}[0]{value};
$nippleData=$i;
#set weights for this nipple data point to be 100 to ensure that
# the mesh surface is fitted to the nipple contour as well.
$node->value(3,100.0);
$node->value(4,100.0);
$node->value(5,100.0);
$dgroup->updateNode($node);

}

}

$options[fields]=["coordinates","weights"];
#write out the data file
writeIpdata("$skinFile",$dgroup,\%options);

$MAXX = max(@X)+7.5;
$MINX = min(@X)-7.5;
$MAXZ = max(@Z);
$MINZ = min(@Z);
$MIDX = ($MAXX+$MINX)/2;
```

```

$MIDZ = ($MAXZ+$MINZ)/2;
$MAXY = max(@Y);

fem def bas;r;TriCubicHerm
fem def;add base;r;BiCubicHerm
fem def;add base;r;TriLinear
fem def;add base;r;BiLinear
fem def nodes;r;$meshFile      # Reads in nodal information
fem def element;r;$meshFile    # Reads in element information

#rescale the mesh in x and z based on overall dimensions of the data cloud
$scaleX=(max(@X)-min(@X)+15)/$initDimX
$scaleY=1.0
$scaleZ= (max(@Z)-min(@Z))/($initDimZ)
fem change node scale by $scaleX,$scaleY,$scaleZ
fem def node;w;initMesh_scaled

fem def node;r;initMesh_scaled
$ngroup=readIpnode("initMesh_scaled");
$numNodes = $ngroup->numberOfNodes();

#get nipple node coordinates
$node = $ngroup->getNode($nippleNode)
$nodeVals = $node->getValuesHash();
$nippleNodeX=$nodeVals->{coordinates}{x}[0]{value};
$nippleNodeY=$nodeVals->{coordinates}{y}[0]{value};
$nippleNodeZ=$nodeVals->{coordinates}{z}[0]{value};

#get mid muscle wall node coordinates
$node = $ngroup->getNode($midChestNode)
$nodeVals = $node->getValuesHash();
$midChestNodeX=$nodeVals->{coordinates}{x}[0]{value};
$midChestNodeY=$nodeVals->{coordinates}{y}[0]{value};
$midChestNodeZ=$nodeVals->{coordinates}{z}[0]{value};

```

```
#translate mesh to the region of the data cloud.  
$translateX=-1*($nippleNodeX-$MIDX)  
$translateY=-1*($midChestNodeY-$MAXY)+10  
$translateZ=-1*($nippleNodeZ-$MIDZ)  
  
fem change node translate by $translateX,$translateY,$translateZ  
  
fem def node;w;initMesh_moved  
read com;exportModified  
q
```

## G.2 Further Customisation of the Initial Mesh

```
#####
#COM FILE: CustomizeInitMesh.com
#Author: Vijay Rajagopal
#Description: Customises the moved initial mesh to
#make the front face follow the skin data cloud contour more.
#####

#load perl libraries for CMISS
use CmUtils
use CmUtils::File::Ipnode
use CmUtils::File::Ipdata
use CmUtils::Objects::NodeGroup
use CmUtils::Objects::Field
use CmUtils::Objects::Node
use CmUtils::Vector

#initial mesh file name
$meshFile="poulBreastRef_unit"

#store node number of the nipple node on the initial mesh
#and the middle node on the back (muscle) face of the mesh
$nippleNode=5;
$midChestNode=12;

#store the row of nodes of the initial mesh to be moved to make better initial mesh.
@bottomNodes = (22,45,8,49,36);
@midNodes = (19,56,5,58,33);
@topNodes = (16,68,2,70,30);
@quadbotNodes = (21,46,7,50,35);
@threequadbotNodes = (20,52,6,54,34);
@quadtopNodes = (18,60,4,62,32);
@threequadtopNodes = (17,64,3,66,31);
@meshNodes = ([@bottomNodes],[@quadbotNodes],[@threequadbotNodes],
```

```
[@midNodes],[@quadtopNodes],[@threequadtopNodes],[@topNodes]);\n\n#num image slices\n$numSlice = 52;\n$botImage = "image01";\n$topImage = "image$numSlice";\n$quadbotImage="image06";\n$threequadbotImage="image20";\n$midImage="image26";\n$quadtopImage="image32";\n$threequadtopImage="image46";\n@datafile = ($botImage,$quadbotImage,$threequadbotImage,$midImage,\n            $quadtopImage,$threequadtopImage,$topImage);\n\n$ngroup = readIpnode("test");\n\nsub moveNodeRow\n{\n    $datafilename = $_[0];\n    @nodeRow = @{$_[1]};\n    $dgroup = readIpdata("$datafilename");\n    $numNodes = $dgroup->numberOfNodes();\n    @nodeNums = $dgroup->getNodeNames();\n\n    #store data file's x,y\n    #create hash of data point associated with x value\n    %hash = ();\n    for($i=0;$i<=($numNodes-1);$i++)\n    {\n        $node = $dgroup->getNode($nodeNums[$i]);\n        $nodeVals = $node->getValuesHash();\n        $X[$i] = $nodeVals->{coordinates}{x}[0]{value};\n        $Y[$i] = $nodeVals->{coordinates}{y}[0]{value};\n        $hash{ $nodeNums[$i] } = $X[$i];\n    }\n}
```

```
#-----#
#  printHashByValue.pl                      #
#                                             #
#  Copyright 1998 DevDaily Interactive, Inc. All Rights Reserved. #
#-----#
```

```
#-----#
#  FUNCTION:  hashValueAscendingNum          #
#                                             #
#  PURPOSE:   Help sort a hash by the hash 'value', not the 'key'. #
#             Values are returned in ascending numeric order (lowest #
#             to highest).                      #
#-----#
```

```
sub hashValueAscendingNum {
    $hash{$a} <=> $hash{$b};
}
```

```
@sorted = sort hashValueAscendingNum (keys(%hash));
#move bottom left most node
$data = $dgroup->getNode($sorted[0]);
$dataVals = $data->getValuesHash();
$dataY = $dataVals->{coordinates}{y}[0]{value};
```

```
$node = $ngroup->getNode($nodeRow[0]);
$node->value(8,$dataY);
$ngroup->updateNode($node);
```

```
#move right most bottom node
$data = $dgroup->getNode($sorted[(@sorted)-1]);
$dataVals = $data->getValuesHash();
$dataY = $dataVals->{coordinates}{y}[0]{value};
```

```
$node = $ngroup->getNode($nodeRow[(@nodeRow)-1]);
$node->value(8,$dataY);
$ngroup->updateNode($node);

for($n=1;$n<=(@nodeRow)-2;$n++)
{
    $node = $ngroup->getNode($nodeRow[$n]);
    $nodeVals = $node->getValuesHash();
    $nodeX = $nodeVals->{coordinates}{x}[0]{value};
    $x=min(@X);
    $dataindex = 0;
    while($x<$nodeX)
    {
        $dataindex = $dataindex+1;
        $data = $dgroup->getNode($sorted[$dataindex]);
        $dataVals = $data->getValuesHash();
        $dataY = $dataVals->{coordinates}{y}[0]{value};
        $x = $dataVals->{coordinates}{x}[0]{value};
    }
    $node->value(8,$dataY);
    $ngroup->updateNode($node);
}

}

&moveNodeRow($datafile[0],$meshNodes[0]);
&moveNodeRow($datafile[1],$meshNodes[1]);
&moveNodeRow($datafile[2],$meshNodes[2]);
&moveNodeRow($datafile[3],$meshNodes[3]);
&moveNodeRow($datafile[4],$meshNodes[4]);
&moveNodeRow($datafile[5],$meshNodes[5]);
&moveNodeRow($datafile[6],$meshNodes[6]);

$filename = "test";
writeIpnode($filename, $ngroup);
read com;exportModified
```

q

### G.3 Modelling the Skin Contour

```
#####
#COM FILE: FitSkin2Init.com
#Author: Vijay Rajagopal
#Description: Fits the modified initial mesh to the skin data cloud
#####

#load perl libraries for CMISS

use CmUtils
use CmUtils::File::Ipnode qw( readIpnode );
use CmUtils::File::Ipfiel qw( writeIpfiel );
use CmUtils::File::Ipelem qw( readIpelem );

#the mesh file to be used in the fit
$Patient="initMesh_moved"

#number of fitting iterations
$tot_itt=6;

#####

#Load mesh files
fem def para;r;surface_fitting      # Declares array dimensions
fem def coor 3,1
fem def bas;r;TriCubicHerm
fem def;add base;r;BiCubicHerm
fem def;add base;r;TriLinear
fem def;add base;r;BiLinear
fem def nodes;r;$Patient      # Reads in nodal information
fem def element;r;$Patient      # Reads in element information
fem def field;r;$Patient      # Reads in field variables
```

```
fem def elem;r;$Patient field # Defines connectivity of field variables
fem update field from geometry          # Updates field

#####
# group front face
fem group face allfaces as FIT_FACE external xi3 high

# group front nodes
fem group nodes 2,8,16..22,30..36,45,49,68,70 as FIT_FACE_NODES
fem group nodes 3..7,46,52,56,60,64,50,54,58,62,66 as OTHER_SKIN_NODES
#
#
# Reads in data information
fem def data;r;Skin

#project data onto surfaces of mesh
fem def xi;c closest_face faces FIT_FACE seed_points 9 search_start 8 cross_boundaries

fem li data error                      # Lists initial data error

# Fitting is done iteratively. In this case six iterations. Also note that for each
# iteration, a new *.ipfit is read in. This helps to relax the Sobelov weights
# gradually.
set echo on
for ($fit_itt=1; $fit_itt<=$tot_itt; $fit_itt=$fit_itt+1)
{
    fem def fit;r;surface_fitting_skin_${fit_itt} geometry faces FIT_FACE
    fem fit
    fem update node fit
    fem def xi;c closest_face faces FIT_FACE seed_points 9 search_start 8 cross_boundaries
    fem li data error
    system "echo ' ======'"
    system "echo ' ITERATION ${fit_itt} DONE' "
```

```
system "echo ' ======'"
}

set echo off

#write out fitted mesh
fem def node;w;skinFittedMesh
fem def elem;w;skinFittedMesh

fem export node;skinFittedMesh as skinFittedMesh offset 1000
fem export elem;skinFittedMesh as skinFittedMesh offset_node 1000 offset_elem 1000
fem export data;skin_proj as skin_proj error
q
```

## G.4 Scaling and Repositioning the Skin Fitted Mesh

```
#####
#COM FILE: MoveSkinMesh.com
#Author: Vijay Rajagopal
#Description: Modifies the back face of the skin fitted mesh to provide
# a good initial face for muscle data fitting
#####

#load perl libraries for CMISS

use CmUtils
use CmUtils::File::Ipnode
use CmUtils::File::Ipdata
use CmUtils::Objects::NodeGroup
use CmUtils::Objects::Field
use CmUtils::Objects::Node
use CmUtils::Vector

$muscleFile = "Muscle"
$meshFile="SkinFittedMesh"
$nippleNode=5;
$midChestNode=12;
$initDimX = 166;
$initDimY = 130;
$initDimZ = 160;

fem def para;r;surface_fitting
fem def coord 3,1
fem def data;r;$muscleFile
$dgroup = readIpdata("$muscleFile");
$numNodes = $dgroup->numberOfNodes();
```

```

for($i=1;$i<=$numNodes;$i++)
{
$node = $dgroup->getNode($i);
$nodeVals = $node->getValuesHash();
$Y[$i] = $nodeVals->{coordinates}{y}[0]{value};

}

#find the smallest data point y value (y is positive from nipple to chest)
$minChestY =min(@Y)

fem def bas;r;TriCubicHerm
fem def;add base;r;BiCubicHerm
fem def;add base;r;TriLinear
fem def;add base;r;BiLinear
fem def nodes;r;$meshFile      # Reads in nodal information
fem def element;r;$meshFile    # Reads in element information

#store the node numbers of the back and front faces
#side nodes are the nodes around the edges of the mesh
@backSideNodes=(29,69,1,67,15,28,27,26,25,24,23,43,9,47,37,38,39,40,41,42);
@frontSideNodes=(30,70,2,68,16,17,18,19,20,21,22,45,8,49,36,35,34,33,32,31);
$numSideNodes=scalar(@backSideNodes);
@backNodes=(65,14,63,61,13,59,57,12,55,53,11,51,48,10,44);
@frontNodes=(66,3,64,62,4,60,58,5,56,54,6,52,50,7,46);
$numBackNodes=scalar(@backNodes);

$ngroup=readIpnode("$meshFile");
$numNodes = $ngroup->numberOfNodes();

#move muscle side nodes 5mm away from front side nodes
#then move rest of nodes to $minChest
$maxfnodeY=0;
for($i=0;$i<$numSideNodes;$i++)
{
$fnode = $ngroup->getNode($frontSideNodes[$i]);

```

```
$fnodeVals = $fnode->getValuesHash();
$fnodeY=$fnodeVals->{coordinates}{y}[0]{value};
$bnode=$ngroup->getNode($backSideNodes[$i]);
$bnodeVals=$bnode->getValuesHash();
$bnodeY=$bnodeVals->{coordinates}{y}[0]{value};
$translateY=-1*($bnodeY-$fnodeY-5);
if($fnodeY>$maxfnodeY)
{
$maxfnodeY=$fnodeY
}
fem change node translate by 0,$translateY,0 node $backSideNodes[$i];

}

#move the rest of the internal muscle nodes 20 mm
#away from data point with smallest y value
for($i=0;$i<$numBackNodes;$i++)
{
$bnode=$ngroup->getNode($backNodes[$i]);
$bnodeVals=$bnode->getValuesHash();
$bnodeY=$bnodeVals->{coordinates}{y}[0]{value};
$translateY=-1*($bnodeY-$minChestY-20);
print "$translateY\n"
fem change node translate by 0,$translateY,0 node $backNodes[$i];

}

fem group node xi3=0 external as MUSCLE
fem update node deriv 1 linear wrt xi node MUSCLE
fem update scale_factor unit
fem update node deriv 2 linear wrt xi node MUSCLE
fem update scale_factor unit
fem update node deriv 3 linear wrt xi node MUSCLE
fem update scale_factor unit
```

```
fem def node;w;skinFittedMoved  
read com;exportModified  
q
```

## G.5 Modelling the Muscle Contour

```
#####
#COM FILE: FitMuscle2Skin.com
#Author: Vijay Rajagopal
#Description: Fits the muscle face to the muscle data
#####

#number of fitting iterations
$tot_itt=5;

fem def para;r;surface_fitting      # Declares array dimensions
fem def coor 3,1
fem def bas;r;TriCubicHerm

# Reads in nodal information
fem def nodes;r;skinFittedMoved
    # Reads in element information
fem def element;r;skinFittedMoved

fem def field;r;skinFittedMoved      # Reads in field variables
fem def elem;r;skinFittedMoved field # Defines connectivity of field variables
fem update field from geometry       # Updates field

# group front face
fem group face allfaces as FIT_FACE external xi3 low

fem group nodes  1,15,23..29,37..42,67,69 as FIT_FACE_NODES

fem def data;r;Muscle
fem def xi;c closest_face faces FIT_FACE seed_points 9 search_start 8 cross_boundaries
```

```
fem li data error          # Lists initial data error

for ($fit_itt=1; $fit_itt<=$tot_itt; $fit_itt=$fit_itt+1)
{
fem def fit;r,surface_fitting_muscle_${fit_itt} geometry faces FIT_FACE
fem fit
fem update node fit
fem def xi;c closest_face faces FIT_FACE seed_points 9 search_start 8 cross_boundaries
fem li data error
system "echo ' ======' "
system "echo ' ITERATION ${fit_itt} DONE' "
system "echo ' ======' "
}

fem export data;muscle_proj as muscle_proj error
fem def node;w;BreastFitted
#have x-z as the xi 1 xi 2 face for skin mechanics
fem def elem;w;BreastFitted

fem export node;BreastFitted as BreastFitted
fem export elem;BreastFitted as BreastFitted
```

## G.6 Adjusting Derivatives Through the Thickness

```
#####
#COM FILE: CalcDeriv.com
#Author: Vijay Rajagopal
#Description: Recalculates s3 derivatives of each node to be normal to
#plane in which node lies
#####

use CmUtils

use CmUtils::File::Ipnode
use CmUtils::Objects::NodeGroup
use CmUtils::Objects::Field
use CmUtils::Objects::Node
use CmUtils::Vector

#Reading in the ipnode file of interest
$meshFile = "BreastFitted"
fem def para;r;surface_fitting
fem def coord 3,1
fem def node;r;$meshFile
$group = readIpnode("$meshFile")

@backSideNodes=(29,69,1,67,15,28,27,26,25,24,23,43,9,47,37,38,39,40,41,42);
@frontSideNodes=(30,70,2,68,16,17,18,19,20,21,22,45,8,49,36,35,34,33,32,31);

@backNodes=(65,14,63,61,13,59,57,12,55,53,11,51,48,10,44);
@frontNodes=(66,3,64,62,4,60,58,5,56,54,6,52,50,7,46);
$numNodes=scalar(@backNodes);
for($i=0;$i<$numNodes;$i++)
{
    #Extracting the values characterising each node
```

```

$bnodes = $group->getNode($backNodes[$i]);
$bnodesVals = $bnodes->getValuesHash();
$fnodes = $group->getNode($frontNodes[$i]);
$fnodesVals = $fnodes->getValuesHash();

#Extracting the derivatives wrt to s1
$fs1[1] = $fnodesVals->{coordinates}{x}[0]{derivatives}[0];
$fs1[2] = $fnodesVals->{coordinates}{y}[0]{derivatives}[0];
$fs1[3] = $fnodesVals->{coordinates}{z}[0]{derivatives}[0];
$bs1[1] = $bnodesVals->{coordinates}{x}[0]{derivatives}[0];
$bs1[2] = $bnodesVals->{coordinates}{y}[0]{derivatives}[0];
$bs1[3] = $bnodesVals->{coordinates}{z}[0]{derivatives}[0];

#Putting these derivatives into a vector
$fv1 = new CmUtils::Vector(($fs1[1],$fs1[2],$fs1[3]));
$bv1 = new CmUtils::Vector(($bs1[1],$bs1[2],$bs1[3]));

#Extracting the derivatives wrt to s2
$fs2[1] = $fnodesVals->{coordinates}{x}[0]{derivatives}[1];
$fs2[2] = $fnodesVals->{coordinates}{y}[0]{derivatives}[1];
$fs2[3] = $fnodesVals->{coordinates}{z}[0]{derivatives}[1];
$bs2[1] = $bnodesVals->{coordinates}{x}[0]{derivatives}[1];
$bs2[2] = $bnodesVals->{coordinates}{y}[0]{derivatives}[1];
$bs2[3] = $bnodesVals->{coordinates}{z}[0]{derivatives}[1];

$fs3 = $fnodesVals->{coordinates}{y}[0]{derivatives}[3];
$bs3 = $bnodesVals->{coordinates}{y}[0]{derivatives}[3];

#Putting these values into a vector
$fv2 = new CmUtils::Vector(($fs2[1],$fs2[2],$fs2[3]));
$bv2 = new CmUtils::Vector(($bs2[1],$bs2[2],$bs2[3]));

#Calculating the cross product of these two vectors
$fv3 = crosssp($fv1,$fv2);

```

```
$fv3 = norm($fv3);
$bv3 = crossp($bv1,$bv2);
$bv3 = norm($bv3);

$fv3=10*$fv3
$bv3=10*$bv3

#Inserting these new values back into the node as derivatives wrt s3
@fs3values = $fv3->list();
    $fnode->value(4,$fs3values[0]);
    $fnode->value(12,$fs3values[1]);
    $fnode->value(20,$fs3values[2]);

@bs3values = $bv3->list();
    $bnode->value(4,$bs3values[0]);
    $bnode->value(12,$bs3values[1]);
    $bnode->value(20,$bs3values[2]);
}

writeIpnnode("BreastFittedFinal", $group);
read com; exportModified
q
```



# Bibliography

- Atkin, R. & Fox, N. (1980), *An Introduction to the theory of Elasticity*, Longman Group.
- Azar, F. (2001), A Deformable Finite Element Model of the Breast for Predicting Mechanical Deformations under External Perturbations, PhD thesis, University of Pennsylvania, Philadelphia.
- Azar, F., Metaxas, D. & Schnall, M. (2000), ‘A finite element model of the breast for predicting mechanical deformations during biopsy procedures’, *Mathematical Methods in Biomedical Image Analysis* pp. 38–45.
- Azar, F., Metaxas, D. & Schnall, M. (2001), ‘A deformable finite element model of the breast for predicting mechanical deformations under external perturbations.’, *Acad Radiol* pp. 965–75.
- Cheng, L., Sands, G., French, R., Withy, S., Wong, S., Legget, M., Smith, W. & Pullan, A. (2005), ‘Rapid construction of a patient specific torso model from 3D ultrasound for noninvasive imaging of cardiac electrophysiology’, *Med. Biol. Eng. Comput* **43**(3), 325–330.
- Cooper, A. (1840), *On the Anatomy of the Breast*, Longman.
- Dawant, B. (2002), Non-rigid registration of medical images: purpose and methods, a short survey, in ‘IEEE, International Symposium on Biomedical Imaging’, pp. 465–468.
- Engeland, S., Snoeren, P., Hendriks, J. & Karssemeijer, N. (2003), ‘A comparison of methods for mammogram registration’, *IEEE Transactions on Medical Imaging* **22**(11), 1436–1444.

- Ferguson, J., Schor, A., Howell, A. & Ferguson, M. (1991), 'Changes in the extracellular matrix of the normal human breast during the menstrual cycle', *Cell and Tissue Research* **268**, 167–177.
- Fernandez, J., Mithraratne, P., Thrupp, S., Tawhai, M. & Hunter, P. (2004), 'Anatomically based geometric modelling of the musculo-skeletal system and other organs', *Biomechanical Modeling in Mechanobiology* **2**, 139–155.
- Fung, Y. (1977), *A First Course in Continuum Mechanics*, Prentice-Hall.
- Fung, Y. (1993), *Biomechanics: Mechanical Properties of Living Tissues*, 2 edn, Springer.
- Gould, P., Ghista, D., Brombolich, L. & Mirsky, I. (1972), 'In-vivo stresses in the human left ventricular wall: Analysis accounting for the irregular 3-dimensional geometry and comparison with idealised geometry analyses', *Journal of Biomechanics* **5**, 521–539.
- Govindjee, S. & Mihalic, P. (1996), 'Computational methods for inverse finite elastostatics', *Computer Methods in Applied Mechanics and Engineering* **136**, 47–57.
- Govindjee, S. & Mihalic, P. (1998), 'Computational methods for inverse deformations in quasi-incompressible finite elasticity', *International Journal for Numerical Methods in Engineering* **43**, 821–838.
- Green, A. & Adkins, J. (1970), *Large Elastic Deformations*, 2 edn, Clarendon Press.
- Gudjonsson, T., Villadsen, R., Nielsen, H., Ronnov-Jessen, L., Bissell, M. & Petersen, O. (2002), 'Isolation, immortalization and characterization of a human breast epithelial cell line with stem cell properties', *Genes and Development* **16**, 693–706.
- Han, L., Noble, J. & Burcher, M. (2003), 'Novel ultrasound indentation system for measuring biomechanical properties of in vivo soft tissue', *Ultrasound in Medicine and Biology* **29**(6), 813–823.
- Hansen, R. & Bissell, M. (2000), 'Tissue architecture and breast cancer: The role of extracellular matrix and steroid hormones', *Endocrine-Related Cancer* **7**, 95–113.

- Hendriks, F., Brokken, D., Oomens, C., Bader, D. & Baaijens, F. (2006), 'The relative contributions of different skin layers to the mechanical behaviour of human skin in-vivo using suction experiments', *Medical Engineering & Physics* **28**, 259–266.
- Humphrey, J. (2002), *Cardiovascular Solid Mechanics - Cells, Tissues, and Organs*, Springer.
- Huyghe, J., vanCampen, D., Arts, T. & Heethaar, R. (1991a), 'The constitutive behaviour of passive heart muscle tissue: A quasi-linear viscoelastic formulation', *Journal of Biomechanics* **24**(9), 841–849.
- Huyghe, J., vanCampen, D., Arts, T. & Heethaar, R. (1991b), 'A two-phase finite element model of the diastolic left ventricle', *Journal of Biomechanics* **24**(7), 527–538.
- Interactive Mammography Analysis Web Tutorial* (1999), website by McGill Faculty of Medicine.
- Kita, Y., Highnam, R. & Brady, M. (1998), Correspondence between different view breast x-rays using a simulation of breast deformation, in 'Conference on Computer Vision and Pattern Recognition', IEEE Computer Society.
- Kopans, D. (2007), *Breast Imaging*, 3 edn, Lippincott Williams and Wilkins.
- Krouskop, T., Wheeler, T., Kallel, K., Garra, B. & Hall, T. (1998), 'Elastic moduli of breast and prostate tissues under compression', *Ultrasonic Imaging* **20**, 260–274.
- Kvistedal, Y. (2004), Multiaxial in-vivo testing of human skin, Master's thesis, Bio-engineering Institute: University of Auckland.
- Lee, A. (2006), Unloaded breast geometry, Technical report, University of Auckland.
- Lochter, A. & Bissell, M. (1995), 'Involvement of extracellular matrix constituents in breast cancer', *Seminars in Cancer Biology* **6**, 165–173.
- Lockett, F. (1972), *Nonlinear Viscoelastic Solids*, Academic Press.

- Malcolm, D., Nielsen, P., Hunter, P. & Charette, P. (2002), 'Strain measurement in biaxially loaded inhomogeneous, anisotropic elastic membranes', *Biomechanics and Modelling in Mechanobiology* **1**, 197–210.
- Malur, S., Wurdinger, S., Moritz, A., Michels, W. & Schneider, A. (2001), 'Comparison of written reports of mammography, sonography and magnetic resonance mammography for preoperative evaluation of breast lesions, with special emphasis on magnetic resonance mammography', *Breast Cancer Research* **3**, 55–60.
- Malvern, L. (1969), *Introduction to the Mechanics of a Continuous Medium*, Prentice-Hall.
- Mammograms: Room for Improvement Cited* (2004), Website article by American Cancer Society. American Cancer Society.
- Mansel, R. & Bundred, N. (1956), *Colour Atlas of Breast Diseases*, Mosby-Wolfe.
- Marias, K., Brady, J., Highnam, R., Parbhoo, S. & Seifalian, A. (1999), 'Registration and matching of temporal mammograms for detecting abnormalities', *Medical Image Analysis and Understanding*.
- McManaman, J. & Neville, M. (2003), 'Mammary physiology and milk secretion', *Advanced Drug Delivery Reviews* **55**, 629–641.
- Nash, M. (1998), Mechanics and Material Properties of the Heart using an Anatomically Accurate Mathematical Model, PhD thesis, University of Auckland.
- Netter, F. (1997), *Atlas of Human Anatomy*, 2 edn, Hoechstetter Printng Company.
- Nickerson, D. (2005), Cardiac Electr-Mechanics: From CellML to the Whole Heart, PhD thesis, Bioengineering Institute, University o Auckland.
- Nielsen, P. (1987), The Anatomy of the Heart: A Finite Element Model, PhD thesis, University of Auckland.
- Nielsen, P., LeGrice, I., Smaill, B. & Hunter, P. (1991), 'Mathematical model of geometry and fibrous structure of the heart', *American Journal of Physiology* **260**, H1365–H1378.

- Oden, J. (1972), *Finite Elements of Nonlinear Continua*, McGraw-Hill.
- Onnasch, D. & Prause, G. (1992), Geometric image correction and iso-center calibration at oblique biplane angiographic views, in 'Proceedings of Computers in Cardiology', pp. 647–650.
- Paszek, M. & Weaver, V. (2004), 'The tension mounts: Mechanics meets morphogenesis and malignancy', *Journal of Mammary Gland Biology and Neoplasia* **9**(4), 325–342.
- Pioletti, D. & Rakotomanana, L. (2000), 'Nonlinear viscoelastic laws for soft biological tissue', *European Journal of Mechanics A/Solids* **19**, 749–759.
- Press, W., Teukolsky, S., Vetterling, W. & Flannery, B. (1992), *Numerical Recipes in C*, 2 edn, Cambridge University Press.
- Researchers Study The Benefits of Using Ultrasound On Women With Dense Breast Tissue* (2002), website article by American Cancer Society.
- Riggio, E., Quattrone, P. & Nava, M. (2000), 'Anatomical study of the breast superficial fascial system: The inframammary fold unit', *European Journal of Plastic Surgery* **23**, 310–315.
- Rivlin, R. (1950), 'Large elastic deformations of isotropic materials VI. Further results in the theory of torsion, shear and flexure', *Philosophical Transactions A* **242**, 173–195.
- Rivlin, R. & Saunders, D. (1951), 'Large elastic deformations of isotropic materials. vii. experiments on the deformation of rubber', *Philosophical Transactions of the Royal Society of London. Series A, Mathematical and Physical Sciences* **243**(865), 251–288.
- Rohlfing, T. & Maurer, C. (2003), 'Volume-preserving nonrigid registration of mr breast images using free-form deformation with an incompressibility constraint', *IEEE Transactions on Medical Imaging* **22**(6), 730–741.
- Rueckert, D., Sonoda, L., Hayes, C., Hill, D., Leach, M. & Hawkes, D. (1999), 'Non-rigid registration using free-form deformations: application to breast mr images', *IEEE Transactions on Medical Imaging* **18**, 712–721.

- Ruiter, N. (2003), Registration of Mammograms and MR-Volumes of the Female Breast based on Simulated Mammographic Deformation, PhD thesis, Mannheim University.
- Ruiter, N. & Stotzka, R. (2006), 'Model-based registration of x-ray mammograms and mr images of the female breast', *IEEE Transactions on Nuclear Science* **53**(1), 204–211.
- Ruiter, N., Muller, T., Stotzka, R., Gemmeke, H., Reichenbach, J. & Kaiser, W. (2002), 'Automatic image matching for breast cancer diagnostics by a 3D deformation model of the mammary gland.', *Biomed Tech (Berl)* **47**(2), 644–7.
- Ruiter, N., Muller, T., Stotzka, R., Gemmeke, H., Reichenbach, J. & Kaiser, W. (2003), 'Finite element simulation of the breast's deformation during mammography to generate a deformation model for registration', *Bildverarbeitung fur die Medizin* pp. 86–90.
- Samani, A. & Plewes, D. (2004), 'A method to measure the hyperelastic parameters of ex-vivo breast tissue samples', *Physics in Medicine and Biology* **49**, 4395–4405.
- Samani, A., Bishop, J., Yaffe, M. & Plewes, D. (2001), 'Biomechanical 3D finite element modeling of the human breast using MRI data', *IEEE Trans Med Imaging* **20**(4), 271–9.
- Samani, A., Zubovits, J. & Plewes, D. (2007), 'Elastic moduli of normal and pathological breast tissues: An inversion-technique-based investigation of 169 samples', *Physics in Medicine and Biology* **52**, 1565–1576.
- Sarvazyan, A., Skovoroda, A., Emelianov, S., Fowlkes, J., Pipe, J., Adler, R., Buxton, R. & Carson, P. (1995), 'Biophysical bases of elasticity imaging', *Acoustic Imaging* **21**, 223–240.
- Schnabel, J., Tanner, C., Castellano-Smith, C., Leach, M., Hayes, C., Degenhard, A., Hose, R., Hill, D. & Hawkes, D. (2001), 'Validation of nonrigid registration using finite element methods', *Lecture Notes in Computer Science* **2082**, 344–357.

- Shim, V., Pitto, R., Streicher, R. & Anderson, I. (2006), Correlation between periacetabular bone density changes and stress distribution after total hip arthroplasty, in '52nd Annual Meeting of the Orthopaedic Research Society'.
- Sivaramakrishna, R. (2005), '3d breast image registration - a review', *Technology in Cancer Research & Treatment* **4**(1), 39–48.
- Smith, G. & Chepko, G. (2001), 'Mammary epithelial stem cells', *Microscopy Research and Technique* **52**, 190–203.
- Spencer, A. (1980), *Continuum Mechanics*, Longman Group.
- Tanner, C., Degenhard, A., Schnabel, J., Smith, A., Hayes, C., Sonoda, L., Leach, M., Hose, D., Hill, D. & Hawkes, D. (2001), A method for the comparison of biomechanical breast models, in 'Proceedings of the Workshop on Mathematical Methods in Biomedical Image Analysis', pp. 11–18.
- Tanner, C., Schnabel, J., Degenhard, A., Castellano Smith, A., Hayes, C., Leach, M., Rose, D., Hill, D. & Hawkes, D. (2002), Validation of volume-preserving non-rigid registration: Application to contrast-enhanced MR-mammography, in 'Medical Image Computing and Computer-Assisted Intervention (MICCAI 2002). Lecture notes in Computer Science', Vol. 2489-I, pp. 307–314.
- Tanner, C., Schnabel, J., Hill, D., Hawkes, D., Leach, M. & Hose, D. (2006), 'Factors influencing the accuracy of biomechanical breast models', *Medical Physics Journal* **33**(6), 1758–1769.
- Tot, T., Tabar, L. & Dean, P. (2002), *Practical Breast Pathology*, Thieme.
- Twizell, E. & Ogden, R. (1983), 'Nonlinear optimization of the material constants in ogden's stress-deformation function for incompressible isotropic elastic materials', *Journal of Australian Mathematics Society* pp. 424–434.
- Ultrasound Imaging of the Breasts* (2006), website article by Imaginis-The Breast Cancer Resource.
- Van Houten, E., Doyley, M., Kennedy, F., Weaver, J. & Paulsen, K. (2003), 'Initial in vivo experience with steady state subzone based mr elastography of the human breast', *Journal of Magnetic Resonance Imaging* **17**, 72–85.

- Vito, R. (1973), 'A note on arterial elasticity', *Journal of Biomechanics* **6**, 561–564.
- Vorherr, H. (1974), *The Breast: Morphology, Physiology and Lactation*, Academic Press Inc.
- Wellman, P. (1999), Tactile Imaging, PhD thesis, Harvard Univeerity.
- Wellman, P., Howe, R., Dalton, E. & Kern, K. (1999), Breast tissue stiffness in compression is correlated to histological diagnosis, Technical report, Harvard University.
- Williams, C. (2000), The biomechanics of normal breast tissue, PhD thesis, Ohio State University.
- Wirth, M. (2000), A Nonrigid Approach to Medical Image Registration: Matching Images of the Breast, PhD thesis, RMIT University.
- Wu, Z. & Sullivan, J. J. (2001), Automatic finite element mesh generation from mri scans for breast cancer investigations, in 'Proceedings of the IEEE 27th Annual Northeast Bioengineering Conference', pp. 59–60.
- Xiao, G., Brady, J., Noble, J., Burcher, M. & English, R. (2002), 'Nonrigid registration of 3d free hand ultrasound images of the breast', *IEEE Transactions on Medical Imaging* **21**, 405–412.
- Yu-Neifert, Q. (1995), A Three-Dimensional Finite Element Model to Predict The Applicability of Holographic Interferometry to Breast Tumour Detection, PhD thesis, Graduate Faculty of the University of Akron.
- Zhang, Z. (1998), 'Determining the epipolar geometry and its uncertainty: A review', *International Journal of Computer Vision* **27**(2), 161–195.
- Zienkiewicz, O. & Taylor, R. (2000a), *The Finite Element Method: Solid Mechanics*, Vol. 2, 5 edn, Butterworth-Heinemann.
- Zienkiewicz, O. & Taylor, R. (2000b), *The Finite Element Method: The Basis*, Vol. 1, 5 edn, Butterworth-Heinemann.